

Search for Higgs Bosons and Supersymmetric Particles in Tau Final States in Proton-Antiproton Collisions at 1.96 TeV

Dissertation zur Erlangung der Doktorwürde
Vorgelegt von

Ingo Torchiani



Fakultät für Mathematik und Physik
Albert-Ludwigs-Universität Freiburg

Dekan: Prof. Dr. Jörg Flum
Leiter der Arbeit: Prof. Dr. Karl Jakobs
Referent: Prof. Dr. Karl Jakobs
Koreferent: Prof. Dr. Ulrich Landgraf
Tag der Verkündigung
des Prüfungsergebnisses: 1. September 2008

*There are more things in heaven and earth, Horatio,
than are dreamt of in your philosophy.*

– Wm. Shakespeare, "Hamlet"

Contents

Introduction	ix
1 Theoretical Aspects	1
1.1 Standard Model	1
1.1.1 Quantum Chromodynamics	2
1.1.2 Electroweak Model	3
1.1.3 Higgs Sector	4
1.1.4 Problems of the Standard Model	6
1.2 Supersymmetry	8
1.2.1 Superfields	9
1.2.2 Lagrangian	10
1.2.3 Supersymmetry Breaking	12
1.2.4 R -Parity	12
1.2.5 Minimal Supersymmetric Standard Model	13
1.2.6 Phenomenological constraints	14
1.2.7 Higgs Sector	15
1.2.8 SUSY Mass Spectrum	17
1.2.9 Gravity Mediated Supersymmetry Breaking	18
1.2.10 Experimental Constraints	20
2 Phenomenology of $p\bar{p}$ Collisions	25
2.1 General Aspects	25
2.2 Factorization	27
2.3 Cross Section and Parton Distribution Functions	27
2.4 Luminosity	30
2.5 Event Generation	31
2.5.1 Parton Shower	31
2.5.2 Fragmentation	31
3 Accelerator and Detector	33
3.1 The Tevatron Accelerator	33
3.2 DØ Detector	35
3.2.1 Tracking Detector	36
3.2.2 Calorimeter System	39
3.2.3 Muon Spectrometer	41
3.2.4 Luminosity Monitor	42
3.2.5 Trigger and Data Acquisition	42
3.2.6 Detector Simulation	44

4	Event Reconstruction and Object Identification	47
4.1	Track Reconstruction	47
4.2	Primary Vertex	48
4.3	Muon Reconstruction and Identification	48
4.4	Tau Reconstruction and Identification	49
4.4.1	Reconstruction Algorithm	49
4.4.2	Classification of Tau Candidates	50
4.4.3	Neural Network	51
4.5	Jet Reconstruction and Identification	58
4.6	Missing Transverse Energy (\cancel{E}_T)	59
5	Data Samples and Monte Carlo Simulation	61
5.1	Data Samples	61
5.1.1	Trigger Selection	62
5.1.2	Integrated Luminosity	62
5.2	Monte Carlo Samples of Standard Model Processes	65
5.3	Monte Carlo Corrections	67
5.3.1	Trigger Efficiency	67
5.3.2	Muon Reconstruction and Identification Efficiency	68
5.3.3	Track Reconstruction Efficiency	70
5.3.4	Transverse Momentum Resolution of Tracks	70
5.3.5	Boson Momentum	71
6	Search for Neutral MSSM Higgs Bosons in $\mu\tau_h$ Final States	73
6.1	The MSSM Higgs Boson Signature at the Tevatron	73
6.1.1	Production Processes	74
6.1.2	Decay Channels	75
6.1.3	Signal Topology	77
6.1.4	Background from Standard Model Processes	77
6.2	Signal Monte Carlo Samples	78
6.3	Background Sample for Multi-Jet Events	78
6.4	Signal Selection	82
6.4.1	Preselection	82
6.4.2	Muon Veto	84
6.4.3	Tau Identification	86
6.4.4	W + Jet Background	88
6.5	Systematic Uncertainties	88
6.6	Results	90
6.7	Extraction of Cross Section Limits	92
6.7.1	Combination with Additional $\Phi \rightarrow \tau\tau$ Analyses	92
6.7.2	Combination with Additional $\Phi b(\bar{b}) \rightarrow b\bar{b}b(\bar{b})$ Analysis	98
6.8	Recent Results from the Tevatron and Outlook	102
7	Reconstruction of Low Energetic Tau Leptons	105
7.1	Motivation	105
7.2	Reconstruction and Identification	106
7.2.1	Reconstruction Algorithm	106

7.2.2	Application of a Likelihood	107
7.3	Data and Monte Carlo Samples	108
7.4	Selection of the Tau Mass Signal in $Z/\gamma^* \rightarrow \tau\tau$ Events	108
7.5	Results	114
8	Search for Associated Chargino/Neutralino Production in $\mu\tau_h\ell$ Final States	117
8.1	Trilepton Signature at the Tevatron	117
8.1.1	Production of Charginos and Neutralinos	117
8.1.2	Decay of Charginos and Neutralinos	119
8.1.3	Signal Topology	120
8.1.4	Background from Standard Model Processes	122
8.2	Signal Monte Carlo Samples	123
8.3	Tau Identification	125
8.4	Background Sample for Multi-Jet Events	125
8.5	Reference Signals	126
8.5.1	$Z/\gamma^* \rightarrow \mu\mu$	126
8.5.2	$Z/\gamma^* \rightarrow \tau\tau$	126
8.5.3	$W^\pm + \text{jets} \rightarrow \mu^\pm\nu_\mu + \text{jets}$	128
8.6	Trilepton Selection	129
8.6.1	Overview	129
8.6.2	Common Selection Criteria	134
8.6.3	Selection using an Isolated Track: $\mu + \tau_1 + \text{track}$	138
8.6.4	Selection using a Second Tau Lepton: $\mu + \tau_1 + \tau_2$	144
8.6.5	Selection using a Low Energetic Tau Lepton: $\mu + \tau_1 + \tau_{LP}$	146
8.7	Systematic Uncertainties	148
8.8	Results	151
8.8.1	The $\mu\tau_h\ell$ Result	151
8.8.2	Combination with Additional Trilepton Searches	157
8.9	Outlook	161
8.9.1	Projection for the Tevatron	161
8.9.2	Search for SUSY at the LHC	162
9	Summary	165
A	Statistical Methods	167
A.1	General Aspects	167
A.2	Confidence Level Computation for Combined Searches with Small Statistics	170
B	Estimation of the Multi-Jet Background for the Chargino/Neutralino Search	173
C	Generated mSURGA Monte Carlo Sample	181
	Lists of Tables and Figures	I
	Bibliography	XV
	Acknowledgements	XVII

Introduction

Elementary particle physics tries to find an answer to no minor question: What is our universe made of?

To our current knowledge, the elementary constituents of matter are quarks and leptons, which interact via four elementary forces: electromagnetism, strong force, weak force and gravity. All forces, except gravity, can be described in one framework, the Standard Model of particle physics. The model's name reflects its exceptional success in describing all available experimental high energy physics data to high precision up to energies of about 100 GeV. An exception is given by the neutrino masses but even these can be integrated into the model.

The Standard Model is based on the requirement of invariance of all physics processes under certain fundamental symmetry transformations. The consideration of these symmetries leads naturally to the correct description of the electromagnetic, weak and strong forces as the exchange of interaction particles, the gauge bosons. However, this formalism has the weakness that it only allows for massless particles. In order to obey the symmetries, a way to introduce the particle masses is given by the Higgs mechanism, which predicts the existence of the only particle of the Standard Model which has yet to be observed: the Higgs boson.

In spite of the success of the Standard Model, it has to be considered as a low energy approximation of a more profound theory for various reasons. For example, the underlying theory is expected to allow for an integration of gravity into the framework and to provide a valid particle candidate for the dark matter in our universe. Furthermore, a solution has to be found to the problem that the Higgs boson as a fundamental scalar is sensitive to large radiative corrections driving its mass to the Planck scale of 10^{19} GeV.

Several models have been proposed to address the remaining open questions of the Standard Model. Currently, the most promising extension of the Standard Model is Supersymmetry, which provides elegant solutions to the named problems by introducing a supersymmetric partner to each Standard Model particle. The superpartners of the matter particles are called squarks and sleptons, while the superpartners of the interaction particles are called gauginos. The mass eigenstates of the gauginos are referred to as charginos and neutralinos, according to their electric charge. Since the predicted supersymmetric particles have not yet been observed, Supersymmetry, if it exists in nature, has to be broken in such a way that the masses of Standard Model particles and of their superpartners differ.

During the last decades, the energies accessible to experiments has steadily increased. The Tevatron Accelerator at the Fermi National Accelerator Laboratory, with the two multipurpose experiments DØ and CDF, provides currently the highest center-of-mass energy ever reached in experiments using collisions of protons and antiprotons ($\sqrt{s} = 1.96$ TeV). The study of the particle collisions allows probing of predictions of the Standard Model and its extensions, e.g. Supersymmetry.

The present thesis describes two searches for particles predicted by the minimal supersymmetric extension of the Standard Model. The considered final states are two of the most promising channels for discovering Supersymmetry at the Tevatron.

Supersymmetry includes the existence of three neutral Higgs bosons (h , H and A). For large regions of the supersymmetric parameter space (at large values of the ratio of the vacuum expectation values of the Higgs fields, $\tan\beta$), an enhancement of the production cross section of the Higgs bosons compared to the Standard Model and a significant decay rate to pairs of tau leptons are expected. The first analysis searches for tau pairs in the final state consisting of a muon and a hadronically decaying tau:

$$p\bar{p} \rightarrow h/H/A \rightarrow \tau^- + \tau^+ \rightarrow \mu + \tau_h + X,$$

where τ_h indicates a hadronically decaying tau.

The second analysis searches for the so-called *trilepton signature* consisting of three charged leptons and missing transverse energy. This signature is expected to arise from the associated production of the lightest chargino and the second lightest neutralino. Again, the analysis focuses on the final state consisting of a muon, a hadronically decaying tau and a third charged lepton of any flavor:

$$p\bar{p} \rightarrow \tilde{\chi}_1^\pm \tilde{\chi}_2^0 \rightarrow \mu + \tau_h + \ell + X.$$

This final state includes the challenging scenario where decays into three tau leptons dominate if one tau decays into a muon. This is in particular expected in the parameter region of Supersymmetry with large values of $\tan\beta$. In order to efficiently reconstruct the signal consisting of leptons with soft transverse momenta, a reconstruction algorithm for low energetic tau leptons is developed. Although only a few Standard Model processes lead to the considered signature, background contributions arise from Standard Model processes with jets that are misidentified as hadronically decaying tau leptons.

Algorithms are developed for both analyses to efficiently separate the expected signals from Standard Model backgrounds and the obtained results are combined with searches in complementary final states.

In chapter 1, an introduction to the Standard Model of particle physics and to Supersymmetry is given where the focus lies on the minimal supersymmetric extension of the Standard Model. Chapter 2 provides an overview of the phenomenology of proton-antiproton collisions, which is followed by a description of the experimental setup in chapter 3. An overview of the reconstruction of the resulting objects of the proton-antiproton collision in the DØ detector is given in chapter 4, while a description of the data sets used is provided in chapter 5. Chapter 6 discusses in detail the search for Higgs bosons decaying to tau pairs including the combination of the results with searches for other final states. The reconstruction of low energetic tau leptons, which is developed for the search for the trilepton signature, is discussed in chapter 7. This analysis is covered in chapter 8.

Theoretical Aspects

This chapter provides a brief introduction to the Standard Model of particle physics and the aspects of Supersymmetry which are relevant for the analyses presented later in this thesis. Thorough introductions into the Standard Model are given in various text books [1, 2, 3], while Supersymmetry is extensively discussed in [4, 5, 6].

Throughout the present thesis *natural units* are used, unless noted otherwise. Within this system the reduced Planck constant \hbar and the speed of light c are $\hbar \equiv c \equiv 1$ and the dimensions of basic quantities can be written in terms of energy

$$[\text{energy}] = [\text{mass}] = [\text{momentum}] = [\text{time}]^{-1} = [\text{length}]^{-1} = [\text{cross section}]^{-2}. \quad (1.1)$$

The energy will be given in units of *electron-volt* (eV). One electron-volt is the amount of kinetic energy gained by an electron passing in vacuum through an electrostatic potential difference of one volt.

1.1 Standard Model

The Standard Model of particle physics is a gauge quantum field theory which describes elementary particles and their interactions. Developed in the second half of the last century, it provides a unified description of the electromagnetic, weak and strong interactions in form of a spontaneously broken $SU(3)_C \times SU(2)_L \times U(1)_Y$ symmetry. The matter components (summarized in Tab. 1.1) are described as fermionic elementary particles carrying spin $\frac{1}{2}$. Their interactions are described as an exchange of bosonic particles carrying spin 1, listed in Tab. 1.2. The Standard Model is an exceptionally successful model, which allows to describe all current high energy physics data to high accuracy up to energies of the order of 100 GeV [7]. An exception is given by the neutrino oscillation and the resulting consequence that neutrinos have small but non-zero masses [8]. But even the integration of the neutrino masses into the Standard Model is possible. However, gravity, the fourth fundamental interaction, evades its integration in form of a quantized theory, which is one of various reasons why the Standard Model is regarded only as an effective low-energy approximation of a more profound theory.

Fermions	Generation			Q [e]	T_3	$SU(3)_C$	$SU(2)_L$	$U(1)_Y$
Quarks	$\begin{pmatrix} u \\ d' \end{pmatrix}_L$	$\begin{pmatrix} c \\ s' \end{pmatrix}_L$	$\begin{pmatrix} t \\ b' \end{pmatrix}_L$	$\frac{2}{3}$	$\frac{1}{2}$	3	2	$\frac{1}{3}$
	u_R	c_R	t_R	$-\frac{1}{3}$	$-\frac{1}{2}$	3	1	$\frac{4}{3}$
	d_R	s_R	b_R	$\frac{2}{3}$	0	3	1	$\frac{4}{3}$
Leptons	$\begin{pmatrix} \nu_e \\ e \end{pmatrix}_L$	$\begin{pmatrix} \nu_\mu \\ \mu \end{pmatrix}_L$	$\begin{pmatrix} \nu_\tau \\ \tau \end{pmatrix}_L$	0	$\frac{1}{2}$	1	2	-1
	e_R	μ_R	τ_R	-1	$-\frac{1}{2}$	1	1	-2
				-1	0	1	1	-2

Table 1.1: The fermions of the Standard Model. The mixing of left handed (L) and right handed (R) eigenstates of the electroweak interaction results in the mass eigenstates. The primed symbols d' , s' , b' indicate the eigenstates of the electroweak interaction, which are connected by the Cabibbo–Kobayashi–Maskawa–Matrix to the mass eigenstates d , s and b . The discovery of neutrino oscillation requires that all neutrinos are massive [8]. As a consequence, they have also right handed contributions.

The Lagrangian \mathcal{L}_{SM} of the Standard Model, which allows to determine the equations of motion by minimizing the action $S = \int d^4x \mathcal{L}_{\text{SM}}$, comprises the terms of the strong interaction, which is described by Quantum Chromodynamics (QCD), the electroweak (EW) interaction and the contributions from the Higgs boson and its interactions:

$$\mathcal{L}_{\text{SM}} = \mathcal{L}_{\text{QCD}} + \mathcal{L}_{\text{EW}} + \mathcal{L}_{\text{Higgs}} + \mathcal{L}_{\text{Yukawa}}. \quad (1.2)$$

The structure of \mathcal{L}_{SM} is determined by symmetry transformations, under which the equations of motion are invariant and which comply with experimental data. The Lagrangian is required to be invariant under global transformations of the Poincaré group (rotations and Lorentz boosts $M^{\mu\nu}$ and translations P^μ)

$$\begin{aligned} [P^\mu, P^\nu] &= 0 \\ [M^{\mu\nu}, P^\sigma] &= -i(P^\mu g^{\nu\sigma} - P^\nu g^{\mu\sigma}) \\ [M^{\mu\nu}, M^{\sigma\tau}] &= i(M^{\mu\sigma} g^{\nu\tau} + M^{\nu\tau} g^{\mu\sigma} - M^{\mu\tau} g^{\nu\sigma} - M^{\nu\sigma} g^{\mu\tau}), \end{aligned} \quad (1.3)$$

with the metric $g_{\mu\nu} = \text{diag}(1, -1, -1, -1)$. Imposing local gauge invariance under $U(1)_Y$ and $SU(2)_L$ transformation, generated by the weak hypercharge Y and the weak isospin operators T_i , introduces the electroweak force. Local $SU(3)_C$ gauge invariance, generated by the eight color-charge operators λ_i , gives rise to the strong force.

1.1.1 Quantum Chromodynamics

The Lagrangian of Quantum Chromodynamics (QCD) describes the strong interactions of quarks and gluons

$$\mathcal{L}_{\text{QCD}} = \sum_{\text{flavors } f} i\bar{q}_f \not{D} q_f - \frac{1}{4} G_{\mu\nu}^i G_i^{\mu\nu}, \quad (1.4)$$

Bosons	Fields	Q [e]	T_3	$SU(3)_C$	$SU(2)_L$	$U(1)_Y$
$U(1)_Y$ gauge field	B	0	0	1	1	0
$SU(2)_L$ gauge field	W^1, W^2, W^3	1, 0, -1	1, 0, -1	1	3	0
$SU(3)_C$ gauge field	$G^1 \dots G^8$	0	0	8	1	0
Higgs field Φ	ϕ^+, ϕ^0	1, 0	$\frac{1}{2}, -\frac{1}{2}$	1	2	1

Table 1.2: The bosons of the Standard Model. The gauge fields carry spin 1, while the Higgs field carries spin 0.

where q_f is a color triplet of quarks of flavor f . The covariant derivative is defined as

$$D_\mu = \partial_\mu + ig \frac{\lambda_i}{2} G_\mu^i, \quad (1.5)$$

with $\not{D} = \gamma^\mu D_\mu$. The generators of the $SU(3)_C$ group are the Gell–Mann matrices λ_i ($i = 1 \dots 8$), G_μ^i describes the eight gluon field potentials and g is a dimensionless coupling strength.

The gluon fields carry color charge, which leads to gluon self interactions, as described by the gluon field tensor

$$G_{\mu\nu}^i = \partial_\mu G_\nu^i - \partial_\nu G_\mu^i - gf_{ijk} G_\mu^j G_\nu^k, \quad (1.6)$$

where f_{ijk} are the non-vanishing totally antisymmetric structure constants.

QCD was developed in the 1970s and in 2004 the Nobel Prize in Physics was awarded to F. Wilczek, D. Gross and D. Politzer for the discovery of *asymptotic freedom*, i.e. the fact that quarks and gluons inside a hadron behave like free particles, interacting with a high-energy probe at short distance. In depth treatment of QCD can be found e.g. in [9].

1.1.2 Electroweak Model

The theory of electroweak interactions, known as the Glashow-Weinberg-Salam model, is based on the gauge group $SU(2)_L \times U(1)_Y$. It unifies the electromagnetic and the weak force. The $SU(2)_L \times U(1)_Y$ group comprises four vector fields, three associated with $SU(2)_L$ denoted as W_μ^i ($i = 1, 2, 3$) and one associated with $U(1)_Y$ denoted as B_μ .

The left-handed fermions transform as doublet under $SU(2)_L$, while the right-handed fermions are singlets. Including the kinetic terms of the gauge bosons, the Lagrangian takes the form

$$\mathcal{L}_{EW} = i\bar{L}\not{D}L + i\bar{R}\not{D}R - \frac{1}{4}W_{\mu\nu}^i W_i^{\mu\nu} - \frac{1}{4}B_{\mu\nu} B^{\mu\nu}, \quad (1.7)$$

where L and R denote respectively the left-handed weak isospin doublets and right-handed isospin singlets as given in Tab. 1.1. To ensure gauge invariance, the covariant derivative D_μ is defined as

$$D_\mu = \partial_\mu + igT_i W_\mu^i + ig' \frac{Y}{2} B_\mu, \quad (1.8)$$

where the $SU(2)_L$ and $U(1)_Y$ couplings are given by g and g' and the generators of both groups are T_i and Y , respectively. Together with the electrical charge Q , the weak isospin T_i

and the weak hypercharge Y satisfy the relation $Q = T_3 + \frac{1}{2}Y$. The field strength tensors of the $SU(2)_L$ and $U(1)_Y$ gauge fields are given by

$$W_{\mu\nu}^i = \partial_\mu W_\nu^i - \partial_\nu W_\mu^i - g\epsilon_{ijk}W_\mu^jW_\nu^k \quad (1.9)$$

$$B_{\mu\nu} = \partial_\mu B_\nu - \partial_\nu B_\mu. \quad (1.10)$$

The term bilinear in $W_{\mu\nu}$ generates the trilinear and quadrilinear self-couplings of the W fields, which are typical for non-abelian gauge theories.

Experiments show that B_μ and W_μ^i do not carry the right quantum numbers to be identified as the observed gauge bosons γ , W^\pm and Z^0 . Instead, the electroweak eigenstates mix among themselves to give the mass eigenstates according to

$$A_\mu = B_\mu \cos \theta_W + W_\mu^3 \sin \theta_W \quad (1.11)$$

$$Z_\mu = -B_\mu \sin \theta_W + W_\mu^3 \cos \theta_W \quad (1.12)$$

$$W_\mu^\pm = \frac{1}{\sqrt{2}}(W_\mu^1 \mp iW_\mu^2), \quad (1.13)$$

with the weak mixing angle $\cos \theta_W = g/\sqrt{g^2 + g'^2}$. The electromagnetic charge is defined in terms of the electroweak charges and the weak mixing angle as $e = g \sin \theta_W = g' \cos \theta_W$.

1.1.3 Higgs Sector

Mass terms of the fermions and gauge bosons are introduced through spontaneous symmetry breaking by the *Higgs mechanism*. A complex scalar $SU(2)_L$ doublet, the Higgs field Φ , is postulated

$$\Phi = \begin{pmatrix} \phi^+ \\ \phi^0 \end{pmatrix} = \frac{1}{\sqrt{2}} \begin{pmatrix} \phi_1^+ + i\phi_2^+ \\ \phi_1^0 + i\phi_2^0 \end{pmatrix}. \quad (1.14)$$

Together with the corresponding Higgs potential

$$V = \mu^2|\Phi|^2 + \lambda|\Phi|^4 \quad (1.15)$$

and the covariant derivative as given in Eq. (1.8), this leads to the Lagrangian

$$\mathcal{L}_{\text{Higgs}} = |D_\mu \Phi|^2 - \mu^2 \Phi^\dagger \Phi - \lambda(\Phi^\dagger \Phi)^2. \quad (1.16)$$

The first term describes the coupling of the electroweak gauge fields and the Higgs field, which generates the masses of the gauge bosons. By choosing $\mu^2 < 0$ and $\lambda > 0$, a potential of the form given in Fig. 1.1 is obtained. The vacuum state corresponds to a certain choice within the continuous circular minimum. Therefore, the vacuum state has a lower symmetry than the potential V itself. This phenomenon is referred to as *spontaneous symmetry breaking*. The vacuum expectation value is chosen to be

$$\Phi_0 = \frac{1}{\sqrt{2}} \begin{pmatrix} 0 \\ v \end{pmatrix}, \quad v^2 = -\frac{\mu^2}{\lambda}. \quad (1.17)$$

Perturbation calculation converges only if it is expanded around the classical minimum. Therefore, the field Φ is expressed by

$$\Phi = \frac{1}{\sqrt{2}} \begin{pmatrix} 0 \\ v + h(x) \end{pmatrix} \quad (1.18)$$

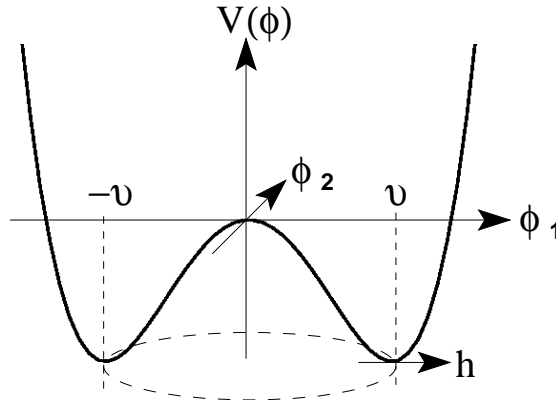


Figure 1.1: The Higgs potential V for the case of a single complex scalar field ϕ .

with the quantum fluctuation $h(x)$. Expressing the Lagrangian of Eq. (1.16) by $h(x)$ and v , one finds that it describes a scalar particle with a mass $M_h = \sqrt{-2\mu^2}$, which is referred to as the Standard Model Higgs boson. The Higgs boson represents one of the four degrees of freedom introduced in Eq. (1.14), while the other three correspond to the masses of the weak vector bosons. In other words, the massless Goldstone bosons introduced by the spontaneous symmetry breaking are turned into the longitudinal polarization of the massive gauge bosons. One finds that the masses of the electroweak gauge bosons are given by

$$M_W = \frac{1}{2}vg \quad M_Z = \frac{1}{2}v\sqrt{g^2 + g'^2} \quad M_\gamma = 0 \quad (1.19)$$

and that the relation

$$\cos \theta_W = \frac{M_W}{M_Z} \quad (1.20)$$

is predicted by the model. The introduction of the Higgs field generates not only the masses of the gauge bosons, also the masses of the fermions are generated by trilinear Yukawa couplings to the Higgs field:

$$\mathcal{L}_{\text{Yukawa}} = -g_f [\bar{L}\Phi R + \bar{R}\Phi_c L] \quad (1.21)$$

with $\Phi_c = -i\tau_2\Phi^*$. The coupling strength of the Higgs boson to a fermion is proportional to the fermion mass given by

$$m_f = \frac{g_f v}{\sqrt{2}}. \quad (1.22)$$

The coupling constants g_f are not predicted and may vary for each fermion. The couplings of the Higgs boson to fermions and massive gauge bosons are summarized in Tab. 1.3.

The Higgs boson is the only particle in the Standard Model which has not yet been observed. Direct searches for Standard Model Higgs bosons at the LEP experiments result in a lower limit on its mass at $M_h = 114.4$ GeV at the 95 % confidence level (CL) [11]. Searches at the Tevatron allow to set upper limits on the production cross section of Standard Model Higgs bosons but they are not yet sensitive to the Standard Model prediction, as shown in Fig. 1.2.

	Fermions	WW	ZZ
Φ	$-\frac{igm_f}{2M_W}$	$igM_W g^{\mu\nu}$	$\frac{igM_Z}{\cos\theta_W} g^{\mu\nu}$

Table 1.3: Couplings of the Standard Model Higgs boson to fermions and massive gauge bosons [10].

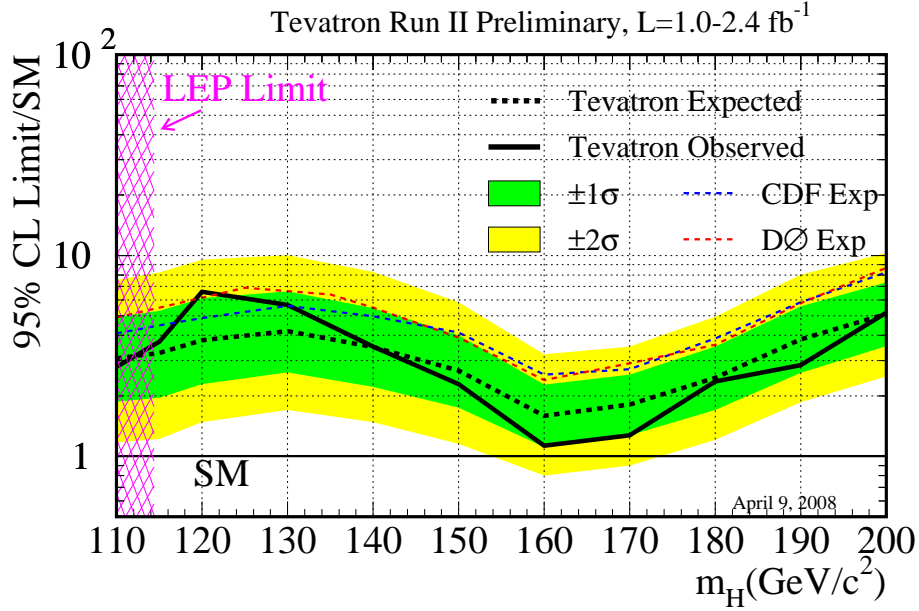


Figure 1.2: Tevatron limit at the 95 % CL on the Standard Model Higgs production cross section divided by the Standard Model prediction as a function of the Higgs mass [12].

As illustrated in Fig. 1.3, a combined fit of electroweak precision data from various measurements at LEP, SLC and at the Tevatron experiments DØ and CDF results in a preferred value for the Higgs boson mass at 87^{+36}_{-27} GeV, assuming the Standard Model to be the correct theory of nature. Since the LEP experiments exclude the region $M_h < 114$ GeV, a light Higgs boson above the LEP limit is expected. Including theoretical and experimental uncertainties, the electroweak precision measurements restrict the Higgs boson mass to $M_h < 160$ GeV at the 95 % CL.

1.1.4 Problems of the Standard Model

The Standard Model is extremely successful in describing all low-energy experimental data currently available. Additionally, it already has allowed for various predictions which could be confirmed by experiments. Nevertheless, the Standard Model is built on many assumptions and leaves many fundamental questions unanswered. Therefore, it is considered to be valid only as an effective low-energy theory. Some major open questions of the Standard Model are listed.

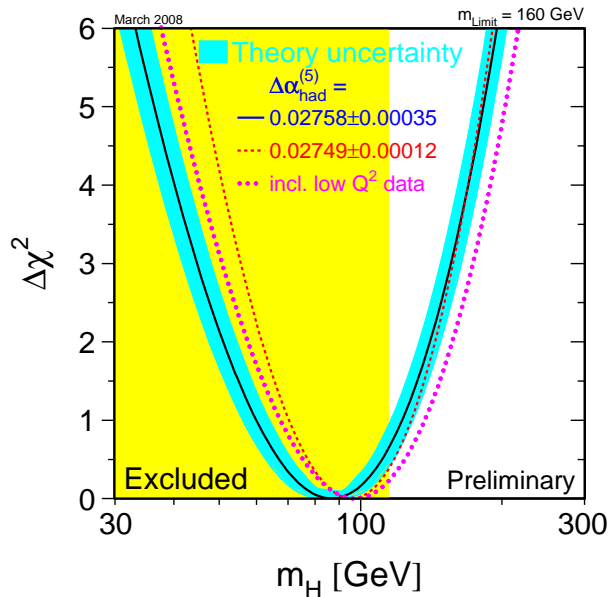


Figure 1.3: The resulting $\Delta\chi^2$ of a fit to electroweak precision data, assuming that the Standard Model provides the correct description of nature. Including low- Q^2 data, such as from the NuTeV collaboration, results in little effects on the fit [13].

- An obvious problem is that *gravity* refuses its integration into the framework of gauge theories. The Standard Model in its present form disregards all gravitational effects. This is a valid approximation at the energy scale that current experiments are operating at due to the weakness of gravity. But at the energy of the Planck Scale ($M_P = 1.2 \times 10^{19}$ GeV) gravity is expected to become strong and can not be neglected anymore. Furthermore, gravity is based on the principle of equivalence, while all phenomena of the Standard Model can be derived from the principle of local gauge invariance [4].
- A puzzling fact of the Standard Model is the *hierarchy* of the masses of the fermions. Why do they vary in the range from the electron neutrino with a mass smaller than 2.3 eV [14] to the top quark with a mass of 172.6 GeV [15]? Additionally, the Standard Model does not provide an explanation of the 17 orders of magnitude lying between the electroweak scale of the order of 100 GeV and the Planck Scale.

The introduction of the Higgs boson with an expected mass of the order of 100 GeV leads to the *fine tuning problem*, which has to be seen in the same context. Radiative corrections to the mass of the Higgs boson from fermion and gauge boson loops (Fig. 1.4) need to be calculated up to the energy scale Λ , to which the Standard Model is supposed to be valid. This implies quantum loop corrections to the squared Higgs mass that are quadratically divergent at the order of $\mathcal{O}(\Lambda^2)$. Standard Model particles as well as still unobserved particles contribute to these corrections. Assuming that the Standard Model is valid up to the Planck Scale, these corrections become extraordinary and need to be canceled by a precise tuning of the squared bare Higgs mass with an accuracy of about 10^{-34} . The cancellation might be feasible but seems to be unnatural [16].

- The Standard Model does not provide a *candidate particle for cold dark matter*. Only

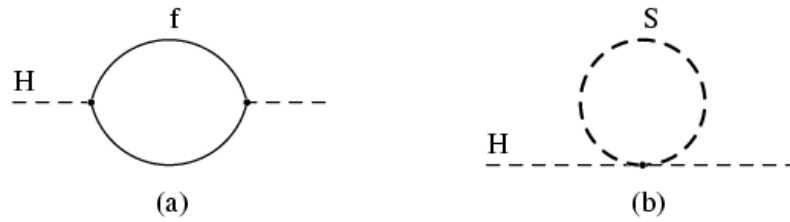


Figure 1.4: Radiative corrections to the squared Higgs boson mass from fermions (a) and bosons (b).

$\approx 4\%$ of the matter in the universe consists of baryonic matter, which belongs to the particle content of the Standard Model, while $\approx 21\%$ is considered as cold dark matter and is not part of the Standard Model. The remaining fraction is mainly assigned to dark energy, corresponding to a cosmological constant, and can not be explained by the Standard Model either [17].

- The running of the electroweak and strong coupling constants suggests a *unification of electroweak and strong force* at a higher energy scale. Extrapolating the currently measured values to higher energy, the coupling constants approach each other, as shown in Fig. 1.5 (left). In Grand Unified Theories (GUT) it is assumed that the three coupling constants meet, as illustrated in Fig. 1.5 (right). Typically, GUTs require a supersymmetric extension of the Standard Model.

1.2 Supersymmetry

In the early 1970s, Supersymmetry (SUSY) was introduced as an extension of the Standard Model [18, 19, 20]. SUSY is a symmetry between fermions and boson such that under global supersymmetry transformation the Lagrangian remains invariant. Obviously, this requires to assign to each particle of the Standard Model a superpartner, a *sparticle*, which is identical to the Standard Model particle in all quantum numbers except the spin, which differs by a half unit. Scalar *sfermions* are the superpartners of the fermions and fermionic *gauginos* are the superpartners of the gauge bosons. Additionally, the theory requires more than one complex Higgs doublet including their superpartners called *higgsinos*.

At first sight, SUSY seems to add complexity but the theory allows to solve various of the open questions of the Standard Model and currently it is considered to be one of the most promising extensions of the Standard Model. SUSY elegantly avoids the quadratically divergent loop corrections to the mass of the Higgs boson and it provides a candidate for the dark matter in the universe. The unification of the coupling constants of electroweak and strong interaction at a energy scale of about 10^{16} GeV seems to allow the formulation of the two forces as a low-energy manifestations of a single interaction, as illustrated in Fig. 1.5. In models requiring invariance of the Lagrangian under local supersymmetry transformations, a gravitational field is introduced naturally and the integration of gravity into a quantized theory can be achieved.

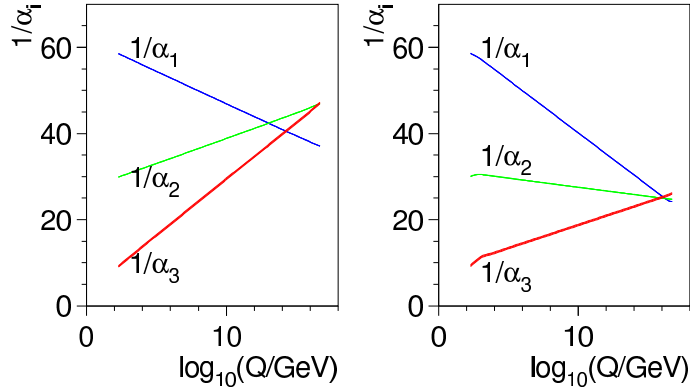


Figure 1.5: Energy scale dependence of the coupling constants in the Standard Model (left) and in a minimal supersymmetric scenario (right) [21].

Since particles and sparticles only differ in their spin, they are expected to have identical masses if SUSY is realized in nature. The fact that sparticles have not yet been observed implies that SUSY is a broken symmetry and that the sparticles are significantly heavier than the corresponding Standard Model partners. Nevertheless, solving the named problems of the Standard Model is still possible if the masses of the sparticles are in the range of $\mathcal{O}(0.1\text{-}1\text{ TeV})$.

The following sections provide a brief introduction into the concepts of Supersymmetry. The phenomenology will be explained in the context of the Minimal Supersymmetric extension of the Standard Model, which provides the theoretical framework for the interpretation of the results of the analyses presented in this thesis.

1.2.1 Superfields

Supersymmetry is a space–time symmetry which transforms bosonic states into fermionic states and vice versa through a fermionic operator Q :

$$Q|\text{Boson}\rangle = |\text{Fermion}\rangle; \quad Q|\text{Fermion}\rangle = |\text{Boson}\rangle. \quad (1.23)$$

The fermionic operator Q , which is an anticommuting spinor, has to satisfy the constraints of the Super–Poincaré algebra, an extension of the Poincaré algebra given in Eq. (1.3):

$$\{Q_\alpha, Q_\beta\} = \{\bar{Q}_{\dot{\alpha}}, \bar{Q}_{\dot{\beta}}\} = 0 \quad (1.24)$$

$$\{Q_\alpha, \bar{Q}_{\dot{\beta}}\} = 2(\sigma^\mu)_{\alpha\dot{\beta}}P_\mu \quad (1.25)$$

$$[P_\mu, Q_\alpha] = 0 \quad (1.26)$$

$$[M_{\mu\nu}, Q_\alpha] = -i(\sigma_{\mu\nu})_{\alpha\beta}Q_\beta, \quad (1.27)$$

with the Pauli Spin matrices σ^i , $\sigma^\mu = (\sigma^0, \sigma^i)$ and $\sigma_{\mu\nu} = \frac{i}{4}(\sigma_\mu\bar{\sigma}_\nu - \sigma_\nu\bar{\sigma}_\mu)$. The concept of a superfield $\Phi(x^\mu, \theta^\alpha, \bar{\theta}_{\dot{\alpha}})$ being the generator of the components of the supersymmetric multiplets was proposed by Salam and Strathdee [22, 23]. Space–time is extended by four fermionic coordinates described as elements of a Majorana spinor. The anticommuting

Grassmann spinors θ^α and $\bar{\theta}^{\dot{\alpha}} = \theta^{\alpha*}$ ($\alpha = 1, 2$) satisfying

$$\begin{aligned}\{\theta^\alpha, \theta^\beta\} &= \{\bar{\theta}_{\dot{\alpha}}, \bar{\theta}_{\dot{\beta}}\} = \{\theta^\alpha, \bar{\theta}_{\dot{\alpha}}\} = 0 \\ [x^\mu, \theta^\alpha] &= [x^\mu, \bar{\theta}_{\dot{\alpha}}] = 0\end{aligned}\quad (1.28)$$

are used to identify points in superspace $z = (x^\mu, \theta^\alpha, \bar{\theta}_{\dot{\alpha}})$. The generators of SUSY transformations Q_α and $\bar{Q}_{\dot{\alpha}}$ are given by the differential operators in superspace

$$Q_\alpha = \frac{\partial}{\partial \theta^\alpha} - i\sigma^\mu_{\alpha\dot{\beta}} \bar{\theta}^{\dot{\beta}} \partial_\mu, \quad \bar{Q}_{\dot{\alpha}} = -\frac{\partial}{\partial \bar{\theta}^{\dot{\alpha}}} + i\theta^\beta \sigma_{\beta\dot{\alpha}}^\mu \partial_\mu. \quad (1.29)$$

The different components of the supermultiplet can be obtained from the Taylor expansion of the superfield in the variables θ^α and $\bar{\theta}_{\dot{\alpha}}$. The resulting representation is reducible to an irreducible vector multiplet and an irreducible chiral multiplet. Superfields satisfying $\Phi = \Phi^*$ are called *vector superfield* and describe the spin 1 gauge bosons and their spin $\frac{1}{2}$ superpartners, the gauginos. In the Wess-Zumino gauge, a vector superfield can be written as

$$V(x, \theta, \bar{\theta}) = \theta \bar{\sigma}^\mu \bar{\theta} A_\mu(x) + i\theta^2 \bar{\theta} \bar{\lambda}(x) - i\theta \bar{\theta}^2 \lambda(x) + \frac{1}{2} \theta^2 \bar{\theta}^2 D(x). \quad (1.30)$$

The gauge bosons are assigned to the vector field A^μ , while the Weyl spinors λ and D correspond to the gauginos and to an auxiliary field, which leads to purely algebraic equations of motion and does not obtain a kinetic term. A chiral superfield describes spin 0 bosons and spin $\frac{1}{2}$ fermions:

$$\begin{aligned}\Phi(x, \theta, \bar{\theta}) &= \phi(x) - i\theta \sigma^\mu \bar{\theta} \partial_\mu \phi(x) - \frac{1}{4} \theta^2 \bar{\theta}^2 \partial_\mu^2 \phi(x) \\ &+ \sqrt{2} \theta \psi(x) + \frac{i}{\sqrt{2}} \theta^2 \partial_\mu \psi(x) \sigma^\mu \bar{\theta} + \theta^2 F(x).\end{aligned}\quad (1.31)$$

The complex scalar field ϕ corresponds to the Higgs bosons and sfermions, while the higgsinos and fermions are represented by the Weyl spinor ψ . The complex scalar F is an auxiliary field. The corresponding *antichiral superfield* is given by Φ^\dagger . The product of two chiral (antichiral) superfields is a chiral (antichiral) superfield, while the product of a chiral and an antichiral superfield is a vector superfield. The operators

$$D_\alpha = \frac{\partial}{\partial \theta^\alpha} - 2i(\sigma^\mu \theta)_\alpha \frac{\partial}{\partial y^\mu}, \quad \bar{D}_{\dot{\alpha}} = -\frac{\partial}{\partial \bar{\theta}^{\dot{\alpha}}}\quad (1.32)$$

with $y^\mu = x^\mu - i\theta \sigma^\mu \bar{\theta}$ are considered as the superspace covariant derivatives.

1.2.2 Lagrangian

The supersymmetric Lagrangian involves the matter fields given by the chiral superfields Φ and the gauge fields given by the vector superfield V . The integral of products of superfields results in the gauge and supersymmetrically invariant action

$$S = \int d^8 z \Phi^\dagger e^{gT^a V^a} \Phi + \int d^6 z \left(\frac{1}{4} W^{a\alpha} W_\alpha^a + W(\Phi) + \text{h.c.} \right). \quad (1.33)$$

The volume element of superspace is given by $d^8 z = d^4 x d^2 \theta^2 d\bar{\theta}^2$ and the integration over Grassmann variables is defined as

$$\int d\theta_a = 0, \quad \int \theta_a d\theta_b = \delta_{ab}. \quad (1.34)$$

Expanding the first term of Eq. (1.33) shows that it includes the kinetic terms for scalar and fermion fields together with their gauge interactions

$$\begin{aligned}\mathcal{L}_{\text{gauge-kin}} &= \int d\theta^2 d\bar{\theta}^2 \Phi^\dagger e^{gT^a V^a} \Phi \\ &= (D^\mu \phi)^*(D_\mu \phi) - i\psi^\dagger \bar{\sigma}^\mu D_\mu \psi - F^* F \\ &\quad - \sqrt{2}g \left[(\phi^* T^a \psi) \lambda^a + \lambda^{\dagger a} (\psi^\dagger T^a \phi) \right] + g(\phi^* T^a \phi) D^a,\end{aligned}\quad (1.35)$$

with the gauge covariant derivative $D_\mu = \partial_\mu + igA_\mu^a T^a$ and the group generators T^a . The first term represents the kinetic terms of all sfermions and Higgs boson, followed by the kinetic term of the all fermions and higgsinos and the contribution from the auxiliary field F . Term four introduces a new type of interaction between fermionic matter fields ψ , its scalar partner ϕ and the gaugino λ . Its strength is determined by the gauge coupling g even if it is not a typical gauge interaction. Since the field D^a can be interpreted as $-g\phi^* T^a \phi$, the last term yields quadrilinear interactions among scalar fields whose strength is also given by the gauge coupling.

Considering $W_\alpha^a = -\frac{1}{4}\bar{D}_{\dot{\alpha}}\bar{D}^{\dot{\alpha}}e^{-V^a}D_\alpha e^{V^a}$ with D_α defined in Eq. (1.32), the second term of Eq. (1.33) proves to represent the dynamics of the gauge fields

$$\mathcal{L}_{\text{SYM}} = \frac{1}{4} \int d^2\theta W^{a\alpha} W_\alpha^a + \text{h.c.} = -\frac{1}{4} F_{\mu\nu}^a F^{\mu\nu a} + i\lambda^{\dagger a} \bar{\sigma}^\mu D_\mu \lambda^a + \frac{1}{2} D^a D^a. \quad (1.36)$$

The self-interactions and the kinetic energies of the gauge bosons are described by the Yang–Mill field strength $F_{\mu\nu}^a = \partial_\mu A_\nu^a - \partial_\nu A_\mu^a - g f^{abc} A_\mu^b A_\nu^c$ and the structure constants of the corresponding gauge group f^{abc} , while the second term represents the dynamics of the gauginos, including their coupling to the gauge field. The contribution of the auxiliary field D^a is referred to as D -term.

The third term of the Lagrangian in Eq. (1.33) is determined by the contributions of the superpotential

$$W(\Phi) = k^i \Phi_i + \frac{1}{2} m^{ij} \Phi_i \Phi_j + \frac{1}{6} y^{ijk} \Phi_i \Phi_j \Phi_k, \quad (1.37)$$

where the Φ_i are chiral superfields, while m^{ij} and y^{ijk} are the mass and Yukawa matrices, respectively. In a renormalizable theory, the superpotential is an at most cubic polynomial in ϕ resulting in the following contributions to the Lagrangian

$$\mathcal{L}_{\text{int}} = \int d^2\theta W(\Phi) + \text{h.c.} = - \sum_j \left| \frac{\partial W}{\partial \phi_j} \right|^2 - \frac{1}{2} \sum_{jk} \frac{\partial^2 W}{\partial \phi_j \partial \phi_k} \psi_j \psi_k + \text{h.c.} \quad (1.38)$$

The first part is referred to as F -term since the auxiliary field of Eq. (1.35) can be written as $F_i = -[\partial W(\Phi)/\partial \phi_i]^*$. It describes scalar mass terms and scalar interactions. The second term introduces fermion masses and interactions of two fermions and a scalar, including the Standard Model Yukawa couplings.

The scalar potential of the theory is given by the part of the Lagrangian containing neither derivatives nor fermions:

$$V = F^* F + \frac{1}{2} D^2. \quad (1.39)$$

1.2.3 Supersymmetry Breaking

Supersymmetry, if it is realized in nature, has to be a broken symmetry since the masses of the Standard Model particles and their superpartners are observed to be different.

Calculating the vacuum expectation value from Eq. (1.25) results in

$$\langle 0|Q_\alpha\bar{Q}_{\dot{\beta}} + \bar{Q}_{\dot{\beta}}Q_\alpha|0\rangle = 2\langle 0|H|0\rangle \quad \text{and} \quad |Q_\alpha|0\rangle|^2 = \langle 0|H|0\rangle. \quad (1.40)$$

If the vacuum state has zero energy, Supersymmetry is unbroken. A vacuum expectation value, which breaks Supersymmetry, is introduced by requiring

$$\langle 0|H|0\rangle = \langle 0|V|0\rangle \neq 0 \quad (1.41)$$

for the scalar potential V of Eq. (1.39). This can be achieved by $\langle 0|F|0\rangle \neq 0$, $\langle 0|D|0\rangle \neq 0$ or both. The two cases are called F -type and D -type supersymmetry breaking. For the F -type model, introduced by O’Raifeartaigh in 1975 [24], it is essential that $k_i \neq 0$ in the superpotential. Based on three interacting chiral superfield, a superpotential is constructed resulting in a vacuum expectation value. Breaking Supersymmetry by D -term contributions is achieved by introducing a term to the Lagrangian which is linear in the gauge superfield V and corresponds to an additional term kD in the scalar potential of the theory. This type of SUSY breaking was suggested by Fayer and Iliopoulos in 1974 [25].

Currently, there is no consensus about the mechanism that causes supersymmetry breaking although it is one of the major focuses of research on Supersymmetry. Various models of supersymmetry breaking have been proposed, typically involving new particles and interactions at high mass scales. The *gravity mediated supersymmetry breaking* and the *gauge mediated supersymmetry breaking* are F -type breaking models [5, 6]. Further models are the *anomalous $U(1)$ mediated supersymmetry breaking* [26, 27], which is motivated by string theory, and the *conformal anomaly mediated supersymmetry breaking* [28], which has been introduced during the last years.

Supersymmetry needs to be broken *softly*, meaning that the theory remains renormalizable and the resulting mass terms are small enough not to re-introduce the problem of quadratic divergences in the calculation of loop corrections to the squared Higgs mass. Therefore, the only mass terms that can be introduced to the Lagrangian are:

- Scalar mass terms $\mu^2\phi^*\phi$;
- Mass terms for the gauginos $m_k\lambda_k\lambda_k$;
- Trilinear scalar interactions origination from the superpotential $W(\Phi)|_{\theta=0}$.

These terms are sufficient to construct realistic supersymmetric models.

1.2.4 R -Parity

Supersymmetry allows to introduce a multiplicative quantum number, called R -parity [29], using the baryon number B , the lepton number L and the spin S of a particle

$$R \equiv (-1)^{3(B-L)+2S}. \quad (1.42)$$

As a consequence, all Standard Model particles have R -parity $+1$, while all new particles predicted by Supersymmetry have R -parity -1 . Requiring the conservation of R -parity implies important phenomenological consequences:

- Supersymmetric particles are always produced in pairs.
- The lightest supersymmetric particle (LSP) is stable.
- All decays of sparticles result in an odd number of LSPs.

Due to strong cosmological constraints on the LSP, it is assumed to be interacting only weakly and to provide a viable candidate for cold dark matter [30]. Current available data does neither allow to observe nor to rule out the R -parity violation (RPV). However, there are strong bounds on RPV, e.g. from the non-observation of the proton decay. The lifetime of a proton is measured to be larger than $10^{32} - 10^{33}$ s [31, 32]. In the present thesis, only R -parity conserving models are considered.

1.2.5 Minimal Supersymmetric Standard Model

In the preceding discussion general Supersymmetry was considered, while all following sections focus on the the Minimal Supersymmetric extension of the Standard Model (MSSM) [33, 34]. The MSSM has to be regarded as a low-energy effective supersymmetric theory, which allows to predict phenomenological consequences and observable implications. The field content of the MSSM is summarized in Tab. 1.4, with the Lagrangian

$$\mathcal{L}_{\text{MSSM}} = \mathcal{L}_{\text{gauge-kin}} + \mathcal{L}_{\text{SYM}} + \mathcal{L}_{\text{int}} + \mathcal{L}_{\text{soft}} \quad (1.43)$$

and the superpotential

$$W_{\text{MSSM}} = \bar{u}\mathbf{y}_u Q H_u - \bar{d}\mathbf{y}_d Q H_d - \bar{e}\mathbf{y}_e L H_d + \mu H_u H_d \quad (1.44)$$

with the 3×3 matrices $\mathbf{y}_{\mathbf{u},\mathbf{d},\mathbf{e}}$ as dimensionless Yukawa coupling parameters in generation space. According to Sec. 1.2.3, the most general set of supersymmetry breaking terms can be written as

$$\begin{aligned} \mathcal{L}_{\text{soft}} = & -\frac{1}{2} \left(M_1 \tilde{B} \tilde{B} + M_2 \tilde{W} \tilde{W} + M_3 \tilde{g} \tilde{g} \right) + \text{h.c.} \\ & - \left(\tilde{u} \mathbf{a}_u \tilde{Q} H_u - \tilde{d} \mathbf{a}_d \tilde{Q} H_d - \tilde{e} \mathbf{a}_e \tilde{L} H_d \right) + \text{h.c.} \\ & - \tilde{Q}^* \mathbf{m}_Q^2 \tilde{Q} - \tilde{L}^* \mathbf{m}_L^2 \tilde{L} - \tilde{u}^* \mathbf{m}_u^2 \tilde{u} - \tilde{d}^* \mathbf{m}_d^2 \tilde{d} - \tilde{e}^* \mathbf{m}_e^2 \tilde{e} \\ & - m_{H_u}^2 H_u^* H_u - m_{H_d}^2 H_d^* H_d - (b H_u H_d + \text{h.c.}). \end{aligned} \quad (1.45)$$

The first line introduces the mass terms for gauginos with the mass parameter M_1 , M_2 and M_3 for bino, wino and gluino. The complex matrices $\mathbf{a}_{\mathbf{u},\mathbf{d},\mathbf{e}}$ in generation space result in additional mass terms corresponding to the Yukawa couplings arising from the superpotential. The third line introduces additional mass term for squarks and sleptons, with the 3×3 matrices in generation space $\mathbf{m}_{\mathbf{Q},\mathbf{L},\tilde{\mathbf{u}},\tilde{\mathbf{d}},\tilde{\mathbf{e}}}$. The last line adds contributions to the Higgs masses, parameterized by the Higgs mass parameters $m_{H_u}^2$ and $m_{H_d}^2$ and the bilinear coupling b . In order to solve the hierarchy problem, the parameters should introduce masses at the scale $M_{\text{soft}} \approx 1$ TeV, with $m_i, \mathbf{a}_i \sim m_{\text{soft}}$ and $\mathbf{m}_1^2, m_{H_u}^2, m_{H_d}^2, b \sim M_{\text{soft}}^2$.

Chiral Superfields (Φ)		Spin 0 (ϕ)	Spin $\frac{1}{2}$ (ψ)	$SU(3)_C$	$SU(2)_L$	$U(1)_Y$
Squarks, Quarks	Q	$(\tilde{u}_L, \tilde{d}_L)$	(u_L, d_L)	3	2	$\frac{1}{3}$
	\bar{u}	\tilde{u}_R^*	u_R^\dagger	$\bar{\mathbf{3}}$	1	$-\frac{4}{3}$
	\bar{d}	\tilde{d}_R^*	d_R^\dagger	$\bar{\mathbf{3}}$	1	$\frac{2}{3}$
Sleptons, Leptons	L	$(\tilde{\nu}_L, \tilde{e}_L)$	(ν_L, e_L)	1	2	-1
	e	\tilde{e}_R^*	e_R^\dagger	1	1	2
Higgs, Higgsinos	H_u	(H_u^+, H_u^0)	$(\tilde{H}_u^+, \tilde{H}_u^0)$	1	2	1
	H_d	(H_d^0, H_d^-)	$(\tilde{H}_d^0, \tilde{H}_d^-)$	1	2	-1
Vector Superfields (V)		Spin $\frac{1}{2}$ (λ)	Spin 1 (A)	$SU(3)_C$	$SU(2)_L$	$U(1)_Y$
Gluinos, Gluons		$\tilde{G}^1 \dots \tilde{G}^8$	$G^1 \dots G^8$	8	1	0
Winos, W bosons		$\tilde{W}^1, \tilde{W}^2, \tilde{W}^3$	W^1, W^2, W^3	1	3	0
Bino, B boson		\tilde{B}	B	1	1	0

Table 1.4: Superfield content of the MSSM.

1.2.6 Phenomenological constraints

The intention of introducing Supersymmetry is to provide an organizing principle comprising the Standard Model. But the required supersymmetry breaking term $\mathcal{L}_{\text{soft}}$ introduces more than 100 additional masses, phases and mixing angles. This large degree of arbitrariness can be significantly reduced by several assumptions based on experimental evidences [35].

Boundaries on lepton number violation result in tight boundaries on the off-diagonal elements of the slepton mass matrices \mathbf{m}_L and \mathbf{m}_e . Especially, the constrain on the muon decay mode $\text{BR}(\mu \rightarrow e\gamma) < 1.210^{-11}$ [36] places strong limits. The strongest limits on the squark mass matrices \mathbf{m}_Q , \mathbf{m}_u and \mathbf{m}_d arise from the $K^0 - \bar{K}^0$ mixing, which affect the d–squark and s–squark mixing and CP violating phases. Further constraints result from $D^0 - \bar{D}^0$ and $B^0 - \bar{B}^0$ mixing. Via loop contributions, flavor changing neutral currents (FCNC) arising from the trilinear coupling of the Higgs bosons and sfermions, contribute to the interactions of the Standard Model. Strong experimental boundaries also exist for these effects, limiting the off–diagonal elements of the matrices \mathbf{a}_u , \mathbf{a}_d and \mathbf{a}_e . The assumption of *soft breaking universality* combines these constraints:

- The squark and slepton matrices are flavor–blind:

$$\mathbf{m}_Q^2 = m_Q^2 \mathbf{1}, \quad \mathbf{m}_{\bar{u}}^2 = m_{\bar{u}}^2 \mathbf{1}, \quad \mathbf{m}_d^2 = m_d^2 \mathbf{1}, \quad \mathbf{m}_L^2 = m_L^2 \mathbf{1}, \quad \mathbf{m}_e^2 = m_e^2 \mathbf{1}. \quad (1.46)$$

- The trilinear couplings of three scalars are proportional to the Yukawa coupling matrices:

$$\mathbf{a}_u = A_u \mathbf{y}_u, \quad \mathbf{a}_d = A_d \mathbf{y}_d, \quad \mathbf{a}_e = A_e \mathbf{y}_e. \quad (1.47)$$

- The only CP violation phase in the MSSM is the one found in the Cabibbo–Kobayashi–Maskawa–Matrix.

Models based on these or similar constraints are referred to as *phenomenological* MSSM [37], in which the number of free parameters is reduced to 22:

- 3 gaugino masses M_1 , M_2 and M_3 ;
- 5 sfermion masses of the first two generations $m_{\tilde{e}_R}$, $m_{\tilde{e}_L}$, $m_{\tilde{u}_R}$, $m_{\tilde{d}_R}$ and $m_{\tilde{q}_L}$;
- 5 sfermion masses of the third generation $m_{\tilde{\tau}_R}$, $m_{\tilde{\tau}_L}$, $m_{\tilde{b}_R}$, $m_{\tilde{t}_R}$ and $m_{\tilde{q}_L^3}$;
- 6 trilinear couplings A_u , A_d , A_e , A_t , A_b and A_τ ;
- 3 parameters that specify the Higgs sector M_A , $\tan\beta$ and μ (see Sec. 1.2.7).

1.2.7 Higgs Sector

In contrast to the Standard Model the MSSM predicts two complex Higgs doublets as indicated in Tab. 1.4, which are required to generate the masses of up-type and down-type fermions and to avoid gauge anomalies [38]. Without loss of generality one can chose $H_u^+ = H_d^- = 0$, implying that the charged component can not get vacuum expectation values and that at the minimum of the Higgs potential electromagnetism is unbroken. The remaining Higgs potential has the form

$$\begin{aligned}
 V_{\text{Higgs}} &= (|\mu|^2 + m_{H_u}^2) |H_u^0|^2 + (|\mu|^2 + m_{H_d}^2) |H_d^0|^2 - (bH_u^0 H_d^0 + \text{h.c.}) \\
 &\quad + \frac{1}{8} (g^2 + g'^2) (|H_u^0|^2 - |H_d^0|^2)^2.
 \end{aligned}
 \tag{1.48}$$

In the configuration of parameters allowing for electroweak symmetry breaking ($2b < 2|\mu|^2 + m_{H_u}^2 + m_{H_d}^2$, $(|\mu|^2 + m_{H_u}^2)(|\mu|^2 + m_{H_d}^2) < b^2$), the potential obtains a shape as in case of the Standard Model, and the vacuum expectation values of the two Higgs fields can be generality chosen to

$$\langle H_u^0 \rangle = v_u \quad \langle H_d^0 \rangle = v_d,
 \tag{1.49}$$

with their ratio typically defined as

$$\tan\beta = \frac{v_u}{v_d}.
 \tag{1.50}$$

The vacuum expectation values are related to the mass of the Z boson according to

$$v^2 = v_u^2 + v_d^2 = \frac{2M_Z^2}{g^2 + g'^2} \approx (174 \text{ GeV})^2.
 \tag{1.51}$$

Electroweak symmetry breaking absorbs three of the eight degrees of freedom of the two complex Higgs doublets into the masses of the Z^0 and W^\pm bosons. The remaining five degrees of freedom correspond to one CP-odd neutral scalar A , two charged scalars H^\pm and two CP-even neutral scalars h and H . The masses at tree-level are determined only by two parameters, generally chosen to be $\tan\beta$ and M_A :

$$\begin{aligned}
 M_A^2 &= \frac{2b}{\sin 2\beta} \\
 M_{H^\pm}^2 &= M_A^2 + M_W^2 \\
 M_{h,H}^2 &= \frac{1}{2} \left(M_A^2 + M_Z^2 \mp \sqrt{(M_A^2 + M_Z^2)^2 - 4M_Z^2 M_A^2 \cos 2\beta} \right).
 \end{aligned}
 \tag{1.52}$$

MSSM Higgs	$b\bar{b}, \tau^+\tau^-$	$t\bar{t}$	WW, ZZ
h	$-\frac{\sin\alpha}{\cos\beta}$	$\frac{\cos\alpha}{\sin\beta}$	$\sin(\beta - \alpha)$
H	$\frac{\cos\alpha}{\cos\beta}$	$\frac{\sin\alpha}{\sin\beta}$	$\cos(\beta - \alpha)$
A	$\tan\beta$	$\cot\beta$	–

Table 1.5: Factors to Higgs boson couplings to fermions and massive gauge bosons predicted by the MSSM with respect to the Standard Model calculation at leading order. The terms are identical for all three generations [10].

Most of the experimental data are interpreted in models assuming CP conservation in the Higgs sector, although in general CP violation in the MSSM Higgs sector can not be excluded. The relations of Eq. (1.52) imply an upper bound on the mass of the lightest neutral Higgs boson at tree-level

$$M_h < |\cos 2\beta| M_Z. \quad (1.53)$$

However, there are significant quantum corrections especially from top–stop–loop diagrams [39] which relax the bound to

$$M_h \lesssim 135 \text{ GeV}. \quad (1.54)$$

At tree-level, the predicted couplings of the neutral MSSM Higgs bosons to fermions and massive gauge bosons is modified compared to the Standard Model by the factors given in Tab. 1.5. The angle α describes the mixing of $H_{u,d}$ to the mass eigenstates h and H :

$$\frac{\sin 2\alpha}{\sin 2\beta} = -\frac{M_A^2 + M_Z^2}{M_H^2 - M_h^2}. \quad (1.55)$$

In the decoupling limit $M_A \gg M_Z$, the masses of A , H and H^\pm are much heavier than M_h and nearly degenerate, while h has the same couplings to quark, leptons and gauge bosons as a Higgs boson in the Standard Model without Supersymmetry.

Benchmark Scenarios

Different benchmark scenarios have been proposed for the interpretation of experimental results [40]. Through radiative corrections, the masses and coupling of the MSSM Higgs sector depend on several parameters in addition to $\tan\beta$ and M_A . Assuming unification of $SU(2)$ and $U(1)$ gaugino masses, the most relevant parameters are the trilinear coupling in the stop sector A_t , the Higgs mass parameter μ , the gaugino mass term M_2 , the gluino mass $m_{\tilde{g}}$ and a common scalar mass M_{SUSY} . Typically A_t is replaced by the stop mixing parameter $X_t = A_t - \mu \cot\beta$. In the presented thesis two benchmark scenarios are considered:

- *m_h^{max} scenario*: The parameters are chosen such that M_h is close to the possible maximum for a given $\tan\beta$. For fixed M_2 , μ , M_{SUSY} and M_g this is achieved by adjusting X_t , resulting in conservative exclusion bounds.
- *No-mixing scenario*: The scenario is defined by a vanishing mixing in the stop sector $X_t = 0$ and a higher SUSY mass scale compared to the m_h^{max} scenario, resulting in a light Higgs boson h .

The parameters are listed in Tab. 1.6.

	M_{SUSY}	μ	M_2	X_t	$m_{\tilde{g}}$
m_h^{max}	1	± 0.2	0.2	2	0.8
no-mixing	2	± 0.2	0.2	0	1.6

Table 1.6: SUSY parameters in units of TeV for the benchmark scenarios considered in the present thesis [40]. Both scenarios are considered for positive and negative μ .

1.2.8 SUSY Mass Spectrum

As a consequence of supersymmetry breaking, sparticles acquire their masses in form of a combination from their coupling to the two Higgs fields and from direct mass terms. The higgsinos and neutral gauginos mix to four neutral mass eigenstates, the neutralinos: $\tilde{\chi}_{1,2,3,4}$. By convention, they are ordered according to increases masses. In the basis of electroweak eigenstates $\psi^0 = (\tilde{B}, \tilde{W}^0, \tilde{H}_d^0, \tilde{H}_u^0)$, the mass terms in the Lagrangian are $\mathcal{L}_{\text{MSSM}} \subset -\frac{1}{2}(\psi^0)^T \mathbf{M}_{\tilde{\chi}^0} \psi^0 + \text{h.c.}$, with

$$\mathbf{M}_{\tilde{\chi}^0} = \begin{pmatrix} M_1 & 0 & -c_\beta s_w M_Z & +s_\beta s_w M_Z \\ 0 & M_2 & +c_\beta c_w M_Z & -s_\beta c_w M_Z \\ -c_\beta s_w M_Z & +c_\beta c_w M_Z & 0 & -\mu \\ +s_\beta s_w M_Z & -s_\beta c_w M_Z & -\mu & 0 \end{pmatrix} \quad (1.56)$$

where the abbreviations $s_\beta = \sin \beta$, $c_\beta = \cos \beta$, $s_W = \sin \theta_W$ and $c_W = \cos \theta_W$ are introduced. The terms $M_{1,2}$ come from the mass terms in $\mathcal{L}_{\text{soft}}$, the $-\mu$ values correspond to the higgsino mass terms and the terms proportional to M_Z originate from the higgs–higgsino–gaugino coupling terms. The mass eigenvalues follow from diagonalizing $\mathbf{M}_{\tilde{\chi}^0}$ (e.g. [30]).

In a similar way the charged mass eigenstates, the charginos, are the result of the mixing of the charged higgsinos and winos. The corresponding Lagrangian has the form $\mathcal{L}_{\text{MSSM}} \subset -\frac{1}{2}(\psi^\pm)^T \mathbf{m}_{\tilde{\chi}^\pm} \psi^\pm + \text{h.c.}$ in the basis $\psi^\pm = (\tilde{W}^+, \tilde{H}_u^+, \tilde{W}^-, \tilde{H}_d^-)$ with the matrices

$$\mathbf{m}_{\tilde{\chi}^\pm} = \begin{pmatrix} 0 & \mathbf{X}^T \\ \mathbf{X} & 0 \end{pmatrix} \quad \text{and} \quad \mathbf{X} = \begin{pmatrix} M_2 & \sqrt{2}s_\beta M_W \\ \sqrt{2}c_\beta M_W & \mu \end{pmatrix}. \quad (1.57)$$

The mass eigenstates are related to the electroweak ones by two unitary 2×2 matrices, which differ for positively and negatively charged states:

$$\begin{pmatrix} \tilde{\chi}_1^+ \\ \tilde{\chi}_2^+ \end{pmatrix} = \mathbf{V} \begin{pmatrix} \tilde{W}^+ \\ \tilde{H}_u^+ \end{pmatrix}, \quad \begin{pmatrix} \tilde{\chi}_1^- \\ \tilde{\chi}_2^- \end{pmatrix} = \mathbf{U} \begin{pmatrix} \tilde{W}^- \\ \tilde{H}_d^- \end{pmatrix} \quad (1.58)$$

and

$$\mathbf{U}^* \mathbf{X} \mathbf{V}^{-1} = \begin{pmatrix} m_{\tilde{\chi}_1^+} & 0 \\ 0 & m_{\tilde{\chi}_2^-} \end{pmatrix}. \quad (1.59)$$

The chargino masses follow

$$\begin{aligned} m_{\tilde{\chi}_{1,2}^\pm}^2 &= \frac{1}{2} [|M_2|^2 + |\mu|^2 + 2 M_W^2 \\ &\mp \sqrt{(|M_2|^2 + |\mu|^2 + 2 M_W^2)^2 - 4 |\mu M_2 - M_W^2 \sin(2\beta)|^2}]. \end{aligned} \quad (1.60)$$

The parameter space region corresponding to $\mu \gg M_i$ is called *gaugino region* since the field content of the lightest chargino and neutralinos is dominated by wino and bino contributions. The lightest neutralinos and the lightest chargino are then referred to as gauginos. On the other hand, if $\mu \ll M_i$, the lightest neutralinos are dominantly higgsinos and the parameter space region is referred to as *higgsino region*.

In case of squarks and slepton masses, the relevant contribution to the Lagrangian has the form $\mathcal{L}_{\text{MSSM}} \subset -(\tilde{f}_L^* \tilde{f}_R^*) \mathbf{m}_{\tilde{f}}^2 \begin{pmatrix} \tilde{f}_L \\ \tilde{f}_R \end{pmatrix}$ and the corresponding mixing matrices are given by

$$\mathbf{m}_e^2 = \begin{pmatrix} m_L^2 + m_e^2 - (\frac{1}{2} - s_W^2)Z_\beta^2 & m_e(A_e - \mu \tan \beta) \\ m_e(A_e - \mu \tan \beta) & m_E^2 + m_e^2 - s_W^2 Z_\beta^2 \end{pmatrix} \quad (1.61)$$

$$\mathbf{m}_{\tilde{u}}^2 = \begin{pmatrix} m_Q^2 + m_u^2 + (\frac{1}{2} - \frac{2}{3}s_W^2)Z_\beta^2 & m_u(A_u - \mu \cot \beta) \\ m_u(A_u - \mu \cot \beta) & m_U^2 + m_u^2 + \frac{2}{3}s_W^2 Z_\beta^2 \end{pmatrix} \quad (1.62)$$

$$\mathbf{m}_{\tilde{d}}^2 = \begin{pmatrix} m_Q^2 + m_d^2 + (-\frac{1}{2} - \frac{1}{3}s_W^2)Z_\beta^2 & m_d(A_d - \mu \tan \beta) \\ m_d(A_d - \mu \tan \beta) & m_D^2 + m_d^2 - \frac{1}{3}s_W^2 Z_\beta^2 \end{pmatrix}, \quad (1.63)$$

with the abbreviations $s_W^2 \equiv \sin^2 \theta_W$, $Z_\beta^2 \equiv M_Z^2 \cos 2\beta$ and the parameters $A_{u,d,e}$ as introduced in Eq. (1.47). The parameters m_L , m_e etc. are the explicit mass terms in the soft supersymmetric breaking Lagrangian $\mathcal{L}_{\text{soft}}$. Remaining terms arise from the coupling to the Higgs fields. For the first and second generation, the off-diagonal terms can be neglected since they are proportional to the masses of the Standard Model partners of the sfermions. In case of the third generation, these terms introduce significant mixing between the two sfermion chirality states due to the large masses of tau lepton, top and bottom quark. The resulting masses for the stau leptons are

$$m_{\tilde{\tau}_{1,2}}^2 = \frac{1}{2} (m_{\tilde{\tau}_L}^2 + m_{\tilde{\tau}_R}^2) - \frac{1}{4} Z_\beta^2 + m_\tau^2 \mp \sqrt{\left[\frac{1}{2} (m_{\tilde{\tau}_L}^2 - m_{\tilde{\tau}_R}^2) - Z_\beta^2 \left(\frac{1}{4} - s_W^2 \right) \right]^2 + m_\tau^2 (A_\tau - \mu \tan \beta)^2}. \quad (1.64)$$

In the discussed MSSM, only left handed fields exist for sneutrinos with the sneutrino mass

$$m_{\tilde{\nu}}^2 = m_L^2 + \frac{1}{2} s_W^2 Z_\beta^2. \quad (1.65)$$

1.2.9 Gravity Mediated Supersymmetry Breaking

The model of gravity mediated supersymmetry breaking is characterized by a hidden sector communicating with the described MSSM through gravity strength interactions. This scenario arises naturally if invariance of the supersymmetric action under local supersymmetry transformation is required. Local Supersymmetry introduces additional terms to the Lagrangian, which can be canceled by including a new gauge field. This gauge field comprises the *graviton* with spin 2 and its superpartner the *gravitino* with spin $\frac{3}{2}$. From the successful integration of gravity into a supersymmetric theory, the model obtained the name *supergravity* (SUGRA). The Lagrangian of the resulting low-energy theory includes terms of unbroken Supersymmetry and the soft breaking terms given Eq. (1.45), but with coupling constants anti-proportional to the Planck Scale M_P . In SUGRA models the scale of supersymmetry breaking is assumed to be at $\sqrt{\langle F \rangle} \approx 10^{11}$ GeV since $M_{\text{soft}} \sim \langle F \rangle / M_P$, with the characteristic mass scale of the soft breaking terms $M_{\text{soft}} \approx 1$ TeV.

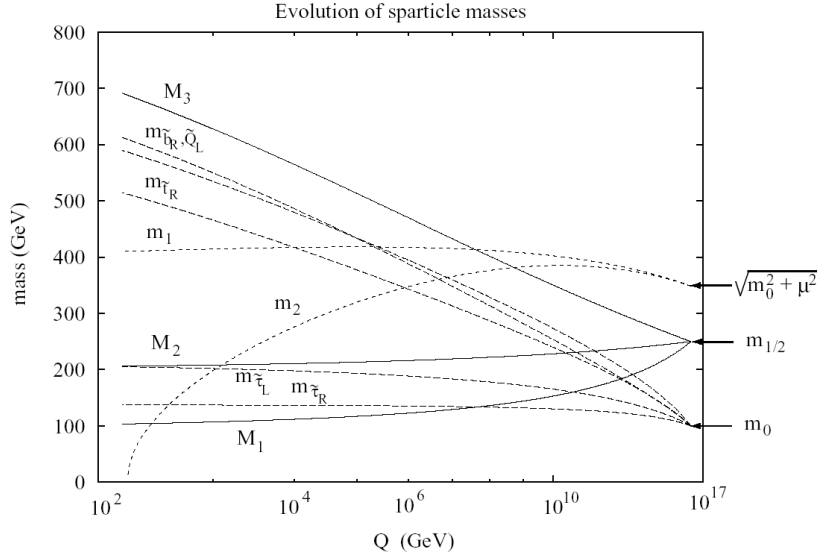


Figure 1.6: Example of the running of the soft supersymmetry breaking parameters from the GUT scale to the electroweak scale [41].

Assuming unification of the couplings and masses at M_{GUT} allows to construct highly predictive models. In the minimal supergravity model (mSUGRA), in which the results of the present thesis will be interpreted, the number of free parameters at the GUT scale is minimized to four continuous and one discrete parameter:

- The gaugino masses unify to a common gaugino mass $m_{1/2} = M_1 = M_2 = M_3$;
- The sfermion and Higgs masses unify to a common scalar mass $m_0^2 = m_{H_u}^2 = m_{H_d}^2$ and $m_0^2 \mathbf{1} = \mathbf{m}_Q^2 = \mathbf{m}_u^2 = \mathbf{m}_d^2 = \mathbf{m}_L^2 = \mathbf{m}_e^2$;
- All trilinear couplings unify to a common trilinear coupling A_0 , with $\mathbf{a}_u = A_0 \mathbf{y}_u$, $\mathbf{a}_d = A_0 \mathbf{y}_d$, $\mathbf{a}_e = A_0 \mathbf{y}_e$;
- The ratio of the vacuum expectation values of Higgs fields $\tan \beta$;
- The sign of the Higgs mass parameter μ .

The effective masses and couplings at the electroweak scale are determined by these parameters through the radiative corrections taken into account when running the renormalization group equations from the GUT scale to the electroweak scale, as illustrated in Fig. 1.6. The dominating fraction of the parameter space corresponds to the gaugino region ($\mu \gg m_{1/2}$) with the relation

$$m_{\tilde{\chi}_1^\pm} \approx m_{\tilde{\chi}_2^0} \approx 2m_{\tilde{\chi}_1^0} \approx \frac{1}{3}m_{\tilde{g}}. \quad (1.66)$$

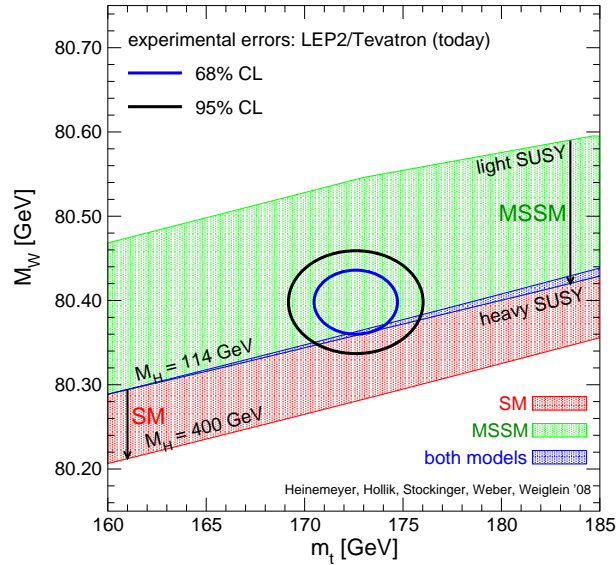


Figure 1.7: Prediction for M_W in the Standard Model and the MSSM as a function of the top quark mass compared to the present experimental results. Taken/updated from [42, 43], including two-loop corrections for the precision observables [44, 45, 46, 47].

1.2.10 Experimental Constraints

In spite of extensive searches during the last decades, Supersymmetry could not yet be discovered. Searches for the direct observations of supersymmetric particles have been performed at the LEP experiments in e^+e^- collisions and at the Tevatron in $p\bar{p}$ collision. A short summary of the current results of interest for the presented thesis is given below.

A complementary approach is given through indirect searches. The precision measurement of the anomalous magnetic momentum of the muon [48] allows to set constraints on the SUSY parameter space as well as on the measurement of the branching ratio of the rare decays $\text{BR}(B_s \rightarrow \mu\mu)$ [49, 50] and $\text{BR}(B \rightarrow X_s\gamma)$ [51, 52].

Further indirect constraints are provided by cosmology. The calculation of the relic abundance of the neutralino from recent cosmological experimental measurements allows to restrict the SUSY parameter space significantly towards values of a few hundred GeV for $m_{1/2}$ and m_0 in the region $\tan\beta \lesssim 40$. For $\tan\beta \approx 50$, the cosmological data allow for significantly heavier sfermion and/or gluino masses [53].

The predictions for the W boson mass M_W as a function of the top quark mass m_t within the Standard Model and the MSSM are illustrated in Fig. 1.7 in the (M_W, m_t) -plane. Varying the SUSY parameters independently of each other results in the allowed region of the MSSM, while the allowed region of the Standard Model results from varying the only free parameter of the model, the Higgs boson mass, in the range $M_H = 114 - 400$ GeV. Light Higgs boson masses in the Standard Model result in an overlap region with the MSSM in the case that all superpartners are heavy (decoupling region). The current experimental data show a slight preference of the MSSM over the Standard Model.

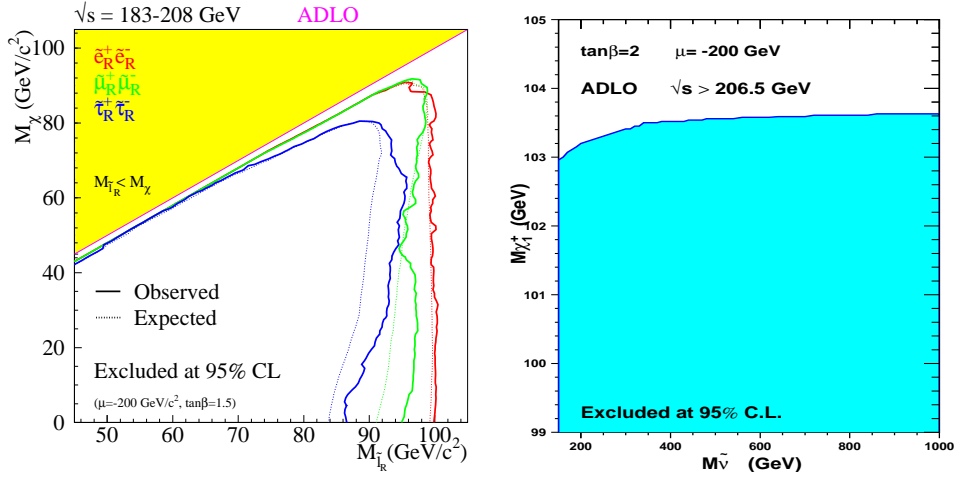


Figure 1.8: Combined exclusion limits from the LEP experiments on the charged slepton masses as a function of the LSP mass (left) [54] and on the mass of the lightest chargino as a function of the sneutrino mass (right) [55].

Direct Searches for Supersymmetric Particles

Direct searches for supersymmetric particles at LEP II by the ALEPH, DELPHI, L3 and OPAL collaborations result in lower limits on the masses of the expected particles. The mass limits are typically close to the kinematical threshold and are interpreted in certain SUSY models, allowing to constrain the parameter space of the model. In Fig. 1.8 (left) the lower limits on the slepton masses are illustrated in the $(m_{\tilde{\tau}}, m_{\tilde{\chi}_1^\pm})$ -plane. Mass limits are placed at $m_{\tilde{e}_R} > 99.9$ GeV, $m_{\tilde{\mu}_R} > 94.9$ GeV and $m_{\tilde{\tau}_1} > 86.6$ GeV [54]. Figure 1.8 (right) shows the lower limit on the mass of the lightest chargino as a function of the sneutrino mass. For large slepton and sneutrino masses, a lower boundary is set at $m_{\tilde{\chi}_1^\pm} > 103.5$ GeV [55], which is close to the kinematic production threshold at LEP.

Figure 1.9 (left) illustrates the results of the LEP experiments in the $(m_0, m_{1/2})$ -plane for $\tan\beta = 10$, $\mu > 0$ and $A_0 = 0$ [56]. For small m_0 , the searches for sleptons allow to exclude values of $m_{1/2}$ below 240 GeV. With increasing m_0 , the limit on the mass of the lightest chargino becomes relevant, which corresponds to $m_{1/2} \gtrsim 160$ GeV. In the intermediate region, charginos decay invisibly into sneutrinos resulting in weaker constraints for $m_0 \approx 70$ GeV. Results from Higgs boson searches allow to extend the excluded region to $m_{1/2} \approx 270$ GeV. This constraint depends strongly on A_0 as illustrated in Fig. 1.9 (right).

Figure 1.10 (left) summarizes several LEP results in the $(\tan\beta, m_{\tilde{\chi}_1^0})$ -plane for negligible stau mixing [57]. The search for Higgs bosons allows to exclude values of $\tan\beta < 2.1$, which is extended by the search for pair production of light charginos to $\tan\beta < 3.3$ in a limited parameter space. A lower bound independent of $\tan\beta$ is placed at $m_{\tilde{\chi}_1^0} > 47$ GeV. Figure 1.10 (right) illustrates the dependence of the limit on the mass of the LSP for different values of the top mass m_{top} . LSP mass below 51 GeV are excluded for any value of $\tan\beta$ and A_0 , within the mSUGRA model. A lower bound on the LSP mass valid for any stau mixing is found at 42 GeV [58].

The DØ collaboration searched for the associated production of lightest chargino and next-

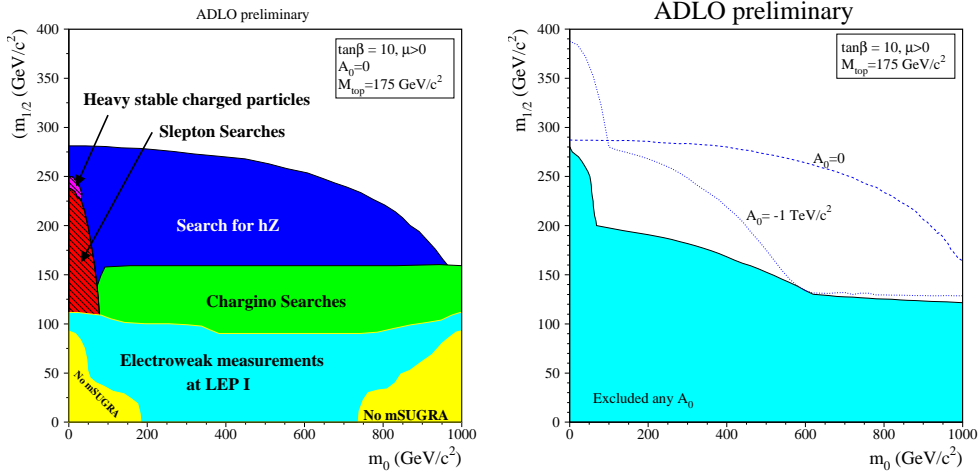


Figure 1.9: Exclusion region at the 95 % CL in the $(m_0, m_{1/2})$ -plane in the mSUGRA model from combined results of the LEP experiments for $A_0 = 0$ (left) and for $A_0 = -1$ TeV and for any value of A_0 (right) [56].

to-lightest neutralino in data recorded during Run I of the Tevatron. The resulting limit at the 95% CL on the associated production cross section of lightest chargino and second lightest neutralino times branching ratio into three leptons is shown in Fig. 1.11 (left). The lines (A) and (B) correspond to limits obtained on different datasets, which result in a combined limit (C) based on a data set corresponding to 95 pb^{-1} . The lines (i) and (ii) indicate the variation of the theoretical cross section times branching ratio in typical SUSY models [59]. The domain labeled *Region excluded by LEP* corresponds to an early chargino mass limit published by the OPAL collaboration in 1996 [60]. The CDF collaboration perform a similar analysis with the results illustrated in Fig. 1.11 (right). Both results are not competitive with the LEP results.

Direct Searches for MSSM Higgs boson

The four LEP collaborations have searched for neural Higgs bosons as predicted by the MSSM. The interpretation of the observed lower limits on the MSSM Higgs production cross section in the m_h^{\max} and no-mixing scenario for positive and negative μ are illustrated in Fig. 1.12 in the $(\tan \beta, M_A)$ -plane [62]. The region $M_A \lesssim 93 \text{ GeV}$ is excluded for all four scenarios independent of $\tan \beta$. The excluded region in terms of $\tan \beta$ depends strongly on M_A and varies between $0.6 < \tan \beta < 2.6$ for large M_A in the m_h^{\max} scenario and $\tan \beta \lesssim 80$ for $M_A \approx 130 \text{ GeV}$ in the no-mixing scenario.

Current results from searches for MSSM Higgs boson at the Tevatron in Run II will be discussed below in comparison to the results of the analysis performed in the presented thesis.

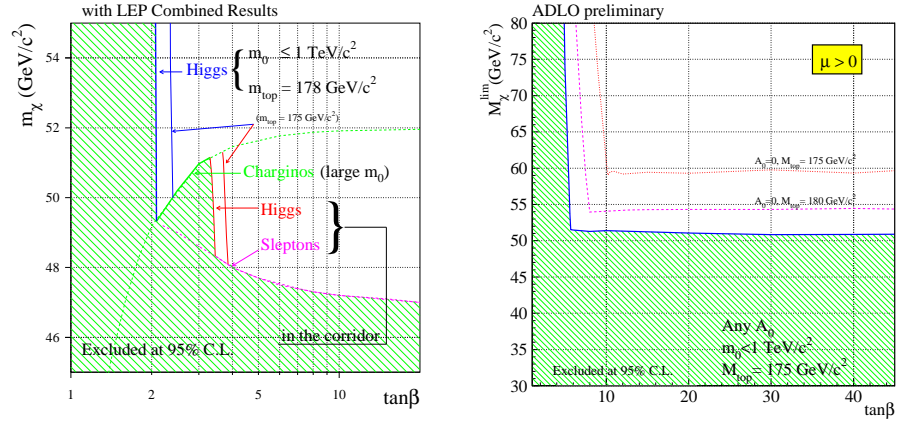


Figure 1.10: Combined LEP exclusion regions in the $(\tan\beta, m_{\text{LSP}})$ -plane. The results from the searches for chargino, slepton and Higgs bosons are combined to place a lower limit on the mass of the LSP as a function of $\tan\beta$ in a constrained MSSM, assuming negligible mixing in the stau sector (left) [57]. The lower limit on $m_{1/2}$ is translated into a lower limit on m_{LSP} in mSUGRA (right) [56].

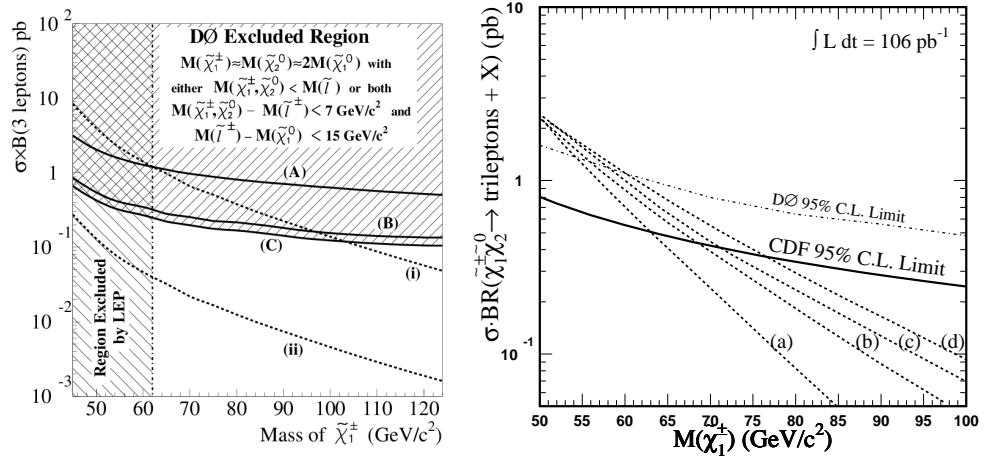


Figure 1.11: *Left*: $D\bar{0}$ Run I upper limit at the 95% CL on the associated production cross section of lightest chargino and second lightest neutralino times branching ratio into three leptons [59]. Further details are given in the text.

Right: The CDF 95% CL limit on cross section times branching ratio into final states with electrons and muons compared to different mSUGRA prediction for $\mu = -400$ GeV, $\tan\beta = 2$ and different values of $m_{\tilde{q}}/m_{\tilde{g}}$ (a) 1.5, (b) 1.2, (c) 1.2 and (d) 1.0 [61].

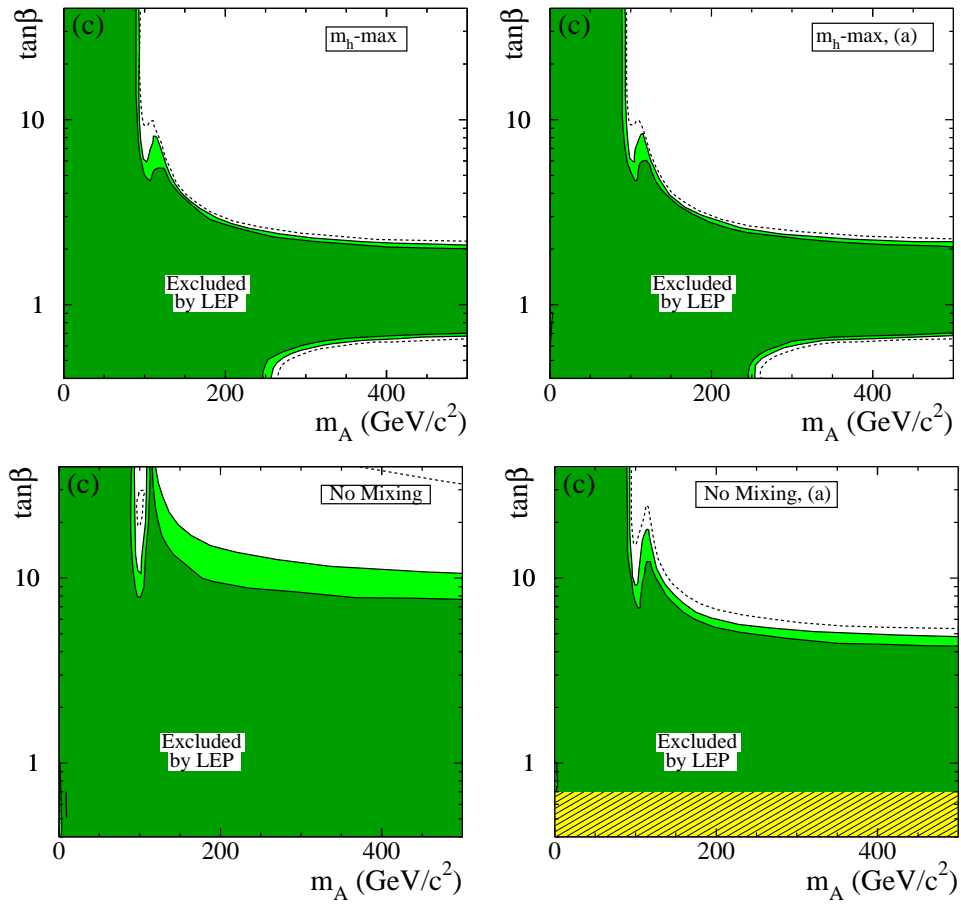


Figure 1.12: Combined results from the searches for neutral MSSM Higgs bosons at the LEP experiments. The results are interpreted in the $(M_A, \tan\beta)$ -plane for the m_h^{\max} scenario (top) and the no-mixing scenario (bottom) for negative μ (left) and for positive μ (right) [62]

2

Phenomenology of $p\bar{p}$ Collisions

The following chapter gives a short introduction into the phenomenology of $p\bar{p}$ collisions including the calculation of cross sections, luminosity and the event simulation.

2.1 General Aspects

Protons and antiprotons are composite objects consisting of quarks and gluons, called *partons*. Therefore, the collisions of protons and antiprotons have to be considered as interactions of partons. The longitudinal momentum fractions of the colliding partons are unknown. The objects resulting from the collision are described by transverse momentum and energy, exploiting the conservation of the total transverse momentum.

The majority of the $p\bar{p}$ interactions are large-distance collisions, where the momentum transfer is small, so-called *soft collisions*. By contrast, the interactions of interest are characterized by a large momentum transfer in a so-called *hard scattering* resulting in particles with large transverse momenta. The effective center-of-mass energy $\sqrt{\hat{s}}$ of the hard scattering is smaller than the maximal center-of-mass energy provided by the collider ($\sqrt{s} = 1.96$ TeV). It is determined by the fraction of the proton/antiproton momentum carried by the interacting partons x_1 and x_2 :

$$\sqrt{\hat{s}} = \sqrt{x_1 x_2 s}. \quad (2.1)$$

In addition, the following processes are of relevance:

- *Initial and final state radiation*: A collision implies accelerated color and electromagnetic charges resulting in bremsstrahlung. Emissions that are associated with the two incoming colliding partons are called *initial state radiation* (ISR). Emissions that are associated with the outgoing objects are called *final state radiation* (FSR). ISR and FSR can significantly affect the cross section of the involved process and modify the event topology by increasing the number of objects in the final state.
- *Beam remnants*: The parton which participates in the hard scattering carries only a part of the momentum of the colliding proton/antiproton. The remaining momentum

is carried by the so-called *remnant*, which is not color neutral and can effect the event topology.

- *Minimum bias events*: Since the cross section of inelastic interactions is several orders of magnitude larger than the cross section of the hard interactions as illustrated in Fig. 2.1, a bunch crossing results in multiple soft inelastic interactions. This type of event is called *minimum bias event*. Its rate depends strongly on the instantaneous luminosity. The average number of minimum bias events amounts to approximately two per bunch crossing for the data set used in the present thesis.
- *Pile-up*: If detector components are not fast enough to resolve individual interactions, the current bunch crossing is overlaid by signals from the previous bunch crossing. For example, the contributions from pile-up affect the calorimeter readout electronics since the shaping time is longer than the bunch spacing time.

The term *underlying event* is used to describe processes taking place beside the hard scattering. In the present thesis, it refers to minimum bias events, beam remnants and possible interactions of the beam remnants [63].

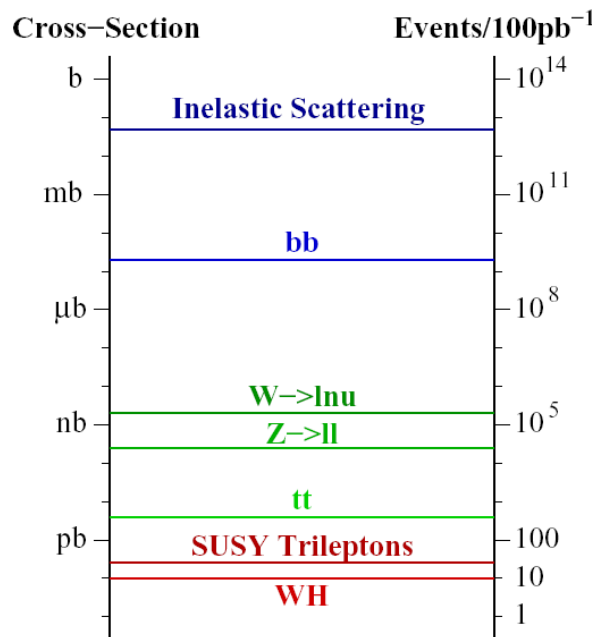


Figure 2.1: The cross sections and the number of expected events for an integrated luminosity of 100 pb^{-1} for selected processes at the Tevatron. Precise values for all processes that are relevant for the present thesis are given in Tab. 5.3.

2.2 Factorization

The underlying principle of factorization in a system is the separation in terms of different momentum scales. For an observable that involves strong interactions, one uses a representation as a product of two or more functions that account for the effects at short and long distances, respectively. Schematically, this can be expressed by

$$\begin{aligned} \text{Physical quantity}(Q^2, \text{hadron momenta}) = & \quad (2.2) \\ \mathcal{C}(Q^2, \text{parton momenta } |k| > \mu) \otimes \mathcal{P}(\text{parton momenta } |k| < \mu, \text{hadron momenta}). \end{aligned}$$

For the function \mathcal{C} , which describes the short distance part, perturbative QCD can be used. The long distance part \mathcal{P} is described by phenomenological functions, it stands for the transition from partons to hadrons. The function \mathcal{P} involves only partons with momenta less than the *factorization scale* μ but does not depend on Q . By introducing the auxiliary scale μ , the dependence on the hard scale Q is isolated (factorized) from the dependence on soft momenta. One advantage of this procedure is that the long distance (soft) function \mathcal{P} is universal, meaning that it can be used for different physical processes. Therefore, knowing one of the functions \mathcal{C} and \mathcal{P} allows to determine the other. Factorization is applicable in all orders of perturbation expansion. Typically, the dependence of an observable on the choice of the factorization scale μ decreases with increasing order of the calculation [64].

The soft component in the initial state of the hadronic interaction is described by parton distribution functions, while the soft component in the formation of hadronic final states is described by fragmentation functions, as explained in the following sections.

2.3 Cross Section and Parton Distribution Functions

The hadronic cross section of a process $\sigma(p\bar{p} \rightarrow V + X)$ (e.g. $V = W, Z$) at a hadron collider is calculated from the partonic cross section $\hat{\sigma}(q\bar{q}' \rightarrow V)$ and integrating over the momentum fractions $x_{i,j}$ of the colliding partons:

$$\sigma(p\bar{p} \rightarrow V + X) = \sum_{i,j} \int dx_i dx_j f_{q_i}(x_i, Q^2) f_{\bar{q}_j}(x_j, Q^2) \hat{\sigma}(q_i \bar{q}_j \rightarrow V). \quad (2.3)$$

The *parton distribution functions* (PDF) are given by $f_{q_i, \bar{q}_j}(x_i, Q^2)$ and the sum runs over all quark/antiquark contributions q_i, \bar{q}_j . The probability of finding a parton i in a hadron with a momentum fraction between x and $x + dx$ is given by $f_i(x, Q^2) dx$. The sum of all parton momenta results in the total momentum of the hadron. The PDFs can be expressed in terms of the proton structure functions of the deep-inelastic scattering ($ep \rightarrow eX$) F_1 and F_2

$$2xF_1(x) = F_2(x) = x \cdot \sum_{\text{quarks}} e_q^2 f_q(x), \quad (2.4)$$

with the electromagnetic charge of a quark e_q . Taking into account the gluon contributions introduces the Q^2 -dependence of the structure functions. For example, a quark with momentum fraction x can result from a quark q' which radiates a gluon $q' \rightarrow qg$. In addition, contributions from $g' \rightarrow gg$ and $g' \rightarrow q\bar{q}$ have to be considered. As a consequence, the structure functions take the form

$$F_2(x, Q^2) = x \cdot \sum_{\text{quarks}} e_q^2 (f_q(x) + \Delta f_g(x, Q^2)). \quad (2.5)$$

The absolute scale of the PDFs has to be measured in experiments, but the dependence on Q^2 can be calculated and is given by the Altarelli–Parisi (DGLAP) equations [65]:

$$\frac{df_{q_i}(x, Q^2)}{d \ln Q^2} = \frac{\alpha_s(Q^2)}{2\pi} \int_x^1 \frac{dy}{y} \left(f_{q_i}(y, Q^2) P_{qq} \left(\frac{x}{y} \right) + f_g(y, Q^2) P_{qg} \left(\frac{x}{y} \right) \right) \quad (2.6)$$

$$\frac{df_g(x, Q^2)}{d \ln Q^2} = \frac{\alpha_s(Q^2)}{2\pi} \int_x^1 \frac{dy}{y} \left(f_{q_i}(y, Q^2) P_{gq} \left(\frac{x}{y} \right) + f_g(y, Q^2) P_{gg} \left(\frac{x}{y} \right) \right). \quad (2.7)$$

The probability that a parton a with momentum fraction x originates from a second parton b with momentum fraction y is given by the splitting function $P_{ab}(x/y)$ with $a, b = q, g$. For example, at leading order the splitting function for a quark emitting a gluon P_{qg} is given by

$$P_{qg}(z = x/y) = \frac{4}{3} \left(\frac{1+z^2}{1-z} \right). \quad (2.8)$$

The dependence on Q^2 can be understood in a similar way as the evolution of masses and couplings towards their bare values with increasing energy scale. For low values of Q^2 , an interaction is sensitive to the cloud of quarks and gluons surrounding a parton. With increasing values of Q^2 , the momentum measurement becomes sensitive to the short distance structure of the partons and the momenta of the bare partons.

Although gluons carry only a low momentum fraction of the proton as illustrated in Fig. 2.2, electron-proton scattering experiments have shown that approximately half of the proton momentum is carried by gluons, while the other half is carried by charged partons, the quarks. Sea quarks typically carry only a small momentum fraction.

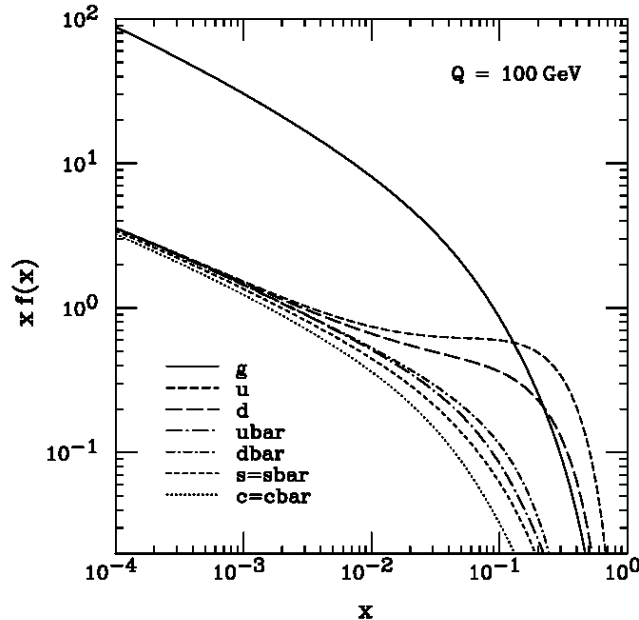


Figure 2.2: Overview of the CTEQ6M PDFs at $Q = 100 \text{ GeV}$, which is characteristic value for the Tevatron [66].

The results from deep inelastic scattering of electrons, muons and neutrinos with nucleons and the measurement of the Drell–Yan deuteron/proton ratio are used for the determination of the PDFs, together with measurements of the lepton charge asymmetry in W decays and the inclusive jet cross section by the CDF collaboration. In the present thesis, the parameterization of the PDFs provided by the CTEQ collaboration [66] are used.

Partonic Cross Section

The Lagrangian of the underlying theory allows to calculate the differential partonic cross section

$$\frac{d\hat{\sigma}}{dQ^2} = \frac{|\mathcal{M}|^2}{F}, \quad (2.9)$$

where \mathcal{M} represents the matrix element of the process under consideration and F the incident flux. For example, the partonic cross section of the Drell–Yan process of Fig. 2.3 is determined by QED:

$$\frac{d\hat{\sigma}_{\text{DY}}}{dQ^2} = \frac{4\pi\alpha^2}{3Q^2} e_q^2 \delta(Q^2 - \hat{s}). \quad (2.10)$$

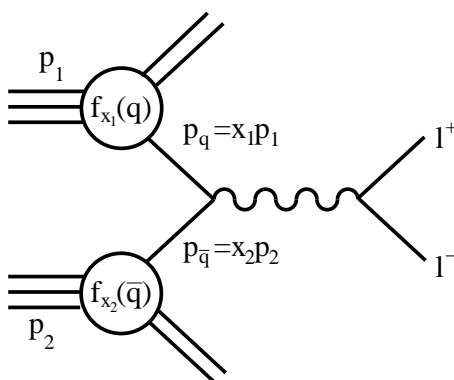


Figure 2.3: Schematic view of the Drell–Yan production of a lepton pair in a $p\bar{p}$ collision. A quark/antiquark pair annihilates to produce a virtual photon: $q\bar{q} \rightarrow \gamma^* \rightarrow \ell^+\ell^-$.

Higher Order Corrections

The calculation of cross sections as discussed above includes only leading order (LO) contributions as shown in Fig. 2.4 (a). A more precise result is achieved by including *next-to-leading order* (NLO) contributions in form of radiation of gluons and photons as shown in Fig. 2.4 (b, c) or virtual corrections shown in Fig. 2.4 (d–f). In a full NLO calculation, the singularities from virtual corrections and the soft and collinear singularities of the real emission cancel by negative interference such that the cross section receives a finite correction. The exact value is obtained by taking into account all possible higher order contributions. Since these higher order calculations are complex, for the majority of the processes only NLO calculation have been performed and just for a few processes next-to-NLO (NNLO) calculations. Although higher order contributions can affect the total cross section as well as the distribution of kinematic and angular quantities, the effects are often small compared to the accessible accuracy

of the experiments. Depending on the observable, it is often sufficient to determine kinematic and angular distributions at LO, and to correct the total cross section by the ratio of NLO to LO calculation, referred to as k -factor:

$$k_{(N)\text{NLO}} = \frac{\sigma_{(N)\text{NLO}}}{\sigma_{\text{LO}}}. \quad (2.11)$$

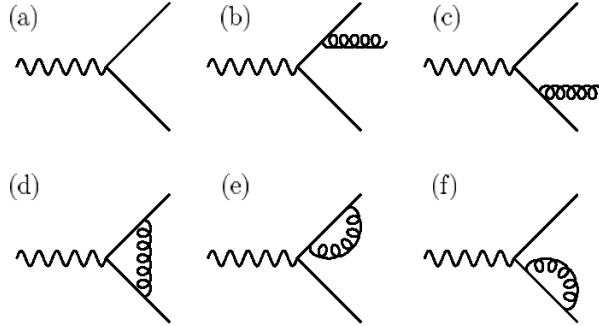


Figure 2.4: NLO QCD contributions for Drell–Yan processes.

2.4 Luminosity

The instantaneous interaction rate R at which a specific process occurs and the corresponding cross section σ are related by the instantaneous luminosity L

$$R = \frac{dN}{dt} = \sigma L. \quad (2.12)$$

The instantaneous luminosity L of $p\bar{p}$ collisions can be calculated from the number of protons n_p and antiprotons $n_{\bar{p}}$ in two bunches colliding at the rate f

$$L = f \frac{n_p n_{\bar{p}}}{4\pi\sigma_x\sigma_y}. \quad (2.13)$$

The term in the denominator represents the effective area of interaction $A_{eff} = 4\pi\sigma_x\sigma_y$ under the assumption of a perfectly Gaussian beam profile with width $\sigma_{x,y}$ in horizontal and vertical direction. The instantaneous luminosity is measured in units of $\text{cm}^{-2}\text{s}^{-1}$.

The total number N of events of a process is obtained by integration of the rate R over time

$$N = \sigma \int L dt. \quad (2.14)$$

The quantity $\mathcal{L} = \int L dt$, called *integrated luminosity*, is used to quantify an amount of $p\bar{p}$ collisions. Cross sections are usually measured in units of *barn* (1 barn = 1 b = $10^{-28} \text{ m}^2 = 10^{-24} \text{ cm}^2$). At the Tevatron, cross sections of physics processes are often in the range of picobarn (pb) or femtobarn (fb) and the integrated luminosity is given in units of pb^{-1} or fb^{-1} .

2.5 Event Generation

An accurate simulation of physics processes is an essential requirement for the analyses presented in the present thesis. The complexity of particle collisions requires the use of Monte Carlo event generators. An event generator simulates the 4-vectors of the particles resulting from an interaction. The simulation includes the hard interaction, the initial and final state radiation, beam remnants and fragmentation. In a second step, the response of the detector to this process is simulated, as will be summarized after introducing the DØ detector in Sec. 3. In the following, samples of simulated events are referred to as *Monte Carlo samples*.

The event generator used in the present thesis is PYTHIA [67]. For the majority of the processes of interest, leading order matrix element calculations for the hard scattering, derived from the Lagrangian of the theory, are supplemented by parton showering and fragmentation. For the simulation of tau lepton decays, the package TAUOLA 2.5 [68, 69] is used. The concepts of the parton shower technique and the fragmentation method applied in PYTHIA are summarized below.

Monte Carlo generators provide a successful tool for simulating particle collisions and the momentum and angular distributions of the resulting objects over several orders of magnitude to high accuracy. Nevertheless, it has to be kept in mind that they only provide an approximation of the real processes taking place in nature.

2.5.1 Parton Shower

Since it is not possible to calculate the full perturbative expansion, the parton shower method is used to describe ISR and FSR. The parton shower technique is a probabilistic iterative process that allows to combine simple expressions for $q \rightarrow qg$, $g \rightarrow gg$ and $g \rightarrow q\bar{q}$ branchings and to build up complex multiparton final states. The probability for a parton splitting into two daughter partons with momentum fractions z and $1 - z$ is described by the Altarelli-Parisi splitting functions $P(z)$ (see Eq. (2.8)) [65]. For the simulation of FSR, the evolution of branchings is performed forwards starting from the energy scale of the hard interaction, while it is performed backwards for ISR. The method leads to a good description of the radiation of collinear and soft partons but has limited predictive power for the emission of hard and wide-angle partons. The simulation of hard parton emission can be included into the matrix-element as it is done e.g. in the event generators SHERPA [70] and ALPGEN [71]. In order to regulate soft and collinear divergences, a lower cut-off at $Q \approx 1$ GeV is introduced. In this region no further branchings are simulated and fragmentation phenomena dominate [63].

2.5.2 Fragmentation

The mechanism discussed so far describes only partons, while experiments observe hadrons, which are neutral in terms of color. In between the fragmentation takes place. The transition from outgoing partons to hadrons cannot be calculated from first principle since perturbation theory breaks down at long distances. The fragmentation is described by probabilistic and iterative methods using branchings parameterized by *fragmentation functions*, which have been measured at LEP [72]. Several models are available to perform the fragmentation. The one implemented in PYTHIA is the Lund string fragmentation model [73, 74].

In the Lund string model, the confinement is represented by a string with a certain energy density between the partons which are moving apart. Quark-antiquark pairs are created

along the string such that the string breaks up into hadrons. The decay of resulting instable hadrons is simulated using matrix elements or results of measurements.

3

Accelerator and Detector

The $D\bar{O}$ experiment, located at the Fermi National Accelerator Laboratory (FNAL) [75] near Chicago, Illinois in USA, is designed to observe the decay products of proton-antiproton collisions provided by the Tevatron collider [76]. After the first run period (Run I) from 1992 to 1996, the Tevatron and the two detectors $D\bar{O}$ [77] and CDF [78] were upgraded. The second run period (Run II) started in April 2001 at a center-of-mass energy of $\sqrt{s} = 1.96$ TeV and higher luminosity. Since then, the accelerator has provided data corresponding to an integrated luminosity of $\approx 4 \text{ fb}^{-1}$ as shown in Fig. 3.1 (top). The increasingly steep rise of the integrated luminosity is a result of the increasing peak luminosity shown in Fig. 3.1 (bottom), which is caused by improvements of the accelerator, in particular of the antiproton production, storage and injection. Until the end of Run II in 2009, an integrated luminosity of about 7 fb^{-1} is expected to be recorded by both experiments. Until the start-up of the Large Hadron Collider (LHC) [79] in the near future, the Tevatron collider provides the world highest center-of-mass energy. This chapter provides a brief description of the accelerator chain and the $D\bar{O}$ detector components of relevance for the later analyses. A brief overview of the simulation of the $D\bar{O}$ detector closes the chapter.

3.1 The Tevatron Accelerator

The Tevatron synchrotron [81] is the last stage of the Fermilab accelerator chain shown in Fig. 3.2, which provides colliding high-energy proton and antiproton beams. Major parameters of the Tevatron are given in Tab. 3.2.

The accelerator chain starts with a *Cockroft-Walton* accelerator yielding negatively charged hydrogen ions (H^-) at an energy of 750 keV. The ions reach 440 MeV in a linear accelerator (LINAC) before their electrons are stripped off by passing through a carbon fiber foil. The energy of the resulting proton beam is increased to 8 GeV in a synchrotron, called *Booster*. The protons are transferred to the *Main Injector* where they reach an energy of 150 GeV.

Antiprotons are produced by focusing proton bunches with an energy of 120 GeV from the Main Injector on a nickel/copper target. The resulting antiprotons are stochastically

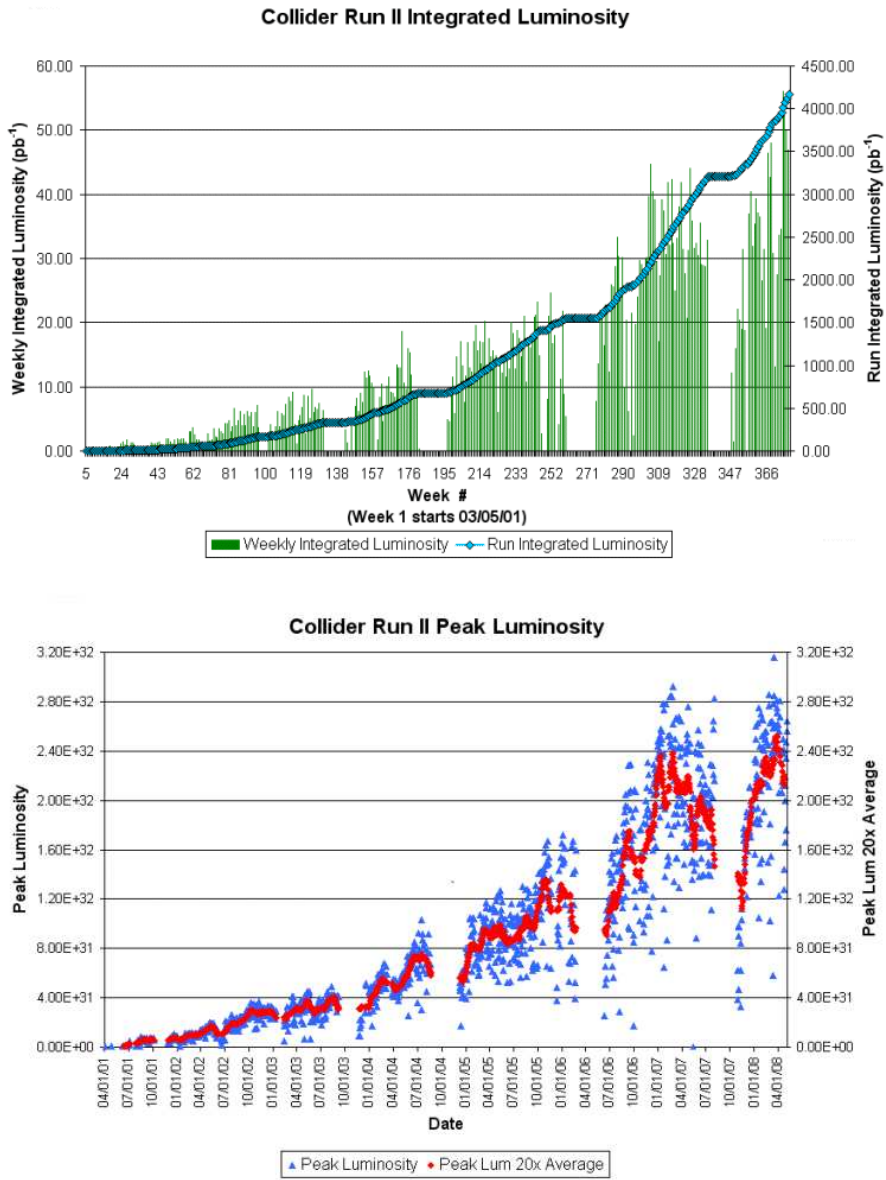


Figure 3.1: The integrated luminosity (top) and the peak luminosity (bottom) during Run II of the Tevatron [80].

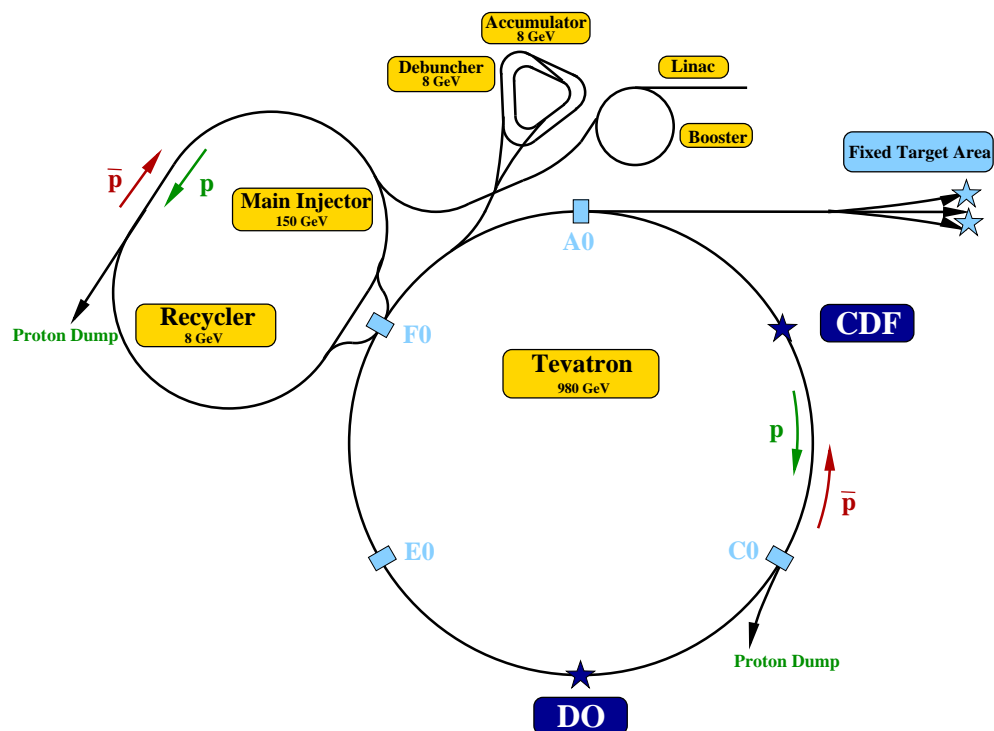


Figure 3.2: Schematic view of the Fermilab accelerator chain showing the different acceleration stages and the two multi-purpose experiments $D\bar{O}$ and CDF.

cooled [82] in the *Debuncher* and stored at an energy of 8 GeV in the *Accumulator*. The production of antiprotons is the limiting factor for increasing the Tevatron luminosity. Bunches of antiprotons are transferred to the Main Injector and accelerated to 150 GeV. A crucial part in increasing the antiproton rate is the *Recycler*, which has a much larger storage capability than the *Accumulator* and allows to reuse antiprotons from a previous collider store. It is located in the Main Injector tunnel.

As soon as a sufficient number of antiprotons are accumulated, 36 proton and 36 antiproton bunches are injected from the Main Injector into the Tevatron. The bunches are grouped into three super-bunches, separated by $2.6 \mu\text{s}$ and containing 12 bunches, which in turn are separated by 396 ns. Protons and antiprotons reach the final energy of 980 GeV and collide at two interaction points where the experiments $D\bar{O}$ and CDF are located.

3.2 $D\bar{O}$ Detector

The $D\bar{O}$ detector shown in Fig. 3.3 is a multi purpose detector [83, 84], consisting of three major subdetectors arranged cylindrically around the interaction point of the colliding protons and antiprotons: central tracking detectors, uranium/liquid-argon calorimeters and a muon spectrometer. The central tracking system includes a silicon microstrip tracker (SMT), a fiber tracker (CFT) and a solenoid providing a magnetic field of 2 T. Toroids inside the muon spectrometer provide a 1.8 T magnetic field.

In the detector description and the later analyses a right-handed coordinate system is

Parameter	Value
Circumference: Tevatron / Main Injector	6.28 km / 3.32 km
Max. beam energy: Tevatron / Main Injector	980 GeV / 150 GeV
Bunches per beam $p \times \bar{p}$	36×36
Bunch spacing	396 ns
Approx. bunch length	60 cm \approx 2 ns
Average number of interactions per crossing	≈ 2
Protons per bunch / transverse emittance	$24.8 \cdot 10^{10}$ / 20π mm-mrad
Antiprotons per bunch / transverse emittance	$5.4 \cdot 10^{10}$ / 15π mm-mrad
Beam half life time	9-10 h
Average store length	21 h

Table 3.1: Major parameters of the Tevatron.

used, in which the z -axis points along the proton direction and the y -axis points upward. The angles ϕ and θ are the azimuthal and polar angles, respectively. The pseudorapidity

$$\eta = -\ln \left(\tan \frac{\theta}{2} \right) \quad (3.1)$$

approximates the true rapidity $y = \frac{1}{2} \ln [(E + p_z)(E - p_z)]$ for finite angles in the limit of massless particles ($m/E \rightarrow 0$). The term *central* refers to the region $|\eta| \lesssim 1.1$ and $|\eta| \lesssim 1.6$ for calorimeter and tracker, respectively. The term *forward* is used for regions at larger $|\eta|$. The pseudorapidity of a trajectory of a particle can be given with respect to the position of the interaction or to the center of the detector. The former is indicated as η and the latter as η_{det} . The r coordinate denotes the perpendicular distance from the z axis. The separation of two objects is usually measured in

$$\Delta \mathcal{R} = \sqrt{(\eta_1 - \eta_2)^2 + (\phi_1 - \phi_2)^2}. \quad (3.2)$$

3.2.1 Tracking Detector

The tracking detector provides a precise measurement of the trajectories of charged particles. A charged particle with transverse momentum p_T will travel on a helix with the radius

$$r[m] = \frac{p_T[\text{GeV}]}{0.3 \cdot B[\text{T}]} \quad (3.3)$$

The tracking detector and its components SMT, CFT and solenoid are illustrated in Fig. 3.4. The detector can locate interaction vertices with a resolution of about $35 \mu\text{m}$ along the beamline and achieve an impact parameter resolution of better than $15 \mu\text{m}$ in $r - \phi$ for charged particles with a transverse momentum $p_T > 10 \text{ GeV}$ at $|\eta_{\text{det}}| = 0$. The relative transverse momentum resolution of the tracking detector is illustrated in in Fig. 3.5.

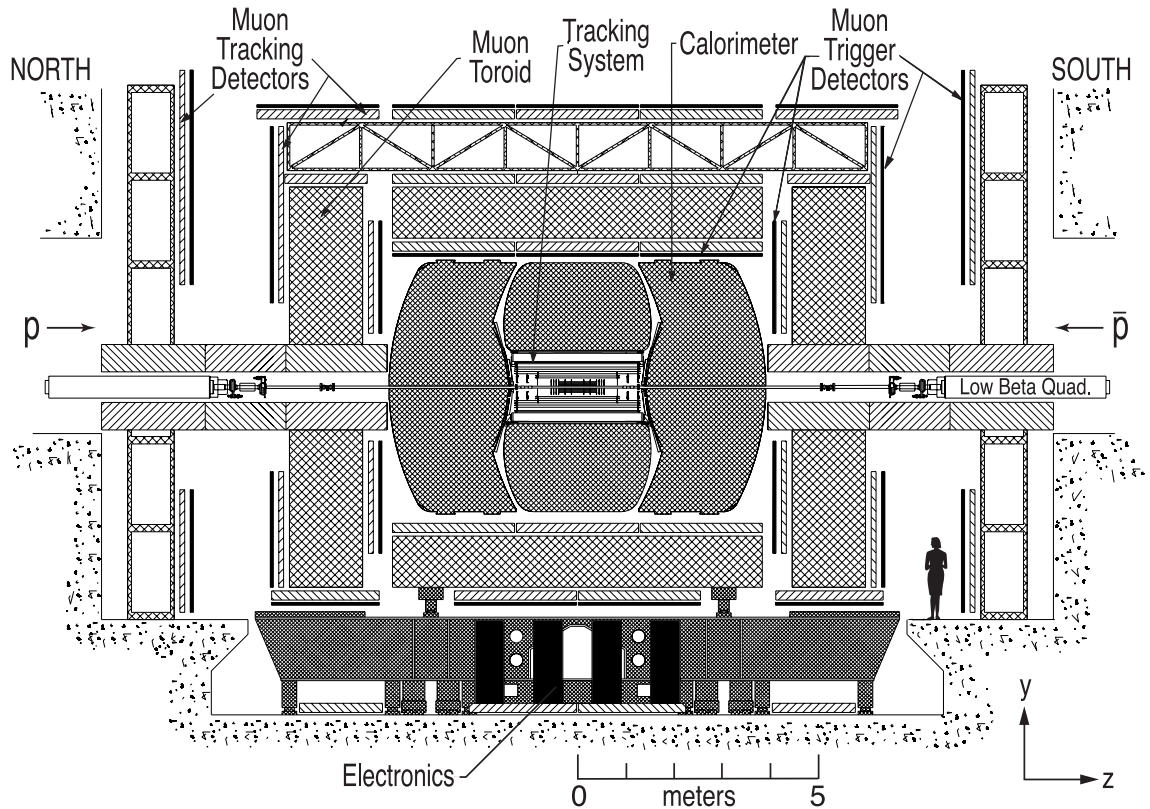


Figure 3.3: The upgraded DØ detector [84].

Silicon Microstrip Tracker (SMT)

The SMT is the innermost tracking detector starting at a radius of 2.7 cm covering the length of the interaction region ($\sigma = 25$ cm). It has $\approx 800,000$ individual strips, with a typical pitch of $50\text{--}80\ \mu\text{m}$, and a design optimized for tracking and vertexing capability at pseudorapidities of $|\eta_{\text{det}}| < 2.5$. In the central region ($|z| < 53$ cm), the system has a six-barrel longitudinal structure, which is interspersed by twelve discs of double sided wedge detectors with an outer radius of 10.5 cm. The six barrels consist of four layers arranged axially around the beam pipe. In the forward region, two large diameter disks with an inner radius of 9.5 cm and an outer radius of 26 cm are located at $|z| = 100.4$ cm and $|z| = 121.0$ cm .

Central Fiber Tracker (CFT)

The CFT surrounds the SMT and provides tracking in the region $|\eta_{\text{det}}| \lesssim 1.7$. It has eight thin coaxial barrels, each supporting two doublets of overlapping scintillating fibers of $835\ \mu\text{m}$ diameter, one doublet being parallel to the collision axis and the other alternating by $\pm 3^\circ$. It covers the radial space from 20 to 52 cm from the center of the beamline. The innermost cylinders are 1.66 m long, the outer six cylinders are 2.52 m long. Light signals are transferred via clear fibers to solid-state photon counters that have $\approx 80\%$ quantum efficiency.

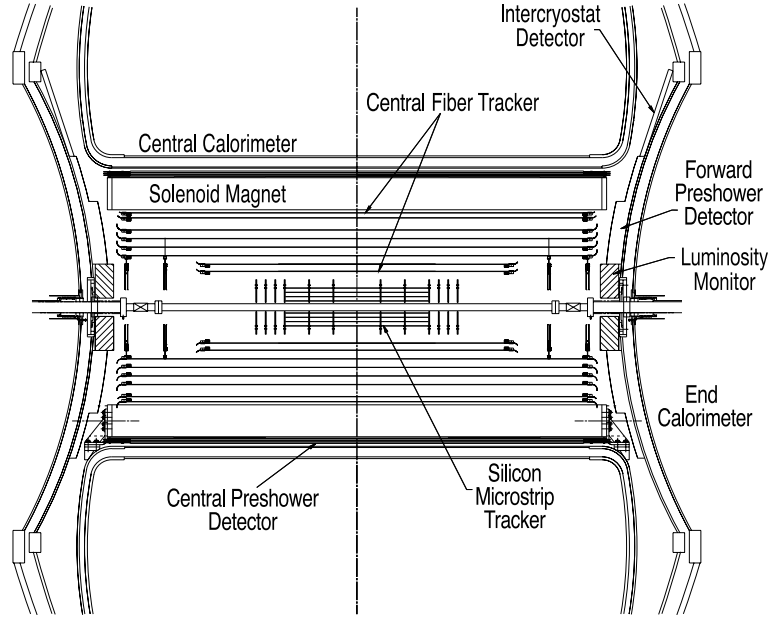


Figure 3.4: The central tracking system [84].

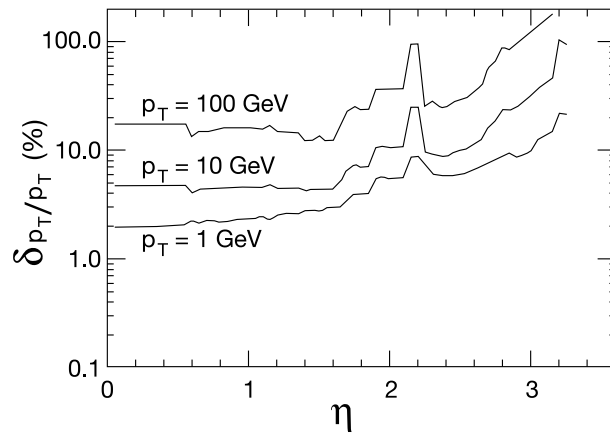


Figure 3.5: Relative transverse momentum resolution of the central tracking system as a function of pseudorapidity for tracks with $p_T = 1, 10$ and 100 GeV [84].

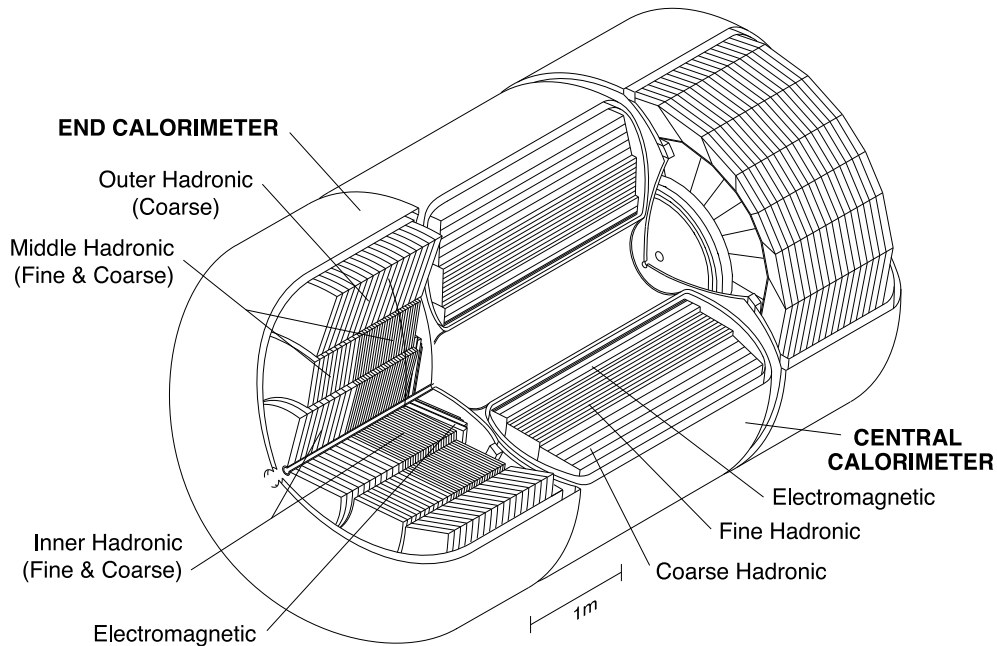


Figure 3.6: Isometric view of the central and two end calorimeters [84].

Solenoid Magnet

The solenoid magnet provides a uniform magnetic field of 2 T inside the tracking volume. It surrounds the CFT at a radius of 60 cm, has a length of 2.7 m and consists of two concentric coils of superconducting Cu:NbTi cable. The operating current is 4.75 kA and the stored energy amounts to 5.3 MJ. The operating temperature of 10 K is reached after a cool-down time of about 40 hours. The superconducting solenoid coils plus the cryostat wall has a thickness measured in electromagnetic interaction length of $X_0 \approx 1$ at $\eta_{\text{det}} = 0$.

3.2.2 Calorimeter System

The $D\emptyset$ calorimeter system consists of three sampling calorimeters and an intercryostat detector. The three liquid-argon/uranium calorimeters are a central calorimeter (CC) covering $|\eta_{\text{det}}| \lesssim 1.1$ and two end calorimeters (EC) that extend coverage to $|\eta_{\text{det}}| \approx 4.2$ as shown in Fig. 3.6. They are housed in separate cryostats maintaining a temperature of approximately 90 K.

The calorimeter readout cells sharing the same η_{det} and ϕ are arranged in towers as shown in Fig. 3.7. Each calorimeter tower contains an electromagnetic (EM) section which is located closest to the interaction region followed by fine hadronic (FH) and coarse hadronic sections (CH). The EM section consists of four layers, while the FH section consists of three and four layers in the CC and EC region, respectively. The CH section has a single readout layer. The two EC inner hadronic modules are cylindrical with inner and outer radii of 3.92 and 86.4 cm, as shown in Fig. 3.6. The thickness of layers is given in Tab. 3.2. The towers in the EM and hadronic modules are $\Delta\eta_{\text{det}} \times \Delta\phi = 0.1 \times 0.1$. The third EM layer (EM3), located at the EM shower maximum, is segmented twice as finely in both η and ϕ . The cell size

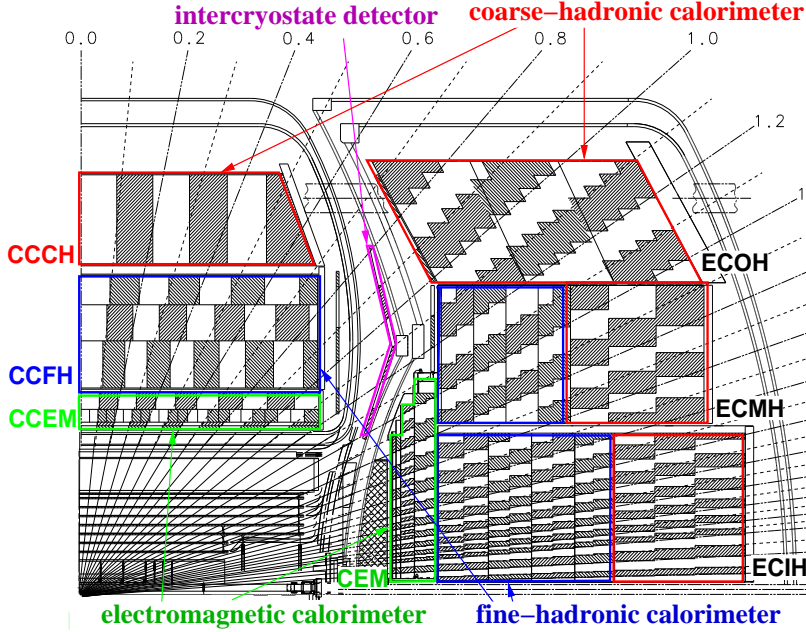


Figure 3.7: Schematic view of a portion of the DØ calorimeter showing the transverse and longitudinal segmentation pattern [84]. IH represents the inner hadronic calorimeter, while MH and OH represent middle and outer hadronic calorimeter.

increases with increasing η_{det} up to a maximum of 0.4×0.4 for $|\eta_{\text{det}}| \approx 4$. The calorimeter system has approximately 47,000 readout channels.

In the region between the central and the forward cryostats ($0.8 < |\eta_{\text{det}}| < 1.4$), the coverage is incomplete and unsampled material degrades the energy resolution. Additional calorimeter readout cells are located in front of the first layer of uranium, called *massless gaps*. The *intercryostat detector* (ICD) provides scintillator sampling covering the region $1.1 < |\eta_{\text{det}}| < 1.4$ and is attached to the exterior surfaces of the EC cryostats. Each scintillator tile covers $\Delta\eta_{\text{det}} \times \Delta\phi \approx 0.3 \times 0.4$

Module	Central Calorimeter	End Calorimeter		
		Inner	Middle	Outer
EC [X_0]	1.4, 2.0, 6.8, 9.8	1.6, 2.6, 7.9, 9.3	–	–
FH [λ_A]	1.3, 1.0, 0.76	4×1.1	4×0.9	–
CH [λ_A]	3.2	4.1	4.4	6.0

Table 3.2: Thickness of the different calorimeter layers measured in units of electromagnetic interaction length X_0 and hadronic interaction length λ_A .

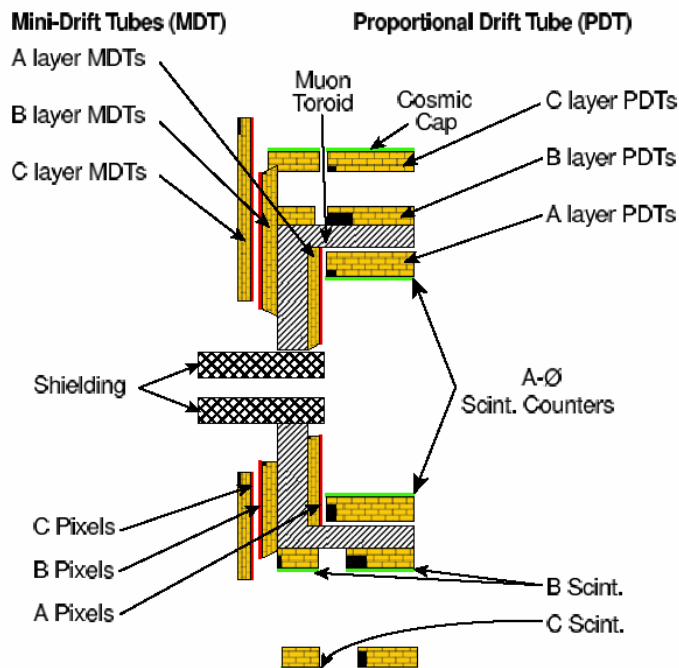


Figure 3.8: Schematic side view of the muon system.

3.2.3 Muon Spectrometer

The muon spectrometer [85] is the outermost component of the $D\phi$ detector. It consists of a central spectrometer ($|\eta_{det}| \leq 1$) and two forward angle muon spectrometers, which extend the coverage up to $|\eta_{det}| \leq 2$ as shown in Fig. 3.8. A center toroid (1.8 T) is located at $318 < r < 427$ cm and two end toroids (1.6 T) at $454 \leq |z| \leq 610$ cm.

The central system includes proportional drift tubes (PDTs), barrel scintillation counters, so-called $A\phi$ -counters, and cosmic ray veto scintillation counters, so-called *cosmic caps*. Three layers of PDTs are located inside (layer A) and outside (layer B and C) of the central toroid. The drift tubes are made of rectangular extruded aluminum tubes of 10.1 cm across and a maximum length of 5.79 m. Layer A has four layers of PDTs, while layers B and C have three. The gas mixture consists of 84 % argon, 8 % CF_4 and 8 % methane. Each drift tube contains an anode wire at the center, parallel to the toroid field lines (operated at 4.7 kV) and cathode pads located above and below the wire (operated at 2.3 kV), to provide hit information along the wire. The drift velocity is approximately $10 \text{ cm}/\mu\text{s}$ and the drift times is of the order of 500 ns. The muon system is only partially instrumented in the bottom region ($4.25 < \phi < 5.15$) to allow for support structure of the detector. The $A\phi$ scintillation counters are positioned alongside the PDTs of layer A, while the cosmic caps are mounted on the outside of layer C, except in the bottom region, where they are partially mounted on layer B. The time resolution is 5 ns and can be improved to 2.5 ns by offline corrections.

The forward region uses mini drift tubes (MDTs) due to their short electron drift time, high segmentation and radiation hardness. As in the central spectrometer, the drift tubes are arranged in three layers with four or three planes of MDTs. Each tube has eight $1 \times 1 \text{ cm}^2$

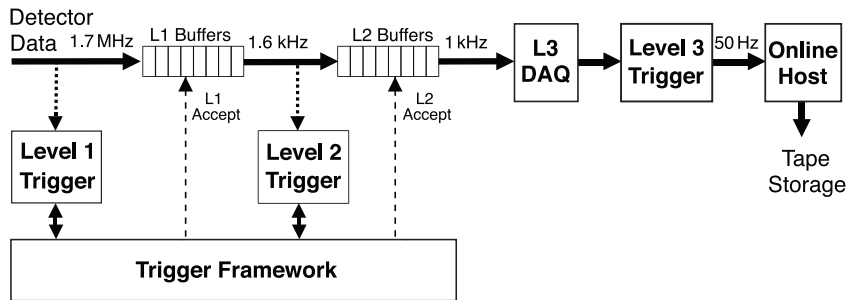


Figure 3.9: Overview of the DØ trigger and data acquisition system [84].

cells with a maximum length of 583 cm. The gas mixture consists of 90 % CF₄ and 10 % methane. The tubes are mounted along the magnetic field lines, contain a gold plated, grounded tungsten anode wire and are operated at 3.2 kV. The maximum drift time is lower than 70 ns. A layer of pixel scintillating counters is mounted on each MDT layer with a segmentation of approximately 0.1×0.08 in $\eta - \phi$ and reaching a time resolution of about 1 ns.

The fast scintillation counters are used for triggering and time measurement. Drift tubes are used for precise position measurement, for a rough momentum determination and also for triggering.

3.2.4 Luminosity Monitor

The luminosity monitor measures the rate of inelastic $p\bar{p}$ collisions in order to determine the Tevatron luminosity at the DØ interaction region. Additionally, it identifies beam crossings with multiple $p\bar{p}$ interactions, provides a fast determination of the z -coordinate of the interaction vertex and measures beam halo rates. Two arrays of 24 plastic scintillation counters with photomultiplier readout are located in front of the EC cryostats at $z = \pm 140$ cm, covering $2.7 < |\eta_{\text{det}}| < 4.4$.

3.2.5 Trigger and Data Acquisition

Trigger and data acquisition systems are designed to accommodate the high luminosity of Run II. There are three distinct levels that form the trigger system. Each succeeding level examines fewer events but in greater detail and with more complexity. The first stage (Level 1 or L1) comprises a collection of hardware trigger elements that reduce the data rate from approximately 2 MHz to about 1.6 kHz in $3.5 \mu\text{s}$ or less. The second stage (Level 2 or L2) reduces the rate within $100 \mu\text{s}$ to 1 kHz. Hardware engines and embedded micro computers associated with specific subdetectors provide information to a global processor to construct a trigger decision based on individual objects as well as object correlations. Events passing L1 and L2 criteria are sent to the Level 3 (L3) farm of microprocessors, which reduces the rate to about 50 Hz. A fast reconstruction of the full precision readout is performed and sophisticated algorithms decide within 200 ms whether the event is stored for offline reconstruction. Figure 3.9 shows a block diagram of the DØ trigger system. In the following,

a brief overview of the trigger components used by the analyses presented later is given. The trigger framework is discussed in detail in [84].

Level 1 Trigger

Level 1 is implemented in custom-designed hardware to provide dead time free trigger decisions. It uses the detector systems indicated in Fig. 3.10. The analyses presented in this thesis rely on the L1MUO and L1CTT components, which evaluate information of the muon system and the central tracking detector, respectively.

The L1CTT system [86] provides fast trigger decisions for charged particles with $p_T > 1.5$ GeV by reconstructing their trajectories in the CFT. The fiber hits of the CFT are compared to approximately 20 000 predefined track equations using combinatorial logic in field programmable gate arrays (FPGAs). It also stores more-detailed event data, e.g. sorted list of track, which are used as seeds by other trigger systems like L1MUO.

The L1MUO system uses hits from the wire chambers, muon scintillation counters and tracks from the L1CTT in order to look for muon-like patterns. There are two subsystems, which use FPGAs to perform combinatorial logic on approximately 60,000 muon channels and up to 480 tracks from the L1CTT per bunch crossing. The first subsystem matches central tracks to muon scintillator hits, while the second one matches scintillator-confirmed track stubs in wire chambers between the two or three layers of the muon system.

Level 2 Trigger

The L2 trigger comprises preprocessors for each detector subsystem working in parallel and a global processor (L2Global) for integration of the data. L2Global provides a trigger decision based on a combination of the physics objects provided by the preprocessors. The preprocessor of interest for the triggers used in the thesis is the L2MUO.

L2MUO evaluates information from L1MUO and from approximately 150 front-end modules of the PDTs, MDTs and scintillation counters [87]. It uses calibration and more precise timing information than L1MUO to improve the quality of the muon candidates. Due to the large amount of front-end inputs, two processing stages are required. The first one finds tracks segments inside the three individual layers of the muon spectrometer, while the second one combines the track elements to L2 muon candidate objects.

Level 3 Trigger

For events passing Level 1 and 2, the entire DØ detector is read out. The L3 trigger decision is therefore based on completely reconstructed physics objects and the relationships between

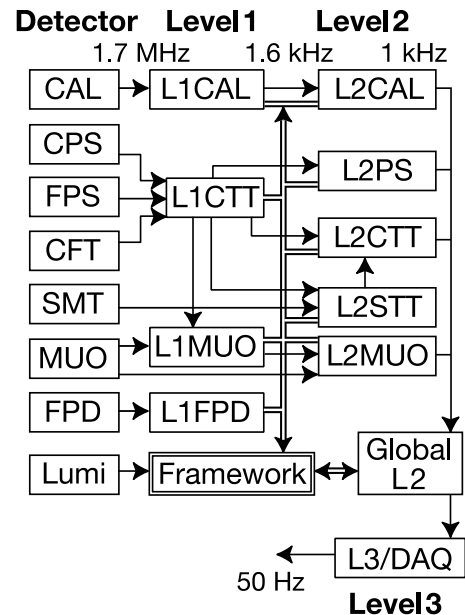


Figure 3.10: Block diagram of the DØ trigger system [84].

them, like rapidity and azimuthal angle separation and their invariant masses. Candidate objects (or relations between them) are generated by object-specific software algorithms (*filter tools*). Reference sets of programmable algorithm parameters are input to the tools via the programmable *trigger list*.

The L3 tracking is based on CFT and SMT information. Two different algorithms reconstruct tracks from hits in CFT and SMT. A global (SMT plus CFT) high-momentum-track finder starts from axial CFT tracks propagated towards the SMT by a linear fit in $r - \phi$. The primary interaction point is determined using CFT tracks. A stand-alone global track filter is a powerful tool in addition to single muon triggers.

The L3 muon tools allow to identify muon tracks in three dimensions. In addition to unpacking data, the tool can call subordinate tools that utilize central tracking and calorimetry. A track match tool extrapolates the muon track to the central tracker allowing for an efficient matching between objects in both subdetectors. Matching of muon and calorimeter objects allows to distinguish isolated from non-isolated muons.

Data Acquisition

The data acquisition system consists of the L3DAQ and the *online host* system (Fig. 3.9). The L3DAQ transports detector component data from the readout crates to the nodes of the Level 3 trigger farm nodes. The online host system receives event data from the L3 farm nodes at a combined rate of approximately 10 MB/s and distributes that data to logging and monitoring tasks. The final repository for the raw event data is tape, maintained in a robotic tape system.

The DØ offline reconstruction program DØRECO [88] is responsible for the reconstruction of physics objects used for analysis. Two types of output format are provided. The *data summary tier* (DST) contains all event information required to perform any analysis (≈ 150 kb per event). In the *thumbnail* format (TMB) a part of the information is dropped and the remaining part is compressed (≈ 20 kb per event). It provides sufficient information for most of the ongoing analyses. Additionally, the data available in TMB format is converted into the common analysis format (CAF) [89, 90], which is based on ROOT [91] and provides a convenient format for physics analyses, but even more information are dropped.

3.2.6 Detector Simulation

All final state particles resulting from the simulation of the $p\bar{p}$ collisions described in Sec. 2.5, are passed to the simulation of the DØ detector, performed by the software packages DØGSTAR [92] and DØSIM [93].

The interactions of all particles with the detector material are simulated by DØGSTAR, which is based on GEANT [94]. Additionally, it models the decay of long-lived particles in the detector. This step is the most time-consuming part of the Monte Carlo generation since all particle interactions are modeled in detail including the ionization in the silicon detectors, the development of electromagnetic and hadronic showers in the calorimeter and further detector components, as illustrated in Fig. 3.11. The simulation of the detector readout is included as well.

The package DØSIM adds several hardware related effects to the simulation. Minimum bias events are overlaid. Pile-up from previous bunch crossings is included as well as noise

in the detector and readout electronics. The output of $D\bar{O}$ SIM has the same format as real data but includes additional Monte Carlo generator information.

Finally, the simulated physics objects are processed by the same reconstruction software $D\bar{O}$ RECO [88] as real data.

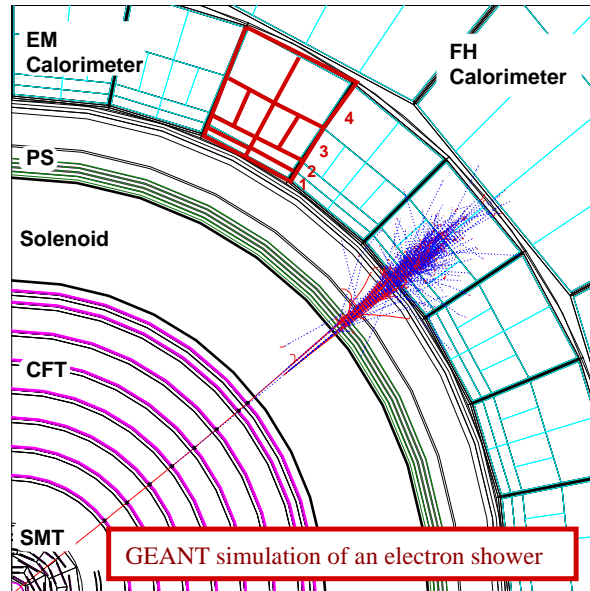


Figure 3.11: GEANT simulation of an electron in the $D\bar{O}$ detector.

4

Event Reconstruction and Object Identification

The event reconstruction and object identification transforms the digital output of the DØ detector into physics objects (e.g. muons, taus and jets) including their 4-momenta and the complete kinematics of the event. For each physics object, algorithms have been developed to ensure high efficiency and accuracy of this process [88].

The following chapter describes the reconstruction and identification of tracks, muons, taus and missing transverse energy since the two analyses discussed in the present thesis rely heavily on them. Additionally, jets and the primary vertex are discussed because their information is required as well. The two analyses use two different versions of the DØ reconstruction and identification software framework. The newer and improved algorithms are described as they are used for the search for associated chargino/neutralino production, called *SUSY analysis* in the following. It will be indicated, if there are significant differences to the version used for the search for neutral MSSM Higgs bosons, which will be referred to as *Higgs analysis*.

4.1 Track Reconstruction

The trajectory of a charged particle is reconstructed in form of a track using the information of hits in the SMT and CFT (Sec. 3.2.1). Both detectors allow full coverage in ϕ , while the SMT can be used up to $\eta_{\text{det}} \lesssim 3.0$ and the CFT reaches only to $\eta_{\text{det}} \lesssim 1.6$. Two algorithms *Alternative Algorithm* (AA) and *Histogram Track Finder* (HTF) are implemented for the track reconstruction.

A road method is used in the AA [95]. Three hits in either SMT barrel or SMT disks serve as starting point, from where the algorithm proceeds outward through SMT and CFT. A hit is associated to the track if it is located within a search window and the result of a χ^2 fit lies below a certain value. Layers, where no hit is found, are counted as a “miss”. The algorithm stops at the outermost layer of the detector or if three misses are found.

The HTF is based on a histogramming method [96]. A particle moving in a homogeneous magnetic field is characterized by its curvature ρ , the distance of the closest approach to the beamline d_0 and the polar angle ϕ at the point of closest approach to the beamline. For particles with small d_0 every pair of points in the coordinates space (x, y) corresponds to a single point in the (ρ, ϕ) plane. Every pair of hits in the tracking detector is filled into a two dimensional histogram. Pairs of hits that belong to the same track will result in a peak in the histogram, while other pairs will be distributed randomly.

Finally, the two lists of reconstructed tracks from both algorithms are merged. The curvature of the track in the magnetic field allows to determine the transverse momentum. The momentum resolution σ_{p_T} decreases with increasing momentum ($\sigma_{p_T}/p_T \sim p_T$). This is contrary to the energy measurement in the calorimeter, where the resolution improves with increasing energy ($\sigma_{E_T}/E_T \sim 1/\sqrt{E_T}$). Furthermore, the measurement of the transverse momentum is affected by the radiation of bremsstrahlung, which reduces the resolution for light particles such as electrons.

4.2 Primary Vertex

The vertex of the hard scattering process in a bunch crossing is called the primary vertex. Its position, which is important for the measurement of the transverse momenta of all physics objects, is determined by a fit based on the tracks pointing to the vertex. Based the number of the tracks associated to a vertex and their transverse momenta, it can be distinguished from other vertices that result for example from soft minimum-bias interactions [97, 98].

4.3 Muon Reconstruction and Identification

Muons are reconstructed based on hits in the wire chambers and the scintillator counters of the muon detector (Sec. 3.2.3). To allow for a high efficiency in the later analyses, muons with relatively loose identification criteria are considered. They are required to have at least two wire hits and one scintillator hit in layer A or at least two wire hits and one scintillator hit in layer BC. Additionally, these hits must be matched to a track which has been reconstructed in the tracking detector. Since the muon momentum is given by the momentum of the matched track, the following criteria ensure that the track is of good quality:

- The track has at least one hit in the SMT.
- The fit of the track results in $\chi^2/\text{ndf} < 4$, where ndf represents the number of degrees of freedom.
- The distance of the track to the beamline at the point of closest approach is smaller than 0.2 mm.

The first and the second criteria are omitted in the Higgs analysis.

Muons are regarded as isolated, meaning they are not part of a jet, if they fulfill the following isolation criteria:

- Isolation in the tracker: The scalar sum of the transverse momenta of the tracks in a cone ($\Delta\mathcal{R} < 0.5$) around the muon track is smaller than 2.5 GeV.

- Isolation in the calorimeter: The transverse energy measured in a hollow cone ($0.1 < \Delta\mathcal{R} < 0.4$) in the calorimeter is smaller than 2.5 GeV. The energy in the CH part of the calorimeter is not included in order to be less affected by noise.

In the Higgs analysis the upper bound is placed at 3.5 GeV for both criteria.

The muon detector is not only sensitive to muons originating from the interaction in the bunch crossing, but also to cosmic muons. This background is suppressed by removing muons which lie outside a time window of 10 ns around the interaction. Further details concerning the muon reconstruction and identification are given in [99, 100].

4.4 Tau Reconstruction and Identification

The reconstruction of tau leptons is more complex than the reconstruction of muons. In contrast to these, tau leptons decay inside the detector and can only be identified by their decay products. The life time of tau leptons ($c\tau = 87 \mu\text{m}$) is too short to be resolved in the detector, and if they decay leptonically, their decay products can not be distinguished from other electrons or muons. However, hadronically decaying tau leptons, which account for about 65 % of all tau decays (Tab. 4.1), can be reconstructed as such. In the following, speaking of tau leptons only refers to hadronically decaying tau leptons.

	Decay Channel	Branching Ratio
Leptonic decays (1-prong)	$\tau^- \rightarrow e^- \bar{\nu}_e \nu_\tau$	17.36 %
	$\tau^- \rightarrow \mu^- \bar{\nu}_\mu \nu_\tau$	17.84 %
Hadronic decays with 1 charged particle (1-prong)	$\tau^- \rightarrow h^- \nu_\tau$	11.59 %
	$\tau^- \rightarrow h^- \nu_\tau \pi^0$	25.95 %
	$\tau^- \rightarrow h^- \nu_\tau 2\pi^0$	10.81 %
	$\tau^- \rightarrow h^- \nu_\tau 3\pi^0$	1.33 %
Hadronic decays with 3 charged particles (3-prong)	$\tau^- \rightarrow h^- h^+ h^- \nu_\tau$	9.87 %
	$\tau^- \rightarrow h^- h^+ h^- \nu_\tau \pi^0$	5.06 %

Table 4.1: Overview of major tau decay channels and their branching ratios [36].

4.4.1 Reconstruction Algorithm

Hadronically decaying tau leptons appear in the detector as narrow isolated jets with a low track and π^0 multiplicity. Therefore, they need to be distinguished from jets and suffer from larger background than electrons and muons. In the following, the reconstruction algorithm for tau leptons is described, which includes the reconstruction of energy clusters in the calorimeter and matching them to tracks [101]. Figure 4.1 shows the efficiency of the algorithm as a function of the visible transverse momentum of a tau lepton $p_T^{\tau, \text{vis}}$, which excludes neutrinos, and as a function of η_{det} .

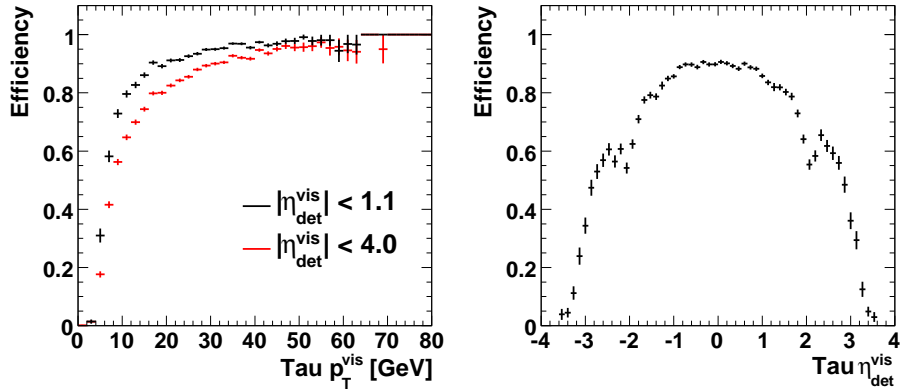


Figure 4.1: Reconstruction efficiency of hadronically decaying tau leptons as a function of $p_T^{\tau, \text{vis}}$ and η_{det}^{τ} as measured in $Z/\gamma^* \rightarrow \tau\tau$ events in Monte Carlo simulation .

Calorimeter Cluster

A simple cone algorithm, seeded by calorimeter towers with a transverse energy more than 1 GeV, reconstructs the energy in a cone with $\Delta\mathcal{R} = 0.3$ (called 0.3-cone). The resulting clusters are regarded as tau candidates if their transverse energy lies above 4 GeV or if its transverse energy is larger than 2 GeV and a track with $p_T > 5$ GeV can be matched to it.

Electromagnetic Clusters

A nearest neighbor algorithm is used to reconstruct the neutral decay products of the tau, which are originating almost exclusively from neutral pions. It is seeded by calorimeter cells in the EM3 layer and takes into account all cells in the electromagnetic calorimeter belonging to the corresponding calorimeter cluster found by the simple cone algorithm in the previous step. The transverse energy of a electromagnetic cluster has to exceed 0.8 GeV.

Track Matching

Up to three tracks can be associated to a tau candidate. It is important to distinguish between tracks from tau decays and tracks from other sources like jets and underlying event. The track matching algorithm sorts all tracks in decreasing p_T that are closer than $\Delta\mathcal{R} < 0.5$ to the calorimeter cluster and have $p_T > 1.5$. The leading track is associated to the tau cluster. Additionally, the second and third track are added if the distance of their z positions to the leading track is less than 2 cm and the invariant mass of the first and second track lies below 1.1 GeV and the invariant mass of all three tracks lies below 1.7 GeV. The z positions are measured at the point of closest approach to the beamline.

4.4.2 Classification of Tau Candidates

The reconstructed tau candidates are classified into three τ -types according to their signature in the detector as illustrated in Fig. 4.2:

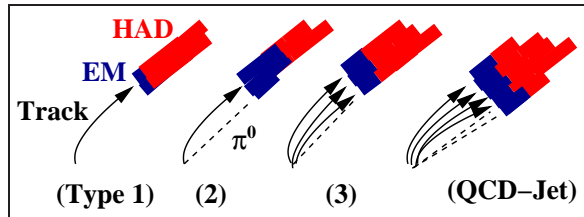


Figure 4.2: Schematic illustration of the signatures of the three τ -types in the detector. The size of the colored areas symbolizes the amount of energy deposited in the electromagnetic (EM) and hadronic (HAD) calorimeter. A jet from background processes is shown for comparison.

- **Type 1:** Calorimeter cluster with exactly one track and no electromagnetic calorimeter cluster (π^\pm -like).
- **Type 2:** Calorimeter cluster with exactly one track and at least one electromagnetic calorimeter cluster (ρ^\pm -like).
- **Type 3:** Calorimeter cluster with more than one track (3-prong).

4.4.3 Neural Network

The identification of tau leptons is based on three neural networks, one for each τ -type [102, 103]. They allow to discriminate tau leptons from objects that are misidentified as taus, so-called *fakes*. The architecture of the used neural network is identical for each τ -type. If n represents the number of variables used, then the neural network consists of an input layer with n_i nodes, one hidden layer containing $n_h = 2n_i + 1$ nodes and one output layer with a single node. Each node of a given layer is connected to all nodes of the neighboring layer but there are neither connections between nodes in the same layer nor direct connections between any input and output node.

The signal training sample consists of Monte Carlo events which contain only decays of a single tau lepton, whereas the background sample is obtained from data. The events used for the background sample have to pass the following criteria, to ensure that the tau candidate is faked by a jet:

- The event contains at least one muon and one tau candidate.
- The muon is part of a jet.
- Muon and tau candidate have the same charge.
- The angle between muon and tau candidate is smaller than $\Delta\phi < 2.7$.

Discriminating Variables

The discriminating variables serve as input for the nodes of the input layer and are selected in order to give the optimal discrimination between tau leptons and jets that fake a tau candidate. They exploit the differences in longitudinal and transversal shower shape in the

calorimeter as well as isolation in calorimeter and tracker. The correlation to the transverse energy of the tau lepton is kept as small as possible. The variables that enter the neural network of each τ -type are defined in the following and are summarized in Tab. 4.2:

- $\text{profile} = \frac{E_T^1 + E_T^2}{E_T}$: the sum of the transverse energy in the two most energetic calorimeter towers $E_T^{1,2}$ divided by the total transverse energy of the tau candidate E_T ;
- $\text{caliso} = \frac{E_T^{\Delta\mathcal{R} < 0.5} - E_T}{E_T}$: the isolation in the calorimeter is calculated from the energy in a 0.5-cone around the tau candidate and E_T of the tau cluster, which is calculated in a 0.3-cone;
- $\text{trkiso} = \frac{p_T^{\text{Rest}}}{p_T^{0.5}}$: the isolation in the tracker defined as the ratio of the scalar sum of the transverse momenta of all tracks in a 0.5-cone which are not associated to the tau candidate p_T^{Rest} and the same quantity of all tracks in the cone;
- $\text{etsum} = \frac{E_T}{E_T + p_T^{\text{tracks}}}$: p_T^{tracks} represents the scalar sum of p_T of all tracks which are associated to the tau candidate;
- $\text{prf3} = \frac{E_T^{\text{EM1}}}{E_T^{\text{EM3}}}$: the ratio calculated from the E_T of the leading electromagnetic cluster and the total transverse energy in a 0.5-cone in calorimeter layer EM3;
- $\text{em12f} = \frac{E_T^{\text{EM1}} + E_T^{\text{EM2}}}{E_T^{\Delta\mathcal{R} < 0.5}}$: the transverse energy in calorimeter layers EM1 and EM2 divided by the total transverse energy in a 0.5-cone;
- $p_T / E_T^{\Delta\mathcal{R} < 0.5}$: the transverse momentum of the most energetic track divided by the total transverse energy in a 0.5-cone;
- p_T / E_T : the transverse momentum of the most energetic track divided by the transverse energy of the calorimeter cluster;
- FHF: the fraction of energy deposited in the FH layers of the calorimeter;
- EMF: the scalar sum of the transverse momenta of all EM clusters divided by the transverse energy of the tau candidate;
- $\text{e1e2} = \sqrt{p_T^{\text{tracks}} \cdot E_T^{\text{EM}}}$: product of p_T^{tracks} (see definition above) and the transverse energy deposited in the EM layers of the calorimeter;
- $\delta\alpha = \sqrt{(\Delta\phi / \sin\theta)^2 + (\Delta\eta)^2}$: the differences $\Delta\phi$ and $\Delta\eta$ are calculated between the sum of the tau tracks and the sum of the electromagnetic clusters, while θ is the azimuthal angle of the calorimeter cluster centroid;
- $\text{RMS}^\tau = \sqrt{\frac{1}{p_T} \sum_{\text{Cal-Tower}} \Delta\phi^2 E_T^{\text{Cal-Tower}} + \Delta\eta^2 E_T^{\text{Cal-Tower}}}$: represents the width of the calorimeter cluster of the tau. The sum runs over all calorimeter towers inside the tau cluster and $\Delta\phi$ and $\Delta\eta$ are calculated between the calorimeter tower and the centroid of the tau cluster;
- η_{det}^τ : to take into account the η_{det}^τ -dependence of other input variables.

Figures 4.3, 4.4 and 4.5 show the distribution of each input variable for the different τ -types as used in case of the SUSY analysis. Signal and background are taken from the training samples. The resulting neural network outputs and the background rejection as a function of efficiency for a given cut value are documented in Fig. 4.6.

Variable	SUSY analysis			Higgs analysis		
	τ -type 1	τ -type 2	τ -type 3	τ -type 1	τ -type 2	τ -type 3
profile	✓	✓	✓	✓	✓	✓
caliso	✓	✓	✓	✓	✓	✓
trkiso	✓	✓	✓	✓	✓	✓
etsum	✓	✓	✓			
prf3		✓				
em12f	✓			✓		
$\frac{p_T}{E_T^{\Delta\mathcal{K}<0.5}}$			✓		✓	✓
$\frac{p_T}{E_T}$				✓		
FHF	✓	✓	✓			
EMF		✓	✓			
$\delta\alpha$		✓	✓		✓	✓
e1e2		✓	✓			
RMS τ	✓	✓	✓			
η_{det}^τ	✓	✓	✓			

Table 4.2: Input variables for the three neural networks used in the SUSY and Higgs analysis.

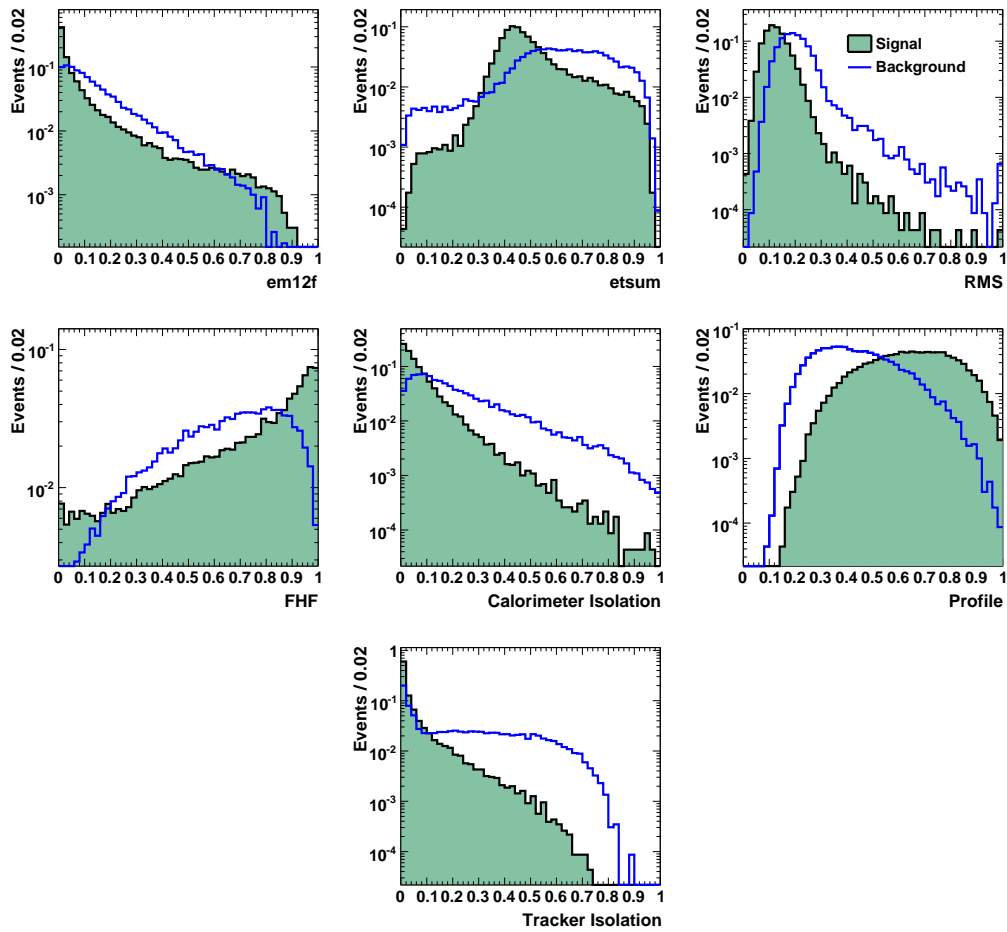


Figure 4.3: Distribution of the neural network input variables for τ -type 1 for signal and background.

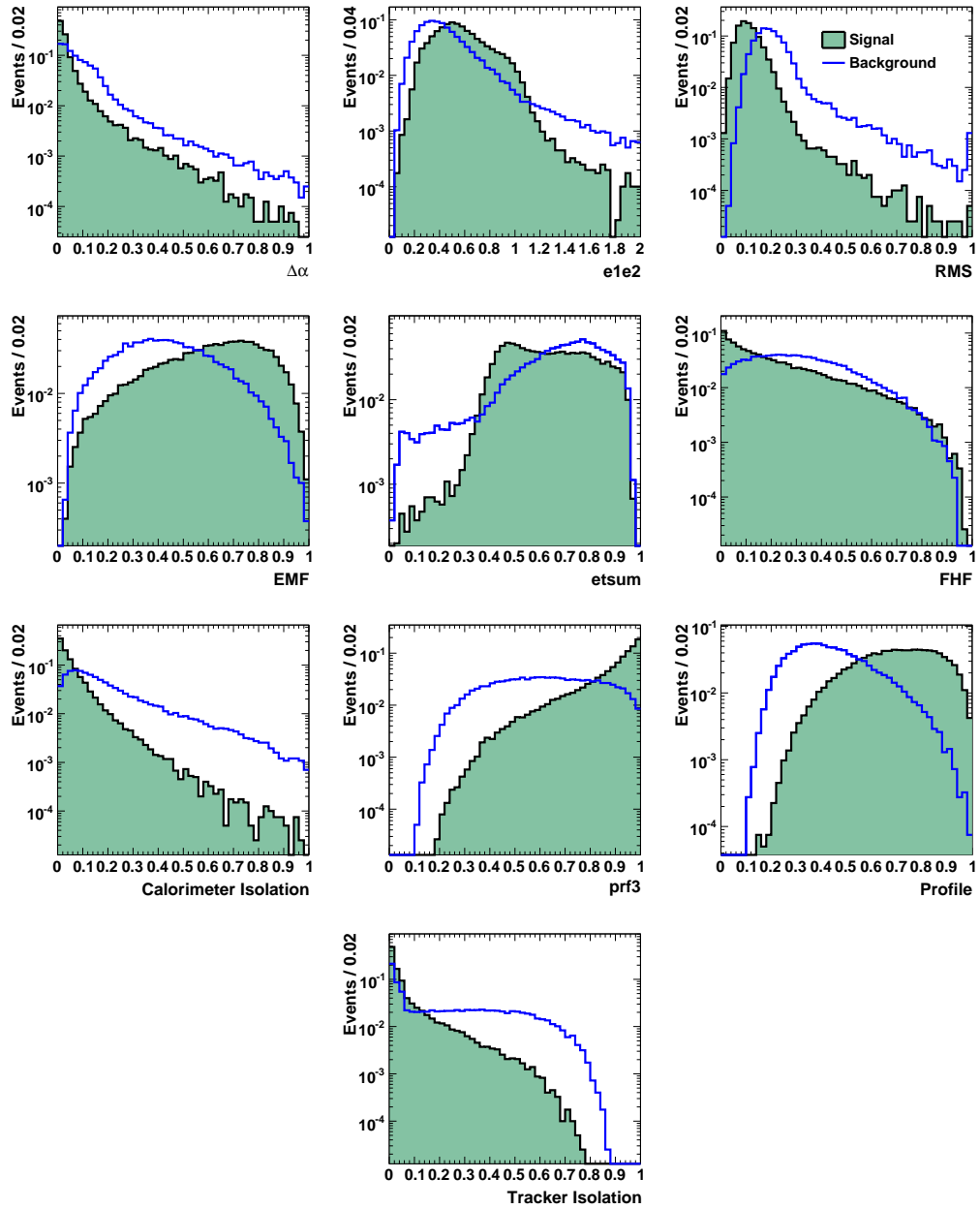


Figure 4.4: Distribution of the neural network input variables for τ -type 2 for signal and background.

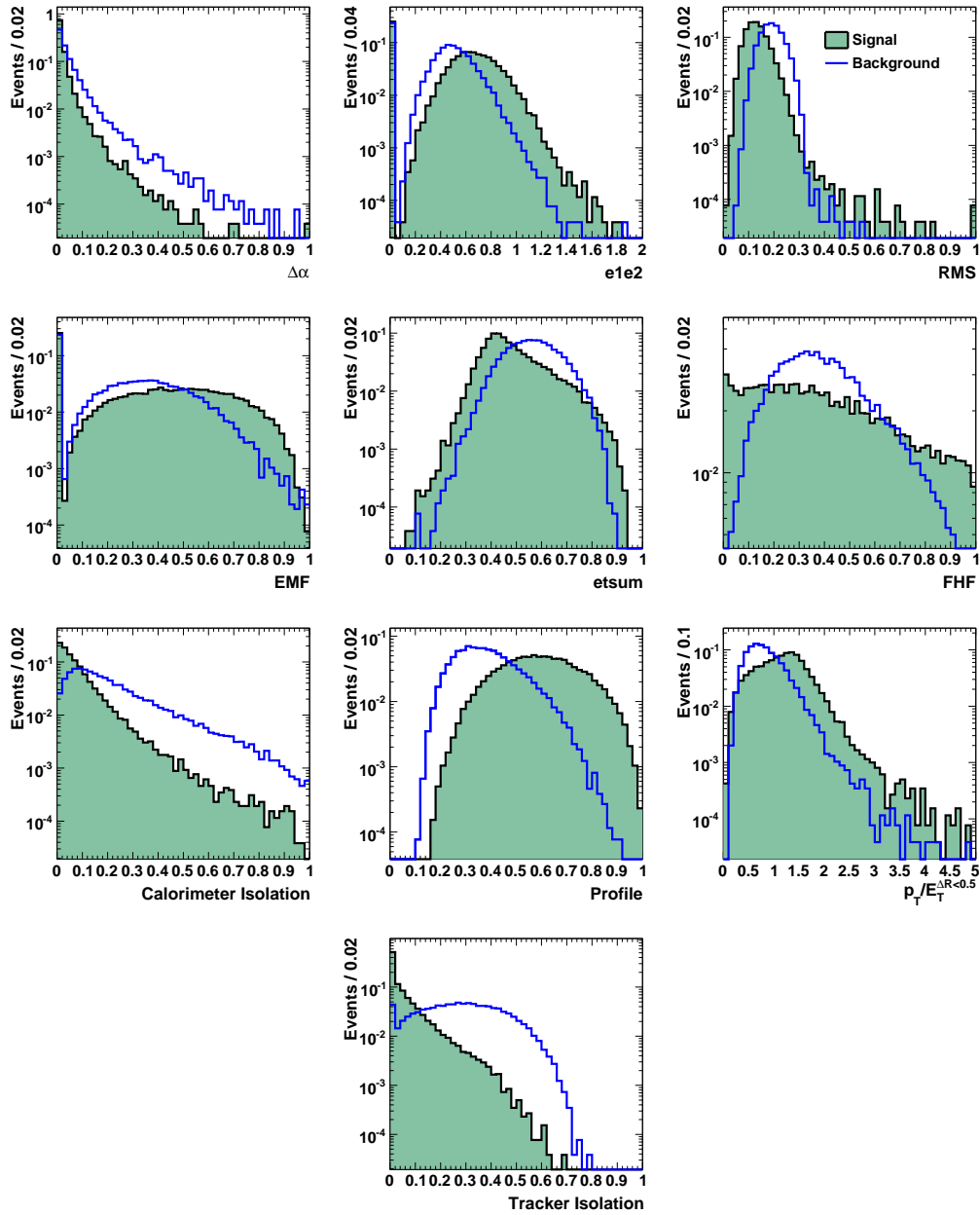


Figure 4.5: Distribution of the neural network input variables for τ -type 3 for signal and background.

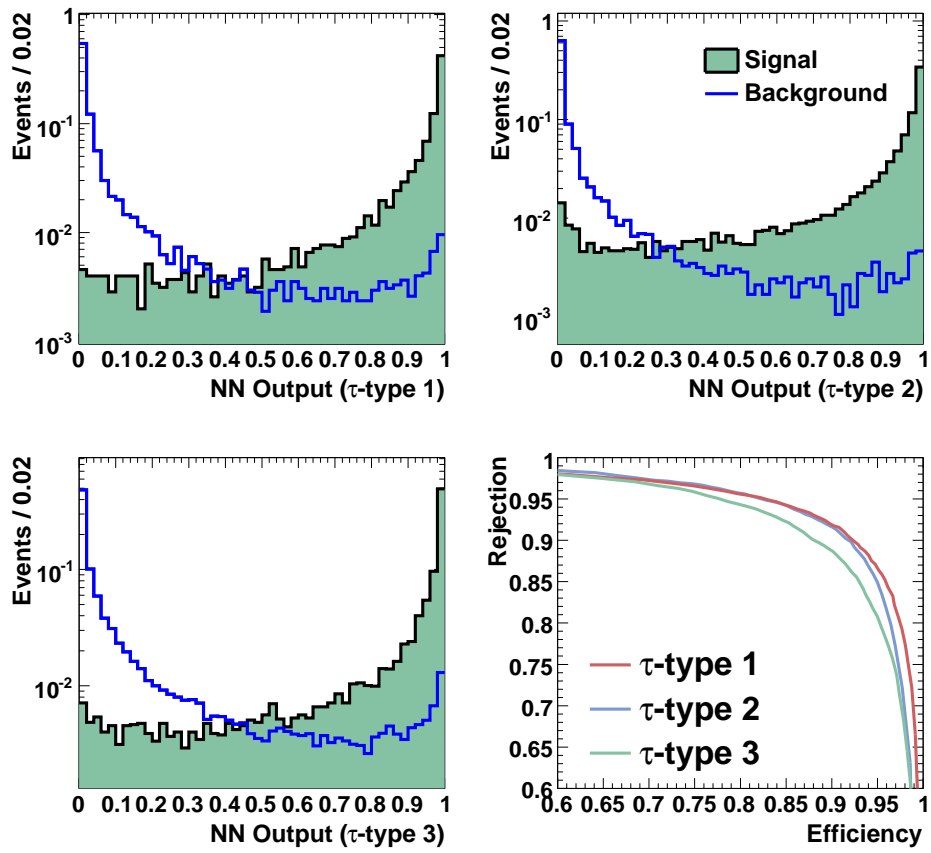


Figure 4.6: Distribution of the neural network output for each τ -type and the background rejection as function of the efficiency for a given cut value.

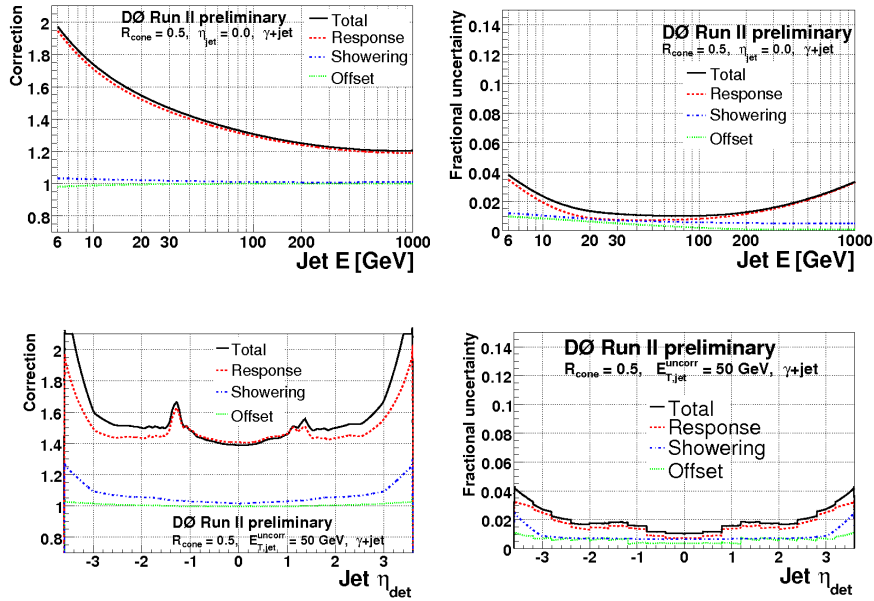


Figure 4.7: Jet energy corrections and the corresponding errors for data as a function of the uncalibrated jet energy for $\eta_{det} = 0$ (top) and as a function of η_{det} for $E_{jet}^{uncorrected} = 50$ GeV (bottom) [104].

4.5 Jet Reconstruction and Identification

Jets are reconstructed based on a simple cone algorithm [105]. In the following, only 0.5-cone jets with a transverse energy larger than 15 GeV and $|\eta_{det}| < 2.5$ are used. To ensure that they are well separated from electromagnetic objects, it is required that the fraction of energy deposited in the EM calorimeter is smaller than 0.9. To remove jets which are faked by noise appearing in the CH calorimeter, the fraction of energy in this region has to be smaller than 0.4. Another quality criterion is the L1 confirmation, which compares the energy of the reconstructed jet to the energy reconstructed by the L1 trigger readout. Jets are accepted only if the ratio of the energy measurements is above a certain threshold, which depends on η_{det} and p_T . Further details about reconstruction and identification of jets are given in [106].

Jet Energy Correction

The measured energy of jets needs to be calibrated [104]. The calorimeter absorbs the energy of the particles in the jet efficiently. But there are effects that can lead to a significant deviation:

- **Calorimeter Response:** The response correction takes into account a number of sizable instrumental effects that distort the jet energy measurement, e. g. material in front of the calorimeter, uninstrumented regions in the detector, non-linear calorimeter response as a function of energy and charged particles that get bent in the magnetic field and deposit their energy far away from the center of the jet and therefore do not get clustered by the jet algorithm. These effects result in the largest contribution to the jet energy correction.

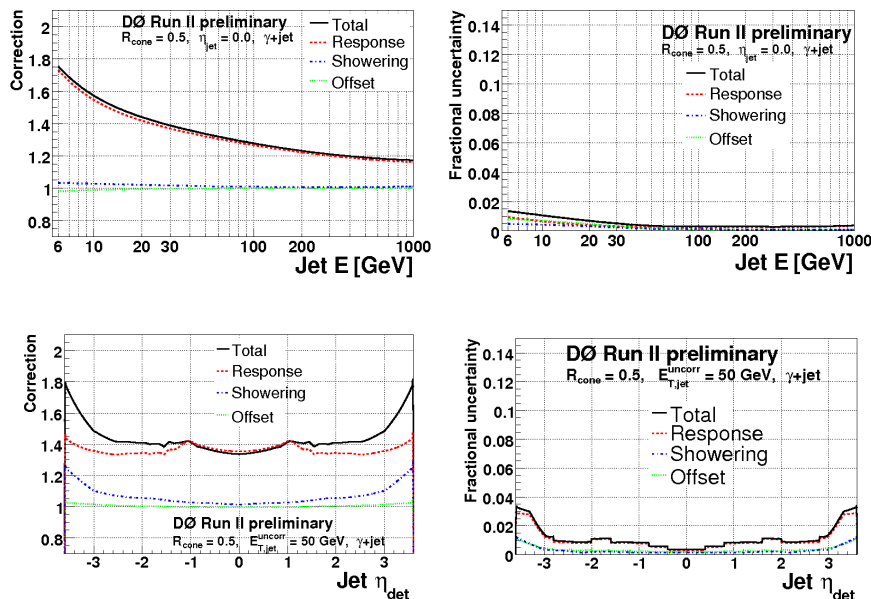


Figure 4.8: Jet energy corrections and the corresponding errors for Monte Carlo simulation as a function of the uncalibrated jet energy for $\eta_{det} = 0$ (top) and as a function of η_{det} for $E_{jet}^{uncorrected} = 50$ GeV (bottom) [104].

- **Energy Offset:** The offset correction subtracts the energy contributions from electronic noise, uranium noise, pile-up and multiple interactions within the same bunch crossing.
- **Showering Corrections:** Shower development that causes energy to leak out of the jet cone and vice versa requires further correction of the jet energy.

Jets need to be calibrated separately in data and Monte Carlo since some of the listed effects are difficult to model in sufficient accuracy. The jet energy corrections for data and Monte Carlo are illustrated in Fig. 4.7 and Fig. 4.8.

4.6 Missing Transverse Energy (\cancel{E}_T)

The missing transverse energy \cancel{E}_T represents the negative vector sum of all energy deposited in the detector. It provides a measure for the transverse momenta of all particles that escape detection, for example neutrinos.

The raw missing transverse energy is given by the vector sum of the energy in all calorimeter cells, except the cells of the CH calorimeter. In order to suppress noise in these cells, they are included only if they belong to a jet. All energy corrections to physics objects, e. g. jet energy corrections, need to be propagated to the raw missing transverse energy. Additionally, the information about muons from the muon system is taken into account, while their energy deposition from ionization in the calorimeter is excluded.

The main contributions to the resolution of \cancel{E}_T are the energy resolution of the calorimeter and noise in the detector or the readout electronics.

5

Data Samples and Monte Carlo Simulation

The first part of this chapter describes the data samples analyzed in both analyses and the trigger requirements applied to record the data. The second part discusses the used Monte Carlo samples and the corrections applied to Monte Carlo events which are needed to compensate small effects from insufficient accuracy of the Monte Carlo simulation.

5.1 Data Samples

The DØ detector started recording high quality data of Run II in August 2002. A major data set of Tevatron Run IIa, which was recorded until June 2004, is analyzed in the Higgs analysis. In February 2006, Tevatron Run IIa ended after recording roughly 4 billion events. These events are analyzed in the SUSY analysis. The data set analyzed in the Higgs analysis is a subset of the data set analyzed in the SUSY analysis.

Data Skims

Preselections of the data, so-called *skims*, are provided by the DØ Collaboration [90] reducing the amount of data which needs to be processed in the specific analyses. The Higgs analysis relies on the MU2TRK skim, which includes all events passing the following criteria:

- A muon is reconstructed in the muon detector;
- Two tracks with $p_T > 5$ GeV are reconstructed in the tracker.

In the SUSY analysis the MU1loose skim is processed, which contains events passing the requirement:

- A muon reconstructed in the muon detector and a central track with $p_T > 8$ GeV matched to it.

Data Quality

The events analyzed by both analyses need to pass certain data quality requirements [107], which ensure that the required detector components have been in good working condition at the time the data was recorded. In the calorimeter, problems occur typically due to noise or readout failures, which accounts for a data loss of about 9 %. Problems in the muon and tracking detectors require to reject 3 % each. Additionally, events with problems in the luminosity readout are discarded from the data sample.

5.1.1 Trigger Selection

Triggers are used to select interesting physics events out of the large number of background events from inelastic $p\bar{p}$ collisions during data taking. This selection is crucial because events that do not release a trigger signal are not stored and are not available for later offline analysis. To ensure high efficiency, complex sets of triggers (*trigger list*) have been developed. The trigger lists undergo continuous optimization to increase the efficiency and to adapt to changes of the instantaneous luminosity. The analyses presented in this thesis rely on triggers which select events based on the characteristic signature of a single muon in the detector (so-called *single muon* triggers). A list of the used triggers is given in Tab. 5.1. Each trigger is implemented as a combination of the trigger terms explained in Tab. 5.2.

The Higgs analysis relies only on two single muon triggers from trigger lists v8-v12, which have been running disjunct in terms of time and cover the whole data taking period considered in the analysis: MU_W_L2M5_TRK10 and MUW_W_L2M3_TRK10. For the SUSY analysis all available single muon triggers in trigger lists v8-v14.6 are combined by a logical OR [108].

5.1.2 Integrated Luminosity

The integrated luminosity of the data sample analyzed in the Higgs analysis is calculated using the rate of inelastic collisions measured with the luminosity monitor (see Sec. 3.2.4):

$$\mathcal{L}_{\text{Higgs}} = \int L dt = (299 \pm 19) \text{ pb}^{-1}. \quad (5.1)$$

The uncertainty is dominated by the uncertainty on the cross section measurement of the inelastic $p\bar{p}$ scattering and by the knowledge of the kinematic distribution for diffractive processes [110, 111].

In case of the SUSY analysis, the integrated luminosity is determined by normalizing the number of expected $Z/\gamma^* \rightarrow \tau\tau$ events from the Monte Carlo simulation to the same number of events observed in data as explained in Sec. 8.5.2:

$$\mathcal{L}_{\text{SUSY}} = \int L dt = (944 \pm 59) \text{ pb}^{-1}. \quad (5.2)$$

The contributions to the uncertainty are the uncertainty on the cross section of the $Z/\gamma^* \rightarrow \tau\tau$ process and the statistical uncertainty of the calculation. The advantage of this method compared to the method used for the Higgs analysis is the cancellation of various systematic uncertainties at leading order (e.g. lepton identification). The determined value is in good agreement with the measurement based on the rate of inelastic collisions measured with the luminosity monitor. The method used for the SUSY analysis is not applicable in case of the Higgs analysis since the $Z/\gamma^* \rightarrow \tau\tau$ resonance may be overlaid by contributions from a Higgs boson signal.

Trigger list	Used triggers
v8-v9	MU_W_L2M5_TRK10, MU_W_L2M0_TRK3, MU_W_L2M0_TRK10
v10-v10.2	MU_W_L2M5_TRK10, MU_W_L2M0_TRK3, MU_W_L2M0_TRK10, MUW_W_L2M5_TRK10
v10.3-v11	MUW_A_L2M3_TRK10, MUW_W_L2M3_TRK10, MU_W_L2M3_TRK10
v12	MUW_W_L2M3_TRK10, MU_W_L2M3_TRK10, MU_A_L2M3_TRK10
v13-v13.1	MUH1_TK12, MUH1_LM15, MUH1_TK10, MUH2_LM3_TK12, MUH2_LM15, MUH3_LM3_TK10, MUH3_LM15, MUH4_TK10, MUH4_LM15, MUH5_LM15, MUH6_TK10, MUH6_LM15, MUH7_TK10, MUH7_LM15
v13.2	MUH1_LM15, MUH1_TK12_TLM12, MUH1_TK10, MUH2_LM6_TK12, MUH2_LM15, MUH3_LM6_TK12, MUH3_LM15, MUH5_LM15, MUH6_TK12_TLM12, MUH6_LM15, MUH7_TK12, MUH7_LM15
v13.3-v13.9	MUH1_LM15, MUH1_TK12_TLM12, MUH1_TK10H, MUH2_LM10_TK12, MUH2_LM4_ITK10, MUH3_LM10_TK12, MUH3_LM4_ITK10, MUH5_LM15, MUH6_TK12_TLM12, MUH6_LM15, MUH7_TK12, MUH7_LM15
v14-v14.5	MUH1_ILM15, MUH1_ITLM10, MUH1_TK12_TLM12, MUH5_LM15, MUH6_LM15, MUH6_TK12_TLM12, MUH7_LM15, MUH7_TK12
v14.6	MUH1_ILM15, MUH1_ITLM10, MUH1_TK12_TLM12, MUH5_LM15, MUH6_LM15, MUH6_TK12_TLM12, MUH7_LM15, MUH7_TK12, MUH8_ILM15, MUH8_ITLM10, MUH8_TK12_TLM12

Table 5.1: List of single muon triggers used in the analyses. The description of the components of the trigger names is given in Tab. 5.2.

Trigger term	Requirement
Level 1	
MU_W	Muon based on scintillator requirements in $ \eta_{\text{det}} < 1.5$
MUW_W	Muon based on scintillator and wire requirements in $ \eta_{\text{det}} < 1.5$
MUW_A	Muon based on scintillator and wire requirements in $ \eta_{\text{det}} < 2.0$
MUH1	Muon based on scintillator requirements in $ \eta_{\text{det}} < 1.5$, and $p_T^{\text{local}} > 10$ GeV, Track $p_T > 10$ GeV
MUH2	Muon based on scintillator and wire requirements in $ \eta_{\text{det}} < 2.0$, Track $p_T > 10$ GeV
MUH3	Muon based on scintillator requirements in $ \eta_{\text{det}} < 2.0$, isolated track $p_T > 10$ GeV
MUH4	Muon based on scintillator and tight wire requirements in $ \eta_{\text{det}} < 1.5$
MUH5	Muon based on scintillator and tight wire requirements in $1 < \eta_{\text{det}} < 2$
MUH6	Muon based on loose scintillator and wire requirements in $ \eta_{\text{det}} < 1.5$, and $p_T^{\text{local}} > 10$ GeV, Track with $p_T > 10$ GeV
MUH7	Muon based on scintillator and wire requirements in $ \eta_{\text{det}} < 1.5$
MUH8	Muon based on scintillator and wire requirements in $ \eta_{\text{det}} < 1.5$, and $p_T^{\text{local}} > 10$ GeV, Track with $p_T > 10$ GeV
Level 2	
L2Mx	Muon with $p_T^{\text{local}} > x$ GeV
MUH2	Muon $p_T^{\text{local}} > 3$ GeV
MUH3	Muon
MUH4, MUH5, MUH7	Muon $p_T^{\text{local}} > 5$ GeV
Level 3	
TRKx, TKx	Track with $p_T > x$ GeV
LMx	Muon with $p_T^{\text{local}} > x$ GeV
ILMx	Muon with $p_T^{\text{loc}} > x$ GeV which is isolated in calorimeter: $E(0.1 < \Delta\mathcal{R} < 0.4) < 3$ GeV
TK10H	Track with $p_T > 10$ GeV (found by histogram algorithm)
ITK10	Track with $p_T > 10$ GeV which is isolated in calorimeter: $E(0.2 < \Delta\mathcal{R} < 0.5) < 2$ GeV and isolated in tracker: $p_T(0.1 < \Delta\mathcal{R} < 0.5) < 1$ GeV
ITLM10	Track with $p_T > 10$ GeV, Muon with $p_T > 10$ GeV which is isolated in calorimeter: $E(0.1 < \Delta\mathcal{R} < 0.4) < 2.2$ GeV and isolated in tracker: $p_T(0.1 < \Delta\mathcal{R} < 0.4) < 2$ GeV

Table 5.2: Description of the trigger names. p_T^{local} indicates that the muon momentum is measured in the muon detector. The isolation variables are calculated as the scalar sum of the energy or p_T in a hollow cone with the given inner and outer radius in calorimeter or tracker, respectively. Further details are given in [109].

5.2 Monte Carlo Samples of Standard Model Processes

Monte Carlo samples of Standard Model processes are used to develop the analyses and to estimate the background of the selections. Only a few Standard Model processes lead to the same final state as the expected signals of the two analyses (an isolated muon, a hadronically decaying tau and \cancel{E}_T). The most important backgrounds are: $Z/\gamma^* \rightarrow \tau\tau$ and $VV \rightarrow \ell\ell + X$, where V represents the vector bosons W and Z . But there are other processes which have a similar signature in the detector and appear as background due to misidentification as discussed in detail for both analyses in Sec. 6 and 8.

A summary of all Standard Model processes that are simulated using Monte Carlo is given in Tab. 5.3. The corresponding leading order Feynman diagrams are shown in Fig. 5.1-5.4. The $Z/\gamma^* \rightarrow \ell\ell$ cross section is calculated with the CTEQ6.1M PDFs [66] as $\sigma(Z/\gamma^* \rightarrow \ell\ell) = \sigma_{LO} \times K_{QCD}(Q^2)$, with LO cross section calculated by PYTHIA LO PDF and the K_{QCD} at NNLO with NLO PDF according to [112, 113]. The $W^\pm \rightarrow \ell^\pm \nu_\ell$ cross section is calculated with NNLO corrections and CTEQ6.1M as listed in [112, 113]. The di-boson cross sections are calculated at NLO in [114] and the $t\bar{t}$ cross section is calculated at NNLO in [115]. In case of the Higgs analysis, all cross sections have been calculated using CTEQ5.1 PDFs [116].

Process	Mass Range [GeV]	$\sigma \times BR$ [pb]	Number of generated events	
			Higgs analysis	SUSY analysis
$Z/\gamma^* \rightarrow \mu\mu$	$15 < M_{\mu\mu} < 60$	409 ± 15	0.3M	2.7M
$Z/\gamma^* \rightarrow \mu\mu$	$60 < M_{\mu\mu} < 130$	241.6 ± 8.7	0.6M	5.9M
$Z/\gamma^* \rightarrow \mu\mu$	$130 < M_{\mu\mu} < 250$	1.96 ± 0.06	0.1M	0.4M
$Z/\gamma^* \rightarrow \mu\mu$	$250 < M_{\mu\mu} < 500$	0.167 ± 0.006	0.1M	0.1M
$Z/\gamma^* \rightarrow \mu\mu$	$M_{\mu\mu} > 500$	$(7.0 \pm 0.3) \times 10^{-3}$	0.1M	0.1M
$Z/\gamma^* \rightarrow \tau\tau$	$15 < M_{\tau\tau} < 60$	409 ± 15	0.3M	2.9M
$Z/\gamma^* \rightarrow \tau\tau$	$60 < M_{\tau\tau} < 130$	241.6 ± 8.7	0.4M	13.7M
$Z/\gamma^* \rightarrow \tau\tau$	$130 < M_{\tau\tau} < 250$	1.96 ± 0.6	0.1M	0.4M
$Z/\gamma^* \rightarrow \tau\tau$	$250 < M_{\tau\tau} < 500$	0.167 ± 0.006	49k	0.1M
$Z/\gamma^* \rightarrow \tau\tau$	$M_{\tau\tau} > 500$	$(7.0 \pm 0.3) \times 10^{-3}$	23k	0.1M
$W^\pm \rightarrow \mu^\pm \nu_\mu$		2583 ± 93	2.8M	6.0M
$W^\pm \rightarrow \tau^\pm \nu_\tau$		2583 ± 93	1.7M	12.2M
WW inclusive		12 ± 0.7	—	2.2M
WW $\rightarrow \ell\ell + X$		1.22 ± 0.07	0.2M	2.2M
WZ inclusive		3.68 ± 0.25	53k	0.5M
ZZ inclusive		1.42 ± 0.08	54k	0.5M
$t\bar{t}$ inclusive		6.77 ± 0.42	—	1.3M
$t\bar{t} \rightarrow b\bar{b}l\nu\nu$		0.67 ± 0.04	0.1M	—
$t\bar{t} \rightarrow b\bar{b}j\ell\nu$		2.68 ± 0.13	0.2M	—

Table 5.3: Cross section times branching ratio ($\sigma \times BR$) and number of generated events for the different background Monte Carlo samples. *Inclusive* indicates that all possible decays are simulated.

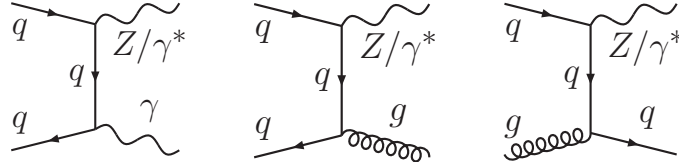


Figure 5.1: Leading order Feynman graphs for $Z + \text{jet}/\gamma$ production.

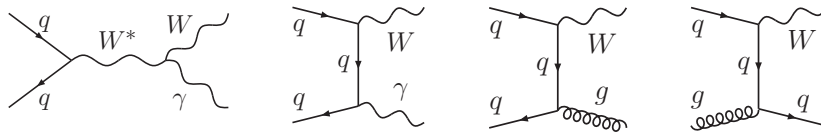


Figure 5.2: Leading order Feynman graphs for $W + \text{jet}/\gamma$ production.

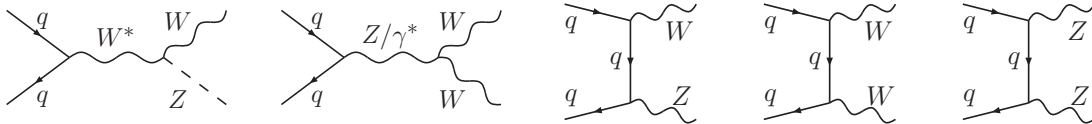


Figure 5.3: Leading order Feynman graphs for di-boson production.

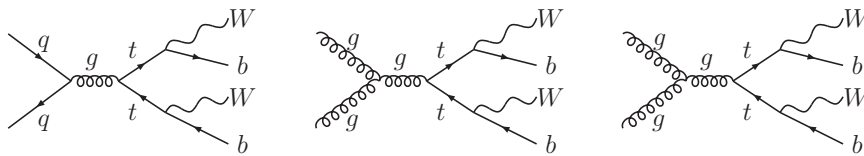


Figure 5.4: Leading order Feynman graphs for $t\bar{t}$ production.

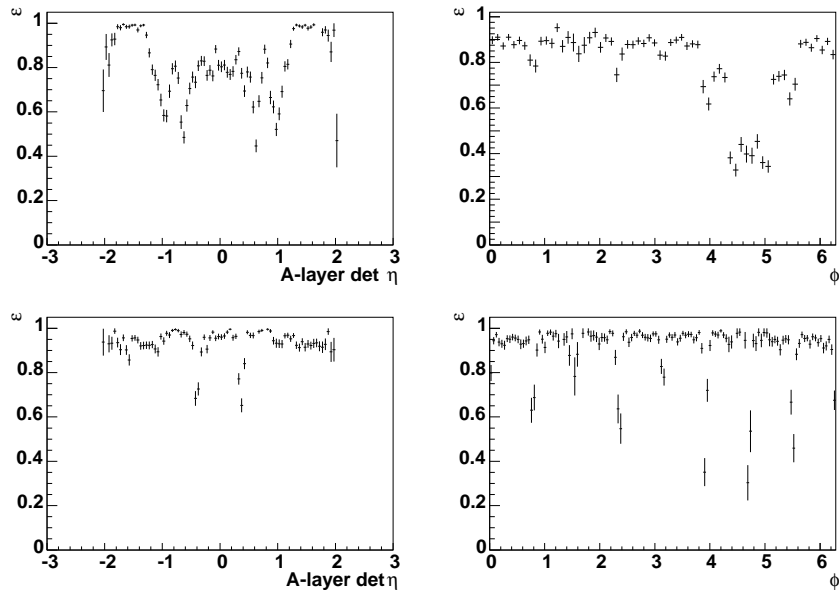


Figure 5.5: Level 1 trigger efficiency for scintillator (top) and wire (bottom) requirements of the trigger term MUW_A (see Tab. 5.2) which is used for the Higgs analysis.

5.3 Monte Carlo Corrections

An accurate simulation of the detector is required to allow for a precise knowledge of efficiencies and resolution. In general, it can be assumed that the simulation performs with sufficient accuracy. Nevertheless, for quantities which are crucial for the analyses, the simulation is compared to data. The following section describes the measurement of these quantities and the required corrections applied to the Monte Carlo simulation.

5.3.1 Trigger Efficiency

The efficiencies of the used triggers need to be measured in data and integrated into the Monte Carlo samples. The trigger efficiency is measured using the *tag and probe method* in a data sample consisting of $Z/\gamma^* \rightarrow \mu\mu$ events [100]. Therefore, events are selected which contain a tag and a probe muon. The tag muon ($p_T^\mu > 30$ GeV) is required to pass calorimeter and tracker isolation criteria (Sec. 4.3) and to have initiated a single muon trigger signal. The probe muon is selected by asking for a track which points to the same vertex as the tag muon and which is also isolated in tracker and calorimeter. The trigger efficiency is defined as the fraction of probe muons which have released the trigger under consideration. Due to detector and trigger design, the efficiency depends on p_T , η_{det} and ϕ . Further dependencies can be neglected as well as background contributions to the data sample used for the measurement of the efficiency.

Figures 5.5-5.7 show the measured efficiencies for the different trigger terms used in the Higgs analysis. These efficiencies are applied to the Monte Carlo samples according to the fraction of integrated luminosity each trigger contributes to. Figure 5.8 presents the efficiency of the logical OR of all triggers used in the SUSY analysis [108]. The dependence of

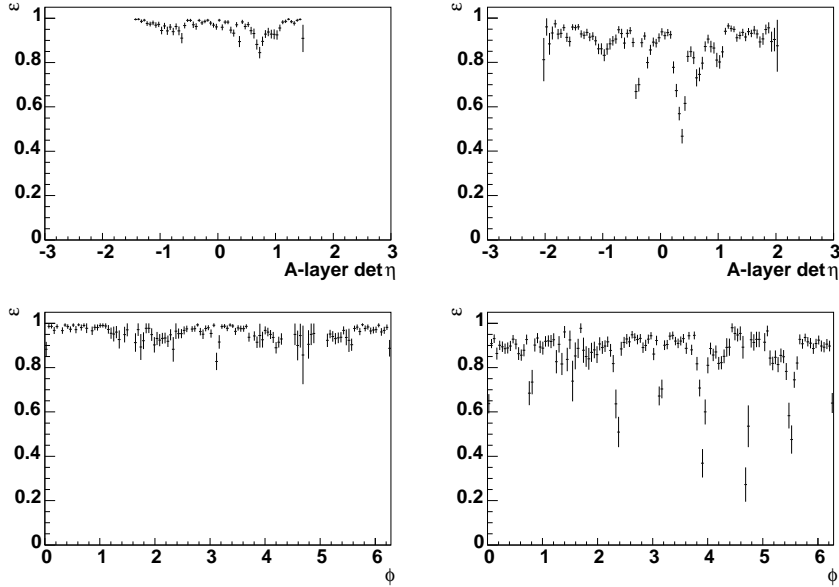


Figure 5.6: Level 2 trigger efficiency for a muon with $p_T > 3$ GeV (left) and $p_T > 5$ GeV (right), which are used for the Higgs analysis and correspond to trigger terms L2M3 and L2M5 (see Tab. 5.2).

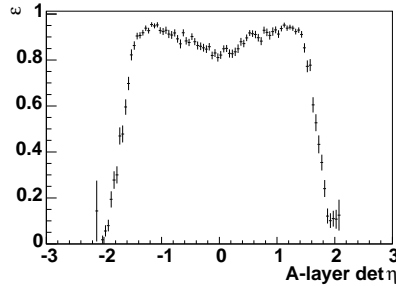


Figure 5.7: Level 3 trigger efficiency for the trigger term TRK10 (see Tab. 5.2) which is used in the Higgs analysis and requires a track with $p_T > 10$ GeV.

the efficiencies of Fig. 5.5 (top right) and Fig. 5.8 (right) on the polar angle ϕ reflects the incomplete coverage of the muon detector in the bottom region (see Sec. 3.2.3).

5.3.2 Muon Reconstruction and Identification Efficiency

The reconstruction efficiency of muons is a crucial quantity for both analyses. To ensure its accurate simulation, it is measured in data and Monte Carlo. This is of particular importance since the analyses use the whole coverage of the muon detector including the region at the bottom of the detector, where the reconstruction of muons is degraded (see Sec. 3.2.3). Similar to the measurement of the trigger efficiency, the tag and probe method is used to determine the efficiency as a function of η_{det} and ϕ . Due to different versions of the reconstruction and

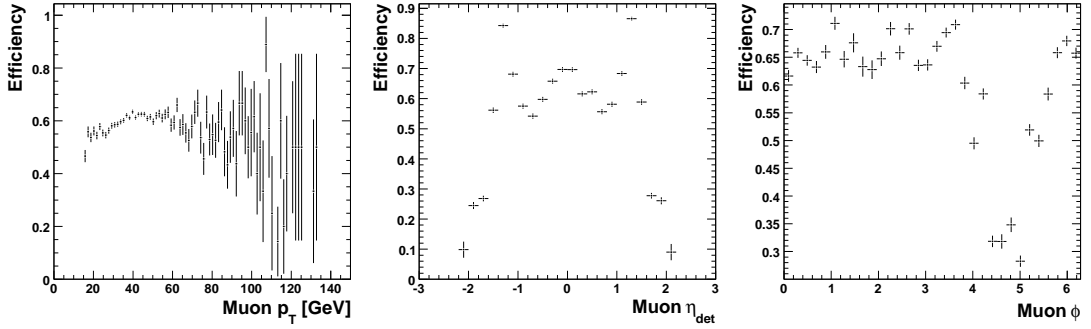


Figure 5.8: Trigger efficiency of the logical OR of all single muon triggers used for the SUSY analysis as function of p_T , η_{det} and ϕ . Periods in which triggers have been turned off are included and appear as inefficiency [100].

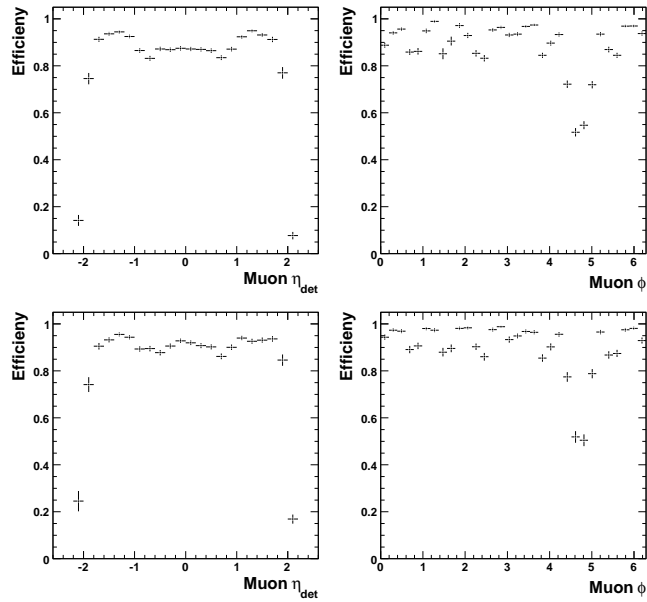


Figure 5.9: Muon reconstruction efficiency measured for the Higgs analysis in data (top) and Monte Carlo (bottom).

simulation software, the efficiencies differ between Higgs analysis (Fig 5.9) and SUSY analysis (Fig. 5.10). In case of the Higgs analysis the average efficiency amounts to $(88.0 \pm 0.2) \%$ in data and $(90.3 \pm 0.3) \%$ in Monte Carlo, while for the SUSY analysis $(91.8 \pm 0.1) \%$ and $(92.4 \pm 0.1) \%$ are observed in data and Monte Carlo, respectively. In order to correct for the difference, the ratio of the efficiencies is applied to all Monte Carlo samples as a function of η_{det} and ϕ .

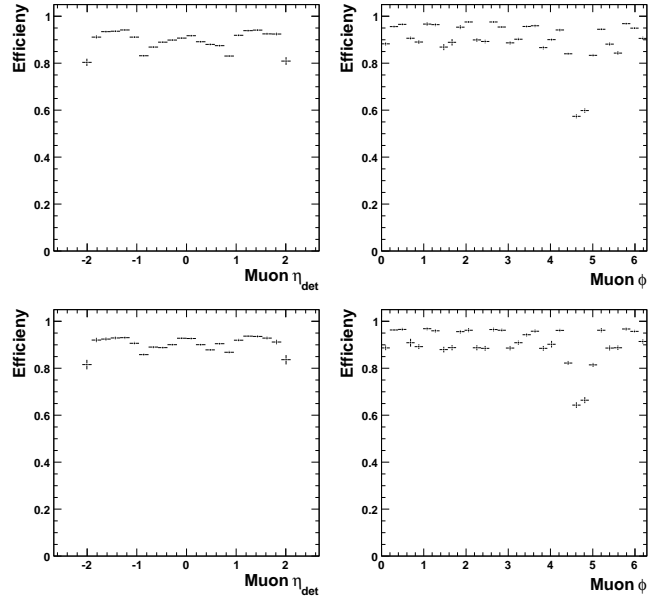


Figure 5.10: Muon reconstruction efficiency measured for SUSY analysis in data (top) and Monte Carlo (bottom) [100].

5.3.3 Track Reconstruction Efficiency

The reconstruction efficiency of tracks is measured in data and Monte Carlo using the tag and probe method in $Z/\gamma^* \rightarrow \mu\mu$ events. The tag muon is selected as described in Sec. 5.3.1. A muon which is reconstructed in the muon detector, without requiring a track to be matched to it, serves as probe object. The probe muon is required to be back-to-back to the tag muon and the transverse momentum measured in the muon detector needs to be larger than 15 GeV. In order to avoid a bias from triggers, the events are required to initiate a di-muon trigger signal. The track reconstruction efficiency is given by the fraction of events in which a track can be matched to the probe muon. Due to differences in data and Monte Carlo, the ratio of the reconstruction efficiency from Monte Carlo to data serves as a correction factor. Since muons and taus require a reconstructed track, this correction factor is applied for both objects as a function of η_{det} and the z position of the track at the point of closest approach to the beamline. The average correction amounts to (0.98 ± 0.01) for the Higgs analysis and (0.88 ± 0.02) for the SUSY analysis. In the SUSY analysis a track has to pass tighter quality criteria compared to the Higgs analysis which are more difficult to model in high accuracy. This leads to a lower efficiency and a degraded agreement between data and simulation compared to the Higgs analysis. The additional criteria are a cut on the χ^2/ndf of the fit of the track ($\chi^2/\text{ndf} < 4$) and the track is required to have at least one hit in the SMT. The track reconstruction efficiency for both analyses is shown in Fig. 5.11.

5.3.4 Transverse Momentum Resolution of Tracks

Since the resolution capability of the tracking detector is overestimated in the detector simulation, the resolution of the track p_T in Monte Carlo needs to be modified to describe the

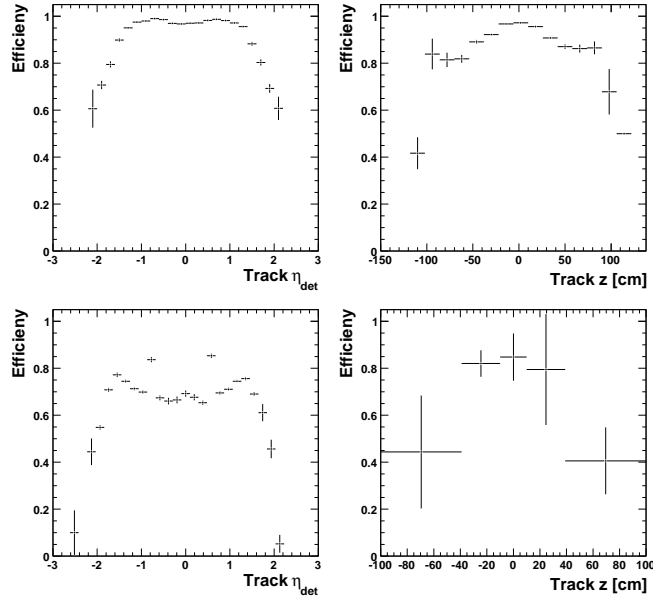


Figure 5.11: Track reconstruction efficiency as measured in data for the Higgs analysis (top) and for the SUSY analysis (bottom).

	Higgs analysis		SUSY analysis			
	A	B	run $< 2 \cdot 10^5$		run $> 2 \cdot 10^5$	
			A	B	A	B
no SMT hits	23	280	4.5	0.56	16.3	0.326
$ \eta_{\text{det}} < 1.6$	13	170	2.8	0.35	11.9	0.238
$ \eta_{\text{det}} > 1.6$	13	170	2.4	0.30	17.2	0.344

Table 5.4: Parameters used for the correction of the track p_T resolution in units of 10^{-4} [100].

data. Therefore, the track p_T is smeared in Monte Carlo using the following function:

$$\frac{1}{p_T} \rightarrow \frac{1}{p_T} + \left(A + \frac{B}{p_T} \right) \text{Gaussian}(0, 1). \quad (5.3)$$

Because of the use of different versions of the reconstruction and simulation software, each analysis has its own sets of parameters. The smearing parameters depend on η_{det} , the number of hits in the SMT and the run number, as summarized in Tab. 5.4 [100].

5.3.5 Boson Momentum

It is observed that the shape of the distribution of the transverse momentum of the boson $p_T(Z)$ in $Z/\gamma^* \rightarrow \ell\ell$ events generated by PYTHIA is different from the transverse momentum observed in data. Therefore, a correction is applied to the PYTHIA samples based on the measurement of the differential Z boson production cross section $\frac{d\sigma}{dp_T(Z)}$ in $Z/\gamma^* \rightarrow \mu\mu$ events

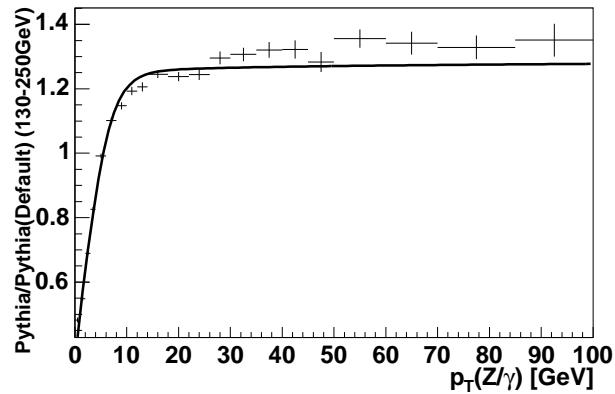


Figure 5.12: Correction factor in the mass region $15 < M_{Z/\gamma^*} < 30$ GeV for the boson transverse momentum which is applied to $Z/\gamma^* \rightarrow \ell\ell$ events generated by PYTHIA [117].

in Run I and Run II of the Tevatron [117]. The correction is determined for four regions of M_{Z/γ^*} : 15-30, 30-60, 60-130 and 130-250 GeV. Figure 5.12 shows the correction factor as a function of $p_T(Z)$, which is fitted by a Fermi function for the lowest mass bin. The correction is also applied to other affected PYTHIA samples like $W^\pm \rightarrow \ell^\pm \nu_\ell$ and $H/A/h \rightarrow \tau\tau$.

6

Search for Neutral MSSM Higgs Bosons in $\mu\tau_h$ Final States

The Higgs sector of the Minimal Supersymmetric extension of the Standard Model (MSSM) is of particular interest because it predicts the existence of a light CP-even neutral Higgs boson with a mass below ≈ 130 GeV. For an interesting region of the MSSM parameter space (at large $\tan\beta$), the Higgs production and the decay into tau pairs is significantly enhanced with respect to the Standard Model. The final state with one leptonically and one hadronically decaying tau lepton is the most promising channel in the search for MSSM Higgs bosons at the Tevatron.

The following chapter gives an introduction into the phenomenology of the production and decay of neutral MSSM Higgs bosons at the Tevatron. After discussing the selection of the signal in the final state consisting of a muon and a hadronically decaying tau, the obtained results are presented in combination with results from searches in the final states $e\tau_h$, $e\mu$ and $b\bar{b}b(\bar{b})$.

6.1 The MSSM Higgs Boson Signature at the Tevatron

The MSSM Higgs sector is based on two complex Higgs doublets, which result in five physical states h (neutral, light, CP even scalar), H (neutral, heavy, CP even scalar), A (neutral, CP odd pseudo-scalar) and H^\pm (charged), assuming the absence of CP violation in the soft symmetry-breaking terms. The mass relation

$$M_h < (M_Z, M_A) < M_H \text{ and } M_{W^\pm} < M_{H^\pm}. \quad (6.1)$$

holds at tree level if one neglects radiative corrections, which are dominated by incomplete cancellation from top and stop loops [39]. At leading order the Higgs sector in the MSSM is fully specified by two parameters generally chosen as $\tan\beta$ and M_A . At large values of $\tan\beta$, the three neutral Higgs bosons are nearly degenerate in mass. If not stated otherwise, they are referred to as $\Phi = h, H, A$.

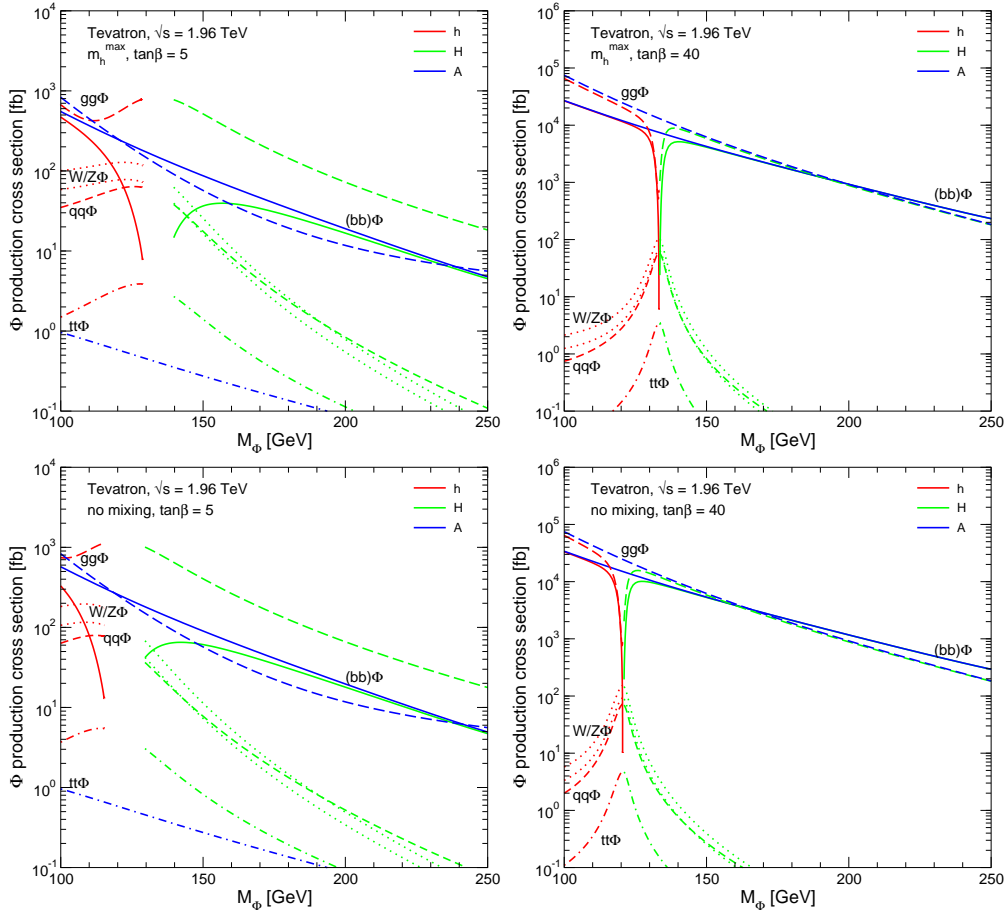


Figure 6.1: Cross section for neutral MSSM Higgs boson production as a function of their masses in the m_h^{\max} scenario (top) and the no-mixing scenario (bottom) for $\tan\beta = 5$ (left) and $\tan\beta = 40$ [118].

6.1.1 Production Processes

The production cross sections of neutral MSSM Higgs bosons at the Tevatron are given in Fig. 6.1 for the m_h^{\max} and the no-mixing scenario (see Sec. 1.2.7) for $\tan\beta = 5$ and $\tan\beta = 40$. The relevant production processes at the Tevatron [119] shown in Fig. 6.2 are:

- The *gluon fusion* is the dominant production mechanism at the Tevatron. It is mediated by triangular loops of heavy quarks and the corresponding SUSY partners: $gg \rightarrow \Phi$.
- The *associated production with heavy quarks*, $gg \rightarrow \Phi t\bar{t}, \Phi b\bar{b}$.

For large $\tan\beta$, the bottom quark contributions dominate in both processes, since the Higgs boson couplings to down-type fermions are enhanced with respect to the Standard Model (see Sec. 1.2.7). The associated production with gauge bosons $q\bar{q} \rightarrow V^*V \rightarrow V\Phi$ [$V = W^\pm, Z; \Phi = h, H$] and the process $V^*V^* \rightarrow \Phi$ [$V = W^\pm, Z; \Phi = h, H$] of Fig. 6.3 play only a minor role since for most of the parameter space one of the two CP-even Higgs bosons has a suppressed coupling to VV and the other couples to VV with the Standard Model strength.

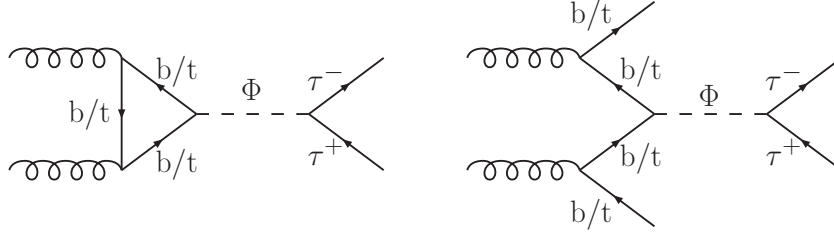


Figure 6.2: Feynman diagrams for the neutral MSSM Higgs boson production processes of interest at the Tevatron with subsequent decay into tau leptons: gluon fusion (left) and associated production with heavy quarks (right).

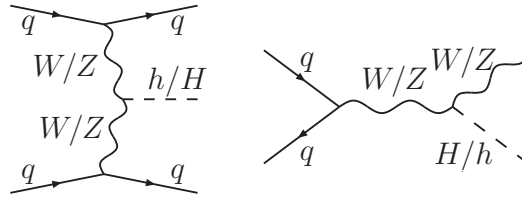


Figure 6.3: Feynman diagrams for the neutral MSSM Higgs boson production processes of minor interest at the Tevatron: gauge boson fusion (left) and associated production with gauge bosons (right).

6.1.2 Decay Channels

The decays of the neutral Higgs bosons in the MSSM depend on their masses and on $\tan\beta$, as illustrated in Fig. 6.4. The relevant decays are described in the following [119]:

- $\Phi \rightarrow f\bar{f}$: At large values of $\tan\beta$ the decay modes $b\bar{b}$ and $\tau^+\tau^-$ are dominating and contribute to the total decay width by 90 % and 8-10 %, respectively. For small $\tan\beta$, they contribute only for neutral Higgs masses below ≈ 150 GeV.
- $\Phi \rightarrow WW, ZZ$: Compared to the Standard Model, these decays are suppressed. They become only sizable for small and moderate values of $\tan\beta$ and in the decoupling limit, where $M_A \gg M_Z$, M_h reaches the upper bound of its mass and behaves like a Standard Model Higgs boson and all other MSSM Higgs bosons are heavy.
- $\Phi \rightarrow gg, \gamma\gamma$: For most of the parameter space the gluonic and photonic decays are not of interest at the Tevatron. An exception are fermiophobic models with suppressed Higgs boson couplings to fermions where the decay $\Phi \rightarrow \gamma\gamma$ is dominant for $M_\Phi < 100$ GeV [119, 120].
- $H \rightarrow hh, AA$; $h \rightarrow AA$: The decay $h \rightarrow AA$ is kinematically possible only for small values of M_A , which are excluded by existing LEP bounds. However, there are still small region in the MSSM parameter space, where it is still kinematically allowed. For

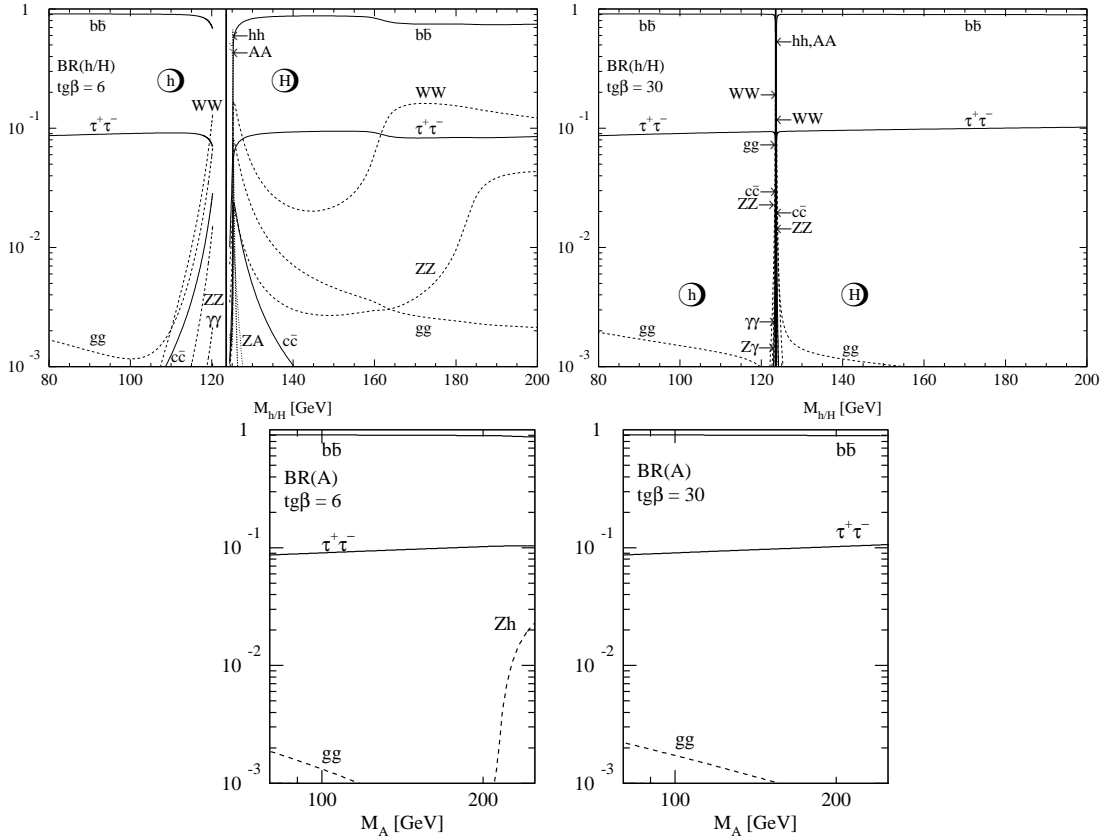


Figure 6.4: Branching ratios of the MSSM Higgs bosons h and H (top) and A (bottom) for $\tan\beta = 6$ (left) and $\tan\beta = 30$ (right). SUSY parameters are chosen such that there are no supersymmetric particle decay modes in the considered Higgs mass ranges [119].

$M_H \lesssim 200$ GeV, the decay mode $H \rightarrow hh, AA$ contributes only for a very limited range of H masses and the decay $H \rightarrow hh$ is kinematically not possible taking into account the LEP bounds on m_h . The process $H \rightarrow AA$ is almost excluded as well by bounds on M_h and M_A .

- $H \rightarrow ZA, H^\pm W^\mp$ and $A \rightarrow Zh$: These processes contribute to the total decay width only at small values of $\tan\beta$ and below the $t\bar{t}$ threshold. But they are almost excluded from LEP bounds for the parameter region of interest.
- $\Phi \rightarrow$ supersymmetric particles: If they are kinematically allowed, decays to Charginos, Neutralinos and third-generation squarks and sleptons can contribute significantly. Taking into account current bounds on the masses of SUSY particles, the parameter space for this type of decay is small for Higgs masses below 130 GeV. The invisible decay $h \rightarrow \chi^0\chi^0$ can become of importance at the upper theoretical limit for M_h . In this analysis it is assumed that SUSY particles are heavy and do not contribute to the decay.

Decay Mode	Fraction
$\tau^+\tau^- \rightarrow e^+\nu_e\bar{\nu}_\tau + e^-\bar{\nu}_e\nu_\tau$	3 %
$\tau^+\tau^- \rightarrow \mu^+\nu_\mu\bar{\nu}_\tau + \mu^-\bar{\nu}_\mu\nu_\tau$	3 %
$\tau^+\tau^- \rightarrow e^+\nu_e\bar{\nu}_\tau + \mu^-\bar{\nu}_\mu\nu_\tau$	6 %
$\tau^+\tau^- \rightarrow e^+\nu_e\bar{\nu}_\tau + \tau_h^-\nu_\tau$	23 %
$\tau^+\tau^- \rightarrow \mu^+\nu_\mu\bar{\nu}_\tau + \tau_h^-\nu_\tau$	23 %
$\tau^+\tau^- \rightarrow \tau_h^+\bar{\nu}_\tau + \tau_h^-\nu_\tau$	41 %

 Table 6.1: Branching ratios of the possible $\Phi \rightarrow \tau\tau$ final states.

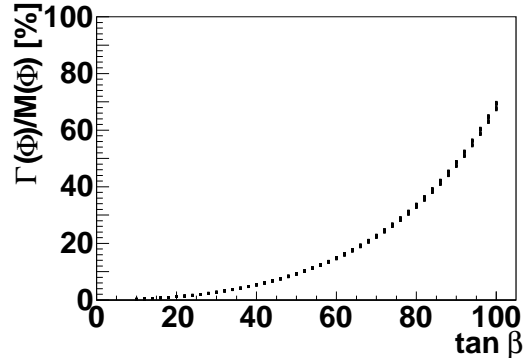
6.1.3 Signal Topology

The analysis described in this chapter focuses on final states including a muon and a hadronically decaying tau lepton ($\Phi \rightarrow \tau\tau \rightarrow \mu\tau_h$). The decay into tau pairs (Fig. 6.2) has a smaller branching ratio than the decay into $b\bar{b}$ but it does not suffer from large di-jet backgrounds.

Since tau leptons are decaying into leptons and hadrons, six final states can be distinguished as shown in Tab. 6.1. The ee and $\mu\mu$ final states have a small total branching ratio of only 3 %, and in combination with the large irreducible background from $Z/\gamma^* \rightarrow \ell\ell$ events, they are difficult to observe. The $e\mu$ final state contributes only 6 % to the total decay width but is less affected by Standard Model backgrounds. The semi-leptonic decays $e\tau_h$ and $\mu\tau_h$ are considered to be the most promising channels. Together, they amount to 46 % of the branching ratio and have only moderate Standard Model backgrounds. If both tau leptons decay hadronically, the sensitivity suffers from the huge background from di-jet events.

Higgs Width

As a result of the increased couplings to down-type fermions, the total decay width of neutral MSSM Higgs bosons increases drastically at large values of $\tan\beta$. Figure 6.5 shows the relative Higgs width as a function of $\tan\beta$ for the m_h^{\max} scenario with $\mu < 0$, where the largest effect is observed. The spread in Fig. 6.5 for a given $\tan\beta$ is a result of different neutral Higgs boson masses ($90 < M_\phi < 300$ GeV). The dependence is studied using FEYN-HIGGS 2.3 [39, 121, 122, 123].


 Figure 6.5: Relative Higgs width as a function of $\tan\beta$ for the m_h^{\max} scenario ($\mu < 0$).

6.1.4 Background from Standard Model Processes

The selection of the $\Phi \rightarrow \tau\tau \rightarrow \mu\tau_h$ signal is affected by background contributions from several Standard Model processes. The cross section of the processes and leading order Feynman diagrams are given in Sec. 5.2.

- $Z/\gamma^* \rightarrow \ell\ell$: The dominant background source for the analysis is the irreducible background from $Z/\gamma^* \rightarrow \tau\tau$ decays. Since muons can be misidentified as hadronically

decaying tau leptons, contributions from $Z/\gamma^* \rightarrow \mu\mu$ are observed in the selection.

- Multi-jet: Due to the large multi-jet production cross section and the sizable rate of jets faking hadronically decaying tau leptons, this background has to be taken into account. Additionally, if a muon inside a jet which results from a bottom quark decay carries a large fraction of the jet transverse momentum, it can pass the isolation criteria.
- $W^\pm \rightarrow \ell^\pm \nu_\ell$: The decay $W^\pm \rightarrow \mu^\pm \nu_\mu$ leads to an isolated muon and missing transverse energy. It amounts to a sizable background, especially if one or more jets are produced in association with the W boson and are misreconstructed as tau leptons. For similar reasons the decay $W^\pm \rightarrow \tau^\pm \nu_\tau$ has to be considered.
- Di-boson (WW, WZ, ZZ): The di-boson processes result in leptons and in most of the cases also in \cancel{E}_T . But the processes have a small cross section and consequently plays only a minor role.
- $t\bar{t}$: The top quark pair production has a small cross section and the subsequent decay into the final state under consideration has a small branching ratio. It gives only minor contributions to the background.

6.2 Signal Monte Carlo Samples

Signal Monte Carlo samples are needed for the optimization of the selection and the determination of the signal efficiency. PYTHIA has been used in combination with CTEQ5L parton distribution functions [116] in order to generate signal samples over the mass range $90 \text{ GeV} < M_\Phi < 300 \text{ GeV}$ (Tab. 6.2). This covers the region above the exclusion limit at the LEP experiments [62] to high masses, where the signal sensitivity at the Tevatron ends due to small signal cross sections. Since for these sample a narrow Higgs boson width is assumed, two signal samples are generated with $\tan\beta = 100$ for Higgs masses of $M_\Phi = 130 \text{ GeV}$ and $M_\Phi = 200 \text{ GeV}$, in order to study the impact of the increasing Higgs boson width.

The signal cross sections of Fig. 6.6 are calculated using FEYNHIGGS 2.3. The complete set of one-loop corrections, all known two-loop corrections and also the contributions from SUSY particles in the gluon fusion production are included. The variations caused by varying the value and sign of μ , while keeping the gluino mass $m_{\tilde{g}}$ the common third generation squark mass parameter M_{SUSY} fixed, reflects the effect of the radiative corrections on the production and decay process [124]. For the determination of the cross sections, the mass of the top quark has been set to the world average of 172.7 GeV [125]. The production cross section of the three neutral Higgs $\Phi = h, H, A$ are added since the bosons are nearly mass degenerate at large values of $\tan\beta$.

6.3 Background Sample for Multi-Jet Events

Events from Standard Model processes that lead to final states with jets are an important background since jets can be misidentified as isolated muons and as tau leptons. In particular, jets resulting from $b\bar{b}$ production are relevant if a muon results from the decay of a bottom quark. The background contributions from *multi-jet* production are determined using data. Since the signal is expected in events with isolated muons, inverting the calorimeter isolation

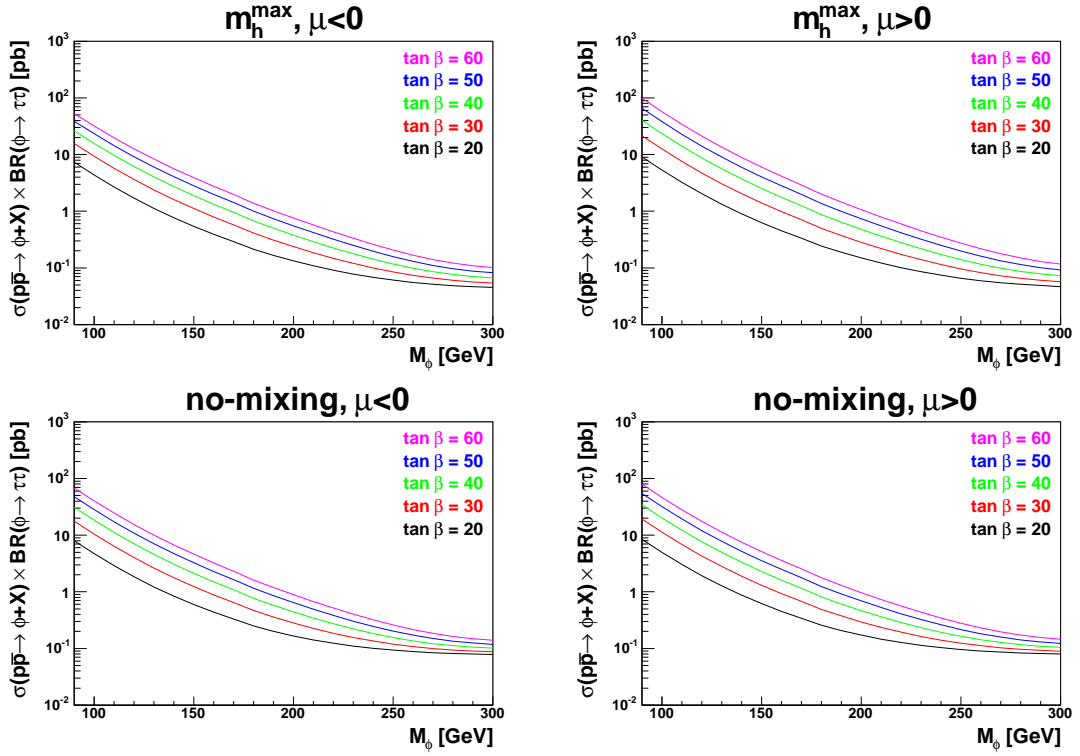


Figure 6.6: Product of cross section and branching ratio for the process $p\bar{p} \rightarrow \Phi + X \rightarrow \tau\tau + X$ as a function of M_Φ for different values of $\tan\beta$.

M_Φ [GeV]	90	100	110	120	130	140	150	160
Number of Events	47k	47k	48k	48k	49k	47k	106k	47k
M_Φ [GeV]	170	180	190	200	250	270	300	
Number of Events	48k	48k	47k	56k	59k	49k	59k	

Table 6.2: Number of generated Monte Carlo events for the process $\Phi \rightarrow \tau\tau$.

criteria and excluding the tracker isolation criteria for muons (Sec. 4.3) allows to select events which contain muons that are part of a jet. This so-called *multi-jet sample* is used to determine the multi-jet contributions at the different stages of the selection. The method assumes that there is no correlation between the muon isolation and the shape of all distributions used in the selection. The only exception is the correlation of isolation and muon transverse momentum, which is discussed below.

The production cross section for events with non-isolated muons, which are lying inside a jet, is much larger than the cross section for processes resulting in isolated muons. As a consequence, the multi-jet sample needs to be normalized to the selected data sample. This normalization is performed in a region of phase space which is dominated by multi-jet events and orthogonal to the region where the signal is expected. The following selection criteria are applied to define that region:

- An upper cut on the neural network output of the tau candidate ($\text{NN}_\tau < 0.8$) removes events from the $Z/\gamma^* \rightarrow \tau\tau$ process.
- Events from $W^\pm \rightarrow \mu^\pm\nu_\mu$ decays are removed by a cut on the transverse mass calculated from muon and missing transverse energy:

$$m_T^\mu = \sqrt{2 \cancel{E}_T p_T^\mu (1 - \cos \Delta\phi)}. \quad (6.2)$$

The transverse mass allows to approximate the W boson mass in the transverse plane by reconstructing p_T^μ and \cancel{E}_T from the decay $W^\pm \rightarrow \mu^\pm\nu_\mu$. A cut is placed at $m_T^\mu < 40$ GeV.

- Contribution from $Z/\gamma^* \rightarrow \mu\mu$ events where a muon is faking a tau candidate are suppressed by requiring that only one muon is reconstructed in the event and that the invariant mass of muon and tau candidate track $M(\mu, \tau\text{-track})$ is smaller than 70 GeV. The background contribution from $Z/\gamma^* \rightarrow \mu\mu$ decays is discussed in more detail in Sec. 6.4.2, where also a distribution of $M(\mu, \tau\text{-track})$ is given.

With these criteria applied, a constant normalization factor is used to scale the integral of multi-jet sample to match the data. After this normalization, one finds that the distributions of p_T^τ (and related quantities) in the multi-jet sample and the data sample disagree in terms of their shape, as shown in Fig. 6.8. This can be explained by the following consideration. The transverse momenta of muon and tau need to be balanced since the multi-jet sample contains dominantly events with two jets from $b\bar{b}$ production, where one jet gives rise to the muon and the other one to the tau candidate. If the muon carries a large fraction of the jet momentum, it is more likely that it passes the isolation criteria since the other particles of the jet are soft. Consequently, the spectra of p_T^μ and p_T^τ are harder for the multi-jet sample. The disagreement is corrected by applying a p_T^τ and τ -type dependent weight to each event of the multi-jet sample. The weight is measured by scaling the multi-jet sample to match the data in every bin of the p_T^τ distribution and parameterized using the exponential function $S(p_T^\tau) = p_0 e^{p_1 p_T^\tau}$. The result is illustrated in Fig. 6.7. The weights are applied to each event of the multi-jet sample during the whole analysis. The effect of the weighting procedure is demonstrated in Fig. 6.8, where the distribution of p_T^τ before and after applying the weights are shown.

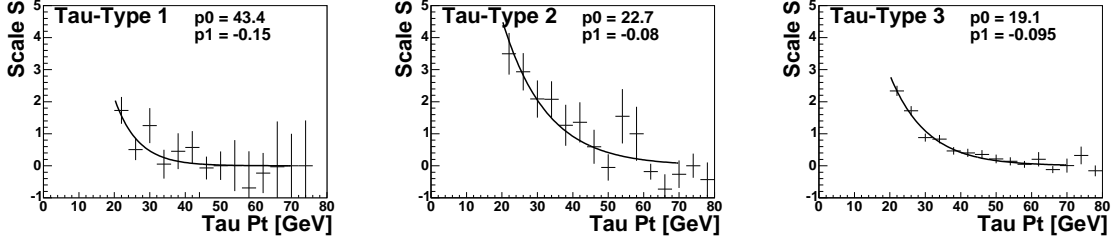


Figure 6.7: The weights of the multi-jet background normalization are parameterized using the function $S(p_T^\tau) = p_0 e^{p_1 p_T^\tau}$ for all three τ -types.

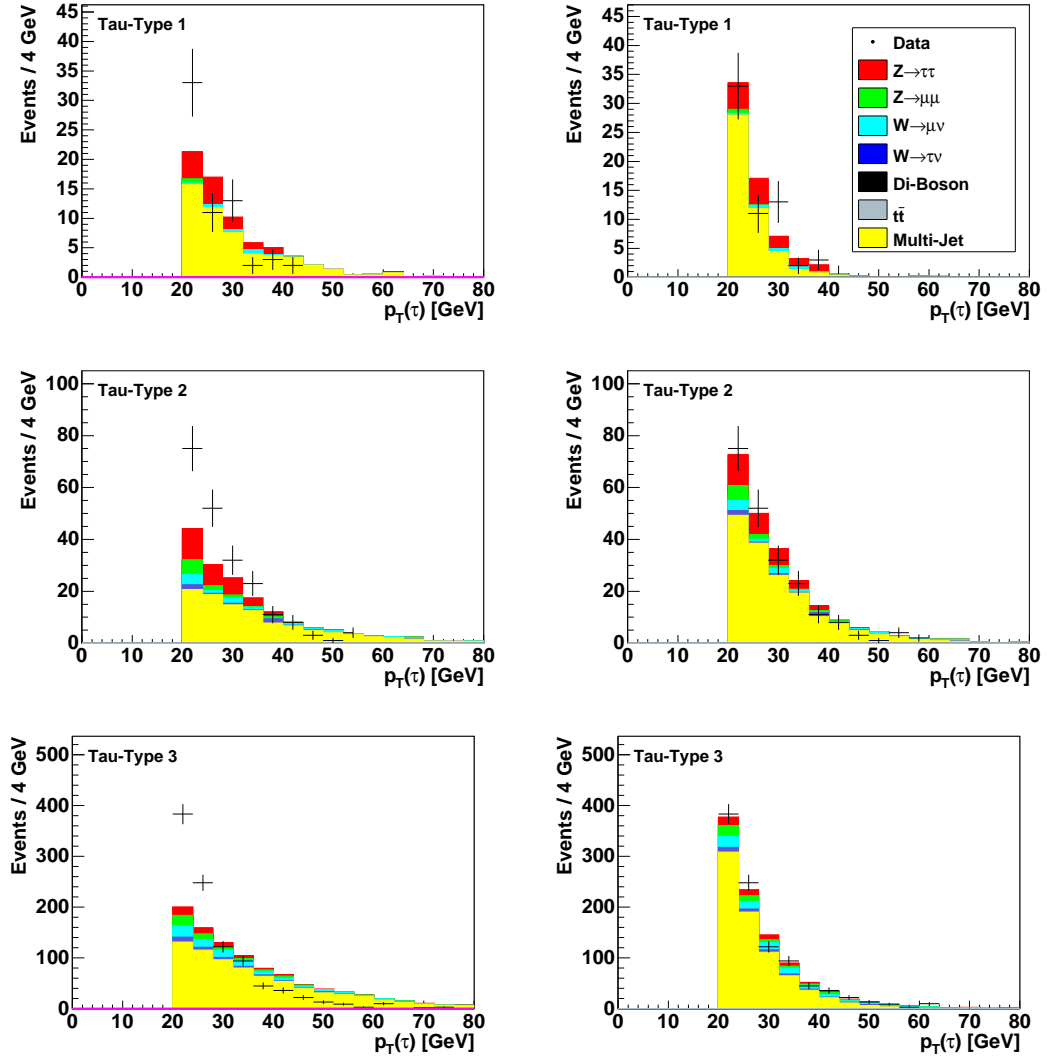


Figure 6.8: Distributions of p_T^τ in the sample dominated by multi-jet events before (left) and after (right) applying the p_T^τ dependent weights for all three τ -types in events with muon and tau having the same charge assigned.

(1) Preselection	Muon: $p_T^\mu > 14$ GeV, isolated in calorimeter and tracker Tau: $p_T^\tau > 20$ GeV, $NN_\tau > 0.3$ Muon and tau have opposite charge assigned (unlike-sign) $\Delta\mathcal{R}(\mu, \tau) > 0.4$ $\Delta z(\mu, \tau) < 1$ cm
(2) Muon-Veto	$\Delta\mathcal{R}(\text{any } \mu, \tau) > 0.15$ Fraction of tau energy in the CH calorimeter $\text{CHF} < 0.7$ $E_T^\tau/p_T^{\tau\text{-track}} > 0.5$
(3) Tau Identification	$NN_\tau > 0.90$ (for τ -type 3: $NN_\tau > 0.95$)
(4) Anti- W	$M_W < 20$ GeV

Table 6.3: Summary of the selection criteria of the Higgs analysis.

6.4 Signal Selection

The signal selection aims for the best separation of signal and background events. The contribution from the backgrounds discussed in Sec. 6.1.4 are suppressed using the criteria described in the following.

The signal events are expected to be detected as an enhancement over the expectation from the Standard Model backgrounds at high values of the invariant mass of muon and tau. In order to increase the separation between signal and the background from $Z/\gamma^* \rightarrow \tau\tau$, missing transverse energy is included into the calculation. The resulting mass will be referred to as *visible mass* M_{vis} :

$$M_{\text{vis}} = \sqrt{(p_\mu + p_\tau + \cancel{p})^2} \quad \text{with} \quad \cancel{p} = (\cancel{E}_T, \cancel{E}_x, \cancel{E}_y, 0). \quad (6.3)$$

It is calculated from the four-vectors of the visible tau decay products p_μ and p_τ and the missing momentum \cancel{p} where the z component of \cancel{p} is zero and the energy equal to the magnitude of \cancel{E}_T .

The optimization of the selection aims for the best expected limit. A Higgs mass of 150 GeV was chosen for the optimization and only the *high-mass region*, defined as $M_{\text{vis}} > 120$ GeV, is considered. The selection criteria are summarized in Tab. 6.3 and explained in the following.

6.4.1 Preselection

The selection starts with the so-called *preselection* including all events that contain an isolated muon ($p_T^\mu > 14$ GeV) and a tau candidate ($p_T^\tau > 20$ GeV). The two leptons are required to have opposite charge assigned, and they must be separated in η and ϕ by $\Delta\mathcal{R} > 0.4$. The threshold on the transverse momentum of the muon is lower than the one of the tau candidate, to account for the additional neutrino in the leptonic decay of the tau. Both leptons are required to originate from the same vertex by a cut on the distance of their z positions at the point of closest approach to the beamline: $\Delta z(\mu, \tau) < 1$ cm. The selection

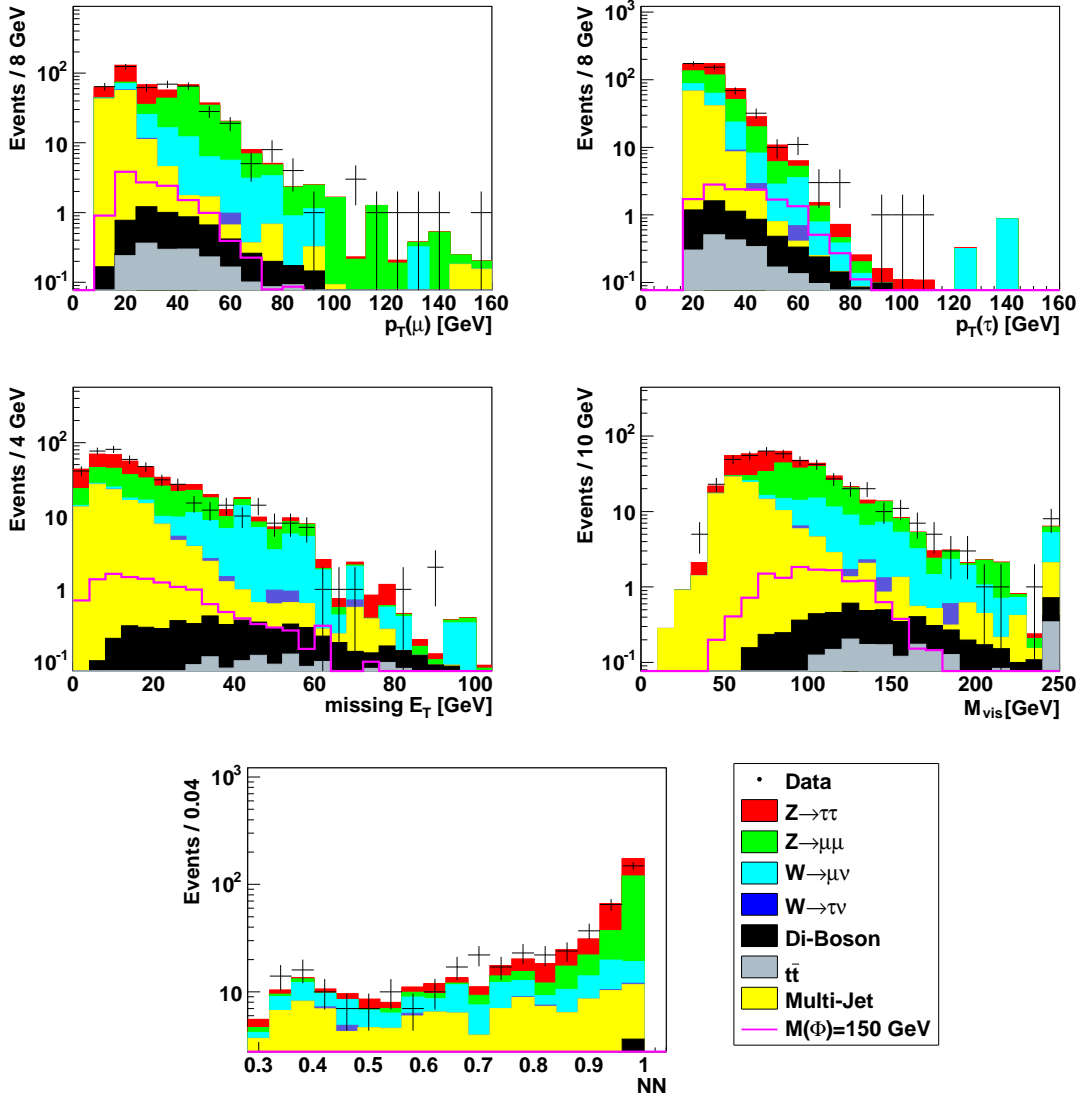


Figure 6.9: The distributions of p_T^μ , p_T^τ , \cancel{E}_T , M_{vis} , and NN_τ at the stage of preselection for τ -type 1. The highest bin of the M_{vis} distribution includes the overflow. The signal is given in an arbitrary normalization.

is split into the three different τ -types of the selected tau candidate (Sec. 4.4.2). This allows a better optimization of the selection and a more detailed study of the data/Monte Carlo agreement.

Figures 6.9-6.11 show the distributions of the three different τ -types for the properties used in the further selection, including the contributions of the different backgrounds from the Standard Model. It is found that data and the expectation from the simulated Standard Model background show good agreement. A simulated signal as expected from a neutral MSSM Higgs boson with a mass of 150 GeV is overlaid in an arbitrary normalization. The dominating background at this stage of the selection depends strongly on the τ -type, due to

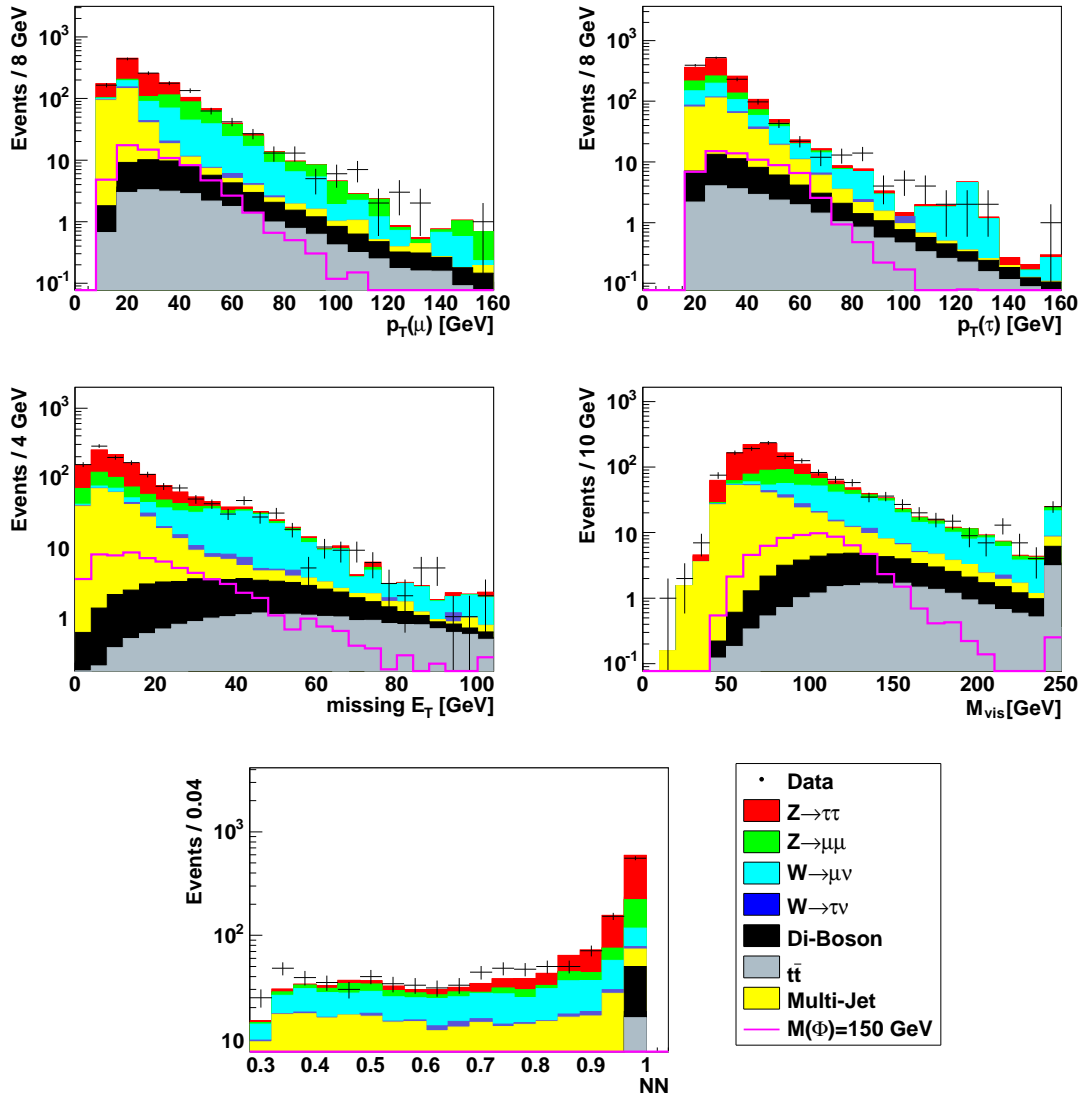


Figure 6.10: The distributions of p_T^μ , p_T^τ , \cancel{E}_T , M_{vis} , and NN_τ at the stage of preselection for τ -type 2. The highest bin of the M_{vis} distribution includes the overflow. The signal is given in an arbitrary normalization.

the different signature seen in the detector. The π -like tau decays (τ -type 1) are affected dominantly by $Z/\gamma^* \rightarrow \mu\mu$, the ρ -like tau decays (τ -type 2) by $Z/\gamma^* \rightarrow \tau\tau$ and the 3-prong decays (τ -type 3) by multi-jet and $W^\pm \rightarrow \mu^\pm\nu_\mu$ events.

6.4.2 Muon Veto

The average transverse energy deposited by a muon in the calorimeter amounts to between 2-5 GeV but it can exceed 20 GeV. In combination with the large production rate of $Z/\gamma^* \rightarrow \mu\mu$ events, this leads to a significant contribution from tau candidates which are faked by a muon

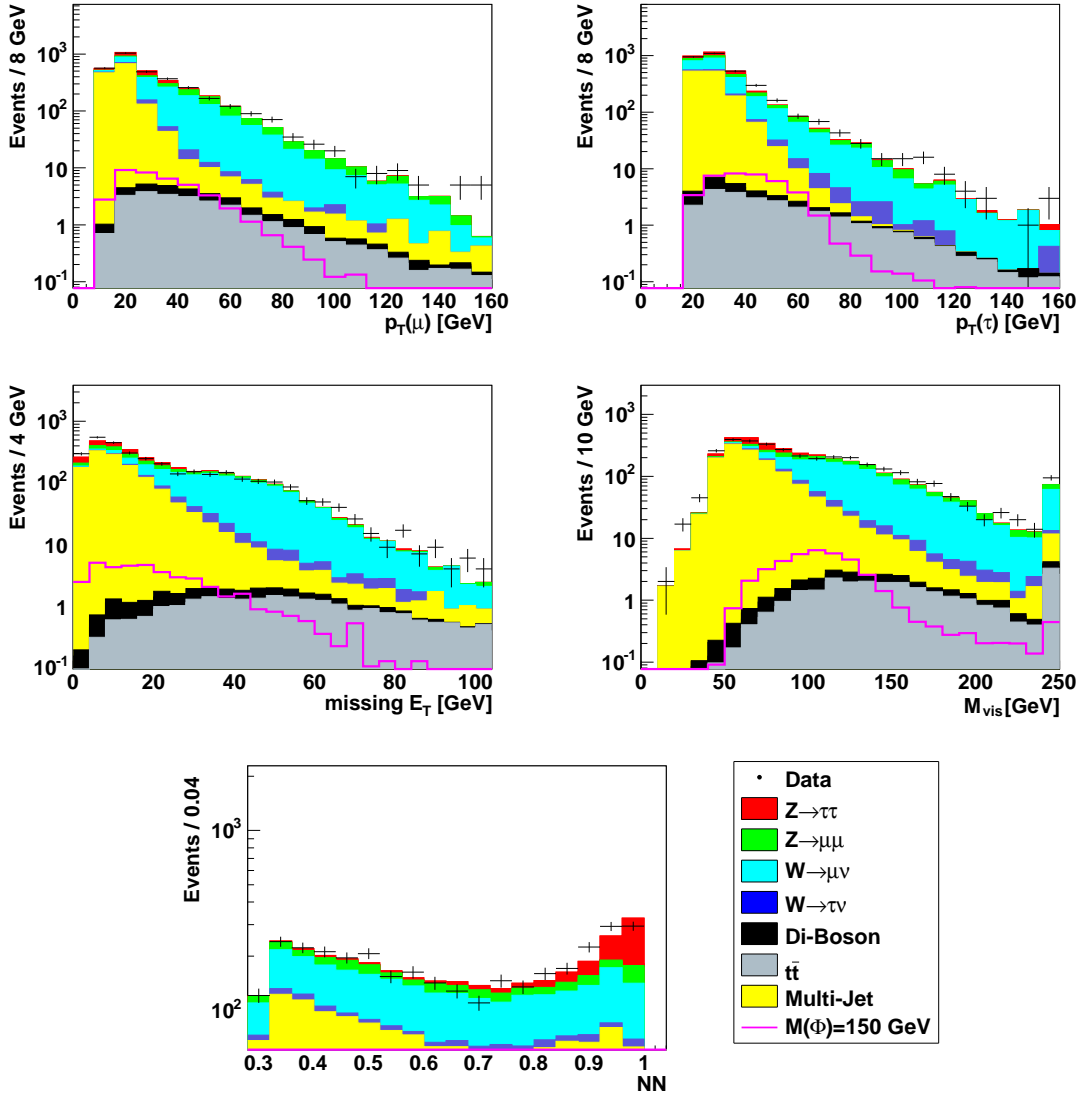


Figure 6.11: The distributions of p_T^μ , p_T^τ , E_T^{miss} , M_{vis} , and NN_τ at the stage of preselection for τ -type 3. The highest bin of the M_{vis} distribution includes the overflow. The signal is given in an arbitrary normalization.

at the stage of the preselection. τ -type 1 is affected the most (Fig. 6.9) but fakes can also be found in τ -type 2 (Fig. 6.10). τ -type 3 is hardly affected because two or three tracks are required (Fig. 6.11). Nevertheless, $Z/\gamma^* + \text{jet} \rightarrow \mu\mu + \text{jet}$ events can be found in τ -type 3 if an additionally produced jet is misidentified as tau.

The tau candidates which are faked by a muon are visualized in Fig. 6.12 (left) by reconstructing the mass of the Z boson M_Z from the muon and the track of the tau candidate. The contamination from muons is suppressed by three criteria. The first one rejects all tau candidates to which a muon with $p_T^\mu > 7$ GeV can be matched. If a muon from a Z boson decay is not reconstructed, it will not be rejected by this criterion. The second criterion is an

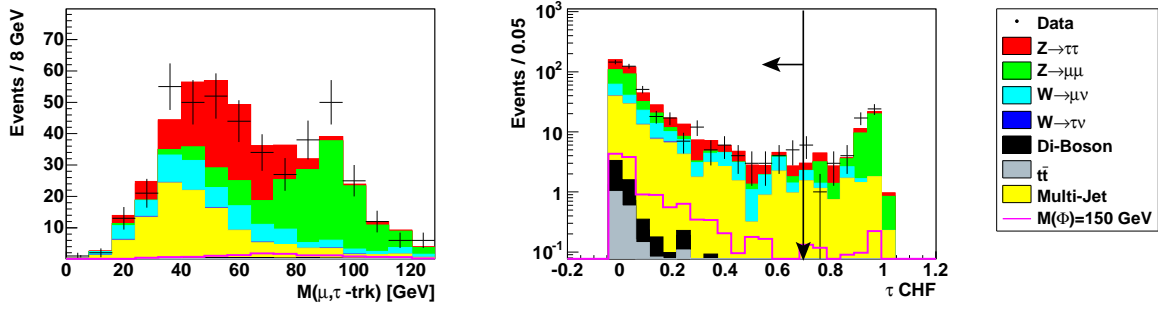


Figure 6.12: The $Z/\gamma^* \rightarrow \mu\mu$ background shows a resonance at M_Z in the $M(\mu, \tau\text{-track})$ distribution (left). Tau candidates have to satisfy $\text{CHF} < 0.7$ (right). The signal is given in an arbitrary normalization.

upper cut at 0.7 on the fraction of energy of the tau candidate which is detected in the CH calorimeter (CHF), illustrated in Fig. 6.12 (right). Muons deposit most of their energy in this part of the calorimeter since it has the maximal thickness in terms of radiation length, while energy showers caused by taus start in layers located closer to the center of the detector. Although muons are rarely misidentified as τ -type 3, the criterion is applied as well in order to be less sensitive to noise appearing in the CH part of the calorimeter. The third criterion rejects a tau candidate if the ratio of the transverse energy reconstructed in the calorimeter E_T^τ and p_T of the tau track is smaller than 0.5.

6.4.3 Tau Identification

The main identification criterion for tau candidates is the neural network output (Sec. 4.4.3). The cut is placed at $\text{NN}_\tau > 0.9$ in case of τ -type 1 and 2. This allows to reject efficiently background contributions from multi-jet events and $W^\pm + \text{jets} \rightarrow \mu^\pm \nu_\mu + \text{jets}$ events, that are the dominating background sources at this stage of the selection. The criteria for τ -type 3 is tightened to $\text{NN}_\tau > 0.95$ since τ -type 3 is affected the most by these backgrounds. The distributions of Fig. 6.13 show good agreement of data and simulated Standard Model background after imposing the NN_τ criterion.

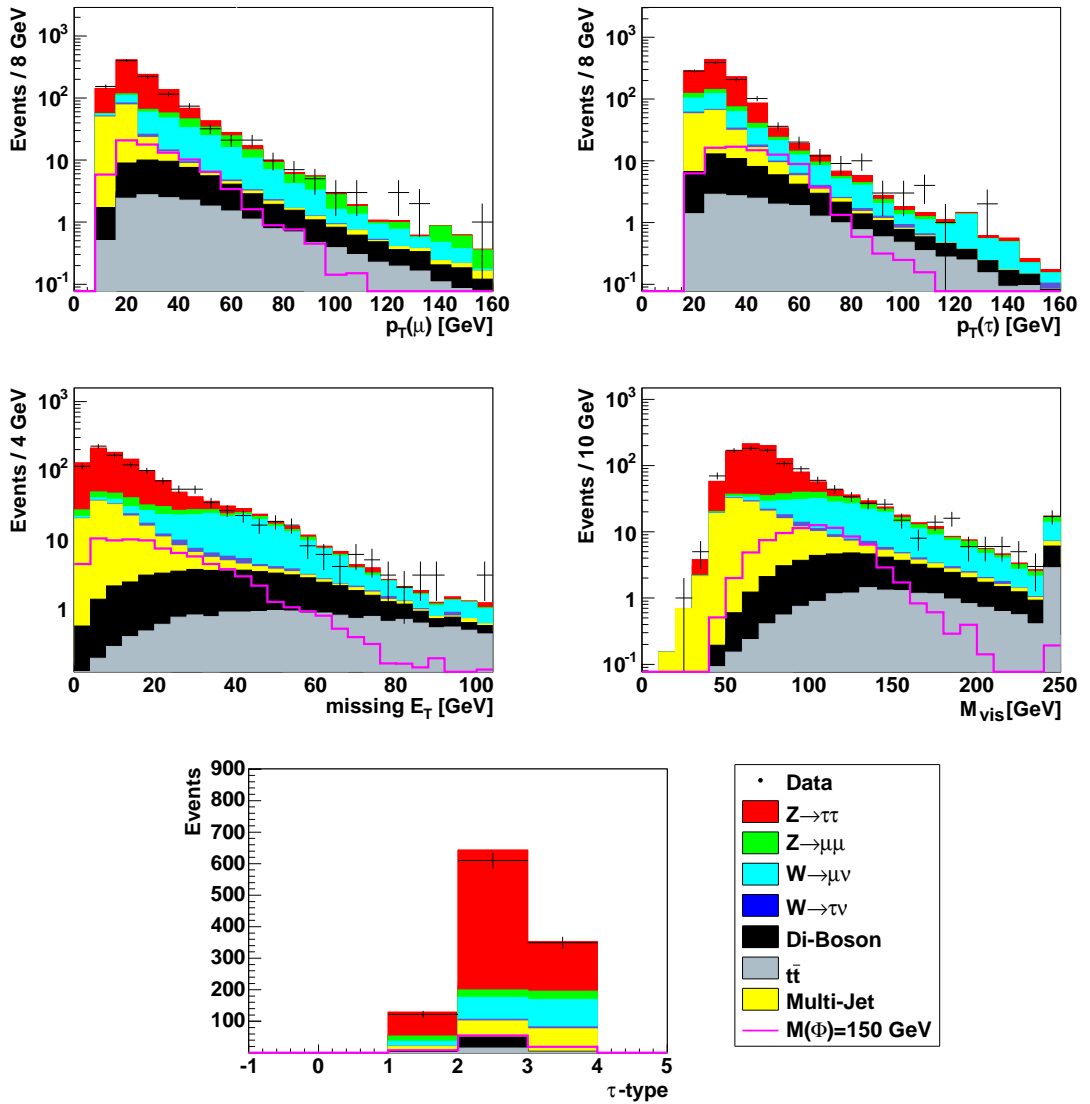


Figure 6.13: Distributions of p_T^{μ} , p_T^{τ} , \cancel{E}_T , M_{vis} and τ -type for the sum off all τ -types after applying the NN_{τ} criterion. The signal is given in an arbitrary normalization.

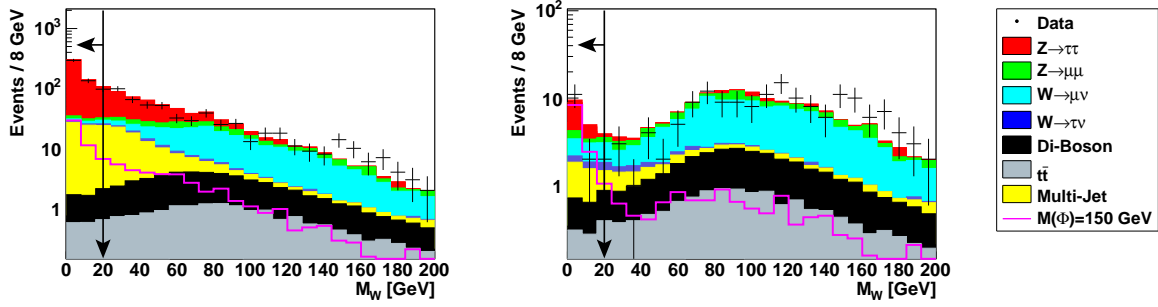


Figure 6.14: The distributions of M_W for the sum of all τ -types after applying the NN_τ criterion (left) and the same distribution for events located in the high-mass region defined as $M_{\text{vis}} > 120$ GeV (right). A cut is applied at $M_W < 20$ GeV. The signal is given in an arbitrary normalization.

6.4.4 $W + \text{Jet}$ Background

After applying the NN_τ criterion, the irreducible $Z/\gamma^* \rightarrow \tau\tau$ process is the dominating background. However, in the high-mass region ($M_{\text{vis}} > 120$ GeV), where the signal is expected, $W^\pm \rightarrow \mu^\pm\nu_\mu$ events dominate. In these events an additionally produced jet is misidentified as tau. Since p_T^τ has to exceed 20 GeV, the W boson recoils against the jet and is boosted strongly. As a consequence, the opening angle between muon and neutrino from the W decay is small and the mass of the W boson can be approximated by

$$\begin{aligned}
 M_W^\mu &= \sqrt{2 \cdot E^\nu \cdot E^\mu \cdot (1 - \cos(\Delta\phi))} \\
 E^\nu &= \cancel{E}_T \times \frac{E^\mu}{p_T^\mu} \\
 \Delta\phi &= \angle(p_T^\mu, \cancel{E}_T),
 \end{aligned} \tag{6.4}$$

as illustrated in Fig. 6.14. The majority of the signal events is located at low values of M_W because \cancel{E}_T points into the direction of the muon, where two neutrinos are produced. In order to remove backgrounds from $W^\pm \rightarrow \mu^\pm\nu_\mu$ an upper boundary is set at $M_W < 20$ GeV. During the optimization for the best expected limit, several values for this criterion and also sets of several other criteria have been considered. Finally, the best result is achieved by a relatively loose cut on M_W , which allows to keep more data and consequently more information.

6.5 Systematic Uncertainties

Various sources of systematic uncertainties on the background expectation and the signal efficiency have been studied. It is found that background and signal are affected by a total systematic uncertainty of 10.3 % and 9.6 %, respectively. The largest contribution of 6.5 % originates from the uncertainty on the measurement of the integrated luminosity. The tau identification and the calibration of the jet energy contribute significantly as well. The uncertainties are studied in the signal region ($M_{\text{vis}} > 120$ GeV) for a Higgs mass of 150 GeV and are summarized in Tab. 6.4.

Source	Background	Signal
Normalization of the multi-jet sample	2.0 %	–
Calibration of jet energy	3.3 %	3.7 %
Muon identification	2.9 %	2.9 %
Muon Resolution	1.7 %	0.5 %
Simulation of trigger efficiency	2.1 %	2.1 %
Tau identification	3.6 %	3.6 %
Tau track reconstruction	2.7 %	2.7 %
Z/γ^* cross section	3.3 %	–
Modeling of p_T of generated boson	1.2 %	1.2 %
Combined uncertainty	7.9 %	7.0 %
Integrated luminosity	6.5 %	6.5 %
Combined total uncertainty	10.3 %	9.6 %

Table 6.4: Relative systematic uncertainties on the events expected from background and signal in the high-mass region after having applied all selection criteria.

- Normalization of the multi-jet sample:** The normalization of the multi-jet sample as a function of p_T^τ and τ -type as described in Sec. 6.3 introduces an uncertainty of 2.0 % on the background expectation. It is determined by varying the parameterizations of the weights within their uncertainties. The uncertainty is relatively small since the multi-jet background is located at low values of M_{vis} , while the signal is located at high values.
- Jet energy calibration:** Although the selection of the Higgs signal does not use a jet requirement explicitly, the systematic uncertainty on the calibration of the jet energy affects the analysis since it is incorporated into the measurement of \cancel{E}_T . Varying the calibration factors within their uncertainty for data and Monte Carlo leads to an uncertainty of 3.3 % and 3.7 % on background and signal expectation, respectively.
- Muon identification and p_T^μ -resolution:** The systematic uncertainty introduced by the corrections applied in Monte Carlo to the modeling of the muon identification and the resolution of their p_T measurement is studied. The estimated uncertainty amounts to 2.9 % for background and signal in case of the muon identification. For the p_T resolution, it amounts to 1.7 % and 0.5 % for signal and background, respectively.
- Trigger simulation:** The simulation of the trigger efficiency as described in Sec. 5.3.1 is varied within its uncertainty and results in an uncertainty of 2.1 % on the signal and background expectation.
- Tau identification:** The systematic uncertainty introduced by using neural networks for the identification of taus is studied in [126]. In case of the present analysis, it introduces an uncertainty of 3.6 % on the signal and background expectation. Additionally, the correction applied to Monte Carlo regarding the track reconstruction efficiency affects the analysis and results in an uncertainty of 2.7 % for signal and background.
- PDF/Scale uncertainty on cross section and $p_T(Z)$ modeling:** The cross sections of the Standard Model processes, as given in Tab. 5.3, are affected by uncertainties

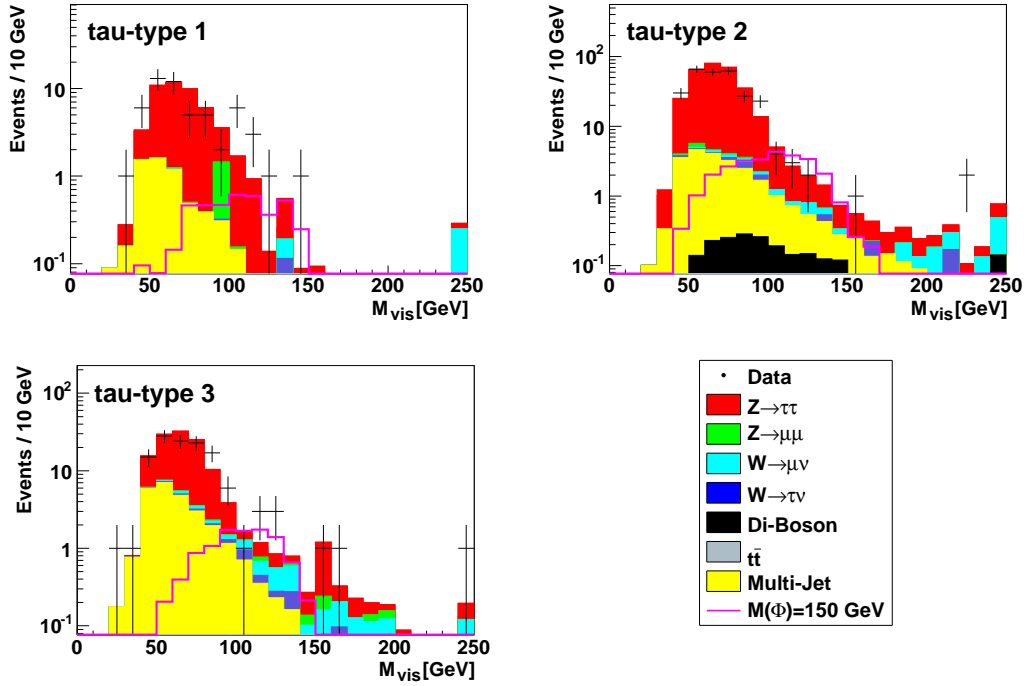


Figure 6.15: Distribution of M_{vis} after applying all selection criteria for τ -type 1, 2 and 3. The highest bin includes the overflow. The signal is given in an arbitrary normalization.

related to the PDF. In particular, the $Z/\gamma^* \rightarrow \tau\tau$ process, which is the dominating background, contributes to the resulting uncertainty of 3.3 %. Furthermore, the background is affected by the uncertainty on the modeling of the transverse momentum of the generated W , Z and Higgs bosons in Monte Carlo, leading to an uncertainty of 1.2 % on background and signal expectation.

6.6 Results

At the final stage of the selection, there are 575 events left in data, while $576 \pm 8(\text{stat}) \pm 61(\text{syst})$ are expected from the Standard Model background. Table 6.5 shows a good agreement of the observed number of events in data and the background expectation for all three τ -types at each stage of the selection. The dominating background after applying all selection criteria is the irreducible $Z/\gamma^* \rightarrow \tau\tau$ process, followed by multi-jet and $W^\pm + \text{jets} \rightarrow \mu^\pm \nu_\mu + \text{jets}$.

Figure 6.15 shows the distributions of M_{vis} for each τ -type at the final stage of the selection. A Higgs signal is expected as an enhancement in data over the expectation from the Standard Model processes in the distribution of the visible mass. For τ -type 2 and 3 this is clearly not the case, while for τ -type 1 an excess in data at $M_{\text{vis}} \approx 110$ GeV is observed. In the region $M_{\text{vis}} > 90$ GeV 13 events are observed in data for τ -type 1, while 7.2 ± 0.9 are expected. Taking into account that a signal is expected to contribute to all τ -types and taking into account the relative small sensitivity in τ -type 1 compared to τ -type 2, this

Tau Type 1				
	Preselection	Muon Veto	Tau ID	Anti- W
Data	459	299	120	57
Sum of Backgrounds	464 ± 10	284 ± 6	122 ± 3	55 ± 2
Multi-jet	115.4 ± 3.3	96.5 ± 3.1	16.4 ± 0.5	6.0 ± 0.3
$Z/\gamma^* \rightarrow \tau\tau$	128.2 ± 3.7	108.8 ± 3.3	74.7 ± 2.8	46.1 ± 2.2
$Z/\gamma^* \rightarrow \mu\mu$	146.7 ± 7.7	16.2 ± 2.6	10.6 ± 1.5	1.5 ± 0.8
$W^\pm \rightarrow \mu^\pm\nu_\mu$	65.5 ± 3.5	56.2 ± 3.2	15.5 ± 0.9	0.8 ± 0.1
$W^\pm \rightarrow \tau^\pm\nu_\tau$	2.3 ± 0.4	1.6 ± 0.3	0.6 ± 0.1	0.11 ± 0.01
WW, WZ, ZZ	4.1 ± 0.1	3.3 ± 0.1	2.7 ± 0.1	0.17 ± 0.02
$t\bar{t}$	2.2 ± 0.1	1.4 ± 0.1	0.9 ± 0.0	0.07 ± 0.01

Tau Type 2				
	Preselection	Muon Veto	Tau ID	Anti- W
Data	1345	1121	581	348
Sum of Backgrounds	1327 ± 12	1090 ± 10.5	614 ± 7	366 ± 6
Multi-jet	276.8 ± 3.5	240.1 ± 3.3	49.5 ± 0.7	24.7 ± 0.5
$Z/\gamma^* \rightarrow \tau\tau$	535.2 ± 7.2	502.0 ± 6.9	427.7 ± 6.3	328.5 ± 5.6
$Z/\gamma^* \rightarrow \mu\mu$	179.9 ± 5.7	50.0 ± 4.0	12.2 ± 0.9	2.1 ± 0.5
$W^\pm \rightarrow \mu^\pm\nu_\mu$	255.6 ± 5.9	230.7 ± 5.6	70.2 ± 1.7	4.2 ± 0.4
$W^\pm \rightarrow \tau^\pm\nu_\tau$	18.9 ± 2.1	17.2 ± 2.0	7.4 ± 0.9	2.5 ± 0.6
WW, WZ, ZZ	38.1 ± 0.3	34.9 ± 0.3	33.7 ± 0.2	2.61 ± 0.07
$t\bar{t}$	22.9 ± 0.2	15.4 ± 0.2	12.9 ± 0.2	0.97 ± 0.04

Tau Type 3				
	Preselection	Muon Veto	Tau ID	Anti- W
Data	3321	3087	332	170
Sum of Backgrounds	3270 ± 20	2895 ± 19	332 ± 4	156 ± 4
Multi-jet	1337.6 ± 9.2	1239.5 ± 8.9	69.0 ± 0.5	31.4 ± 0.3
$Z/\gamma^* \rightarrow \tau\tau$	347.9 ± 6.0	313.8 ± 5.6	156.6 ± 4.0	117.2 ± 3.4
$Z/\gamma^* \rightarrow \mu\mu$	304.9 ± 10.5	239.2 ± 9.6	10.2 ± 0.6	1.0 ± 0.2
$W^\pm \rightarrow \mu^\pm\nu_\mu$	1145.9 ± 12.6	993.3 ± 11.4	85.7 ± 1.0	4.3 ± 0.2
$W^\pm \rightarrow \tau^\pm\nu_\tau$	98.2 ± 4.8	83.9 ± 4.3	5.8 ± 0.3	1.6 ± 0.2
WW, WZ, ZZ	9.4 ± 0.3	8.1 ± 0.2	3.0 ± 0.1	0.27 ± 0.03
$t\bar{t}$	26.2 ± 0.4	17.3 ± 0.3	1.9 ± 0.1	0.18 ± 0.03

Table 6.5: Number of the events observed in data and the events expected from the Standard Model backgrounds at different stages of the selection each τ -type. Only statistical uncertainties are given.

Efficiency for ($M_\phi = 150$ GeV) [%]				
	Preselection	Muon Veto	Tau ID	Anti- W
τ -type 1	0.47 ± 0.02	0.39 ± 0.01	0.3 ± 0.01	0.17 ± 0.01
τ -type 2	2.42 ± 0.04	2.20 ± 0.03	1.98 ± 0.03	1.27 ± 0.03
τ -type 3	1.46 ± 0.03	1.25 ± 0.03	0.71 ± 0.02	0.51 ± 0.02

Table 6.6: Efficiency of the selection for a neutral MSSM Higgs boson of mass $M_\phi = 150$ GeV at different stages of the selection for all three tau types. Only statistical uncertainties are given and the branching ratio in $\mu\tau_h$ final states is included.

excess is not consistent with the presence of a Higgs signal in data. Hence no evidence for a signal of a neutral Higgs boson decaying to a pair of tau leptons is observed.

The selection efficiency at each stage of the selection for each τ -type is given in Tab. 6.6 for a Higgs mass of 150 GeV. Including the branching ratio into $\mu\tau_h$ final states, the selection efficiency after the last selection criteria amounts to (0.17 ± 0.02) % for τ -type 1, (1.3 ± 0.1) % for τ -type 2 and (0.51 ± 0.05) % for τ -type 3.

Since no evidence for a neutral MSSM Higgs boson decaying to a pair of tau leptons is observed, an upper limit on the product of production cross section and branching ratio into tau leptons, $\sigma \times \text{BR}(\Phi \rightarrow \tau\tau)$, is set.

6.7 Extraction of Cross Section Limits

The results are translated into a model independent upper limit on the product of the production cross section times branching ratio into tau leptons $\sigma \times \text{BR}(\Phi \rightarrow \tau\tau)$. The limit is calculated as a function of M_ϕ at the 95 % confidence level (CL) using the likelihood-ratio method in the modified frequentist approach as discussed in Sec. A, which allows to combine several analysis channels. In a second step, this limit is translated into a limit in the $(M_A, \tan\beta)$ -plane within the MSSM.

In order to increase the sensitivity, the result of the analysis at hand is combined with searches for neutral MSSM Higgs bosons decaying to tau pairs in the $e\tau_h$ and $e\mu$ final state. Afterwards, results from the search for $\Phi b(\bar{b}) \rightarrow b\bar{b}b(\bar{b})$ are included.

6.7.1 Combination with Additional $\Phi \rightarrow \tau\tau$ Analyses

The search for neutral MSSM Higgs bosons in $\mu\tau_h$ final states is combined with complementary searches in the $e\tau_h$ and $e\mu$ final states [127, 128]. The analyses use data corresponding to an integrated luminosity of 328 pb^{-1} and 348 pb^{-1} , respectively. The selection of the $e\tau_h$ final state is identical to the $\mu\tau_h$, except for the criteria against $Z/\gamma^* \rightarrow \mu\mu$ events, which are replaced by criteria removing $Z/\gamma^* \rightarrow ee$ events. The selection of the $e\mu$ applies slightly different selection criteria accounting for an additional neutrino in the final state and different dominating backgrounds. Table 6.7 summarizes the number of events selected by the three analyses.

The signal efficiency for each selection is given as a function of the Higgs mass in Fig. 6.16. The combined efficiency of all three selections rises from 1.0 % at $M_\Phi = 90$ GeV to 5.9 % at $M_\Phi = 300$ GeV, due to the increasing \cancel{E}_T and p_T of the reconstructed leptons. The $e\tau_h$ selection is less efficient than the $\mu\tau_h$ selection due to tighter selection criteria against

Analysis	$e\tau_h$	$\mu\tau_h$	$e\mu$
Data	337	575	41
Total expected	296 ± 38	576 ± 62	44 ± 5
Multi-jet	144 ± 19	62 ± 7	2.1 ± 0.4
$Z/\gamma^* \rightarrow \tau\tau$	130 ± 17	492 ± 53	39 ± 5
$Z/\gamma^* \rightarrow ee, \mu\mu$	12 ± 2	5 ± 1	0.6 ± 0.1
$W \rightarrow e\nu, \mu\nu, \tau\nu$	9 ± 1	14 ± 2	0.3 ± 0.2
Di-boson	0.4 ± 0.1	3.1 ± 0.3	1.0 ± 0.1
$t\bar{t}$	0.3 ± 0.1	1.2 ± 0.2	0.06 ± 0.02
Efficiency %	3.6 ± 0.4	8.6 ± 0.8	4.3 ± 0.5

Table 6.7: Observed number of events in data, expected background events and the signal efficiency for a Higgs boson with $M_\Phi = 150$ GeV excluding the tau branching ratio for the three analysis channels used in the combination. Statistical and systematic uncertainties are added in quadrature, assuming no correlation. The numbers of the $e\tau_h$ and the $e\mu$ analysis are taken from [128].

background from $Z/\gamma^* \rightarrow ee$ events. These criteria are necessary because electrons are much more likely misreconstructed as hadronically decaying tau leptons than muons. The relatively large rate for electrons being reconstructed as taus causes an overlap of ≈ 7 % of $\mu\tau_h$ and $e\mu$ analysis for signal and background. The overlap between $\mu\tau_h$ and $e\tau_h$ selection is negligibly small.

In order to extract as much information as possible from the selected events and to achieve the best result in terms of the expected limit, the remaining events at the final stage of the $e\tau_h$ and $\mu\tau_h$ selections are split into subsamples. The subsamples are formed according to the τ -type since the three τ -types result in significantly different signal-to-background ratios. Additionally, the three resulting samples are split into two bins of the M_W spectrum ($M_W < 6$ GeV and 6 GeV $< M_W < 20$ GeV). Figure 6.17 shows that splitting the M_W spectrum into two regions allows to separate two regions which differ significantly in signal-to-background ratio. This separation of the M_W spectrum leads to an improvement of about 20% in terms of expected limit. Together with the $e\mu$ selection, the 13 separate M_{vis} distributions of Fig. 6.18 are obtained. Figure 6.19 shows the distribution of M_{vis} for the $e\mu$ analysis and for the sum of $\mu\tau_h$ and $e\tau_h$ analyses in the M_W region with the highest signal-to-background ratio ($M_W < 6$ GeV).

The systematic uncertainties on the estimate of the expected numbers of background and signal events of the three selections are introduced by numerous measurements: integrated luminosity (6.5 %), trigger efficiency (1–4 %), lepton identification and reconstruction efficiencies (2–5 %), jet and tau energy calibration (2–6 %), PDF uncertainty (3–4 %), and modeling of multi-jet background (2–9 %). All except the last one are correlated between the three final states. Details are given for the $\mu\tau_h$ final state in Sec. 6.5.

The resulting expected and observed upper limits at the 95 % CL on $\sigma \times \text{BR}(\Phi \rightarrow \tau\tau)$ are shown in Fig. 6.20 as a function of M_Φ . The limits are valid independently of any model, assuming a Standard Model width of the Higgs boson. The expected limit improves from 32 pb at $M_\Phi = 90$ GeV to 0.63 pb at $M_\Phi = 300$ GeV, due to the increasing separation from the $Z/\gamma^* \rightarrow \tau\tau$ resonance and the increasing efficiency of the selection. For comparison, the

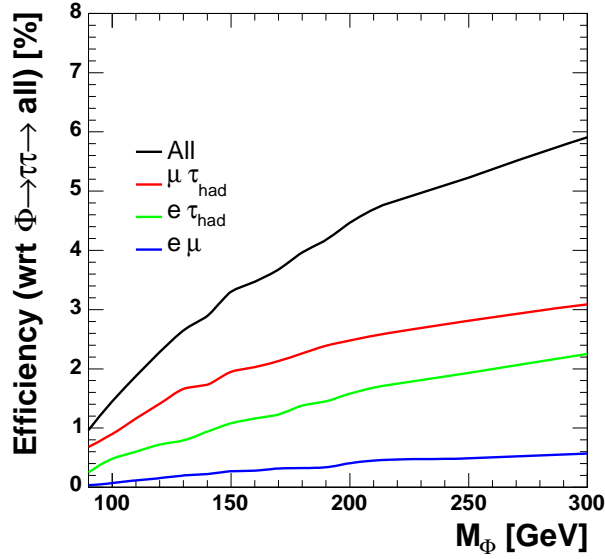


Figure 6.16: Signal efficiency as a function of M_ϕ for the process $p\bar{p} \rightarrow \phi \rightarrow \tau\tau$ for each analysis and the sum of all analyses. The tau branching ratios are included in the signal efficiencies.

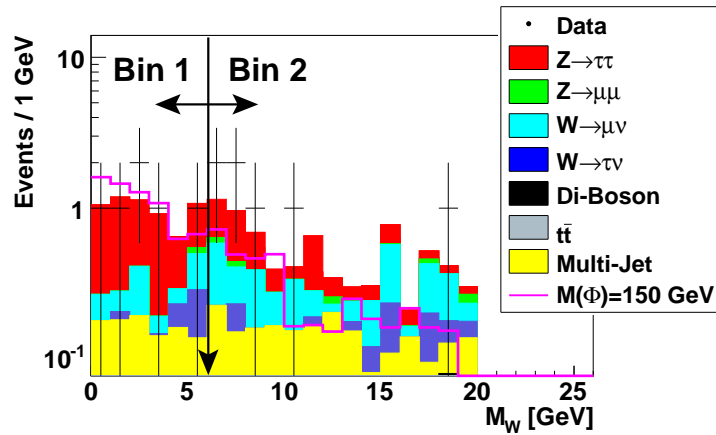


Figure 6.17: Distribution of M_W in the high-mass region $M_{vis} > 120$ GeV after applying all selection criteria of the $\mu\tau_h$ for the sum of all τ -types. The sample is split into two bins according to different signal-to-background ratios: $M_W < 6$ GeV and $6 \text{ GeV} < M_W < 20$ GeV. The signal is given in an arbitrary normalization.

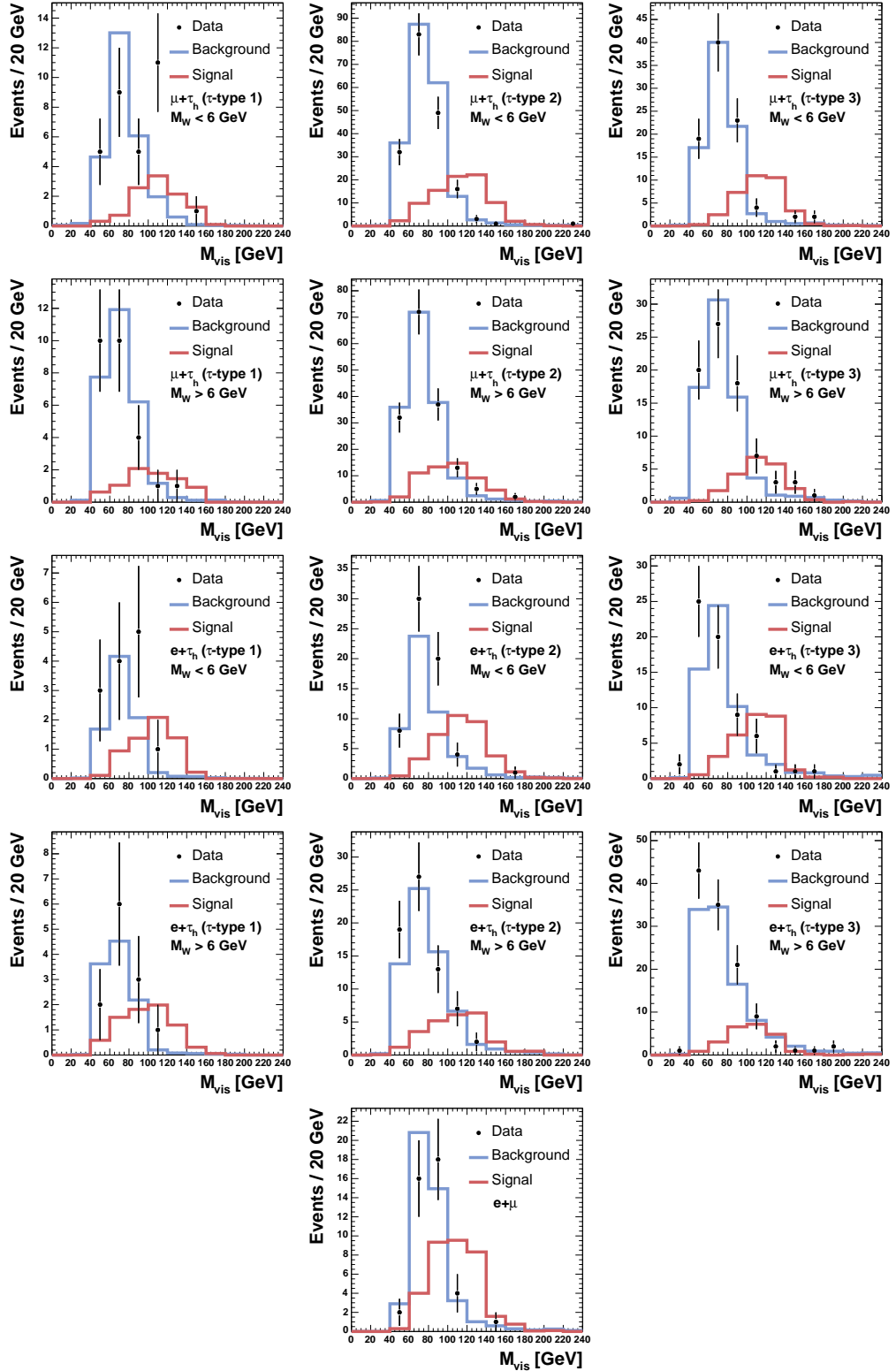


Figure 6.18: The M_{vis} distributions of all 13 channels used in the combination of the $\Phi \rightarrow \tau\tau$ analysis. The 13 channels include the $e\mu$ analysis and two times six channels from the $e\tau_h$ and $\mu\tau_h$ analysis, which are divided into subsamples with different signal-to-background ratios. The signal expectation is given for a Higgs mass of 150 GeV in an arbitrary normalization.

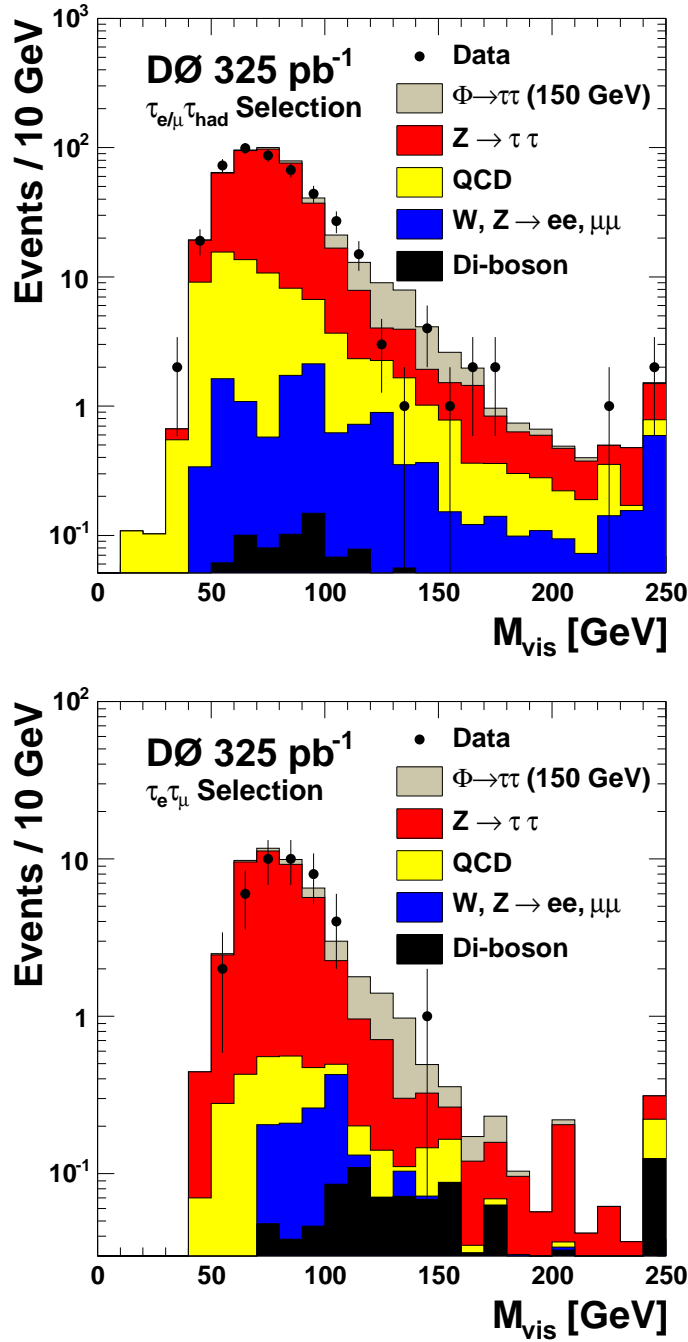


Figure 6.19: The distribution of the visible mass M_{vis} for the sum of the two final states involving hadronically decaying tau leptons (top) and for the $e\mu$ (bottom) final state after applying all selection criteria. The top distribution shows the subsample with the largest signal-to-background ratio ($M_W < 6$ GeV). The Higgs signal is normalized to the cross section excluded by the combination of the three $\Phi \rightarrow \tau\tau$ analysis. The indicated integrated luminosity represents the average of the three final states and the highest bin includes the overflow.

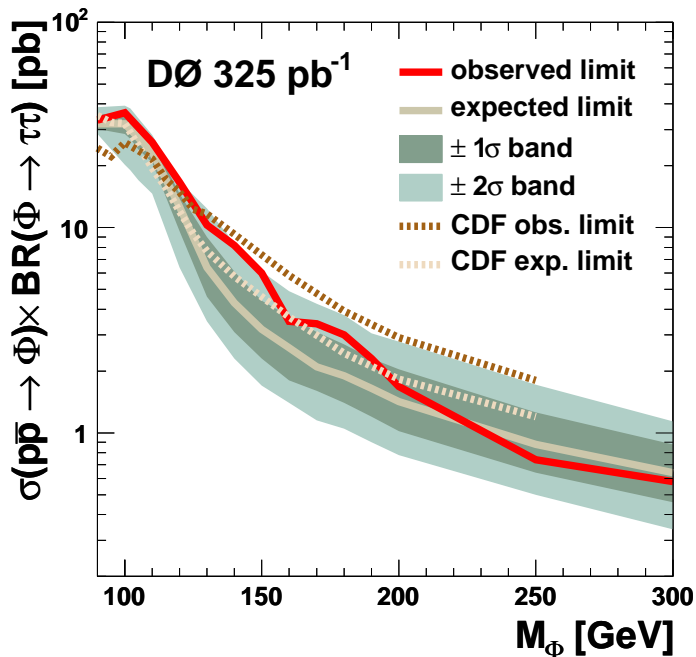


Figure 6.20: The observed and expected 95 % CL upper limits on $\sigma \times \text{BR}(\Phi \rightarrow \tau\tau)$ as a function of M_Φ including error bands from systematic and statistical uncertainties. The limit is model independent as long as a narrow width of the Higgs boson is assumed. The indicated integrated luminosity represents the average of the three final states. The CDF analysis used data corresponding to an integrated luminosity of 310 pb^{-1} [129].

CDF result is shown. It is obtained from $e\tau_h$ and $\mu\tau_h$ selections using data corresponding to an integrated luminosity of 310 pb^{-1} [129]. Both results are comparable, while the limit from the presented analysis is slightly stronger for high values of M_Φ and weaker for small values due to differences in the optimization of the selections.

Within the MSSM the upper limit on the production cross section can be interpreted as limit on $\tan\beta$ as a function of M_A . Figure 6.21 shows the results for the m_h^{max} and the no-mixing scenario, which are defined in Sec. 1.2.7. The difference of the results for the two values of the Higgs mass parameter $\mu = +0.2 \text{ TeV}$ and $\mu = -0.2 \text{ TeV}$ can be interpreted as the effect resulting from radiative corrections. The presented analysis excludes a significant fraction of the SUSY parameter space for all considered scenarios, down to $\tan\beta \approx 60$ for $M_A = 90 \text{ GeV}$. The limits weaken at large values of M_A since the cross section for the Higgs production decreases with increasing M_A (Fig. 6.6). In order to ensure that the comparison to the CDF result is not affected by systematic differences in the calculation of the Higgs production cross sections in the four scenarios, the CDF curves are calculated from the cross section limit given in Fig. 6.20. As in the cross section limit, the limits on $\tan\beta$ from the CDF analysis are slightly tighter for small M_A and weaker towards high values of M_A . The LEP experiments [62] exclude neutral MSSM Higgs masses below 93 GeV , depending slightly on the scenario. They also exclude $\tan\beta < 3$ for the m_h^{max} scenario for the whole considered mass

range and in case of the no-mixing scenario $\tan\beta < 6$ and $\tan\beta < 10$ for $\mu = +0.2$ TeV and $\mu = -0.2$ TeV, respectively. For illustration purposes the limits are shown up to $\tan\beta = 100$, ignoring the potentially sizable contributions from higher-order corrections. The combined result represented the most stringent limit on the production of neutral MSSM Higgs bosons at hadron colliders at the time of publication.

Impact of Higgs width

The width of the neutral MSSM Higgs boson increases drastically in the high $\tan\beta$ regime, as discussed in Sec. 6.1.3. The signal Monte Carlo used throughout the three analyses are generated assuming a Standard Model Higgs boson width, therefore the effect on the expected limit is studied for $\tan\beta = 100$ using Higgs masses of $M_\Phi = 130$ GeV and $M_\Phi = 200$ GeV. The enlarging Higgs width leads to two effects. On the one hand, events get shifted towards the large background of the Z resonance, or even below it, degrading the sensitivity. On the other hand, events are shifted to larger values of M_{vis} where the background decreases and the sensitivity is increased. It is found that effect of the event shift to higher M_{vis} values overwhelms, resulting in a higher sensitivity for the large Higgs width at $\tan\beta = 100$. As a consequence, neglecting the effects from the broadening Higgs width leads to conservative limits.

Impact of Mass Differences of h , H and A

Throughout the analysis, it is assumed that the three neutral MSSM Higgs bosons h , H and A are mass degenerate, which is not necessarily a valid assumption for all regions of the SUSY parameter space. In order to verify this assumption, the parameter space is considered where $M_\Delta = |M_{(h,H)} - M_A|$ is larger than the achievable M_{vis} resolution and the contributions of $\sigma(p\bar{p} \rightarrow h, H) \times \text{BR}(\tau\tau)$ to the total cross section are significant compared to the uncertainty on the signal efficiency. Figure 6.22 indicates the region in the $(M_A, \tan\beta)$ -plane where $M_\Delta > 0.1 \cdot M_A$ and the contribution of $\sigma(p\bar{p} \rightarrow h, H) \times \text{BR}(\tau\tau) > 0.1 \cdot \sigma(p\bar{p} \rightarrow h, H, A) \times \text{BR}(\tau\tau)$. It is found that regions with significant mass differences are not probed by this analysis.

6.7.2 Combination with Additional $\Phi b(\bar{b}) \rightarrow b\bar{b}b(\bar{b})$ Analysis

The DØ collaboration has also performed a search for neutral MSSM Higgs bosons produced via the associated production with bottom quarks and subsequent decay into bottom quarks $p\bar{p} \rightarrow \Phi b(\bar{b}) \rightarrow b\bar{b}b(\bar{b})$ in data corresponding to an integrated luminosity of 260 pb^{-1} [130]. Events containing at least three jets from bottom quarks are selected and the spectrum of the invariant $b\bar{b}$ mass of the two leading jets of Fig. 6.23 (left) is used to set limits on the production cross section and in the $(M_A, \tan\beta)$ -plane.

The $\Phi b(\bar{b}) \rightarrow b\bar{b}b(\bar{b})$ result is re-interpreted in the benchmark scenarios that are used in the $\Phi \rightarrow \tau\tau$ analysis presented in this thesis, and in order to increase the sensitivity, both analyses are combined. This means that the invariant mass spectrum given in Fig. 6.23 (left) enters the limit calculation, which is discussed in the previous section, as an additional channel. The resulting limits in the $(M_A, \tan\beta)$ -plane are given for the m_h^{max} and no-mixing scenario in Fig. 6.24.

Combining the $\Phi \rightarrow \tau\tau$ and $\Phi b(\bar{b}) \rightarrow b\bar{b}b(\bar{b})$ results improves the limits in the $(M_A, \tan\beta)$ -plane significantly. Especially, in the m_h^{max} scenario with $\mu < 0$, where the $\Phi b(\bar{b}) \rightarrow b\bar{b}b(\bar{b})$ production cross section is the largest, the limit is tightened to $\tan\beta = 55$, depending strongly

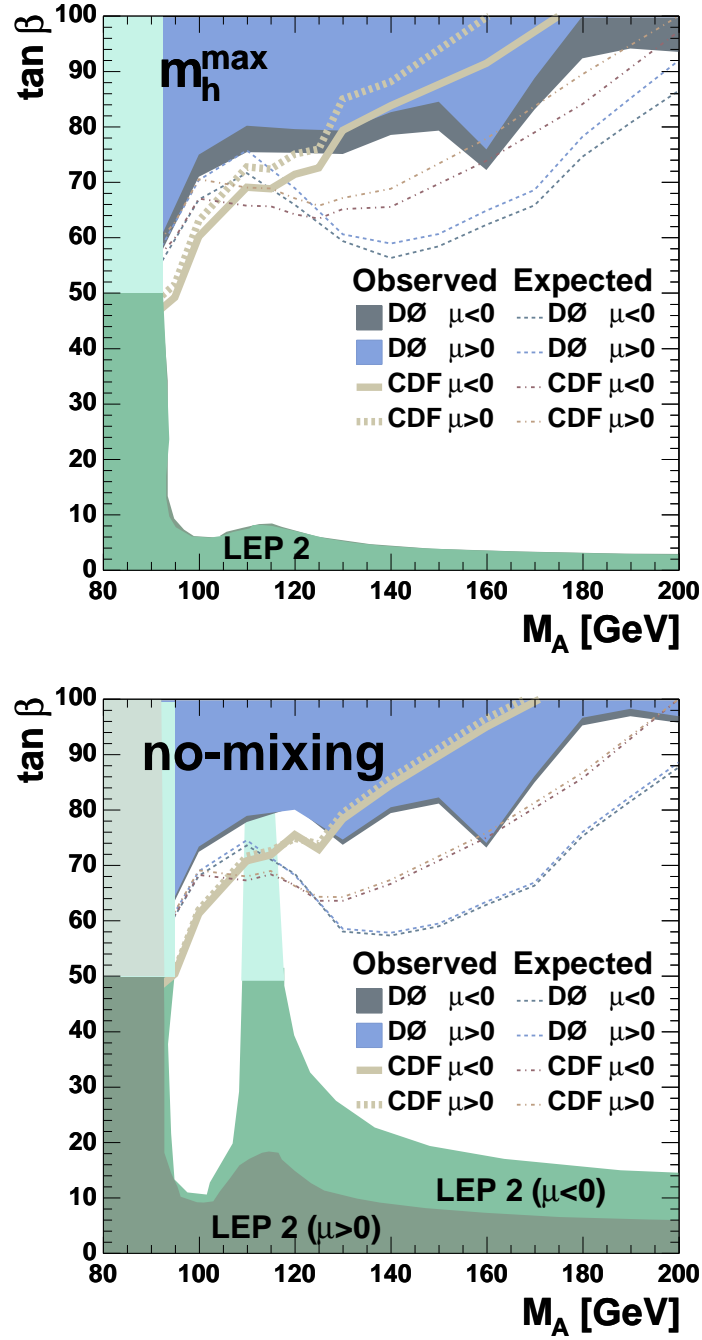


Figure 6.21: Regions which are excluded at the 95 % CL by the combined $\Phi \rightarrow \tau\tau$ analysis in the $(M_A, \tan \beta)$ -plane for the m_h^{\max} and the no-mixing scenario for $\mu = +0.2$ TeV and $\mu = -0.2$ TeV ($m_{\text{top}} = 172.7$ GeV). The exclusion regions from the LEP experiments [62] are extrapolated for values $\tan \beta > 50$.

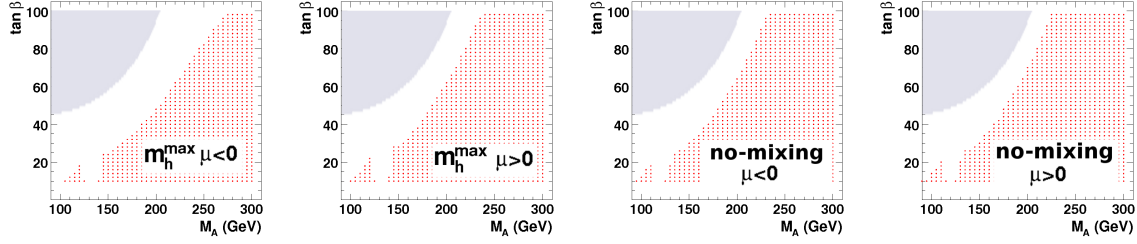


Figure 6.22: Region with sizeable contributions of $\sigma(p\bar{p} \rightarrow h, H) \times \text{BR}(\tau\tau)$ to the total cross section and sizeable differences of $M_{h,H}$ and M_A for the considered scenarios (dots). The approximate regions probed by the presented analyses are sketched by the shaded areas.

on M_A . Only a small improvement is observed for in the m_h^{\max} case with $\mu < 0$, due to the small production cross section. In the no-mixing scenario, the excluded region increases in a similar amount for $\mu < 0$ and $\mu > 0$ and reaches to $\tan\beta = 62$, again depending on M_A . Compared to the CDF result, the combination of $\Phi \rightarrow \tau\tau$ and $\Phi b(\bar{b}) \rightarrow b\bar{b}b(\bar{b})$ analyses leads to significantly extended exclusion limits in the $(M_A, \tan\beta)$ -plane for most values of M_A . The effect from radiative corrections on the production cross section can be seen in the variation of the limit between positive and negative μ . The $\tau^+\tau^-$ final state is less affected by these corrections than the $b\bar{b}$ final state because contributions from sbottom-gluino loops cancel in the $\tau^+\tau^-$ final state [124].

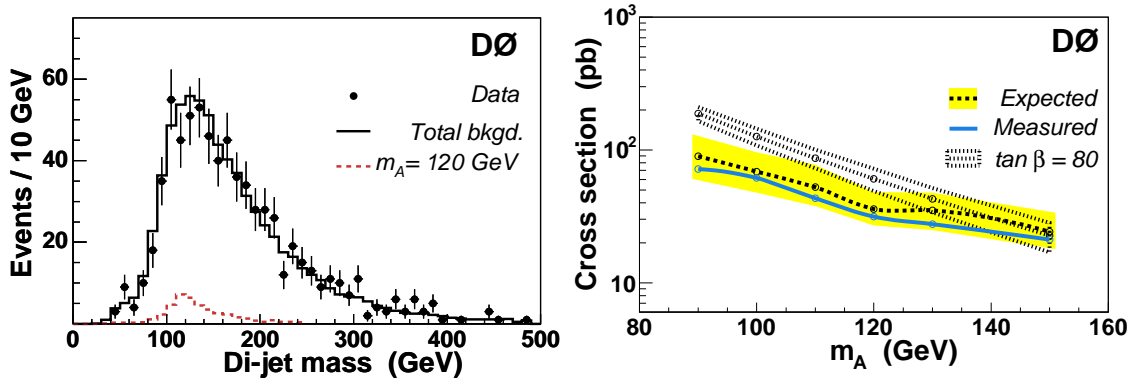


Figure 6.23: *Left:* Invariant mass spectrum of the two leading jets from bottom quarks in events with at least three jets from bottom quarks as selected in the $\Phi b(\bar{b}) \rightarrow b\bar{b}b(\bar{b})$ analysis. Data corresponding to 260 pb^{-1} of integrated luminosity have been analyzed. The signal of a 120 GeV Higgs boson is normalized to the cross section which can be excluded at the 95 % CL [130].

Right: The expected and observed upper limits on the signal cross section, together with the 1σ error band. The signal cross section is given for the no-mixing scenario for $\tan\beta = 80$ including the theoretical uncertainty [130].

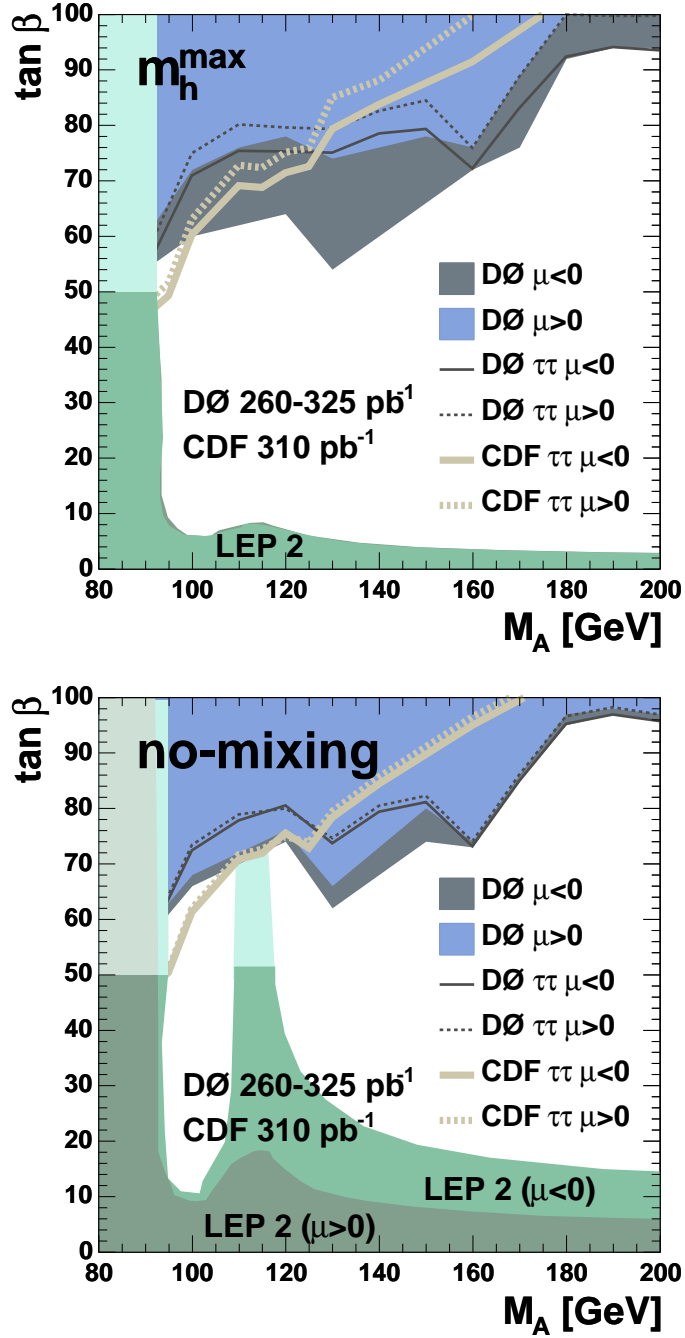


Figure 6.24: Regions which are excluded at the 95 % CL in the $(M_A, \tan \beta)$ -plane for the m_h^{\max} and the no-mixing scenario for $\mu = +0.2$ TeV and $\mu = -0.2$ TeV ($m_{\text{top}} = 172.7$ GeV) after the combination of the results from the $\Phi \rightarrow \tau\tau$ analysis (labeled as $D\emptyset \tau\tau$) and the $\Phi b(\bar{b}) \rightarrow b\bar{b}b(\bar{b})$ analysis [130]. The LEP limits [62] have been extrapolated for $\tan \beta > 50$.

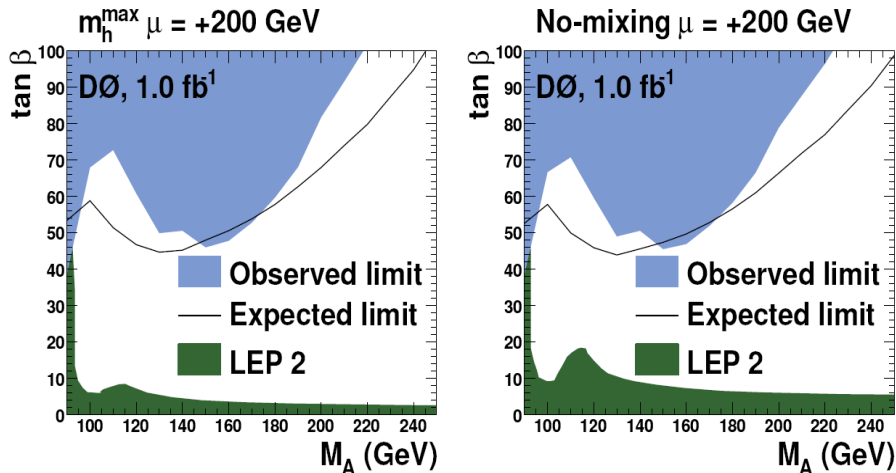


Figure 6.25: Current $D\bar{O}$ exclusion limits at the 95 % CL in the $(M_A, \tan\beta)$ -plane for the m_h^{\max} and the no-mixing scenario from the search for $\Phi \rightarrow \tau\tau$ using data corresponding to an integrated luminosity of 1 fb^{-1} [131].

6.8 Recent Results from the Tevatron and Outlook

The analysis discussed in this chapter is based on a portion of the Tevatron Run IIa data set corresponding to an integrated luminosity of 299 pb^{-1} , which was recorded between August 2002 and June 2004. Since then, the $D\bar{O}$ and CDF collaborations continued recording and analyzing data. $D\bar{O}$ performed an update of the search for $\Phi \rightarrow \tau\tau$ on a data set corresponding to an integrated luminosity of 1 fb^{-1} [131]. Since the higher data statistics increases the sensitivity of the search, the updated analysis extends the excluded region in the $(M_A, \tan\beta)$ -plane to $\tan\beta \approx 40 - 50$ for small values of M_A , depending on M_A and the considered SUSY scenario (Fig. 6.25). The CDF collaboration presents preliminary results of the search for $\Phi \rightarrow \tau\tau$ in the $e\tau_h$ and $\mu\tau_h$ final states using 1.8 fb^{-1} of recorded data [132], resulting in slightly stronger constraints on the SUSY parameter space, as shown in Fig. 6.26. The search for $\Phi b(\bar{b}) \rightarrow b\bar{b}b(\bar{b})$ has been updated based on data corresponding to 1 fb^{-1} , extending the mass range over which the search is performed [133].

$D\bar{O}$ and CDF expect to record data corresponding to about 7 fb^{-1} by the end of Tevatron Run II in the year 2009. The higher statistics and better understanding and simulation of the detector, together with improved analysis techniques, will allow to increase the sensitivity of the search for $p\bar{p} \rightarrow \Phi \rightarrow \tau\tau$ and to probe extended regions of the SUSY parameter space. An estimate of the exclusion potential is given in Fig. 6.27 (left) [134]. It is assumed that both experiments perform searches with similar sensitivity. A further assumption is an improvement of the signal efficiency by 30 %, due to additional searches in the fully hadronic decay channel $\Phi \rightarrow \tau\tau \rightarrow \text{had} + \text{had}$, better understanding of the detector and an improved measurement of tau energy. The study predicts a sensitivity of the search for $\Phi \rightarrow \tau\tau$ to $\tan\beta \approx 20$ for combined results from $D\bar{O}$ and CDF using the data set expected by the end of Run II of the Tevatron.

At the end of Run II of the Tevatron, the delivered luminosity will not be sufficient to extend the sensitivity over the whole $(M_A, \tan\beta)$ -plane. Only the start of the Large Hadron

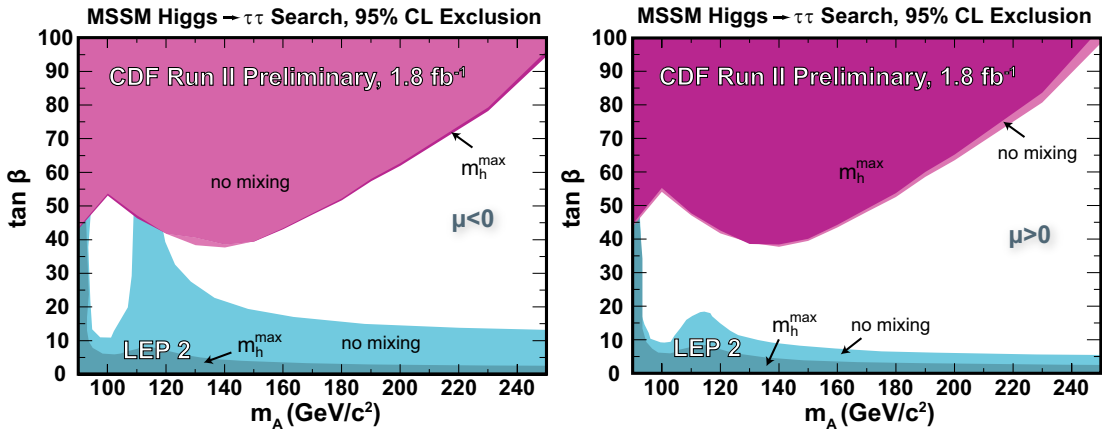


Figure 6.26: Current CDF exclusion limits in the $(M_A, \tan\beta)$ -plane for the m_h^{\max} and the no-mixing scenario for $\mu > 0$ and $\mu < 0$ from the search for $\Phi \rightarrow \tau\tau$ in the $e\tau_h$ and $\mu\tau_h$ final state using 1.8 fb⁻¹ of data [132].

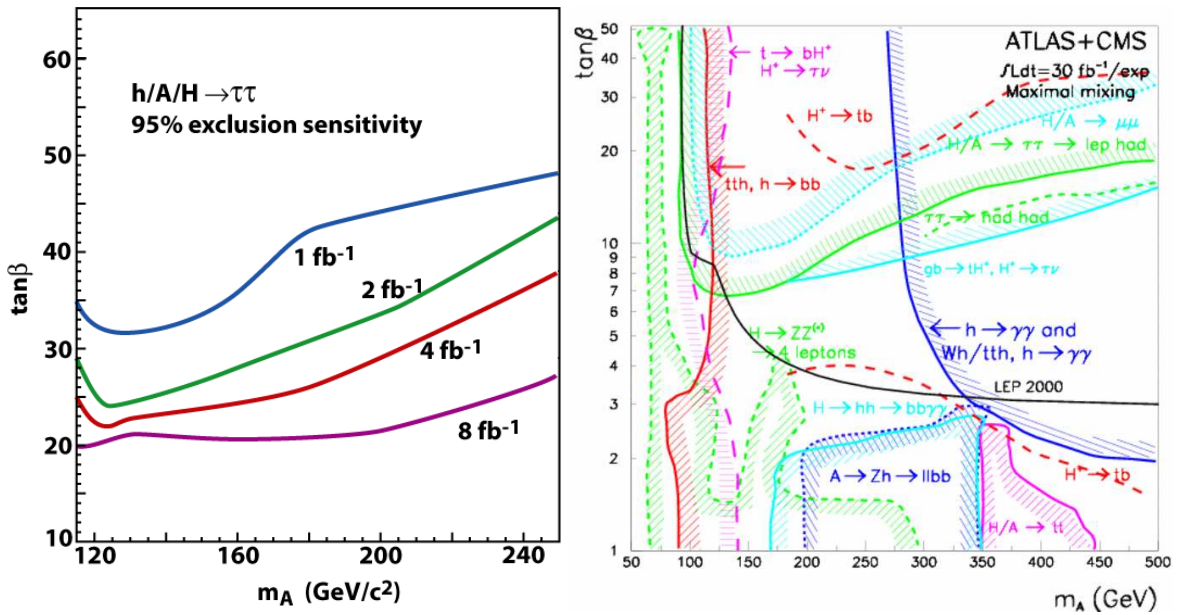


Figure 6.27: *Left*: Projection of the exclusion potential at the 95 % CL for combined D0 and CDF searches for $\Phi \rightarrow \tau\tau$ in the $(M_A, \tan\beta)$ -plane [134].

Right: Combined sensitivity of the ATLAS and CMS experiments for the discovery of MSSM Higgs bosons in the maximal mixing scenario for an integrated luminosity of 30 fb⁻¹, which corresponds to three years of data taking at low luminosity. The 5 σ discovery curves are shown in the $(M_A, \tan\beta)$ -plane for individual channels [135].

Collider, with the experiments ATLAS and CMS, will allow to study the complete SUSY parameter space of interest in the near future, as shown in Fig. 6.27 (right). Combined searches for $\Phi \rightarrow \tau\tau$ from ATLAS and CMS using data corresponding to an integrated luminosity of 30 fb^{-1} will allow to probe the whole $(M_A, \tan\beta)$ -plane.

7

Reconstruction of Low Energetic Tau Leptons

This chapter discusses the reconstruction of low energetic tau leptons. The motivation and the description of the developed reconstruction algorithm are followed by the discussion of the selection of the tau mass signal in $Z/\gamma^* \rightarrow \tau\tau \rightarrow \mu\tau_h$ events.

7.1 Motivation

The reconstruction and identification of low energetic hadronically decaying tau leptons is especially developed for the search for associated chargino/neutralino production described in Sec. 8. For the following discussion, it is anticipated that one of the most promising signatures in the search for SUSY at the Tevatron is the final state including three charged leptons with small transverse momenta. In particular for large values of $\tan\beta$, the cascade decay of chargino and neutralino to taus is expected to dominate in a significant fraction of the SUSY parameter space. Compared to the charged leptons of first and second generation, the reconstructible transverse momentum of taus $p_T^{\tau,\text{vis}}$ is reduced due to the escaping neutrinos resulting from the tau decay. Therefore, high reconstruction efficiency for low energetic tau leptons is crucial for the search for associated chargino/neutralino production in tau final states. In addition to the efficient reconstruction, the challenge is to suppress the large background contributions resulting from low energetic jets. A detailed discussion of the phenomenology of the SUSY signal follows in Sec. 8.

The efficiency of the DØ standard reconstruction of hadronically decaying tau leptons, as it is discussed in Sec. 4.4, diminishes for small visible transverse tau momenta ($p_T^{\tau,\text{vis}} \lesssim 12$ GeV), as shown in Fig. 4.1. Due to the tau mass of 1.8 GeV, the tau decay products no longer appear as a narrow isolated jet but as objects well separated in the detector (see Fig. 7.1 (left)). As a consequence, their energy is not located in a narrow cone with $\Delta\mathcal{R} = 0.3$ as assumed in the standard reconstruction. The strategy to reconstruct the low energetic tau leptons which are not found by the standard algorithm is to reconstruct the decay products separately and to use the reconstructed tau mass for the separation from jet backgrounds. The focus is on tau leptons with a visible transverse momentum of $3 \text{ GeV} \lesssim p_T^{\tau,\text{vis}} \lesssim 12 \text{ GeV}$ decaying into one charged and at least one neutral hadron. For these tau decays, the distribution of the

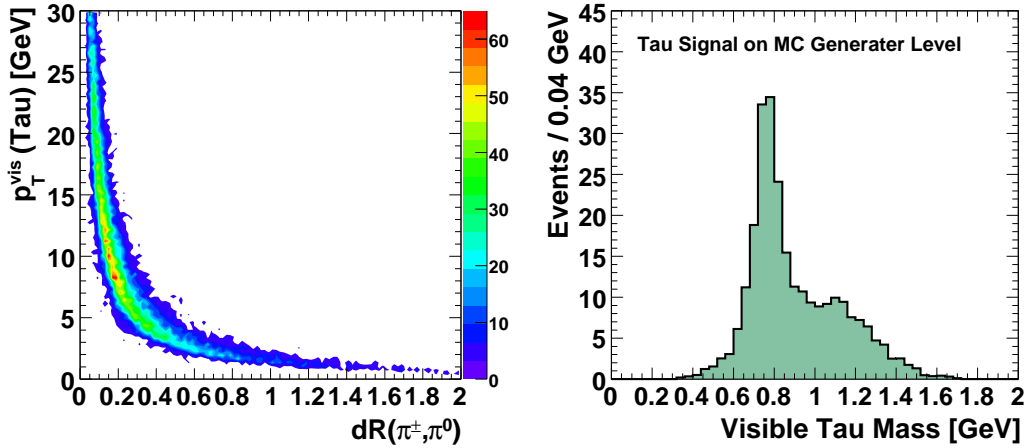


Figure 7.1: *Left*: Distance between charged and neutral decay products of a hadronic tau decay vs. $p_T^{\tau, \text{vis}}$ calculated from the generator level information in Monte Carlo. *Right*: The visible tau mass calculated from the decay products of hadronical 1-prong tau decays, excluding the 4-momentum of the neutrino, on generator level in $Z/\gamma^* \rightarrow \tau\tau$ Monte Carlo events.

visible tau mass at Monte Carlo generator level is shown in Fig. 7.1 (right). It is composed of a resonance at the mass of the ρ meson ($m_\rho = 0.78$ GeV) and a relatively wider resonance corresponding to the a_1 meson ($m_{a_1} = 1.2$ GeV).

The reconstruction of low energetic tau leptons is developed using Monte Carlo samples. Therefore, its performance needs to be verified in data. The $Z/\gamma^* \rightarrow \tau\tau$ process is the only process at the Tevatron providing a sufficient amount of tau leptons. A selection in the $\mu\tau_h$ final state is developed to select low energetic taus in $Z/\gamma^* \rightarrow \tau\tau$ events and the results obtained in data and Monte Carlo are compared.

It is important to notice that this selection serves as a reference selection and as an important verification of the developed reconstruction algorithm but not as an independent analysis. As a consequence, parts of the analysis are studied and described in less detail than in case of the Higgs and SUSY analysis.

7.2 Reconstruction and Identification

7.2.1 Reconstruction Algorithm

Tau leptons which have a visible transverse momentum of $3 \text{ GeV} \lesssim p_T^{\tau, \text{vis}} \lesssim 12 \text{ GeV}$ and decay into a charged and at least one neutral hadron are reconstructed. The typical signature seen in the detector is illustrated in Fig. 7.2 (left). It consists of well separated objects that are a track, a cluster in the hadronic calorimeter (resulting in most of the cases from a charged pion) and clusters in electromagnetic calorimeter (typically resulting from neutral pions). The algorithm uses tracks ($p_T > 0.5$ GeV) as seed which are isolated in the tracking detector ($\text{iso}^{\text{trk}} < 4$ GeV). The isolation criterion iso^{trk} corresponds the scalar sum of the p_T of all

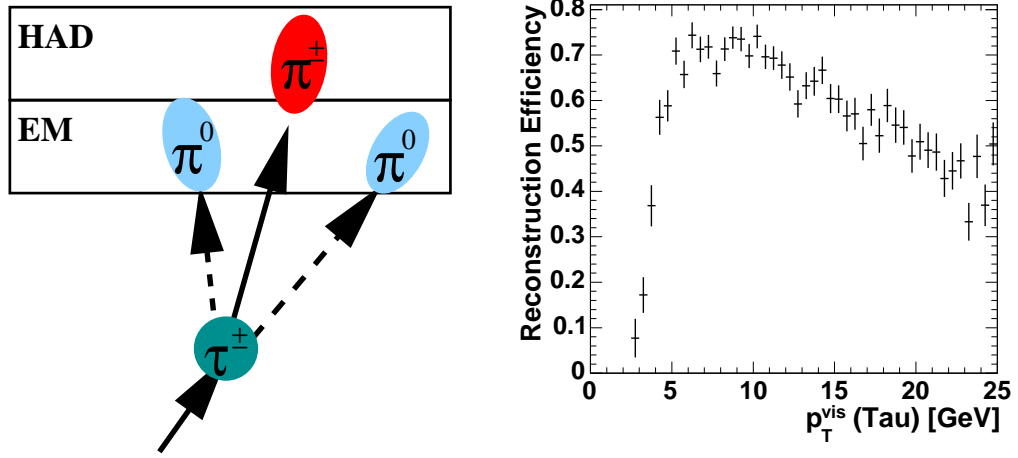


Figure 7.2: Schematic illustration of the signature in the hadronic (HAD) and electromagnetic (EM) calorimeter (left) and the reconstruction efficiency in SUSY Monte Carlo events (right) of low energetic tau decays.

tracks in a cone with $\Delta\mathcal{R} = 0.5$ around the considered track candidate. EM clusters are reconstructed using a nearest neighbor algorithm in the calorimeter [136]. The two leading EM cluster in a hollow cone ($0.1 < \Delta\mathcal{R} < 1.0$) are associated to the track if their transverse energy is larger than 1 GeV. EM clusters inside $\Delta\mathcal{R} < .1$ are not considered in order to reject possible energy depositions in the EM calorimeter from the charged particle identified as track. The visible tau mass can be calculated using the track and the EM clusters, neglecting the 4-momentum of the escaping neutrino. The efficiency of this reconstruction process is shown as a function of $p_T^{\tau,\text{vis}}$ in Fig. 7.2 (right). The efficiency starts to raise from $p_T^{\tau,\text{vis}} \approx 3$ GeV to a plateau of about 70 % at $p_T^{\tau,\text{vis}} \approx 5$ GeV. After reaching the plateau, it drops for $p_T^{\tau,\text{vis}} \gtrsim 10$ GeV due to the decreasing resolution capability for the tau decay products. This efficiency drop is the natural consequence of the optimization for low transverse momenta.

7.2.2 Application of a Likelihood

The tau candidates reconstructed by the algorithm discussed in the previous section can result from misinterpretation of other objects in the detector. In order to reject the dominating jet background efficiently, a likelihood discriminator is constructed based on five variables:

- m_τ : the visible tau mass calculated from the reconstructed track and the EM clusters;
- $\text{iso}^{\text{trk}} = \sum_{\text{Tracks}}^{\Delta\mathcal{R} < 0.5} p_T$: the isolation of the tau track in the tracking detector is calculated from the scalar sum of all track p_T in a cone with $\Delta\mathcal{R} = 0.5$ around the tau track, excluding the tau track itself;
- $\text{iso}^{\text{cal}} = \sum_{\text{Cluster}}^{\Delta\mathcal{R} < 1.0} E_T / p_T^\tau$: the scalar sum of the transverse energy E_T of all cluster in a cone with $\Delta\mathcal{R} = 1.0$ is divided by the total transverse momentum of the tau;
- N^{trk} : the number of tracks in a cone with $\Delta\mathcal{R} = 1.0$, excluding the tau track;

- N^{clus} : the number of calorimeter clusters in a cone with $\Delta\mathcal{R} = 1.0$, excluding the EM cluster associated to the tau.

Figure 7.3 shows these variables for signal and background. A SUSY Monte Carlo sample with a high content of low energetic tau leptons, as it will be discussed later in the SUSY analysis (Sec. 8.2), provides the tau leptons for the signal sample. Jets from $W^\pm + \text{jets} \rightarrow \mu^\pm\nu_\mu + \text{jets}$ Monte Carlo events serve as background sample (Sec. 5.2). The resulting likelihood distribution (called LH_τ in the following) is shown in Fig. 7.4 for signal and background events. For a given event i the likelihood is defined as

$$\begin{aligned} \text{LH}_\tau(i) &= \frac{P_S(i)}{P_S(i) + P_B(i)} \\ P_{S,B}(i) &= \prod_{k=1}^n p_{S,B;k}(x_k(i)), \end{aligned} \quad (7.1)$$

where $p_{S,B;k}$ represents the probability density function (p.d.f.) for signal (S) and background (B) for the k^{th} out of n input variables. The PDF for each input variable is normalized: $\int_{-\infty}^{\infty} p_{S,B;k}(x_k(i)) dx_k = 1, \forall k$.

7.3 Data and Monte Carlo Samples

The data sample used in the following selection is the complete Tevatron Run IIa data set, corresponding to an integrated luminosity of $944 \pm 59 \text{ pb}^{-1}$ recorded by single muon triggers (see Sec. 5.1). The used Monte Carlo samples are subsamples of the $Z/\gamma^* \rightarrow \tau\tau$ and $Z/\gamma^* \rightarrow \mu\mu$ samples used for the SUSY analysis, as described in Sec. 5.2. Since the $Z/\gamma^* \rightarrow \tau\tau$ process results in two leptons with opposite charge (*unlike-sign* events), the background from further Standard Model processes is estimated from data by selecting events containing a muon and a tau candidate which have the same charge assigned (so-called *like-sign* events). This method exploits that the rate of the misidentification of jets as leptons is independent of the lepton charge and therefore can be assumed to be the same for unlike-sign and like-sign events. The like-sign event sample dominantly contains multi-jet events from QCD processes and $W^\pm + \text{jets} \rightarrow \mu^\pm\nu_\mu + \text{jets}$ events and is referred to as *jet background*.

7.4 Selection of the Tau Mass Signal in $Z/\gamma^* \rightarrow \tau\tau$ Events

The tau mass signal is selected in $Z/\gamma^* \rightarrow \tau\tau$ events in the $\mu\tau_h$ final state. The main challenge is the suppression of the overwhelming background from low energetic jets which are misidentified as taus. Another important background is the $Z/\gamma^* \rightarrow \mu\mu$ process. It has a large cross section and a muon results in a track, while the EM cluster in the calorimeter can originate from the minimal ionization of the muon itself or from low energetic jets in the event. The signal selection criteria are summarized in Tab. 7.1 and explained in the following.

Preselection

At the stage of preselection a muon ($p_T^\mu > 15 \text{ GeV}$) which is isolated in the tracking detector and the calorimeter (Sec. 4.3) is required. Additionally, a tau candidate ($p_T^\tau > 3 \text{ GeV}$, $p_T^{\tau\text{-track}} < 12 \text{ GeV}$) is required to be reconstructed by the algorithm for low energetic tau

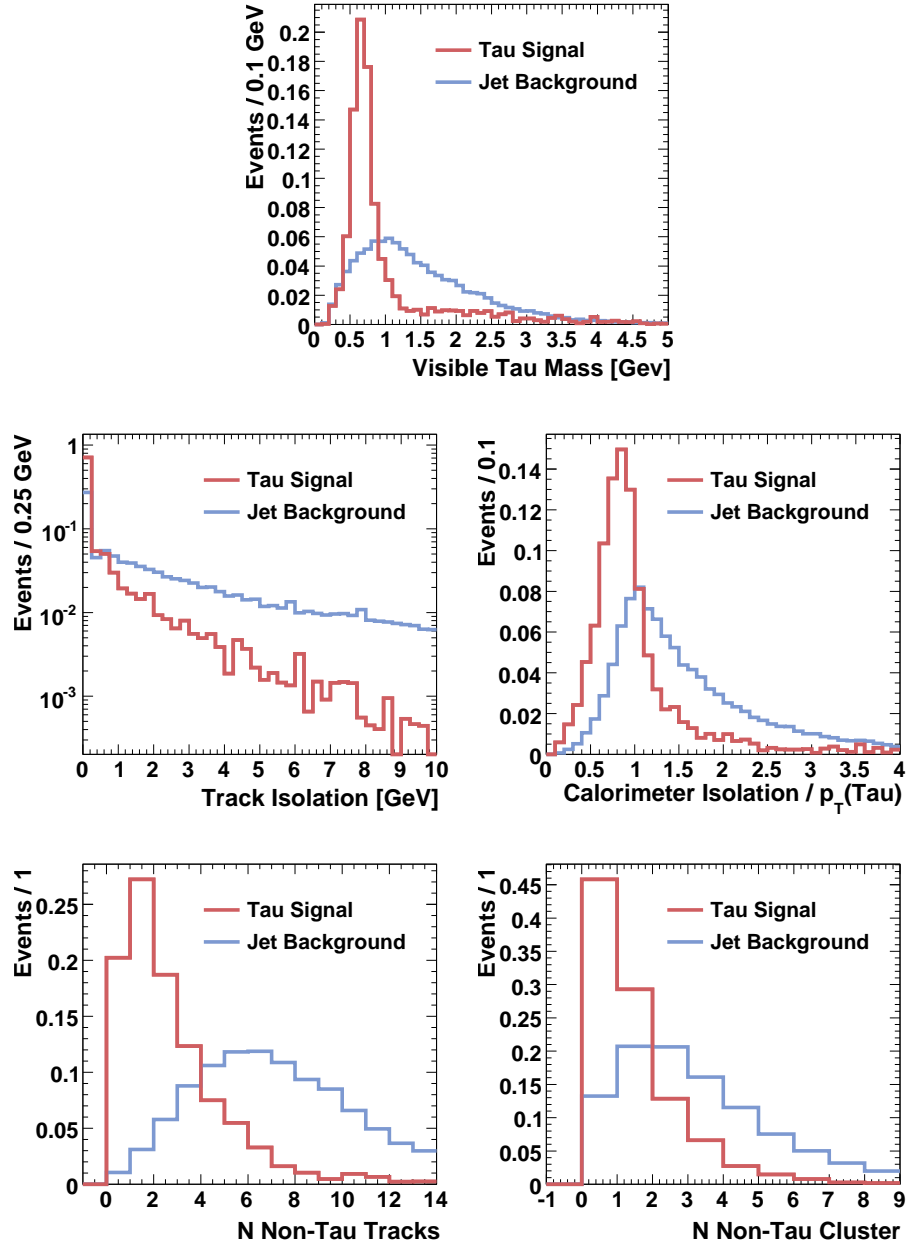
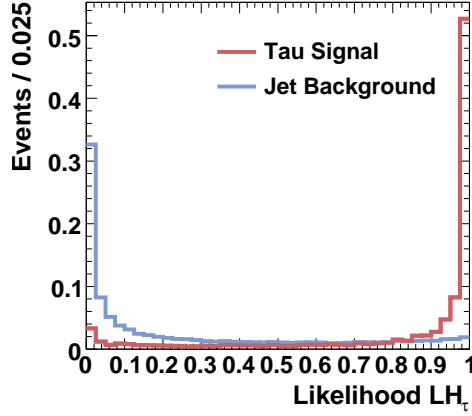


Figure 7.3: The reconstructed visible tau mass (top) and the further variables included in the likelihood discriminator for the identification of low energetic tau leptons LH_τ in signal (SUSY) and background ($W^\pm + \text{jets} \rightarrow \mu^\pm \nu_\mu + \text{jets}$) Monte Carlo events. The a_1 resonance is not visible in the visible tau mass distribution since the reconstruction efficiency for two EM clusters that pass the p_T threshold is significantly lower.


 Figure 7.4: The distribution of the likelihood discriminator LH_τ for signal and background.

(1) Preselection	Muon: $p_T^\mu > 15$ GeV, isolated in calorimeter and tracker Tau: $p_T^\tau > 3$ GeV, reconstructed by low energetic tau algorithm $0.5 \text{ GeV} < p_T^{\tau\text{-track}} < 12$ GeV Exactly one EM cluster associated to the tau candidate Muon and tau originate from the same vertex: $\Delta z < 1.5$ cm Muon and tau have opposite charge assigned $\Delta\phi(\mu, \tau\text{-track}) > 2.75$ $\Delta\phi(\mu, \cancel{E}_T) > 2.75$
(2) Anti- $Z/\gamma^* \rightarrow \mu\mu$	No muon overlaps with the tau candidate $\Delta\mathcal{R}(\tau\text{-track}, \text{any } \mu) > 0.15$.
(3) Back-to-back	$\Delta\phi(\mu, \tau) > 2.9$
(4) Threshold of p_T^τ	$p_T^\tau > 6$ GeV
(5) Range of p_T^μ	$p_T^\mu < 35$ GeV
(6) Tau likelihood	$LH_\tau > 0.95$

 Table 7.1: Summary of the selection criteria of the tau mass signal in $Z/\gamma^* \rightarrow \tau\tau$ events.

leptons. The upper cut on $p_T^{\tau\text{-track}}$ removes a large fraction of the background from jets and $Z/\gamma^* \rightarrow \mu\mu$ events. Tau candidates with two EM clusters are not considered because the signal-to-background ratio is too small. The tracks of the reconstructed muon and tau are required to have opposite charge assigned (unlike-sign). It is ensured that both tracks originate from the same vertex by a cut on the distance of the z positions of the tracks at the point at closest approach to the beamline: $\Delta z < 1.5$ cm.

Since these selection criteria are relatively loose, two additional criteria are applied in the preselection to suppress tau candidates from resulting from jets. The first criteria exploits that in the $Z/\gamma^* \rightarrow \tau\tau$ signal muon and tau lepton are back-to-back: $\Delta\phi(\mu, \tau\text{-track}) > 2.75$. The second criterion asks for $\Delta\phi(\mu, \cancel{E}_T) > 2.75$ and is motivated in the following. Consider the hadronically decaying tau τ_1 from the process $Z/\gamma^* \rightarrow \tau_1\tau_2$ with $\tau_1 \rightarrow h\nu_{\tau_1}$ and $\tau_2 \rightarrow \mu\nu_{\mu}\nu_{\tau_2}$. If it results in a hadron h with $p_T^h \lesssim 12$ GeV, the neutrino ν_{τ_1} must obtain a large fraction of the total momentum of τ_1 . Therefore, \cancel{E}_T points into the direction of the hadronically decaying tau lepton τ_1 , despite the fact that two neutrinos occur in the leptonic decay of τ_2 . Together with the back-to-back topology of $Z/\gamma^* \rightarrow \tau\tau$ events, this leads to the usage of $\Delta\phi(\mu, \cancel{E}_T)$. Using the angle $\Delta\phi(\tau, \cancel{E}_T)$ is less efficient since p_T^μ is larger than p_T^h and yields a better estimate of the direction of the two tau leptons before their decay.

The distributions of Fig. 7.5 show reasonable agreement of data and simulation in terms of relevant kinematic properties at the stage of preselection. The distribution of the likelihood discriminator LH_τ is given in Fig. 7.6.

Further selection criteria

Background contribution from $Z/\gamma^* \rightarrow \mu\mu$ decays are suppressed by rejecting all tau candidates with a track to which a muon can be matched in $\Delta\mathcal{R} < 0.15$. The requirement $\Delta\phi(\mu, \tau) > 2.9$ exploits the fact that $Z/\gamma^* \rightarrow \tau\tau$ events result in back-to-back topologies. It tightens the relative loose cut on $\Delta\phi(\mu, \tau\text{-track})$ used in the preselection. A significant fraction of the jet background is removed by raising the threshold on p_T^τ to 6 GeV. Background contributions from $W^\pm + \text{jets} \rightarrow \mu^\pm\nu_\mu + \text{jets}$ events are rejected by an upper cut on $p_T^\mu < 35$ GeV, while the $Z/\gamma^* \rightarrow \tau\tau$ signal, which results in lower p_T^μ , is kept. Distributions of the used quantities are shown in Fig. 7.5. The last step of the selection is a tight cut on the likelihood discriminator of the low energetic tau identification $\text{LH}_\tau > 0.95$, which removes remaining contributions from jet backgrounds (Fig. 7.6).

Monte Carlo Correction

After having applied all selection criteria, it is found that the distributions of p_T^τ and related quantities are not modeled in sufficient accuracy. As Fig. 7.7 shows, the spectrum of p_T^τ in data is softer than expected from Monte Carlo. The reason for this difference is investigated leading to the conclusion that it is neither caused by a different resolution capability of clusters in the calorimeter in data and simulation nor by different efficiencies of the likelihood LH_τ . Effects from insufficient accuracy of the background modelling can be excluded as well. A small inconsistency is found in the reconstruction efficiencies of the used calorimeter cluster in data and Monte Carlo at low energies. But correcting the Monte Carlo for this effect does not lead to a satisfying improvement. As a consequence, a correction factor as function of p_T^τ is determined and applied to each simulated event in order to take into account the different identification efficiencies of low energetic taus in data and simulation. It is calculated

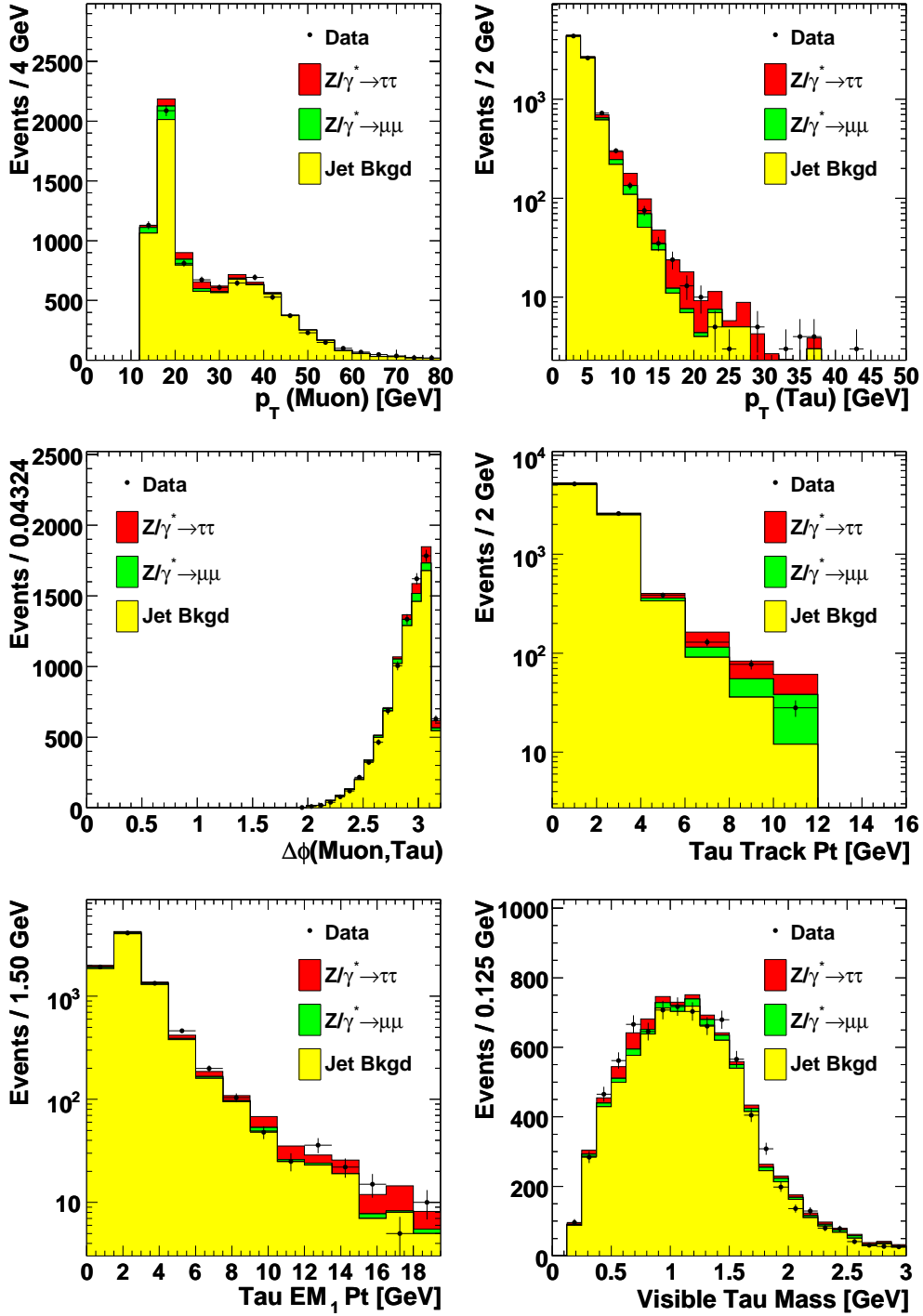


Figure 7.5: Distribution at the stage of preselection of the transverse momenta of muon and tau (p_T^μ , p_T^τ) (top), the azimuth between them $\Delta\phi(\mu, \tau)$ and the transverse momentum of the reconstructed track $p_T^{\tau\text{-track}}$ (center), and the transverse momentum of the leading EM cluster $p_T^{EM_1}$ and the visible tau mass reconstructed from these two objects (bottom).

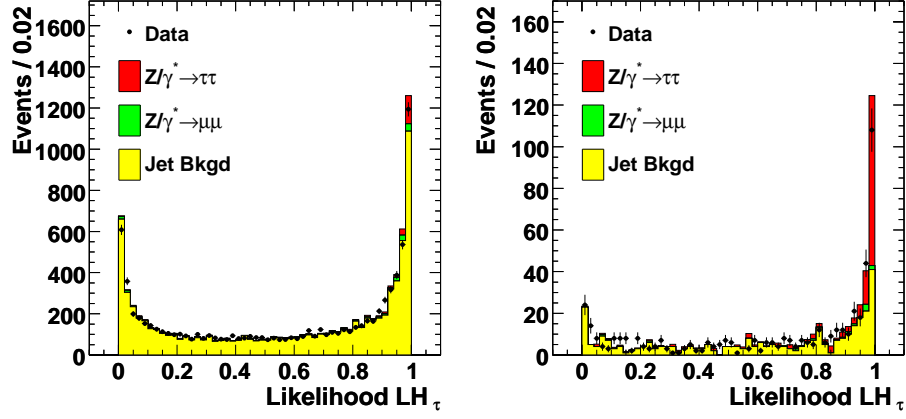


Figure 7.6: Distributions of the likelihood discriminator used for the identification of low energetic tau leptons LH_τ , at the stage of preselection (left) and before the cut on the discriminator itself is applied (right).

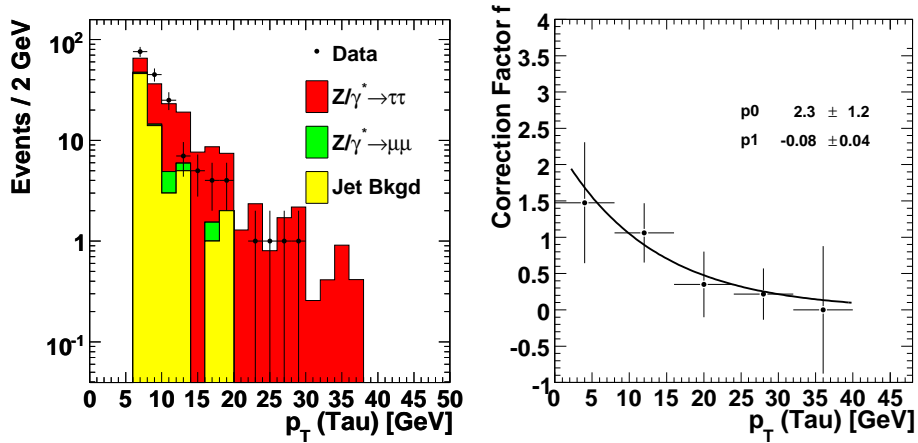


Figure 7.7: Distribution of p_T^τ after all selection criteria are applied (left). Correction factor for the efficiency of the identification of low energetic tau leptons in simulation, parameterized by an exponential function: $f(p_T^\tau) = p_0 e^{p_1 p_T^\tau}$ (right).

	Data	Sum	$Z/\gamma^* \rightarrow \tau\tau$	$Z/\gamma^* \rightarrow \mu\mu$	Like-Sign
(1) Preselection	8332	8463 ± 12	312 ± 4	254 ± 5	7897 ± 89
(2) Anti $Z/\gamma^* \rightarrow \mu\mu$	7958	8087 ± 18	285 ± 3	120 ± 3	7682 ± 88
(3) Back-to-back	3283	3247 ± 16	204 ± 3	48 ± 2	2995 ± 55
(4) $p_T^\tau > 6$ GeV	614	634 ± 4	169 ± 2	15 ± 1	450 ± 21
(5) $p_T^\mu < 35$ GeV	468	477 ± 3	149 ± 2	14 ± 1	314 ± 18
(6) Likelihood LH_τ	170	178 ± 2	103 ± 2	5 ± 1	70 ± 8

Table 7.2: Number of events observed in data and expected for the $Z/\gamma^* \rightarrow \tau\tau$ signal and background contributions at different stages of the selection. Only statistical uncertainties are given.

by scaling the $Z/\gamma^* \rightarrow \tau\tau$ Monte Carlo sample to match the data for every bin in p_T^τ and parameterizing the p_T^τ dependent scaling factor using an exponential function, as shown in Fig. 7.7.

7.5 Results

At the final stage of the selection, a clear signal the tau mass is observed in $Z/\gamma^* \rightarrow \tau\tau$ events in the $\mu\tau_h$ final state using the reconstruction algorithm developed for low energetic tau leptons, as illustrated in Fig. 7.8 (top). There are 170 events observed in data, while $103 \pm 2(\text{stat}) \pm 7(\text{lumi})$ are expected from the $Z/\gamma^* \rightarrow \tau\tau$ signal and $75 \pm 8(\text{stat})$ from the sum of all backgrounds. The observed and expected number of events show a reasonable agreement of data and simulation at every stage of the selection (Tab. 7.2). In Fig. 7.8 (bottom) the resulting distributions of the reconstructed invariant mass from muon and tau is presented. As expected, the signal of the tau mass results in a resonance at the mass of the ρ meson. Due to the escaping neutrinos, the signal of the Z boson in the distribution of the invariant mass of muon and tau is located at lower values than the Z mass itself. This shift is amplified by upper bounds on the visible transverse momenta of the two leptons p_T^μ and p_T^τ . The systematic uncertainties on signal and background are not studied since this selection only serves as a verification of the developed reconstruction algorithm for low energetic tau leptons.

The successful reconstruction of the $Z/\gamma^* \rightarrow \tau\tau$ resonance in the $\mu\tau_h$ final state shows that the reconstruction algorithm developed for low energetic tau leptons performs in reasonable agreement in data and simulation. Furthermore, the reconstructed signal of the visible tau mass is well modeled in the simulation. Corrections which are applied to the simulation take into account small differences in terms of identification efficiency. As a consequence, the algorithm is used in the search for associated production of Chargino and Neutralino which is described in Sec. 8.

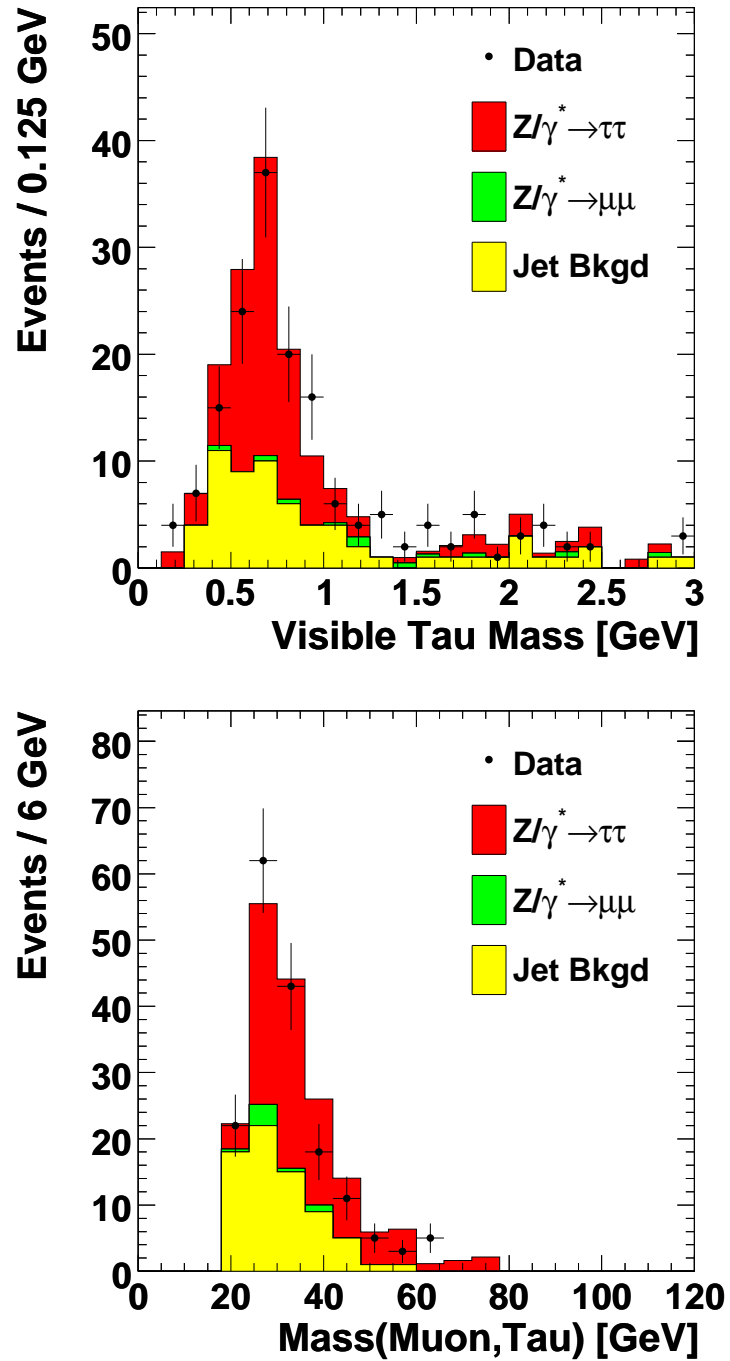


Figure 7.8: *Top*: Signal of the visible tau mass in $Z/\gamma^* \rightarrow \tau\tau$ events reconstructed in the $\mu\tau_h$ final state using the reconstruction algorithm for low energetic tau leptons. *Bottom*: The reconstructed invariant mass of muon and tau for data and simulation.

8

Search for Associated Chargino/Neutralino Production in $\mu\tau h\ell$ Final States

The associated production of the lightest chargino and the second lightest neutralino with subsequent decays to three leptons and missing transverse energy, the so-called *trilepton* signature, is one of the most promising channels in the search for Supersymmetry at the Tevatron. The following chapter describes the phenomenology of this process assuming R -parity conserving and its selection in the final state with a muon, a hadronically decaying tau and a third lepton. The results of this analysis are combined with searches in further trilepton channels. An outlook on the search for SUSY at the Tevatron and at the LHC closes the chapter.

SUSY signatures with tau leptons are well motivated since they arise in a variety of models of low-energy Supersymmetry, e.g. gravity mediated (SUGRA) or minimal gauge-mediated models. In these models, there are parameter regions where the branching ratio into stau is enhanced, due to enhanced couplings to gauginos or because the lightest stau is lighter than the lightest selectron and smuon. Depending on the particular scenario, the final states resulting from the decay of gaugino pair production may be dominated by one of the combinations lll , $ll\tau$, $l\tau\tau$ or $\tau\tau\tau$.

8.1 Trilepton Signature at the Tevatron

8.1.1 Production of Charginos and Neutralinos

At hadron colliders, SUSY particles are expected to be produced in weak interactions, resulting in charginos, neutralinos and sleptons, and in strong interactions, which lead mainly to squarks and gluinos. Assuming the conservation of R -parity, only pairs of SUSY particles are produced, but even in case of R -parity violation the pair production dominates.

The dominant production process of gaugino pairs at the Tevatron is the quark anti-quark annihilation with a gauge boson exchange in the s -channel, as shown in Fig. 8.1 (left). The

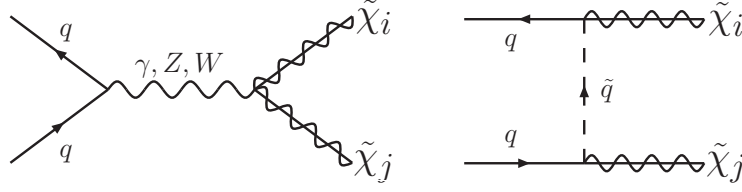


Figure 8.1: Leading order diagrams for the production of chargino/neutralino pairs in quark-antiquark collisions.

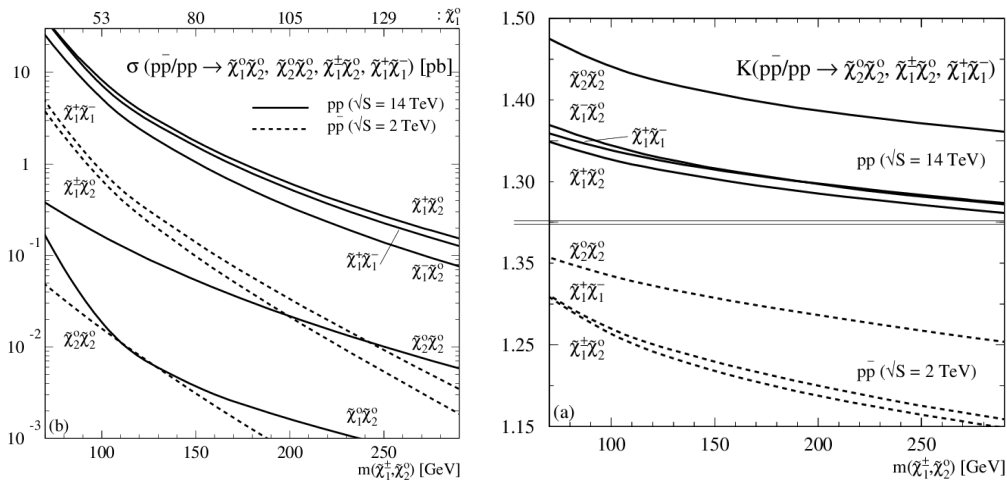


Figure 8.2: Next-to-leading order cross section and resulting k -factor for chargino/neutralino pair production as a function of the gaugino masses. The cross sections are calculated in the mSUGRA scenario with the parameters $m_0 = 100$ GeV, $A_0 = 300$ GeV, $\mu > 0$ and $\tan\beta = 4$, while $m_{1/2}$ is varied [139].

squark exchange in the t -channel, as illustrated in Fig. 8.1 (right), is expected to be suppressed because squark masses are typically heavy in GUT-constrained SUSY models. In addition the Tevatron experiments already exclude squark and gluino masses below 300-400 GeV [137, 138]. Other production processes of gauginos have significantly smaller cross sections or lead to final states which can not be separated from large Standard Model background processes [139].

As illustrated in Fig. 8.2, the production cross section decreases with increasing gaugino mass since the cross section for hard interactions decreases with the effective center-of-mass energy \hat{s} and the density of valence quarks decreases with increasing momentum fraction x . The cross section is expected to be the largest for chargino and neutralino masses just above the LEP lower limits [55], where it reaches values of the order of 1 pb. NNLO correction are expected to be small. The pair production of sleptons has a significantly smaller cross section [139].

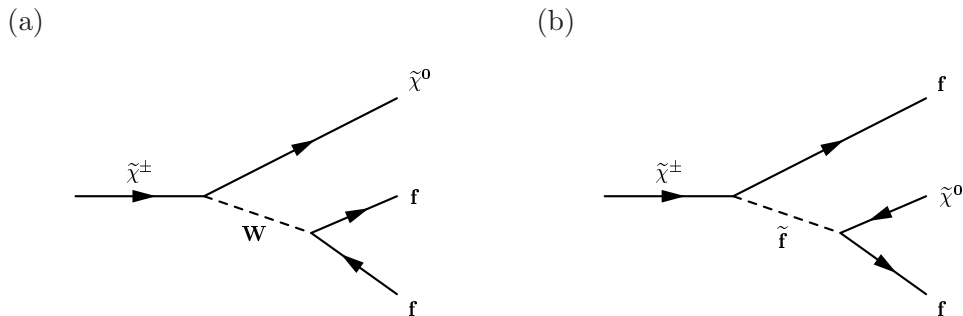


Figure 8.3: Decay modes of the chargino via a W boson (a) and via a sfermion (b).

8.1.2 Decay of Charginos and Neutralinos

Assuming conservation of R -parity, charginos and neutralinos decay rapidly either directly or via cascades into LSP and Standard Model particles. The decays are mediated by gauge bosons or sfermions.

Large regions of the parameter space are dominated by 3-body decays of heavy charginos via virtual W bosons into a pair of fermions and a lighter neutralino, as shown in Fig. 8.3 (a). For mass differences larger than M_W between chargino and lighter neutralino, 2-body decays into real W bosons dominate. If sfermions are light enough or the decay via W bosons is suppressed, the fermion mediated decay of Fig. 8.3 (b) is the favored decay mode. The resulting sfermion decays into its Standard Model partner and a lighter neutralino. In the fermion mediated case, 2 and 3-body decays are possible as well, depending on the mass difference of the involved particles. The only difference of the resulting final state to the gauge mediated decay is a change in the event kinematics. The decays of heavy neutralinos are almost identical to the decays of charginos (Fig. 8.4). However, the decays are mediated by Z bosons instead of W bosons.

The branching ratio into the different fermions is determined by the field content of the gauginos, the sfermion masses and the sfermion chirality. If neutralino and chargino have a high wino field content, they favor a coupling to the left handed fermions and their supersymmetric partners. If neutralino and chargino have a high higgsino field content, they favor a coupling to heavy leptons. If neutralino and chargino have a high photino field content, they prefer a coupling to charged sfermions and fermions. If kinematically possible, the decay mediated by real sfermions and gauge bosons is preferred.

Stau Mixing

The off-diagonal elements in the stau mass matrix of Eq. (1.61), $m_\tau (A_\tau - \mu \tan \beta)$, introduce a mixing between the two stau chirality states (see Sec. 1.2.8). The proportionality to the Standard Model lepton mass results in significant difference of the field content and masses of the staus compared to the sleptons of the first and second generation. Due to the splitting between the slepton masses of the first two and the third generation, the lightest stau can become considerably lighter than the lightest (the right-handed) selectron and smuon. Furthermore, the lightest stau acquires a left-handed component, which introduces couplings to the wino and bino contributions of chargino and neutralino.

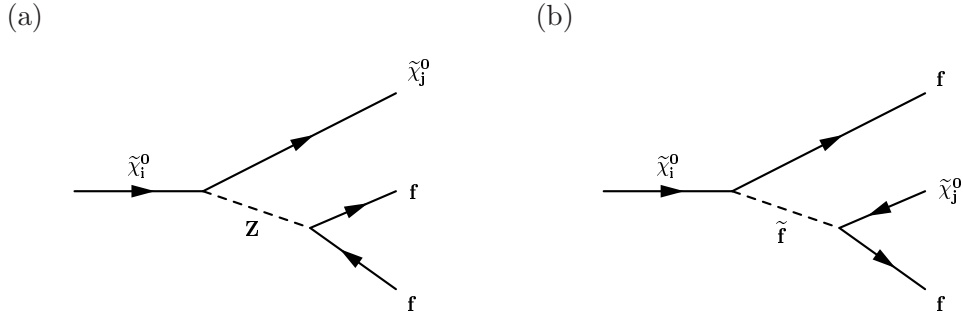


Figure 8.4: Decay modes of the neutralino via a Z boson (a) and via a sfermion (b) for $i > j > 0$.

If one assumes that A_τ and μ are of the order of the electroweak scale, the degree of stau mixing is determined by $\tan\beta$. For large values of $\tan\beta$, the decay of the lightest chargino and the second lightest neutralino into staus is enhanced over the decay into sleptons of the other two generations. Regions in the supersymmetric parameter space exist, typically for large $\tan\beta$, where the mass hierarchy $m_{\tilde{\chi}_1^0} < m_{\tilde{\tau}_1} < m_{\tilde{\chi}_1^\pm} < m_{\tilde{\mu}_R}$ holds and $\text{BR}(\tilde{\chi}_1^\pm \tilde{\chi}_2^0 \rightarrow \tau\tau\tau + X)$ is close to 100 %, resulting in a challenging scenario [140]. In the present analysis, one of the considered scenarios is the one satisfying the mass hierarchy $m_{\tilde{\chi}_1^0} < m_{\tilde{\chi}_1^\pm} < m_{\tilde{\tau}_1} < m_{\tilde{\mu}_R}$ in order to study the transition from minimal to maximal stau mixing.

8.1.3 Signal Topology

The common detector signature of gaugino pair production is a significant amount of missing transverse energy arising from LSPs and/or neutrinos, together with combinations of jets and charged leptons. The pair production of the lightest chargino is expected to result in final states consisting of four jets, two jets and one charged lepton or two charged leptons. The associated production of the lightest chargino and the second lightest neutralino is expected to result in final states consisting of four jets, two jets and two charged leptons, two jets and one charged lepton or three charged leptons. The production cross section for combinations of heavier charginos and neutralinos is significantly smaller.

The most promising of the listed channels is the *trilepton channel*, which consists of three charged leptons and missing transverse energy. The background from Standard Model processes is expected to be significantly lower than for the other final states. The presented analysis searches for the final state consisting of a muon, a hadronically decaying tau, a third lepton and missing transverse energy ($\mu\tau_h\ell$). The channels $e\ell\ell$, $\mu\mu\ell$ are discussed in [141], while the $e\mu\ell$ and $e\tau_h\ell$ channels are addressed in [142] and [143], respectively. A search in the final state with two muons which have the same charged assigned is performed in [144].

Figure 8.5 (left) indicates the regions of different decay modes of the lightest chargino and the second lightest neutralino in the mSUGRA model in the $(m_0, m_{1/2})$ -plane. In the parameter region where $m_{\tilde{\chi}_1^\pm} < M_W + m_{\tilde{\chi}_1^0}$ and $m_{\tilde{\chi}_2^0} < M_Z + m_{\tilde{\chi}_1^0}$, the sfermion mediated decays of chargino and neutralino dominate. For larger values of $m_{\tilde{\chi}_1^\pm}$ and $m_{\tilde{\chi}_2^0}$ the decays into real W and Z bosons are dominating. The line $m_{\tilde{\chi}_2^0} \approx m_{\tilde{\ell}}$ separates the region of 2-body decays via sleptons at small m_0 from the 3-body decay region at large m_0 . For the parameter

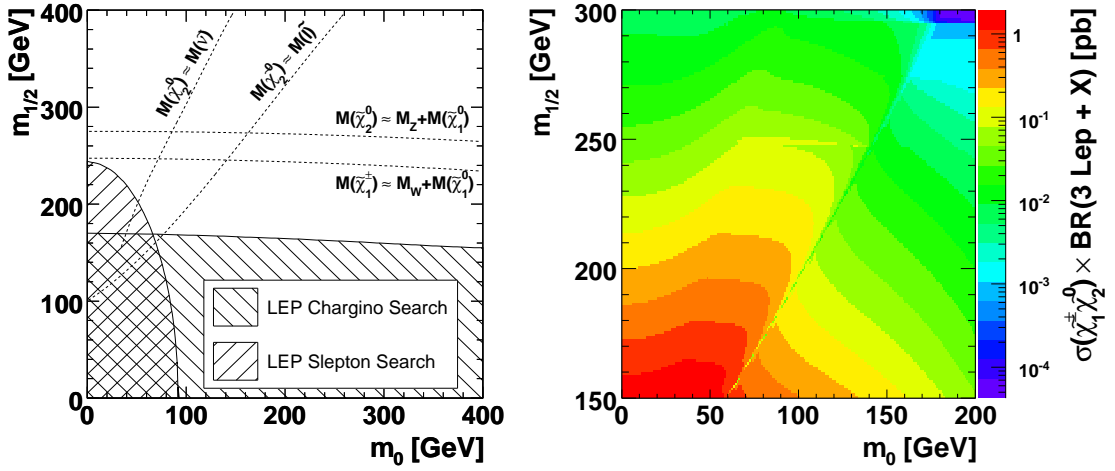


Figure 8.5: *Left:* Regions of changing kinematics in the decays of the lightest chargino and the second lightest neutralino in the mSUGRA model for $\tan\beta = 3$, $A_0 = 0$ and $\mu > 0$. The limits $m_{\tilde{e}} > 99.9$ GeV and $m_{\tilde{\chi}_1^\pm} > 103.5$ GeV from the LEP experiments are indicated [54, 55]. *Right:* The trilepton cross section in the $(m_0, m_{1/2})$ -plane for $\tan\beta = 3$, $A_0 = 0$ and $\mu > 0$.

space where $m_{\tilde{\nu}} < m_{\tilde{\chi}_2^0}$, the decay into real sneutrinos is possible. In the 2-body decay region of the considered mSUGRA scenario, the decay into staus is favored since the high wino field content of the lightest chargino and second lightest neutralino leads to a helicity suppressed decay into selectrons and smuons.

Figure 8.5 (right) shows the *trilepton cross section* $\sigma(\tilde{\chi}_1^+ \tilde{\chi}_2^0) \times \text{BR}(3 \text{ Leptons} + X)$ in the $(m_0, m_{1/2})$ -plane, in the region where sensitivity of the presented trilepton search is expected. Its shape is determined by the decreasing production cross section $\sigma(\tilde{\chi}_1^+ \tilde{\chi}_2^0)$ with increasing gaugino masses towards larger $m_{1/2}$ and the changing branching ratio into three leptons. The cross sections and SUSY spectra are determined as explained in Sec. C.

The kinematics of the cascade decays of chargino and neutralino result from the mass differences of the particles involved. The region of 3-body decays (the sleptons are heavier than the gauginos) and 2-body decays (the sleptons are significantly lighter than the gauginos) result in similar spectra of the lepton transverse momenta. For these scenarios all three momenta are large enough for efficient reconstruction in the detector. In the transition region where the sleptons are only slightly lighter than the neutralino, the available phase space for the lepton from the decay of the neutralino is reduced. The resulting softness the lepton momentum leads to a decrease of the reconstruction efficiency.

The $\mu\tau_h\ell$ – Signature

The analysis discussed in the following sections reconstructs the signature of the three leptons in the final state consisting of a muon, a hadronically decaying tau and a third charged lepton of any generation ($\mu\tau_h\ell$). This analysis includes the final state consisting of three taus if one of them decays leptonically into a muon and another one hadronically.

Consequently, the analysis is expected to be sensitive for scenarios with large $\tan\beta$, where

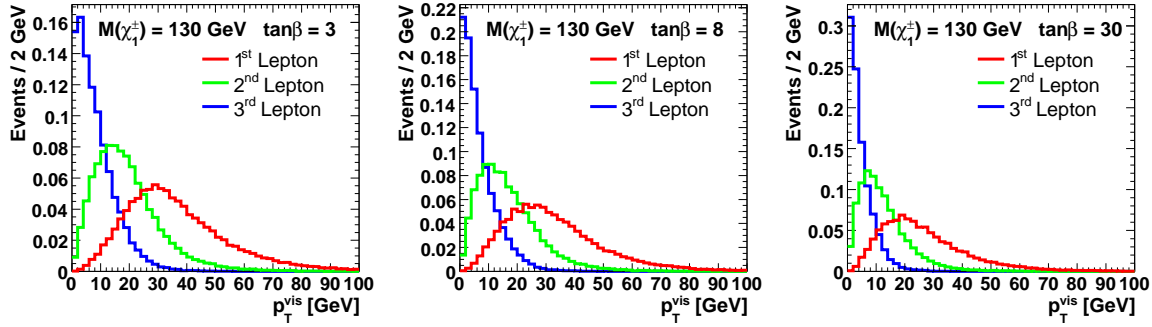


Figure 8.6: Generator level distribution of the transverse momentum of the three leptons for typical SUSY points considered in the analysis ($A_0 = 0$, $\mu > 0$ and $m_\Delta = m_{\tilde{\tau}_1} - m_{\tilde{\chi}_2^0} = 1$ GeV). In case of taus the visible transverse momentum is shown.

the stau mixing results in a lower stau mass compared to selectrons and smuons, and in the 2-body decay region, where the decay to staus is dominating as well.

Tau leptons need to be detected by their visible decay products, while the resulting neutrinos escape detection. This leads to a significant lower visible transverse momentum for tau leptons and requires a high efficiency of the reconstruction at low transverse momenta. Therefore, one of the challenges of the analysis is the extreme softness of the lepton p_T spectra in the final state as shown in Fig. 8.6.

These considerations lead to the following regions in the SUSY parameter space where sensitivity is expected:

- Low chargino and neutralino masses \Rightarrow large production cross section;
- Low slepton masses \Rightarrow large branching ratio of chargino and neutralino into leptons;
- Moderate values of $\tan\beta$ \Rightarrow increased branching ratio into taus but still sufficiently hard lepton p_T spectra for an efficient identification.

8.1.4 Background from Standard Model Processes

Since the final state under consideration consists of three charged leptons and missing transverse energy, most Standard Model processes can be suppressed efficiently. However, there are several processes that can lead to a similar signature in the detector, due to misidentification of the leptons and/or mismeasurement of \cancel{E}_T . In particular, the identification of hadronically decaying taus is affected by background processes resulting in jets. The relevant background processes are discussed in the following. The corresponding cross sections and the leading order Feynman diagrams are given in Sec. 5.2.

- Di-boson: WW , WZ , ZZ

The most important irreducible background process is the WZ production with subsequent decays to three charged leptons and a neutrino, which results in missing transverse energy. The ZZ process can lead to the second irreducible final state if the two Z bosons

decay into pairs of charged leptons and one pair consists of taus. Since the production cross section for ZZ is significantly smaller than the one for WZ , its contribution is not critical. The WW process contributes to the background if both W bosons decay leptonically and an additional photon or jet is misidentified as third lepton.

- $Z/\gamma^*(+\text{jets}) \rightarrow \ell\ell(+\text{jets})$

The process $Z/\gamma^* \rightarrow \tau\tau$ can result in a muon, a hadronically decaying tau and missing transverse energy. If an additional jet or photon is radiated, it contributes to the background. The muon decay channel, $Z/\gamma^* \rightarrow \mu\mu$, is of relevance as well and can be misinterpreted in two ways. On the one hand, a muon can fake the hadronically decaying tau. This rate is small but in combination with the large Z/γ^* production cross section it becomes important. On the other hand, a muon can be identified as the third lepton and an additional photon or jet results in the hadronically decaying tau. The background from the decay to electron pairs, $Z/\gamma^* \rightarrow ee$, is negligible.

- $W^\pm(+\text{jets}) \rightarrow \ell^\pm\nu_\ell + (\text{jets})$

If additional jets are radiated, the W boson production with subsequent decay into a muon and a neutrino, $W^\pm + \text{jets} \rightarrow \mu^\pm\nu_\mu + \text{jets}$, constitutes the background which is the most challenging to suppress. It has a large cross section, leads to a significant amount of missing transverse energy and jets can be misinterpreted as hadronically decaying taus. The decay into a tau and a neutrino, $W^\pm + \text{jets} \rightarrow \tau^\pm\nu_\tau + \text{jets}$, has to be considered as well but it is less crucial. The fraction of events where the tau decays to a muon contributes dominantly to the background. The case where the tau is identified as hadronically decaying tau is suppressed since the rate for the misinterpretation of a radiated soft jet as a muon is relatively small.

- $t\bar{t}$ production

The pair production of top quarks leads to final states with two leptons, two b-jets and missing transverse energy where one of the jets can be misinterpreted as a third lepton. This background is less critical since it can be suppressed efficiently by exploiting the presence of high- p_T jets and the product of production cross section and relevant branching ratio is small.

- Multi-jet

Even if no isolated lepton occurs, the production of jets in QCD processes has to be taken into account since its cross section is several orders of magnitude larger than the expected signal cross section, as illustrated in Fig. 2.1. Jets can be misidentified as leptons and as hadronically decaying taus in particular. Missing transverse energy often results from the mismeasurement of the energy of a jet.

8.2 Signal Monte Carlo Samples

Signal Monte Carlo samples are used for the optimization of the selection and for the determination of the signal efficiency. They are generated for a large set of combinations of SUSY parameters, so-called *SUSY points* (see Sec. C). The SUSY points of Tab. 8.1 represent only a subset of all SUSY points which are used as reference points during the development of the selection. In order to cover the range from minimal to maximal stau mixing, they are chosen from the 3-body decay region with a large branching ratio into leptons where

$\tan\beta$	m_0	$m_{1/2}$	$m_{\tilde{\chi}_1^\pm}$	$m_{\tilde{\chi}_2^0}$	$m_{\tilde{\chi}_1^0}$	$m_{\tilde{\mu}_R}$	$m_{\tilde{\tau}_1}$	$\sigma \times \text{BR}$
3	104	198	130.0	132.6	71.8	134.7	133.6	0.108
6	105	195	130.0	131.8	72.0	136.1	132.8	0.103
8	107	193	130.0	131.5	71.9	137.7	132.5	0.108
10	120	192	130.0	131.3	71.9	139.9	132.2	0.117
15	120	190	130.0	131.0	71.8	147.3	132.1	0.143
20	131	189	130.0	130.8	71.6	156.2	131.8	0.168
30	157	188	130.0	130.7	71.5	178.3	131.7	0.205

Table 8.1: Parameters and masses of the reference SUSY points. All have $A_0 = 0$, positive μ and $m_\Delta = m_{\tilde{\tau}_1} - m_{\tilde{\chi}_2^0} = 1$ GeV. All masses are given in units of GeV while the trilepton cross section $\sigma \times \text{BR}$ is given in units of pb.

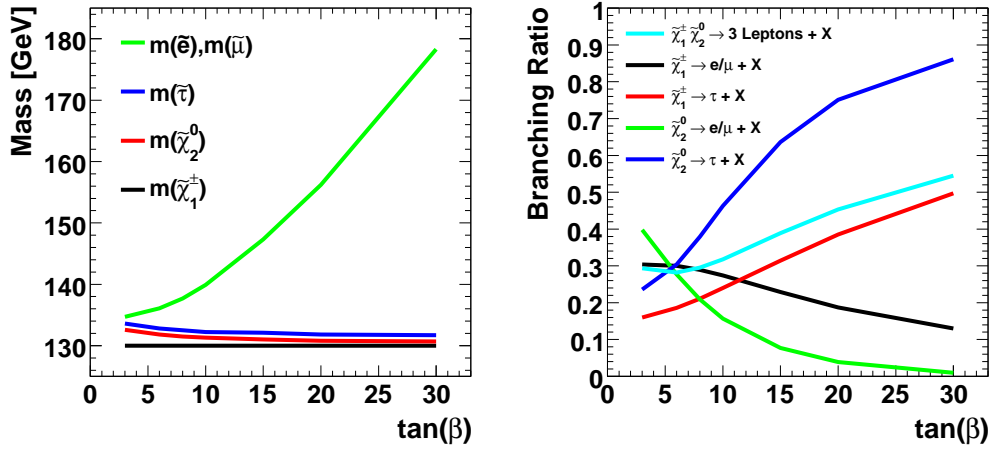


Figure 8.7: Masses of the relevant SUSY particles (left) and branching ratio of chargino and neutralino into leptons (right) as function of $\tan\beta$ for the SUSY points given in Tab. 8.1.

$m_{\tilde{e}_R, \tilde{\mu}_R} > m_{\tilde{\tau}_1} > m_{\tilde{\chi}_2^0}$, as illustrated in Fig. 8.7. In order to ensure that the branching ratio into the three different lepton flavors is the only varied property, the mass of the lightest chargino is fixed for these reference points. The value of $m_{\tilde{\chi}_1^\pm} = 130$ GeV is chosen since sensitivity is expected in this region. The selected SUSY points comply with the LEP limits from direct sparticle searches where especially the lower limit on the masses of the sleptons, the lightest chargino and $\tan\beta$ are important.

For the generation of the signal samples, the Monte Carlo generator PYTHIA is used in combination with the CTEQ6L1 parton distribution functions [66], while SUSY spectra, branching ratios and cross sections are calculated using the software given in Sec. C.

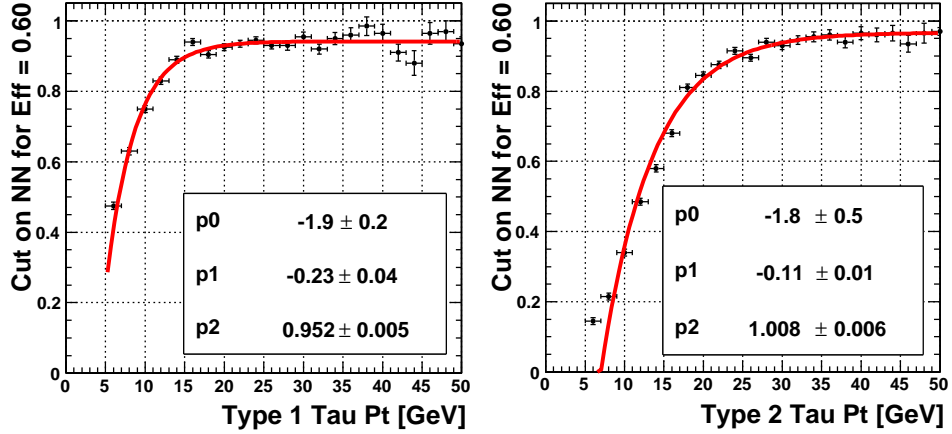


Figure 8.8: The cut values on the neural network output NN_τ as a function of p_T^τ for a fixed efficiency of 60% (points) for τ -type 1 (left) and τ -type 2 (right). They are parameterized using a fit by an exponential (line): $NN_\tau^{\text{cut}}(p_T^\tau) = p_0 e^{p_1 p_T^\tau} + p_2$.

8.3 Tau Identification

The tau identification criteria developed for the Higgs analysis (see Sec. 6.4) are adopted to account for the soft tau transverse momenta expected in the trilepton signal.

The main difference is a modification of the cut on the neural network output NN_τ . Since the efficiency for a given cut shows a strong dependence on p_T^τ , the cut on NN_τ is applied as a function of p_T^τ for an efficiency of 60 %, as illustrated in Fig. 8.8¹. In order to avoid applying too tight selection criteria, which would unnecessarily reduce the selection efficiency no tighter cut than $NN_\tau > 0.9$ is imposed. To ensure a minimal background suppression, no looser cut than $NN_\tau > 0.25$ is used.

The tau candidates have to pass the muon veto criteria described in Sec. 6.4.2 with a tighter cut on the energy fraction deposited in the CH calorimeter $CHF < 0.4$. Only 1-prong tau decays are considered by rejecting τ -type 3 candidates. It is found that the sensitivity of the selection for 3-prong tau decays is too small to contribute to the result due to the large jet background from $W^\pm + \text{jets} \rightarrow \mu^\pm \nu_\mu + \text{jets}$ and multi-jet events, which can not be suppressed efficiently.

8.4 Background Sample for Multi-Jet Events

The background from multi-jet events is determined from data by inverting the calorimeter isolated criteria for the selected muon as described in Sec. 6.3. Since the SUSY signal is expected at low lepton momenta, the contribution from this background is larger compared to the Higgs analysis and a more detailed study is required, as discussed in Sec. B.

¹Within the scope of the present analysis, an attempt has been made to reduce the p_T^τ -dependence and to improve the performance of the neural network at small p_T^τ by retraining the neural network separately for different p_T^τ . The retraining successfully removed the dependence on p_T^τ but could not improve the performance in terms of efficiency and background rejection. This implies that by choosing the working point of the original neural network as a function of p_T^τ , the same performance could be achieved for the retrained and original neural network.

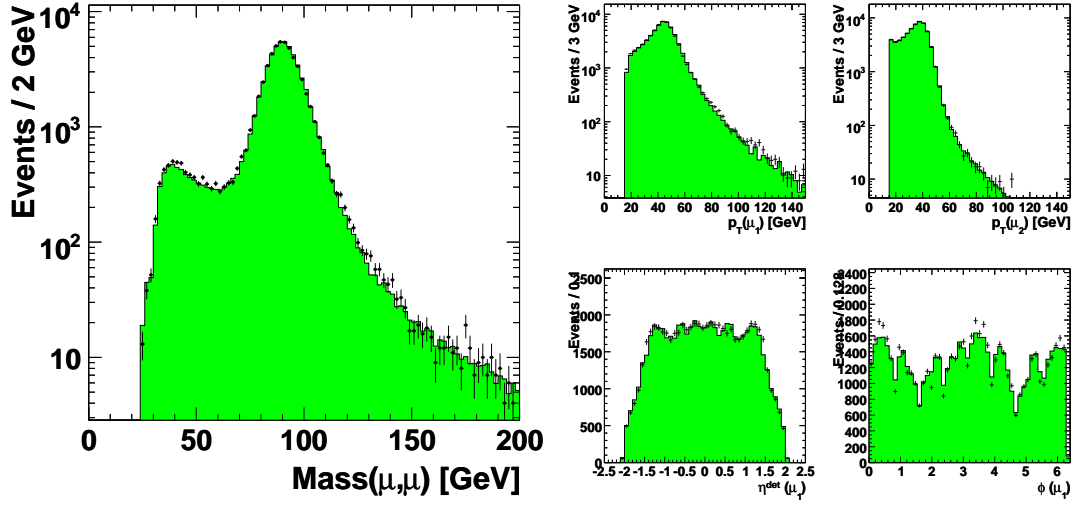


Figure 8.9: Distribution of the invariant di-muon mass, p_T of the leading and next-to-leading muon, η_{det} and ϕ of the leading muon in Monte Carlo (filled histogram) and data (dots).

8.5 Reference Signals

Since the selection of the SUSY signal relies on an accurate efficiency estimation from the simulation of the reconstruction and identification of muon and tau leptons, reference signals are selected. The reference signals $Z/\gamma^* \rightarrow \mu\mu$ and $Z/\gamma^* \rightarrow \tau\tau$ serve as a cross check of the various corrections that are applied to Monte Carlo events. The selection of $W^\pm \rightarrow \mu^\pm\nu_\mu$ signal allows to verify the simulation of the misidentification of jets as tau leptons.

8.5.1 $Z/\gamma^* \rightarrow \mu\mu$

The spectrum of the di-muon invariant mass of Fig. 8.9 is reconstructed by selecting events containing two isolated opposite sign muons with $p_T > 15$ GeV. The distribution shows good agreement concerning the identification of muons and their p_T resolution in data and simulation.

8.5.2 $Z/\gamma^* \rightarrow \tau\tau$

The spectrum of the mu-tau invariant mass of Fig. 8.10 is selected by requiring an isolated muon with $p_T^\mu > 15$ GeV, a hadronically decaying tau satisfying the criteria given in Sec. 8.3 and imposing the following requirements:

- The threshold on the reconstructed transverse momentum of the tau is raised to $p_T^\tau > 16$ GeV in order to suppress background from multi-jet events.
- Since $Z/\gamma^* \rightarrow \tau\tau$ decays result in a back-to-back topology, the signal-to-background ratio can be increased by requiring $\Delta\phi(\mu, \tau) > 2.5$.

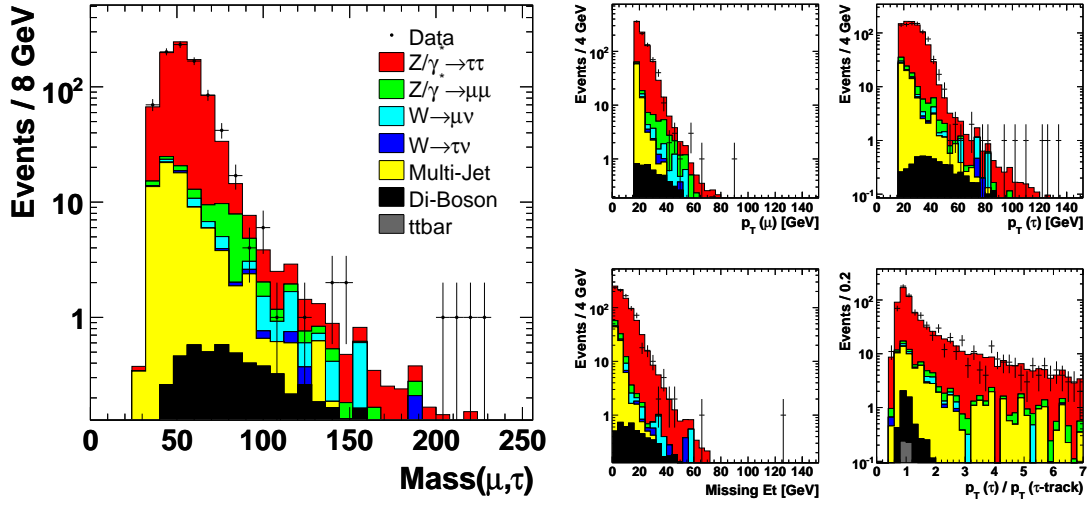


Figure 8.10: Distribution of invariant mu–tau mass, p_T^μ , p_T^τ , E_T and $p_T^\tau/p_T^{\tau\text{-track}}$ in data and the various Standard Model contributions in a selection optimized for $Z/\gamma^* \rightarrow \tau\tau$ decays.

- Background contributions from $W^\pm \rightarrow \mu^\pm \nu_\mu$ decays where an additional jet is misidentified as tau are suppressed by $m_T^\mu < 15$ GeV, where m_T^μ represents the transverse mass calculated from p_T^μ and E_T according to Eq. 6.2.
- Muon and tau have opposite charge assigned.

In the described $Z/\gamma^* \rightarrow \tau\tau$ selection the luminosity of the data set used in the SUSY analysis is determined. Since the cross section of all simulated Standard Model processes is known, the normalization factor which scales the integral of all Monte Carlo distributions to data is used to determine the integrated luminosity. In order to reduce further background contributions, the integral is only calculated in the mass region $40 < M(\mu, \tau) < 90$ GeV. The obtained integrated luminosity amounts to (944 ± 59) pb $^{-1}$. The uncertainty on the luminosity is given by the quadratic sum of the statistical uncertainty of the calculation and the uncertainty on the $Z/\gamma^* \rightarrow \tau\tau$ cross section, which includes the uncertainties related to PDFs.

After the normalization, data and simulation show reasonable agreement. The distribution of $p_T^\tau/p_T^{\tau\text{-track}}$ demonstrates the good agreement of the tau energy measurement in the calorimeter in data and simulation. The DØ collaboration has used a similar selection of $Z/\gamma^* \rightarrow \tau\tau$ decays in order to measure the $Z/\gamma^* \rightarrow \tau\tau$ cross section in the $\mu\tau_h$ final state [126].

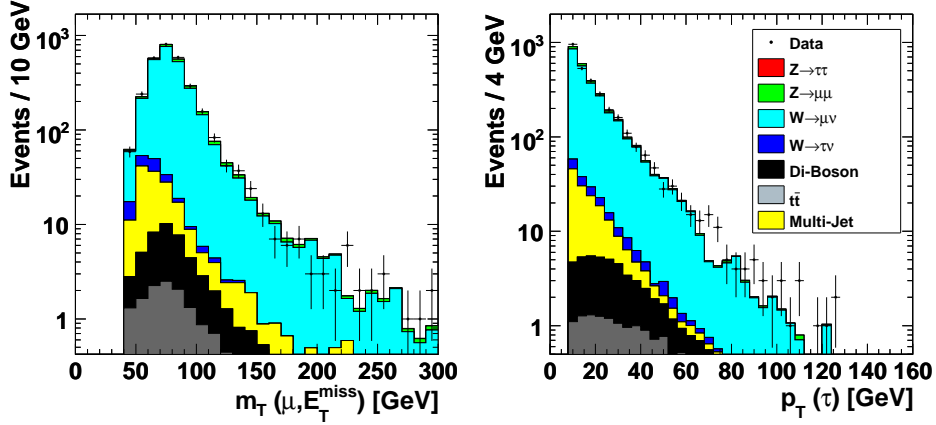


Figure 8.11: Distribution of the transverse mass m_T^μ and the tau transverse momentum p_T^τ in data and the various Standard Model contributions in a selection optimized for $W^\pm \rightarrow \mu^\pm \nu_\mu$ decays.

8.5.3 $W^\pm + \text{jets} \rightarrow \mu^\pm \nu_\mu + \text{jets}$

The mass of the W boson in $W^\pm \rightarrow \mu^\pm \nu_\mu$ decays can be approximated in the transverse plane by calculating the transverse mass m_T^μ from p_T^μ and \cancel{E}_T as defined in Eq. (6.2). By applying the following selection criteria, a data sample dominated by $W + \text{jets}$ is selected where the jet is misidentified as hadronically decaying tau:

- An isolated muon ($p_T^\mu > 15$ GeV) is required according to the criteria given in Sec. 4.3.
- A tau candidate satisfying the selection criteria given in Sec. 8.3 is selected. In order to suppress $Z/\gamma^* \rightarrow \tau\tau$ and possible signal contributions, the NN_τ criterion is inverted: $NN_\tau < NN_\tau^{\text{cut}}(p_T^\tau)$.
- The criterion $\cancel{E}_T > 20$ GeV removes multi-jet contributions.
- Only one muon is reconstructed in the event in order to remove $Z/\gamma^* \rightarrow \mu\mu$ events.
- The transverse mass m_T^μ is required to be larger than 40 GeV.

Comparing the kinematics of the selected events in data to the prediction of the simulation allows to verify the simulation of the misidentification of jets as tau leptons, e.g. shown in Fig. 8.11 for the transverse mass and for the tau transverse momentum. Further details and comparisons of data and simulation concerning the simulation of the lepton misidentification have been studied within the scope of the present thesis and are documented in [145].

8.6 Trilepton Selection

The following section describes the selection criteria developed to efficiently separate the SUSY signal from Standard Model background processes.

8.6.1 Overview

The starting point of the $\mu\tau_h\ell$ selection is the requirement of an isolated muon ($p_T > 15$ GeV) and a hadronically decaying tau ($p_T > 8$ GeV) identified by the criteria given in Sec. 4.3 and 8.3, respectively. This stage of the selection is referred to as *preselection*. In order to maximize the efficiency of the selection, the third lepton, which is for most of the SUSY parameter space the softest lepton, is identified using three different reconstruction algorithms: isolated track, hadronically decaying tau and low energetic hadronically decaying tau. The presence of neutrinos and LSPs in the final state is exploited for further background suppression.

This leads to the following structure of the selection: First a set of six common selection criteria is imposed (Tab. 8.2, Criteria 0-6) that use only the muon, the leading hadronically decaying tau (τ_1) and \cancel{E}_T . Afterwards, the selection is separated into three subselections which use different approaches for the identification of the third lepton. Before discussing the selection in detail in the following sections, an overview is given.

- $\mu + \tau_1 + \text{track}$

The *track selection* (Tab. 8.2, Criteria 7-13) relies on an isolated track ($p_T > 3$ GeV) for the reconstruction of the third lepton.

The characteristic signature of all charged leptons is a track reconstructed in the central tracker. The advantage of using a track instead of using electron, muon and tau identification criteria is the avoidance of inefficiencies that occur in the object identification of the specific leptons. It allows a high identification efficiency for electrons, muons and taus to low transverse momenta of about 3 GeV. Isolation criteria are used to suppress jet backgrounds. The efficiency of the isolation criteria drops for taus with decreasing p_T^τ due to the increasing spread of their decay products, as discussed in Sec. 7.1. Although 3-prong tau decays have been taken into consideration during the development of the isolation criteria, the selection is only efficient for 3-prong tau decays with a large $p_T^{\tau,\text{vis}}$ where the tau decay products are inside the inner radii of the hollow cones considered for the isolation criteria.

- $\mu + \tau_1 + \tau_2$

The *tau selection* (Tab. 8.2, Criteria 14-20) identifies the third lepton as a hadronically decaying tau ($p_T > 4$ GeV). The tau is required to pass the identification criteria described in Sec. 8.3. It is referred to as τ_2 .

Obviously, this selection is expected to increase the sensitivity in regions of the SUSY parameter space with a large branching ratio into tau leptons. The disadvantage of this approach compared to the isolated track is a decreased efficiency caused by the reconstruction algorithm of taus and the cut on the neural network output, which is needed to suppress background events containing jets.

- $\mu + \tau_1 + \tau_{LP}$

The *low- p_T tau selection* (Tab. 8.2, Criteria 21-25) uses the reconstruction algorithm for low energetic hadronically decaying tau leptons as described in Sec. 7. The low energetic tau has to pass the threshold of $p_T > 3$ GeV and is referred to as τ_{LP} .

The advantage of this selection is the high efficiency for tau leptons with a visible transverse momentum down to $p_T^\tau \gtrsim 3$ GeV. It is expected to increase the sensitivity of the analysis in SUSY parameter regions with a large branching ratio into tau leptons with small transverse momenta. The challenge is the efficient suppression of the background from jets in $W^\pm + \text{jets} \rightarrow \mu^\pm \nu_\mu + \text{jets}$ and multi-jet events, which is expected to be significantly larger than in case of the other two selections.

In order to remove the overlap between the three selections, events which pass all selection criteria of the $\mu + \tau_1 + \text{track}$ selection are not considered in the $\mu + \tau_1 + \tau_2$ and $\mu + \tau_1 + \tau_{LP}$ selection. Furthermore, events that pass all criteria of the $\mu + \tau_1 + \tau_2$ selection do not enter the $\mu + \tau_1 + \tau_{LP}$ selection. In other words, only events that are rejected by the criteria 7-13, enter the selection at stage 14. Respectively, only events that are removed by criteria 7-20 are considered at stage 21. The overlap is treated in this way since it is found that the signal-to-background ratio decreases from the $\mu + \tau_1 + \text{track}$ to $\mu + \tau_1 + \tau_2$ to $\mu + \tau_1 + \tau_{LP}$ selection.

The optimization of the selection is performed for a SUSY point with $\tan\beta = 8$ and $m_{\tilde{\chi}_1^\pm} = 130$ GeV (see Tab. 8.1). The maximal sensitivity in a combination with further trilepton searches is expected in this parameter region.

Table 8.3 summarizes the number of events observed in data after each step of the selection, including the expectation for the Standard Model background processes. The number of expected signal events and the signal efficiency are listed in Tab. 8.4.

In order to reduce the statistical uncertainty on the Standard Model background expectation which is caused by the limited statistics of the Standard Model Monte Carlo samples, the background after the last two criteria of each selection is determined in a loose selection. This means that preceding selection criteria are relaxed in order to increase the statistics of the Monte Carlo samples. Instead of imposing the criteria, their rejection is determined and applied in form of a scaling factor. It is important to ensure that the relaxed criteria are chosen in such a way that the correlation with the last selection stages is small. Therefore, the relaxed and the tight selections are compared at earlier stages of the selection where both sample have sufficiently large statistic. The relaxed criteria are the cut on the neural network output of the tau identification NN_τ , the track isolation criteria and the cut on the likelihood used for the identification of the low energetic tau LH_τ . This method is used for the $W^\pm \rightarrow \mu^\pm \nu_\mu$, $W^\pm \rightarrow \tau^\pm \nu_\tau$ and multi-jet samples. The uncertainty introduced by this procedure is taken into account as a systematic uncertainty.

In the distributions shown in this section (Fig. 8.12-8.24) that present comparisons of data and simulation, the signal of the reference SUSY point with $\tan\beta = 8$ is illustrated by an open histogram in an arbitrary normalization.

Summary of the Selection Criteria		
Common Criteria		
Preselection	0	Isolated muon $p_T > 15$ GeV Tau $p_T^{\tau_1} > 8$ GeV, p_T dependent cut on NN_τ
Criteria involving \cancel{E}_T	1	$\cancel{E}_T > 20$ GeV
	2	$\text{Sig}(\cancel{E}_T) > 8 \sqrt{\text{GeV}}$
	3	$m_T^\mu > 20$ GeV
	4	$m_T^\tau > 8$ GeV
Anti Z/γ^*	5	$\Delta\phi(\mu, \tau) < 2.9$
Anti $t\bar{t}$	6	$H_T < 80$ GeV
Track Selection $\mu + \tau_1 + \text{track}$		
Track Selection	7	Isolated quality track $p_T^{\text{track}} > 3$ GeV
Anti Z/γ^* and WZ	8	$M(\mu, \text{track}) < 60$ GeV
	9	$M(\tau_1, \text{track}) < 60$ GeV
	10	$M(\mu, \tau_1) < 60$ GeV
	11	$\Delta\phi(\text{track}, \cancel{E}_T) > 0.5$
Anti $W^\pm + \text{jets} \rightarrow \mu^\pm \nu_\mu + \text{jets}$ and multi-jet	12	$\text{LH}_W^{\text{track}} > 0.4$
	13	$p_T^{\text{track}} \times \cancel{E}_T > 300$ GeV ²
Tau Selection $\mu + \tau_1 + \tau_2$		
Second Tau selection	14	Second Tau $p_T^{\tau_2} > 4$ GeV, p_T dependent cut on NN_τ
Anti Z/γ^* and WZ	15	$M(\tau_1, \tau_2) < 60$ GeV
	16	$M(\mu, \tau_2\text{-track}) < 60$ GeV
	17	$\Delta\phi(\tau_2, \cancel{E}_T) > 0.5$
	18	$p_T\text{-Balance} = p_T(\mu + \tau_1 + \cancel{E}_T)/p_T^{\tau_2} < 3.5$
Anti $W^\pm + \text{jets} \rightarrow \mu^\pm \nu_\mu + \text{jets}$ and multi-jet	19	$\text{LH}_W^{\tau_2} > 0.2$
	20	$NN_\tau(\tau_1) \times NN_\tau(\tau_2) > 0.7$
Low- p_T Tau Selection $\mu + \tau_1 + \tau_{LP}$		
Low- p_T tau selection	21	Low- p_T tau $p_T^{\tau_{LP}} > 3$ GeV, $\text{LH}_\tau > 0.95$
Anti Z/γ^* and WZ	22	$M(\mu, \tau_{LP}\text{-track}) < 60$ GeV
	23	$M(\tau_1, \tau_{LP}) < 60$ GeV
	24	$\text{LH}_W^{\tau_{LP}} > 0.7$
Anti $W^\pm + \text{jets} \rightarrow \mu^\pm \nu_\mu + \text{jets}$ and multi-jet	25	$p_T^{\tau_{LP}} \times \cancel{E}_T > 300$ GeV ²

Table 8.2: Summary of the selection criteria. First the ‘‘Common Criteria’’ (criteria 0-6), are applied. Afterwards, the selection splits up into the three subselections: ‘‘Track Selection’’ (criteria 7-13), ‘‘Tau Selection’’ (criteria 14-20) and ‘‘Low- p_T Tau Selection’’ (criteria 21-25).

Cut	Data	Sum	$Z/\gamma^* \rightarrow \tau\tau$	$Z/\gamma^* \rightarrow \mu\mu$	$W^\pm \rightarrow \mu^\pm\nu_\mu$	$W^\pm \rightarrow \tau^\pm\nu_\tau$	Di-boson	$t\bar{t}$	Multi-jet
Common Criteria									
0	6251	6237.8± 19.8	2424.40± 5.01	669.62± 8.27	1249.4± 16.9	104.91± 3.66	122.23± 0.65	45.77± 0.39	1621.5 ±23.4
1	2066	2094.4± 16.2	415.09± 2.06	202.43± 2.49	1077.3± 15.7	61.79± 2.80	99.65± 0.59	42.60± 0.38	195.54±5.80
2	1704	1763.3± 15.7	242.60± 1.55	175.35± 2.13	1022.2± 15.2	55.43± 2.66	90.17± 0.56	23.49± 0.28	154.08±5.45
3	1620	1688.4± 15.7	177.66± 1.36	174.12± 2.13	1020.4± 15.2	54.16± 2.64	86.82± 0.55	22.23± 0.27	152.97±5.45
4	1279	1224.4± 14.6	22.86± 0.50	94.39± 1.60	892.4± 14.2	50.24± 2.53	82.66± 0.53	21.23± 0.27	60.68±3.34
5	1225	1172.7± 14.3	13.48± 0.37	88.08± 1.54	867.9± 14.0	49.44± 2.51	78.03± 0.52	18.79± 0.25	56.95±3.34
6	1180	1153.9± 14.3	12.28± 0.36	87.77± 1.54	866.3± 14.0	49.44± 2.51	76.37± 0.51	4.88± 0.13	56.81±3.35
Track Selection $\mu + \tau_1 + \text{track}$									
7	103	110.1± 5.1	1.66± 0.13	31.46± 0.96	61.7± 5.0	1.33± 0.42	7.84± 0.18	0.38± 0.04	5.75±1.02
8	83	75.9± 4.9	1.52± 0.13	4.13± 0.42	59.1± 4.9	1.33± 0.42	3.76± 0.12	0.30± 0.03	5.75±1.02
9	82	75.2± 4.9	1.50± 0.13	4.10± 0.41	59.1± 4.9	1.33± 0.42	3.14± 0.11	0.30± 0.03	5.75±1.02
10	79	68.1± 4.6	1.35± 0.12	4.00± 0.41	53.6± 4.6	1.33± 0.42	2.04± 0.09	0.16± 0.02	5.62±1.03
11	67	52.8± 4.1	0.64± 0.08	2.11± 0.26	42.4± 4.0	1.33± 0.42	1.66± 0.08	0.13± 0.02	4.52±0.92
12	4	2.9± 0.4	0.06± 0.03	0.18± 0.10	2.0± 0.3	0.05± 0.03	0.51± 0.05	0.08± 0.02	0.03±0.02
13	0	0.8± 0.1	0.03± 0.03	0.03± 0.03	0.3± 0.1	0.02± 0.02	0.36± 0.04	0.05± 0.01	0.02±0.02
Tau Selection $\mu + \tau_1 + \tau_2$									
14	20	22.6± 2.6	0.45± 0.07	0.96± 0.16	17.2± 2.6	0.14± 0.14	2.75± 0.10	0.10± 0.02	1.00±0.45
15	18	19.7± 2.5	0.42± 0.07	0.96± 0.16	16.1± 2.5	0.14± 0.14	1.00± 0.06	0.08± 0.02	1.00±0.45
16	17	18.6± 2.4	0.40± 0.07	0.92± 0.16	15.1± 2.4	0.14± 0.14	0.92± 0.06	0.06± 0.01	1.00±0.45
17	14	14.6± 2.1	0.19± 0.05	0.74± 0.14	11.9± 2.1	0.14± 0.14	0.78± 0.05	0.04± 0.01	0.82±0.41
18	7	8.0± 1.5	0.12± 0.04	0.52± 0.12	6.4± 1.5	0.14± 0.14	0.49± 0.04	0.01± 0.01	0.35±0.25
19	3	1.8± 0.5	0.06± 0.03	0.17± 0.07	1.3± 0.4	0.02± 0.02	0.31± 0.03	0.01± 0.01	0.03±0.03
20	1	0.7± 0.2	0.04± 0.03	0.06± 0.04	0.3± 0.2	0.02± 0.02	0.25± 0.03	0.01± 0.01	0.03±0.03
Low-p_T Tau Selection $\mu + \tau_1 + \tau_{LP}$									
21	34	37.0± 2.4	0.65± 0.09	5.61± 0.48	24.7± 2.3	1.67± 0.48	3.01± 0.10	0.15± 0.02	1.23±0.48
22	33	34.8± 2.4	0.65± 0.09	3.77± 0.37	24.7± 2.3	1.67± 0.48	2.77± 0.10	0.15± 0.02	1.23±0.48
23	33	34.3± 2.4	0.61± 0.08	3.54± 0.36	24.7± 2.3	1.67± 0.48	2.49± 0.09	0.14± 0.02	1.11±0.43
24	2	2.1± 0.6	0.09± 0.04	0.58± 0.12	1.1± 0.5	0.06± 0.04	0.42± 0.04	0.05± 0.01	0.04±0.02
25	1	0.7± 0.2	0.09± 0.04	0.12± 0.07	0.3± 0.1	0.02± 0.02	0.17± 0.03	0.02± 0.01	0.03±0.03

Table 8.3: Number of events selected in data and number of events expected from Standard Model processes after each step of the selection. First the “Common Criteria” (criteria 0-6), are applied. Afterwards, the selection splits up into the three subselections: “Track Selection” (criteria 7-13), “Tau Selection” (criteria 14-20) and “Low- p_T Tau Selection” (criteria 21-25). The overlap between the three selections is subtracted. Only statistical uncertainties are given.

Number of expected signal events				
Cut	$\tan\beta = 3$	$\tan\beta = 8$	$\tan\beta = 15$	$\tan\beta = 30$
Common Criteria				
0	8.22± 0.11	6.11± 0.09	4.99± 0.08	4.04± 0.07
1	6.78± 0.10	4.87± 0.08	3.80± 0.07	2.90± 0.06
2	6.22± 0.10	4.42± 0.08	3.32± 0.06	2.55± 0.06
3	5.89± 0.10	4.16± 0.07	3.16± 0.06	2.42± 0.06
4	5.59± 0.10	3.91± 0.07	2.95± 0.06	2.28± 0.05
5	5.25± 0.09	3.67± 0.07	2.82± 0.06	2.17± 0.05
6	5.15± 0.09	3.58± 0.07	2.74± 0.06	2.11± 0.05
Track Selection $\mu + \tau_1 + \text{track}$				
7	3.25± 0.07	2.04± 0.05	1.18± 0.03	0.69± 0.03
8	2.94± 0.07	1.87± 0.05	1.11± 0.03	0.65± 0.03
9	2.82± 0.07	1.80± 0.05	1.08± 0.03	0.65± 0.03
10	2.41± 0.06	1.59± 0.05	0.95± 0.03	0.59± 0.03
11	2.11± 0.06	1.39± 0.04	0.82± 0.03	0.52± 0.02
12	1.59± 0.05	1.00± 0.04	0.49± 0.02	0.22± 0.01
13	1.25± 0.05	0.77± 0.03	0.35± 0.02	0.13± 0.01
Tau Selection $\mu + \tau_1 + \tau_2$				
14	1.01± 0.04	0.68± 0.03	0.40± 0.02	0.30± 0.02
15	1.00± 0.04	0.67± 0.03	0.40± 0.02	0.30± 0.02
16	0.94± 0.04	0.63± 0.03	0.38± 0.02	0.30± 0.02
17	0.84± 0.04	0.54± 0.03	0.33± 0.02	0.27± 0.02
18	0.74± 0.04	0.47± 0.02	0.27± 0.02	0.20± 0.01
19	0.67± 0.03	0.40± 0.02	0.22± 0.01	0.17± 0.01
20	0.61± 0.03	0.35± 0.02	0.17± 0.01	0.12± 0.01
Low-p_T Tau Selection $\mu + \tau_1 + \tau_{LP}$				
21	0.41± 0.03	0.31± 0.02	0.21± 0.02	0.20± 0.02
22	0.39± 0.03	0.31± 0.02	0.21± 0.02	0.20± 0.02
23	0.37± 0.03	0.29± 0.02	0.20± 0.02	0.20± 0.02
24	0.21± 0.02	0.13± 0.01	0.08± 0.01	0.06± 0.01
25	0.15± 0.02	0.10± 0.01	0.05± 0.01	0.04± 0.01

Signal efficiency [%]				
Cut	$\tan\beta = 3$	$\tan\beta = 8$	$\tan\beta = 15$	$\tan\beta = 30$
Common Criteria				
0	8.06± 0.14	5.99± 0.12	3.70± 0.10	2.09± 0.07
1	6.65± 0.13	4.78± 0.11	2.81± 0.09	1.50± 0.06
2	6.10± 0.12	4.34± 0.11	2.46± 0.08	1.32± 0.06
3	5.78± 0.12	4.08± 0.10	2.34± 0.08	1.25± 0.06
4	5.48± 0.12	3.83± 0.10	2.19± 0.08	1.18± 0.06
5	5.15± 0.11	3.60± 0.10	2.09± 0.08	1.12± 0.05
6	5.05± 0.11	3.51± 0.10	2.03± 0.08	1.09± 0.05
Track Selection $\mu + \tau_1 + \text{track}$				
7	3.19± 0.09	2.00± 0.07	0.88± 0.05	0.36± 0.03
8	2.88± 0.09	1.84± 0.07	0.82± 0.05	0.34± 0.03
9	2.77± 0.08	1.77± 0.07	0.80± 0.05	0.34± 0.03
10	2.36± 0.08	1.56± 0.06	0.70± 0.05	0.31± 0.03
11	2.07± 0.07	1.37± 0.06	0.61± 0.04	0.27± 0.03
12	1.56± 0.06	0.98± 0.05	0.36± 0.03	0.12± 0.02
13	1.23± 0.06	0.76± 0.05	0.26± 0.03	0.07± 0.01
Tau Selection $\mu + \tau_1 + \tau_2$				
14	0.99± 0.05	0.67± 0.04	0.30± 0.03	0.16± 0.02
15	0.98± 0.05	0.66± 0.04	0.30± 0.03	0.15± 0.02
16	0.93± 0.05	0.62± 0.04	0.28± 0.03	0.15± 0.02
17	0.82± 0.05	0.53± 0.04	0.25± 0.03	0.14± 0.02
18	0.73± 0.04	0.46± 0.04	0.20± 0.02	0.10± 0.02
19	0.65± 0.04	0.39± 0.03	0.17± 0.02	0.09± 0.02
20	0.60± 0.04	0.34± 0.03	0.12± 0.02	0.06± 0.01
Low-p_T Tau Selection $\mu + \tau_1 + \tau_{LP}$				
21	0.41± 0.03	0.31± 0.03	0.16± 0.02	0.10± 0.02
22	0.39± 0.03	0.30± 0.03	0.16± 0.02	0.10± 0.02
23	0.37± 0.03	0.29± 0.03	0.15± 0.02	0.10± 0.02
24	0.21± 0.02	0.13± 0.02	0.06± 0.01	0.03± 0.01
25	0.14± 0.02	0.10± 0.02	0.04± 0.01	0.02± 0.01

Table 8.4: Signal efficiency and number of the expected signal events after each step of the selection excluding overlap. Only statistical uncertainties are given. The parameter of the SUSY points are listed in Tab. 8.1.

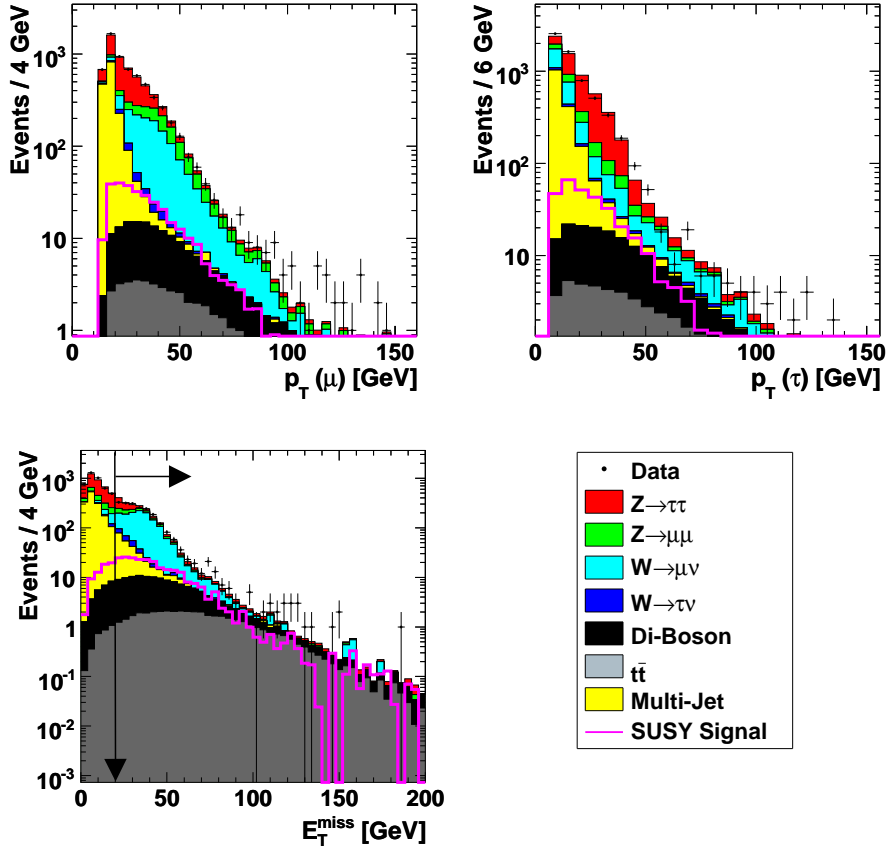


Figure 8.12: Distributions of p_T^μ , p_T^τ and \cancel{E}_T at the level of preselection. A cut is placed at $\cancel{E}_T > 20$ GeV.

8.6.2 Common Selection Criteria

At the level of preselection an isolated muon ($p_T^\mu > 15$ GeV) and a tau ($p_T^\tau > 8$ GeV) satisfying the criteria listed in Sec. 4.3 and 8.3 are required.

The first step to suppress the dominating background from multi-jet events is to require $\cancel{E}_T > 20$ GeV and $\text{Sig}(\cancel{E}_T) > 8 \sqrt{\text{GeV}}$ where $\text{Sig}(\cancel{E}_T)$ represents the significance of \cancel{E}_T . It can be determined by projecting the energy resolution of a given jet onto the direction of the missing transverse energy and performing the sum over all jets in an event:

$$\text{Sig}(\cancel{E}_T) = \frac{\cancel{E}_T}{\sqrt{\sum_{\text{Jets}} \sigma_{E_T(\text{jet})}^2 |E_T}}. \quad (8.1)$$

The two criteria exploit the presence of neutrinos and LSPs in the signal, while in multi-jet events \cancel{E}_T typically originates from a mismeasurement of the jet energy. Therefore, the amount of \cancel{E}_T in multi-jet events and its significance is small as shown in Fig. 8.12 (bottom) and 8.13, respectively. The two criteria remove 90 % of the multi-jet background while 72 % of the signal pass the criteria (for the SUSY point with $\tan\beta = 8$). Furthermore,

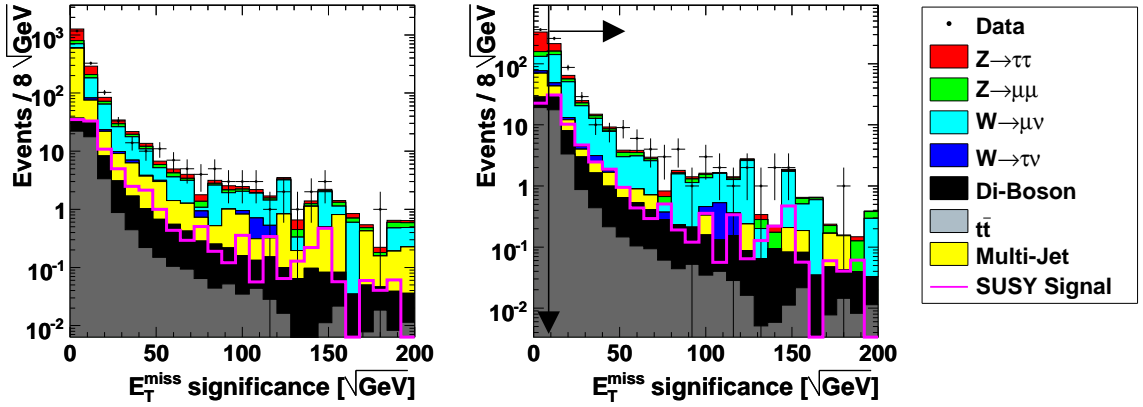


Figure 8.13: Distributions of $\text{Sig}(\cancel{E}_T)$ at the level of preselection (left) and before the cut $\text{Sig}(\cancel{E}_T) > 8 \sqrt{\text{GeV}}$ is applied (right).

these criteria suppress 70 % of the $Z/\gamma^* \rightarrow \mu\mu$ background where \cancel{E}_T arises usually from the mismeasurement of a muon.

Background events from $Z/\gamma^* \rightarrow \tau\tau$ decays which pass the previous criteria are characterized by a significant amount of missing transverse energy which points along the direction of either the muon or the tau, since the neutrinos tend to be collinear with the visible decay products of the taus. This leads to low values of transverse mass, defined in Eq. (6.2), either calculated from p_T^μ and \cancel{E}_T or from p_T^τ and \cancel{E}_T , as shown in Fig. 8.14. Cuts are placed at $m_T^\mu > 20 \text{ GeV}$ and $m_T^\tau > 8 \text{ GeV}$, which remove 91 % of the $Z/\gamma^* \rightarrow \tau\tau$ events, while 88 % of the signal passes the criterion. Additionally, these criteria suppress events where \cancel{E}_T points into the direction of one of the leptons due to a mismeasurement of their energy. This is visible in particular for the multi-jet background in the distribution of m_T^τ of Fig. 8.14 (bottom right).

Before addressing the background from the $W^\pm \rightarrow \mu^\pm \nu_\mu$ process, which is the dominating background process after applying all criteria described above, two further selection steps are discussed. The two selection steps are a cut on the angle in the transverse plane between muon and tau $\Delta\phi(\mu, \tau_1)$, shown in Fig. 8.15 (top), and a cut on the scalar sum of the p_T of all jets in the event, excluding tau jets

$$H_T = \sum_{\text{Jets}} p_T^{\text{Jet}}, \quad (8.2)$$

shown in Fig. 8.15 (bottom). The first criterion ($\Delta\phi(\mu, \tau_1) < 2.9$) exploits the back-to-back topology of $Z/\gamma^* \rightarrow \ell\ell$ decays. The second criterion ($H_T < 80 \text{ GeV}$) uses the high jet activity arising from $t\bar{t}$ production and removes 75 % of the remaining background from $t\bar{t}$ production, while it keeps 98 % of the signal. It is important to notice that these two criteria do not address the main background at the current stage of the selection. But at later selection stages where the sum of all backgrounds is at the order of one event, they significantly improve the signal-to-background ratio.

At this point, the selection splits up into the three subselections: Track Selection, Tau Selection and Low- p_T Tau Selection. Since the three selections are similar, the most detailed

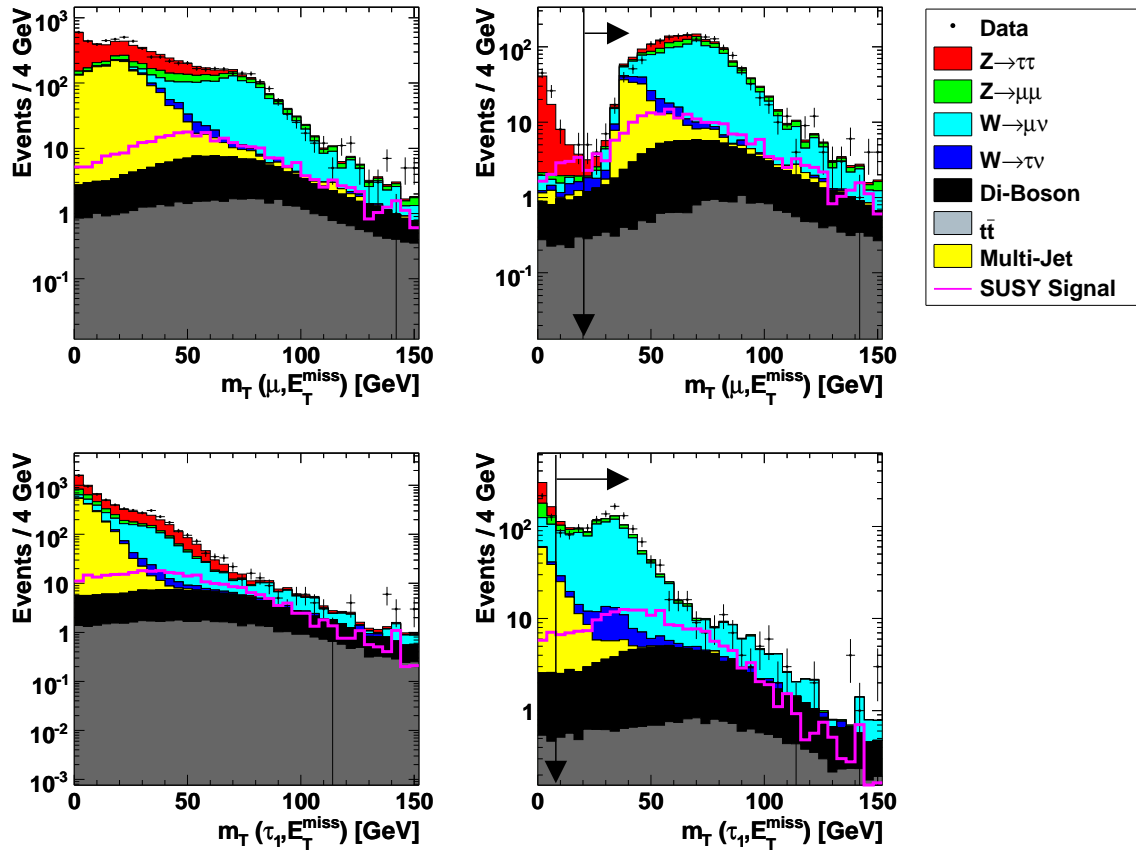


Figure 8.14: Distributions of m_T^μ and $m_T^{\tau_1}$ at the level of preselection (left) and before the cut on the quantity itself is applied (right). Cuts are placed at $m_T^\mu > 20$ GeV and $m_T^{\tau_1} > 8$ GeV.

discussion follows for the Track Selection, while the discussion of the Tau Selection and the Low- p_T Tau Selection is brief.

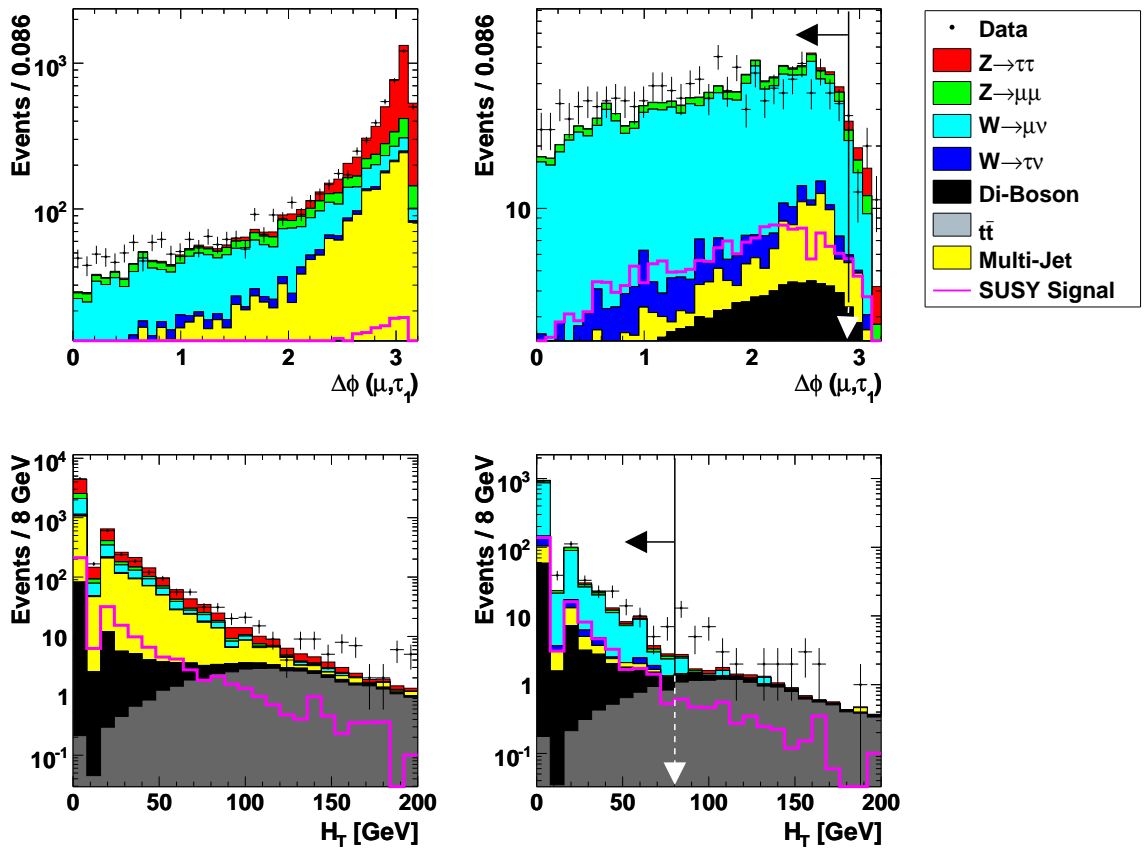


Figure 8.15: Distributions of $\Delta\phi(\mu, \tau_1)$ and H_T at the level of preselection (left) and before the cut on the quantity itself is applied (right). Cuts are placed at $\Delta\phi(\mu, \tau_1) < 2.9$ and $H_T < 80$ GeV.

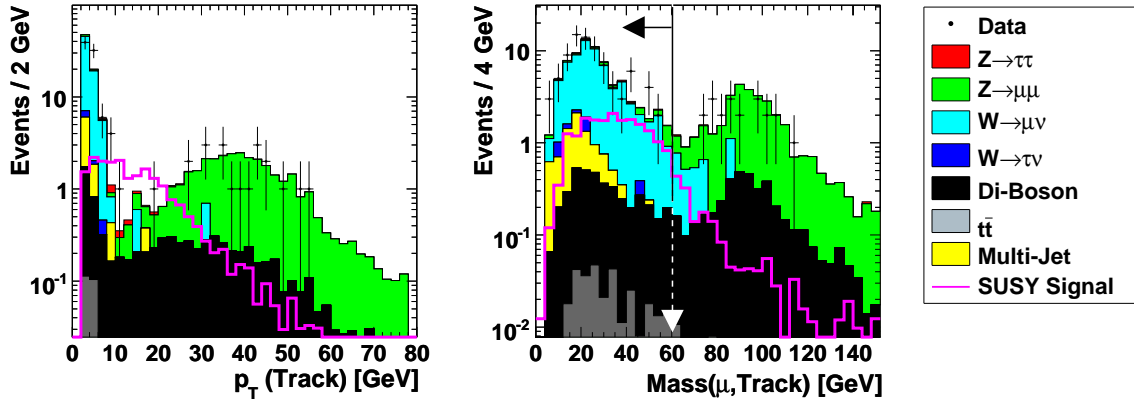


Figure 8.16: Distributions of p_T^{track} and $M(\mu, \text{track})$ after requiring an isolated track (Tab. 8.2, Criterion 7). A cut is placed at $M(\mu, \text{track}) < 60$ GeV.

8.6.3 Selection using an Isolated Track: $\mu + \tau_1 + \text{track}$

A high-quality track ($p_T^{\text{track}} > 3$ GeV), which is well separated from the first and second lepton ($\Delta\mathcal{R} > 0.4$), is used to efficiently identify the third lepton. In order to ensure a precise measurement of its transverse momentum p_T^{track} , the χ^2 per degree of freedom of the track fit is required to be smaller than four. Additionally, at least 17 hits in the SMT and the CFT or 14 hits in the CFT alone are required. Tracks without CFT hits are removed.

Obviously, the selection of the track is affected by large background contributions from jets. This background can be suppressed efficiently by imposing isolation criteria in the tracker and the calorimeter [146]. The leading track which fulfills the following two isolation criteria is considered as the third lepton.

- **Isolation in the Tracker** The scalar sum of the transverse momenta of all tracks in a hollow cone ($0.1 < \Delta\mathcal{R} < 0.4$) around the track is required to be less than 1 GeV.
- **Isolation in the Calorimeter** In the calorimeter the isolation of the track is defined as the sum of transverse energy deposition in the cells of the electromagnetic and fine hadronic calorimeter in a hollow cone ($0.2 < \Delta\mathcal{R} < 0.4$) around the extrapolation of the track into the calorimeter. The sum is required to be smaller than 3 GeV and smaller than 60 % of $\sqrt{p_T^{\text{track}}}$.

After imposing the common selection criteria (Tab. 8.2, Criteria 0-6), the signal efficiency for requiring an isolated track is 57 % (for the SUSY point with $\tan\beta = 8$) while 90 % of the sum of all backgrounds are rejected. Although the loss of efficiency is significant, the isolated track results in a handle for further background suppression, which would not be possible otherwise. Figure 8.16 (left) shows the agreement of data and simulation concerning the p_T^{track} distribution.

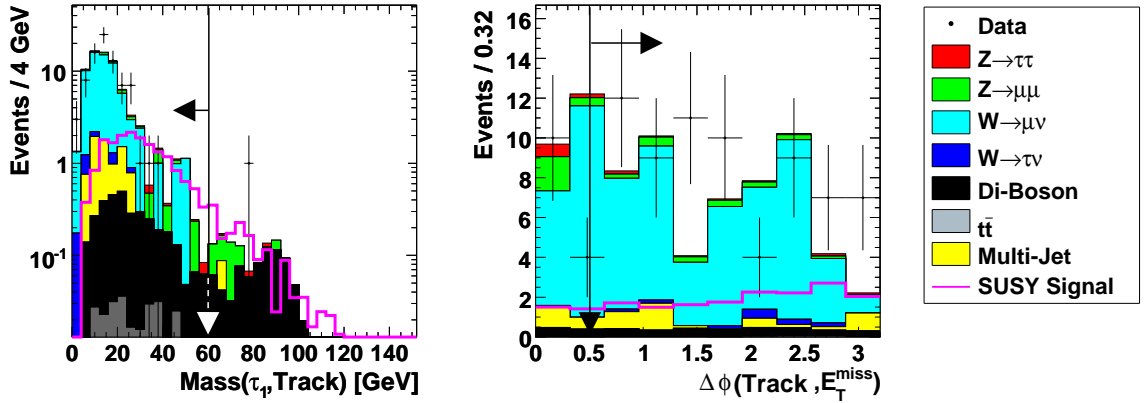


Figure 8.17: Distributions of $M(\tau_1, \text{track})$ and $\Delta\phi(\text{track}, \cancel{E}_T)$ after requiring an isolated track to be reconstructed (Tab. 8.2, Criterion 8). Cuts are placed at $M(\tau_1, \text{track}) < 60$ GeV and $\Delta\phi(\text{track}, \cancel{E}_T) > 0.5$.

Suppression of $Z/\gamma^* \rightarrow \mu\mu$ and WZ Events

As visible in the distribution of $M(\mu, \text{track})$ of Fig. 8.16 (right), background contributions from $Z/\gamma^* \rightarrow \mu\mu$ events peak at the mass of the Z boson. In these events, the muon pair is reconstructed by the muon and the isolated track, while the hadronically decaying tau (τ_1) results from misidentification of an additional radiated jet. This topology is efficiently suppressed by requiring $M(\mu, \text{track}) < 60$ GeV, which rejects 87 % of the mentioned events and accepts 92 % of the SUSY signal.

A similar background arises from the WZ process, which results in a peak at the mass of the Z boson in the invariant mass of τ_1 and track, as shown in Fig. 8.17 (left). In $WZ \rightarrow \mu\nu_\mu ee$ decays, typically one electron is reconstructed as isolated track and the other one is misidentified as τ_1 . The resonance of the Z boson becomes visible since the probability for an electron being misidentified as a hadronically decaying tau is significant due to the similar signature in the calorimeter. If τ_1 and track have opposite charge, a cut at $M(\tau_1, \text{track}) < 60$ GeV removes efficiently a significant amount of the WZ background.

The remaining background contribution from $Z/\gamma^* \rightarrow \mu\mu$ decays can only pass all previous criteria if the muon which results in the isolated track is not reconstructed in the muon detector. This implies that it results in a significant amount of \cancel{E}_T , since it is not included in the \cancel{E}_T calculation. Therefore, \cancel{E}_T points into the direction of the isolated track resulting in a small angle in the transverse plane between muon and \cancel{E}_T (Fig. 8.17 (right)). To reject these events, a cut is applied at $\Delta\phi(\cancel{E}_T, \text{track}) > 0.5$.

Construction of a Likelihood Discriminant to Suppress $W^\pm \rightarrow \mu^\pm\nu_\mu$ Background

After applying all previous selection criteria, the dominating background are $W^\pm \rightarrow \mu^\pm\nu_\mu$ events where additional jets are radiated. A significant difference in terms of kinematics to the SUSY signal is the p_T of the tau candidate and the isolated track since they result from misidentified jets. Therefore, $p_T^{\tau_1}$ and p_T^{track} are typically softer than in the signal and increasing the threshold on $p_T^{\tau_1}$ and p_T^{track} allows to suppress this background. A further

criterion is the transverse mass m_T^μ , which in case of background approximates the mass of the W boson (disregarding the escaping neutrino). It is found that cuts on each of the named quantities allow to suppress the background but the most efficient background reduction is achieved by using a multivariate technique in form of a likelihood discriminant as defined in Eq. (7.1).

Six variables are selected, which exploit the differences between $W^\pm \rightarrow \mu^\pm \nu_\mu$ background and SUSY signal. Distributions of the set of variables is shown in Fig. 8.18. They have been chosen out of several others since the chosen set results in the best performance of the likelihood discriminator in terms of signal efficiency and background suppression. The variables are:

- m_T^μ : In background events, the transverse mass approximates the mass of the W boson.
- $m_T^{\tau_1}$: In background events, \cancel{E}_T tends to point into the direction of the tau due to mismeasurement of its energy.
- m_T^{track} : In background events, \cancel{E}_T tends to point into the direction of the track due to mismeasurement of its energy deposition in the calorimeter.
- $p_T^{\tau_1} \times \cancel{E}_T$: In case of signal events, $p_T^{\tau_1}$ tends to be harder than for background events since in the background it results from a misidentified jet. A significant amount of \cancel{E}_T is also characteristic for the signal.
- $p_T^{\text{track}} \times \cancel{E}_T$: For the background p_T^{track} tends to be softer than in the signal since it results from a misidentified jet.
- $p_T^{\tau_1} \times p_T^{\text{track}}$: The p_T of both objects is expected to be smaller in background since they result from misidentified jets.

The limited statistic of the background sample is increased by obtaining the probability density functions (p.d.f.s) of the six input variables at the preselection level where an additional isolated track is required. The linear correlations between the variables are removed by transforming the p.d.f.s using the square-root of their covariance matrix. Afterwards, the p.d.f.s are smoothed using a Gaussian form of kernel density estimators [147].

Since the resulting likelihood distribution $\text{LH}_W^{\text{track}}$ strongly peaks at one, it is transformed using an inverse sigmoid function

$$\text{LH}_W^{\text{track}} \rightarrow \text{LH}_W^{\text{track}} = -\frac{1}{\tau} \ln \left(\frac{1}{\text{LH}_W^{\text{track}}} - 1 \right), \quad (8.3)$$

which allows to zoom into the peaks at one and zero, resulting in a better visualization of $\text{LH}_W^{\text{track}}$. The parameter τ is set to 15. Figure 8.19 shows the resulting likelihood discriminant and the background rejection as a function of the signal efficiency for a given cut on $\text{LH}_W^{\text{track}}$ where the separation capability between signal and background events is illustrated.

Suppression of $W^\pm \rightarrow \mu^\pm \nu_\mu$ Events and Optimization

The likelihood criteria $\text{LH}_W^{\text{track}}$ in combined with a cut on $p_T^{\text{track}} \times \cancel{E}_T$, which allows to suppress a significant fraction of the background from di-boson processes and especially from the WZ process. Although this quantity is included in the likelihood discriminant $\text{LH}_W^{\text{track}}$, a cut on

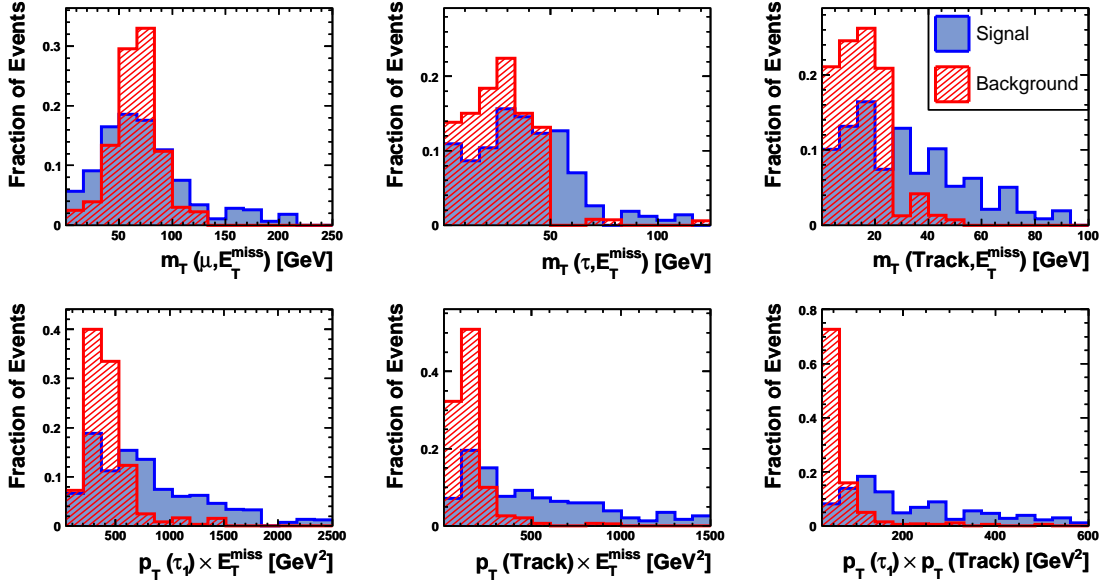


Figure 8.18: Distributions of the variables used for the construction of the likelihood discriminator to separate the SUSY signal from $W^\pm + \text{jets} \rightarrow \mu^\pm \nu_\mu + \text{jets}$ background events.

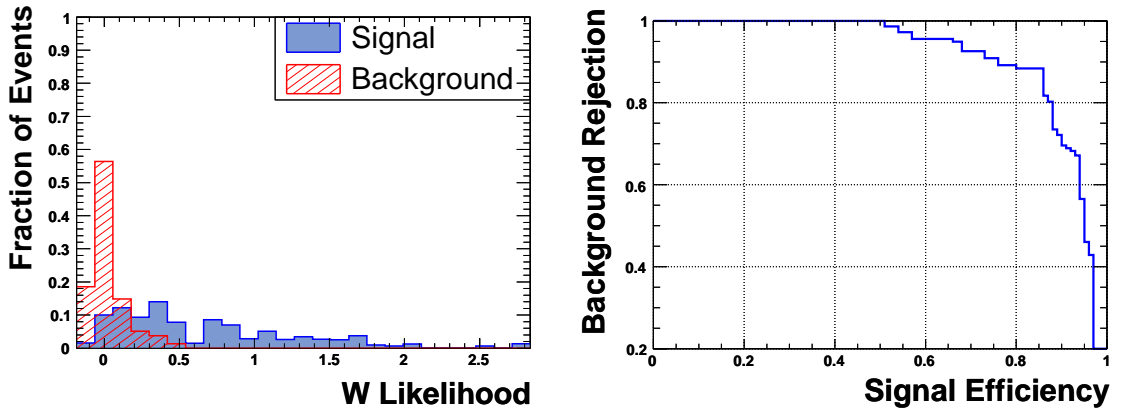


Figure 8.19: *Left:* Distribution of the resulting likelihood discriminator $\text{LH}_W^{\text{track}}$ used for the separation of SUSY signal and $W^\pm \rightarrow \mu^\pm \nu_\mu$ background, after the transformation by the inverse sigmoid function given in Eq. (8.3). *Right:* Background rejection as a function of the signal efficiency for a given cut on $\text{LH}_W^{\text{track}}$.

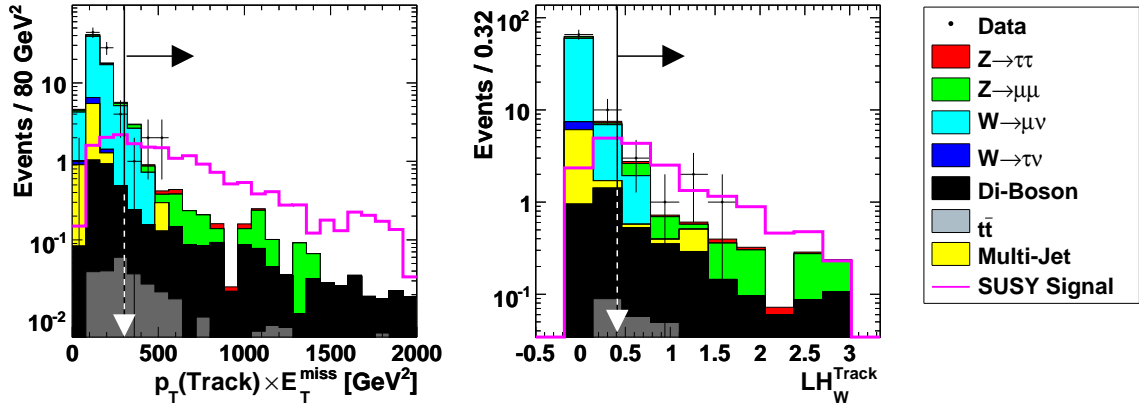


Figure 8.20: Distributions of $p_T^{\text{track}} \times \cancel{E}_T$ and $\text{LH}_W^{\text{track}}$ after requiring an isolated track to be reconstructed and the cut $M(\mu, \text{track}) < 60$ GeV (Tab. 8.2, Criterion 8). The optimal cuts are found at $p_T^{\text{track}} \times \cancel{E}_T > 300$ GeV² and $\text{LH}_W^{\text{track}} > 0.4$.

the product of $p_T^{\text{track}} \times \cancel{E}_T$ is useful since the likelihood is not designed to separate signal from WZ events. The cuts on $\text{LH}_W^{\text{track}}$ and $p_T^{\text{track}} \times \cancel{E}_T$ of Fig. 8.20 are optimized simultaneously in a two dimensional scan for the best expected limit, as illustrated in Fig. 8.21. The optimal cuts are found to be $p_T^{\text{track}} \times \cancel{E}_T > 300$ GeV² and $\text{LH}_W^{\text{track}} > 0.4$.

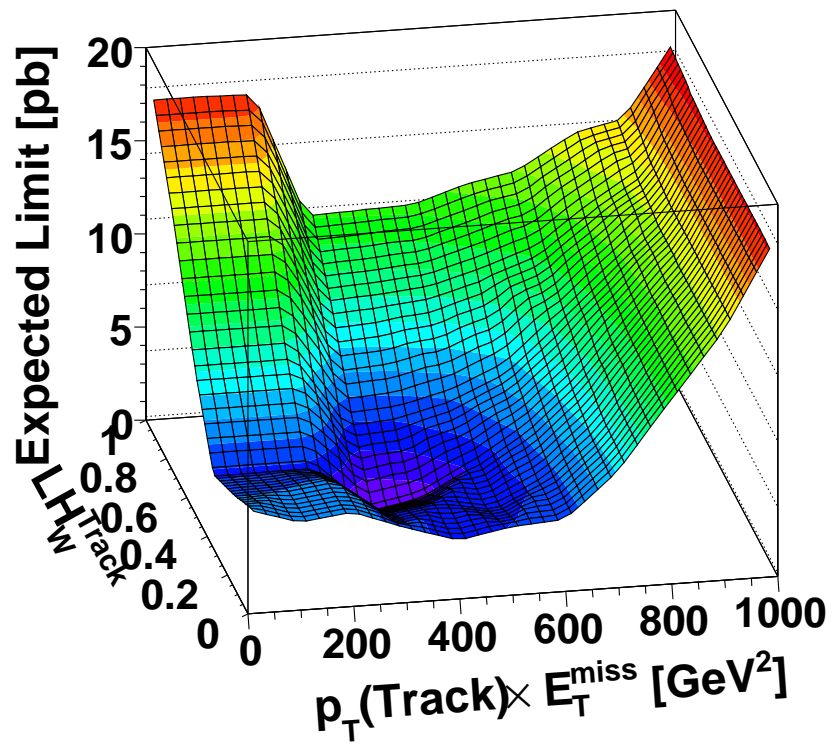


Figure 8.21: The expected limit as a function of a lower cut on LH_W^{track} and $p_T^{\text{track}} \times \cancel{E}_T$. The minimum is located at $LH_W^{\text{track}} > 0.4$ and $p_T^{\text{track}} \times \cancel{E}_T > 300 \text{ GeV}^2$.

8.6.4 Selection using a Second Tau Lepton: $\mu + \tau_1 + \tau_2$

After imposing the common selection criteria (Tab. 8.2, Criteria 0-6), a hadronically decaying tau ($p_T^{\tau_2} > 4$ GeV) is required to be reconstructed in the event according to the criteria given in Sec. 8.3. The signal efficiency of this step amounts to 20 % (for SUSY point $\tan\beta = 8$, including the branching ratio of the tau decay), while 98 % of the sum of all backgrounds are rejected. Figure 8.22 (top left) shows a good simulation of $p_T^{\tau_2}$.

As in the track selection, the suppression of WZ production, with $Z/\gamma^* \rightarrow ee$, is achieved by imposing $M(\tau_1, \tau_2) < 60$ GeV (Fig. 8.22 (top right)). The signal of $Z \rightarrow ee$ decays from the WZ production becomes visible because two electrons are misidentified as hadronically decaying taus. Events with mismeasured $p_T^{\tau_2}$ are removed by $\Delta\phi(\tau_2, \cancel{E}_T) > 0.5$ (Fig. 8.22 (center left)).

A first suppression of the $W^\pm \rightarrow \mu^\pm\nu_\mu$ background is achieved by exploiting that the sum of the four-vectors of the muon, the leading tau (τ_1) and \cancel{E}_T tends to be balanced to the next-to-leading tau lepton. The quantity

$$p_T\text{-Balance} = \frac{p_T(\mu + \tau_1 + \cancel{p})}{p_T(\tau_2)} \quad (8.4)$$

is defined with $\cancel{p} = (\cancel{E}_T, \cancel{E}_x, \cancel{E}_y, 0)$. For signal events, it is expected to result in a peak close to one while for background from $W^\pm \rightarrow \mu^\pm\nu_\mu$ decays the distribution is relatively flat or has a longer tail towards large positive values, as shown in Fig. 8.22 (bottom right). A cut is placed at $p_T\text{-Balance} < 3.5$.

In contrast to the track selection, it is found that the best expected limit is achieved by combining a likelihood discriminant with a cut on the product of the two neural network outputs used for the identification the two tau candidates $\text{NN}_\tau^{\tau_1} \times \text{NN}_\tau^{\tau_2}$ shown in Fig. 8.22 (center right). The product exploits that in $W^\pm \rightarrow \mu^\pm\nu_\mu$ and multi-jet events both tau candidates result from misidentified jets, leading to a low NN_τ . The variables used in the likelihood discriminant are adopted: $m_T^\mu, m_T^{\tau_1}, m_T^{\tau_2}, p_T^{\tau_1} \times \cancel{E}_T, p_T^{\tau_2} \times \cancel{E}_T, p_T^{\tau_1} \times p_T^{\tau_2}$. The resulting likelihood of Fig. 8.22 (bottom left) is referred to as $\text{LH}_W^{\tau_2}$. The optimal cuts are found by a two dimensional scan: $\text{LH}_\tau > 0.2$ and $\text{NN}_\tau^{\tau_1} \times \text{NN}_\tau^{\tau_2} > 0.7$.

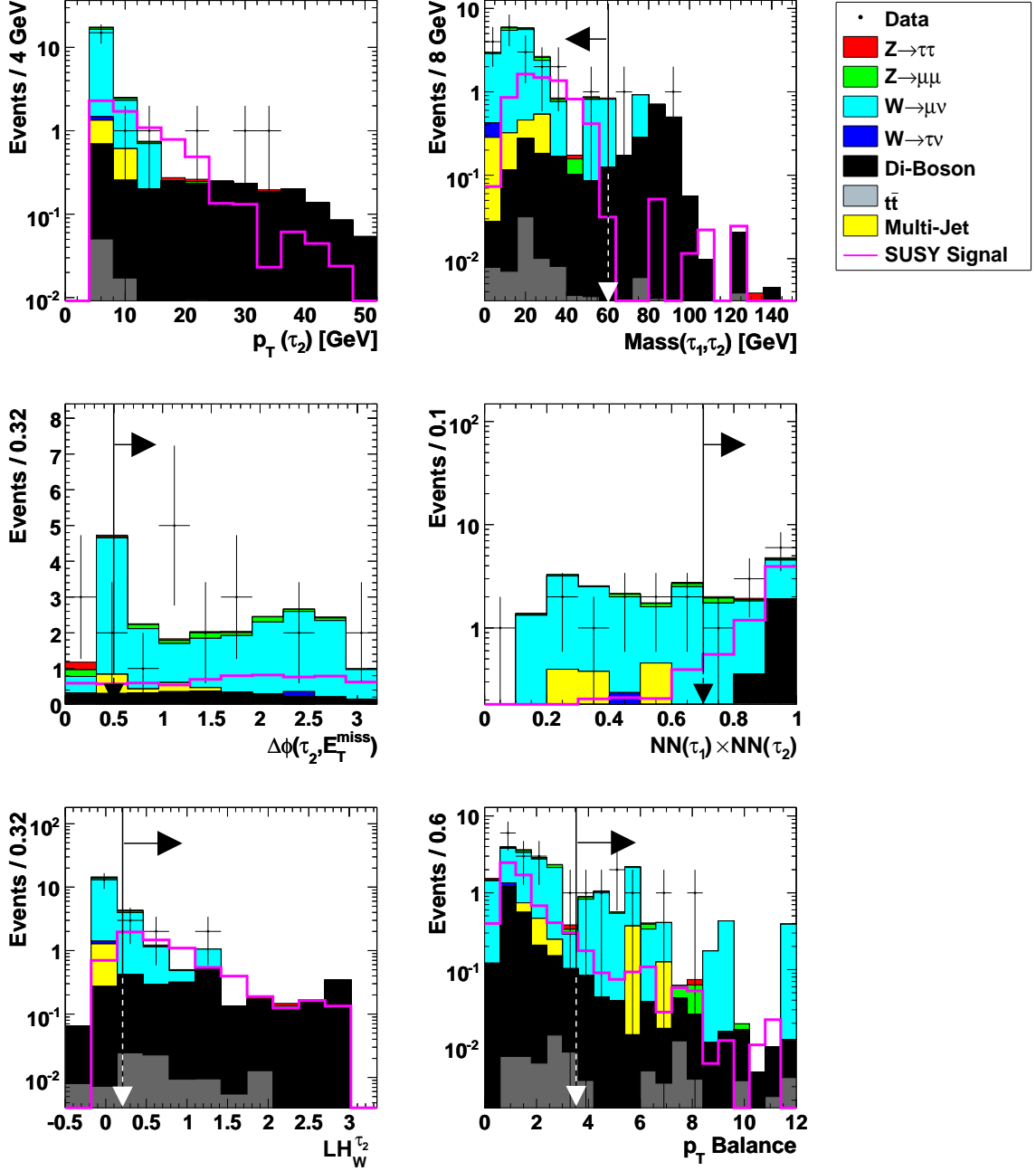


Figure 8.22: Distributions of variables used in the $\mu + \tau_1 + \tau_2$ selection after requiring a second hadronically decaying tau to be reconstructed (Tab. 8.2, Criterion 14). Cuts are placed at $M(\tau_1, \tau_2) < 60$ GeV, $\Delta\phi(\tau_2, \cancel{E}_T) > 0.5$, $NN_{\tau_1} \times NN_{\tau_2} > 0.7$, $LH_W^{\tau_2} > 0.2$ and $p_T\text{-Balance} > 3.5$.

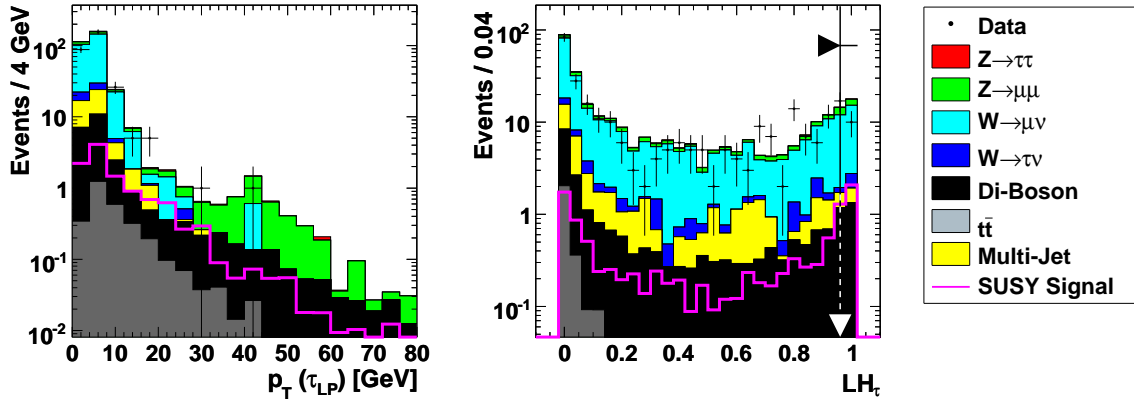


Figure 8.23: Distributions of $p_T^{\tau LP}$ and LH_τ at selection stage 21 (see Tab. 8.2) where the LH_τ criterion is omitted. A cut is applied at $LH_\tau > 0.95$.

8.6.5 Selection using a Low Energetic Tau Lepton: $\mu + \tau_1 + \tau_{LP}$

After imposing the common selection criteria (Tab. 8.2, Criteria 0-6), a hadronically decaying tau lepton ($p_T^{\tau LP} > 3$ GeV) is required to be reconstructed in the event. It is reconstructed and identified according to the criteria introduced in Sec. 7: $LH_\tau > 0.95$, $\Delta\mathcal{R}(\text{any } \mu, \tau_{LP}) > 0.15$. The distributions of $p_T^{\tau LP}$ and LH_τ of Fig. 8.23 and Fig. 8.24 (top left) show good agreement of data and simulation. The signal efficiency of this step amounts to 9 % (for the SUSY point with $\tan\beta = 8$, including the branching ratio of the tau decay), while 97 % of the sum of all backgrounds is rejected. For the considered SUSY point the branching ratio into tau leptons is only moderately enhanced and the reconstruction only aims for low energetic tau leptons which are not yet reconstructed by the previous two selections.

As in the previous two selections, contributions from $Z/\gamma^* \rightarrow \ell\ell$ and WZ decays are suppressed by $M(\mu, \tau_{LP}\text{-track}) < 60$ GeV (Fig. 8.24, top right) and $M(\tau_1, \tau_{LP}) < 60$ GeV (Fig. 8.24, center left). The dominating background arises from $W^\pm \rightarrow \mu^\pm\nu_\mu$ decays, which are suppressed by using a likelihood discriminant $LH_W^{\tau LP}$ constructed from the variables m_T^μ , $m_T^{\tau_1}$, $m_T^{\tau LP}$, $p_T^{\tau_1} \times \cancel{E}_T$, $p_T^{\tau LP} \times \cancel{E}_T$ and $p_T^{\tau_1} \times p_T^{\tau LP}$. Similar to the track selection, the optimal cuts in terms of best expected limit are found by a two dimensional scan: $p_T^{\text{track}} \times \cancel{E}_T > 300$ GeV² (Fig. 8.24, center right) and $LH_W^{\tau LP} > 0.7$ (Fig. 8.24, bottom).

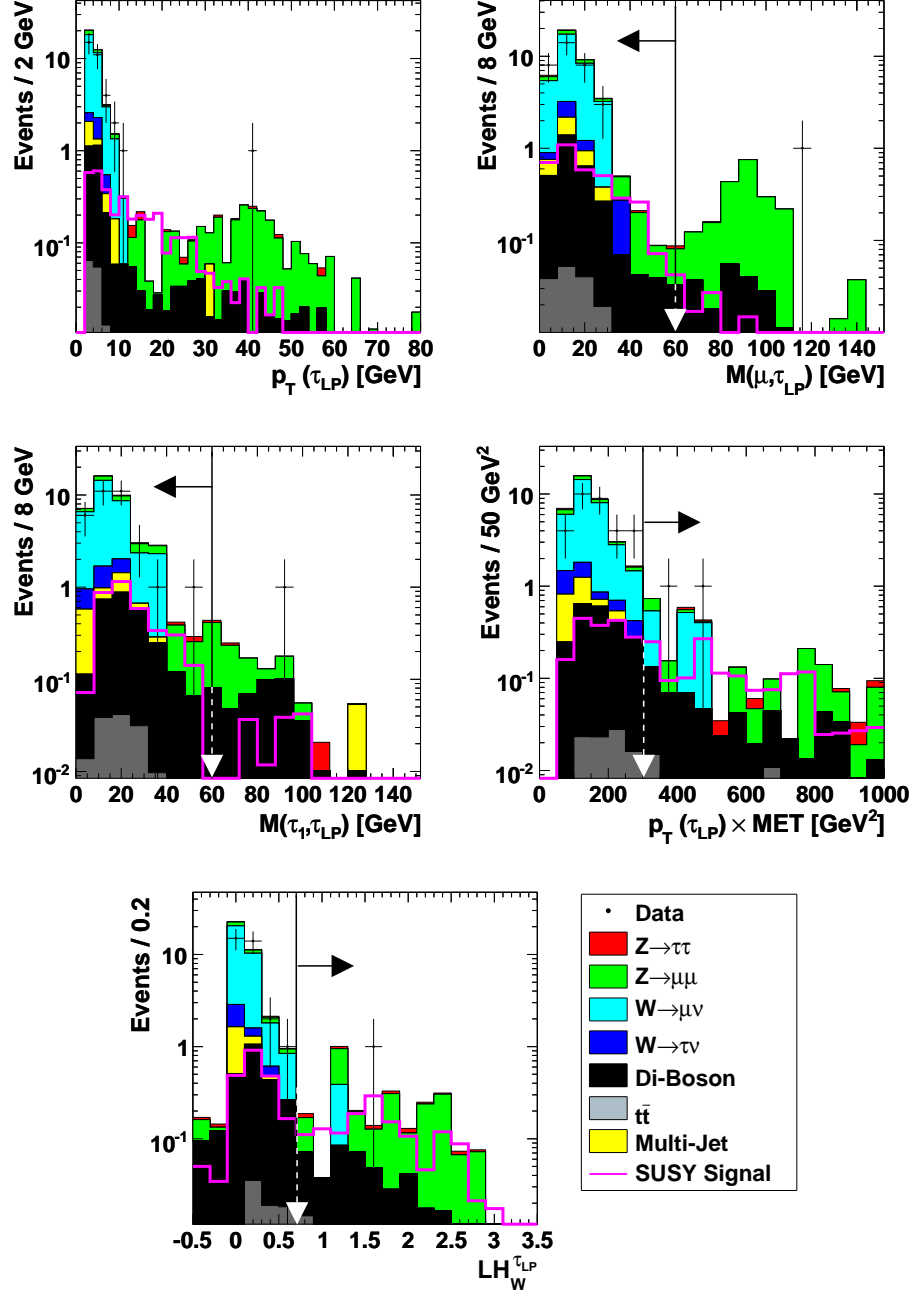


Figure 8.24: Distributions of variables used in the $\mu + \tau_1 + \tau_{LP}$ selection after requiring a hadronically decaying tau to be reconstructed by the algorithm for low energetic taus (Tab. 8.2, Criterion 21). Cuts are placed at $M(\mu, \tau_{LP}) < 60$ GeV, $M(\tau_1, \tau_{LP}) < 60$ GeV, $p_T^{\tau_{LP}} \times \cancel{E}_T > 300$ GeV² and $LH_W^{\tau_{LP}} > 0.7$.

8.7 Systematic Uncertainties

Various sources of systematic uncertainties have been studied to investigate their influence on signal and background expectation.

The systematic uncertainties are determined after applying all selection criteria. The total systematic uncertainty for each subselection is given by the square root of the quadratic sum of the individual uncertainties since the individual contributions are uncorrelated. The following enumeration refers to Tab. 8.5 where the contributions are summarized.

1. The uncertainty introduced by the correction of the p_T resolution of the isolated track

Source	Systematic uncertainty in [%]					
	$\mu + \tau_1 + \text{track}$		$\mu + \tau_1 + \tau_2$		$\mu + \tau_1 + \tau_{LP}$	
	B	S	B	S	B	S
1 Isolated track resolution	+1.8 -1.4	+1.2 -0.9	—	—	—	—
2 Isolated track reconstruction	± 1.2	± 1.2	—	—	—	—
3 Tau ID (τ_2)	—	—	± 5	± 5	—	—
4 Tau track reconstruction (τ_2)	—	—	± 1.2	± 1.2	—	—
5 Tau energy scale (τ_2)	—	—	± 2.6	± 2.6	—	—
6 Low- p_T tau identification	—	—	—	—	± 12	± 12
7 Low- p_T tau track reconstruction	—	—	—	—	± 1.2	± 1.2
8 Low- p_T tau track resolution	—	—	—	—	+1.9 -1.3	+1.1 -0.9
9 Modeling of $W^\pm \rightarrow \mu^\pm \nu_\mu$ background	± 4.0	—	± 6.5	—	± 5.3	—
10 Likelihood discriminant LH_W	± 11	± 6	± 13	± 8	± 12	± 7
11 Rejection factors	± 3.7	—	± 11	—	± 7.9	—
12 Jet energy scale	+4.5 -2.1	+1.8 -1.1	+4.0 -2.3	+1.5 -1.3	+4.3 -2.3	+1.4 -1.3
13 Jet reconstruction efficiency	± 3.2	± 0.8	± 2.8	± 1.1	± 3.0	± 1.1
14 Boson p_T simulation	± 3.3	—	± 3.7	—	± 3.8	—
15 WW, WZ cross section	± 3.1	—	± 3.1	—	± 2.9	—
16 Signal cross section	—	± 3.5	—	± 3.5	—	± 3.5
17 Multi-jet normalization	± 0.5	—	± 0.9	—	± 0.9	—
Quadratic sum	± 14	± 7	± 20	± 11	± 21	± 14
18 Integrated luminosity	± 6.3	± 6.3	± 6.3	± 6.3	± 6.3	± 6.3
Quadratic sum	± 15	± 10	± 21	± 12	± 22	± 16

Table 8.5: Summary of the relative systematic uncertainties in percent on the expectation of the background from Standard Model processes (B) and on the signal prediction (S) after all selection criteria are applied.

- (Sec. 5.3.4) has been determined by varying the correction parameters within $\pm 1\sigma$ [148].
2. The correction applied to the Monte Carlo simulation for the reconstruction efficiency of the isolated track (Sec. 5.3.3) is varied within $\pm 1\sigma$, as determined in [100].
 3. The uncertainty on the identification of the hadronically decaying tau leptons is taken from [131].
 4. The correction applied to the Monte Carlo simulation for the reconstruction efficiency of the τ -track is varied within $\pm 1\sigma$, as determined in [100] (Sec. 5.3.3).
 5. The uncertainty on the tau energy has been estimated by comparing the $p_T^\tau/p_T^{\tau\text{-track}}$ distribution in data and Monte Carlo in a $Z/\gamma^* \rightarrow \tau\tau$ dominated sample (similar to Fig. 8.10) in [131].
 6. The parameters of the correction factor determined in Sec. 7.4 for the reconstruction efficiency of low energetic tau leptons are varied within a range, which leads to an acceptable increase/decrease of the $Z/\gamma^* \rightarrow \tau\tau$ contributions to the selection given in Tab. 7.2.
 7. The correction applied to the Monte Carlo simulation for the reconstruction efficiency of the track of the low energetic tau is varied within $\pm 1\sigma$, as determined in [100] (Sec. 5.3.3).
 8. The uncertainty introduced by the correction of the track p_T resolution of the low energetic tau (Sec. 5.3.4) has been determined by varying the correction parameters within $\pm 1\sigma$ [148].
 9. The systematic uncertainty on the Monte Carlo simulation in terms of the misidentification of taus and isolated tracks in case of the $W^\pm \rightarrow \mu^\pm \nu_\mu$ background has been studied in detail. Further information can be found in [145].
 10. The uncertainty introduced by the likelihood LH_W for the three selections is evaluated by comparing to results obtained using spline fits instead of kernel density estimators for the determination of the p.d.f.s. The effects from mismodeling of the correlations between the used variables in Monte Carlo is assumed to be small compared to the given uncertainty. The size of the uncertainty is driven by the limited statistics of the sample used for obtaining the background p.d.f.s.
 11. The uncertainty introduced by using a relaxed selection for the determination of the rejection of the final selection criteria are taken from the statistical uncertainty on the rejection calculation. This uncertainty affects the $W^\pm \rightarrow \mu^\pm \nu_\mu$, $W^\pm \rightarrow \tau^\pm \nu_\tau$ and multi-jet samples.
 12. The jet energy scale has been varied within $\pm 1\sigma$ as determined in [104]. Its contribution to the total systematic uncertainty is relatively small since the selection does not use a jet requirement explicitly and is only affected through the usage of \cancel{E}_T and H_T .
 13. The uncertainty introduced by corrections that are applied to the simulation in terms of jet reconstruction has been determined by performing the analysis with and without applying the corrections [149].

14. The uncertainty introduced by applying corrections to the simulated transverse momentum of W and Z boson (Sec. 5.3.5) has been determined by comparison to results obtained by using a different correction, which is optimized on Monte Carlo events produced by the Sherpa [70] event generator.
15. The uncertainty on the WW and WZ background is varied within $\pm 1\sigma$ (Sec. 5.2).
16. The uncertainty on the signal cross section is varied within $\pm 1\sigma$.
17. The uncertainty on the multi-jet normalization, which is discussed in Sec. B, has been estimated by varying the overall normalization factor within its statistical uncertainty and by varying the slope of the RMS^{τ} dependent correction by an amount which would lead to an acceptable increase/decrease of the multi-jet background. In spite of the complex normalization procedure, the contribution of this uncertainty stays small because the multi-jet background gives only small contributions to the background at the end of the selection.
18. The uncertainty on the integrated luminosity is taken from the quadratic sum of the uncertainty on the cross section for $Z/\gamma^* \rightarrow \tau\tau$ (Tab. 5.3) and the statistical uncertainty on the calculation (see Sec. 8.5.2).

Since the integrated luminosity of the data sample which is used in the analysis, is determined by scaling the Monte Carlo events to data using the $Z/\gamma^* \rightarrow \tau\tau$ signal, as described in Sec. 8.5.2, the systematic uncertainties on the muon identification, the identification of the leading tau and the trigger efficiency are assumed to cancel at leading order and are not considered. The systematic uncertainty on the signal has been studied using the SUSY point $\tan\beta = 8$. The correlations between the three subselections of the following uncertainties are taken into account: jet reconstruction, jet energy scale, modelling of boson transverse momentum, the di-boson and signal cross sections, the modelling of the multi-jet background, the luminosity measurement, the track reconstruction and momentum resolution of all objects.

In combination with the uncertainty on the luminosity measurement of 6.3 %, the total systematic uncertainty amounts to 15 % and 10 % for background and signal in case of the isolated track selection, 20 % and 11 % for the selection using a second tau and 22 % and 15 % for the selection using a low energetic tau.

Selection	Data	Expected Background from Standard Model	Signal Expectation $\tan \beta = 8$
$\mu + \tau_1 + \text{track}$	0	$0.8 \pm 0.1(\text{stat}) \pm 0.1(\text{syst})$	$0.77 \pm 0.03(\text{stat}) \pm 0.08(\text{syst})$
$\mu + \tau_1 + \tau_2$	1	$0.7 \pm 0.2(\text{stat}) \pm 0.1(\text{syst})$	$0.35 \pm 0.02(\text{stat}) \pm 0.04(\text{syst})$
$\mu + \tau_1 + \tau_{LP}$	1	$0.7 \pm 0.2(\text{stat}) \pm 0.2(\text{syst})$	$0.10 \pm 0.01(\text{stat}) \pm 0.02(\text{syst})$
Total	2	$2.2 \pm 0.3(\text{stat}) \pm 0.2(\text{syst})$	$1.22 \pm 0.04(\text{stat}) \pm 0.09(\text{syst})$

Table 8.6: Number of events observed, events expected from Standard Model processes and events expected for signal point $\tan \beta = 8$ after applying all selection criteria.

8.8 Results

No evidence for the associated production of the lightest chargino and the second lightest neutralino with subsequent decays to three leptons is observed. Upper limits on the trilepton cross section $\sigma(\tilde{\chi}_1^\pm \tilde{\chi}_2^0) \times \text{BR}(3 \text{ Leptons} + X)$ are extracted. These limits are compared to predictions from the mSUGRA model in order to constrain the mSUGRA parameter space. The result of the $\mu\tau_h\ell$ analysis is discussed first, followed by the combination with additional searches for trilepton final states.

8.8.1 The $\mu\tau_h\ell$ Result

The number of observed events in data and the background expectations from Standard Model processes after applying all selection criteria are summarized in Tab. 8.6. The sum of the expected events from Standard Model background processes in the three subselections amounts to $2.2 \pm 0.3(\text{stat}) \pm 0.3(\text{syst})$ while two events are observed in the data. The dominating background contributions result from $WZ \rightarrow 3\text{Leptons}$ decays and $W^\pm \rightarrow \mu^\pm \nu_\mu$ decays where additional jets are radiated. From the $\mu + \tau_1 + \text{track}$ to the $\mu + \tau_1 + \tau_2$ and the $\mu + \tau_1 + \tau_{LP}$ selection, the relative background contribution from $W^\pm \rightarrow \mu^\pm \nu_\mu$ decays increases due to the increasing misidentification probability of jets as the third lepton.

The display of the remaining event in data in the $\mu + \tau_1 + \tau_2$ selection and its kinematic properties are given in Fig. 8.25 and Tab. 8.7. All three reconstructed objects carry a clear signature of well identified leptons. The muon ($p_T^\mu = 37 \text{ GeV}$) is reconstructed based on hits in all three layers of the muon spectrometer and matched to a track identified in the central tracking system. The leading tau ($p_T^\tau = 25 \text{ GeV}$) has a track matched to its calorimeter cluster as well and it has a high neural network output ($\text{NN}_\tau = 1.00$). The large energy fraction deposited in the electromagnetic calorimeter ($\text{EMF} = 0.98$) suggests the interpretation as an electron being reconstructed as a hadronically decaying tau. By contrast, the next-to-leading tau ($p_T^\tau = 23 \text{ GeV}$) can be considered as a real hadronically decaying tau lepton with a central track, a high neural network output ($\text{NN}_\tau = 0.96$) and a small fraction of the energy deposited in the electromagnetic calorimeter ($\text{EMF} = 0.13$). As a consequence, the event contains the signature of all three lepton flavors accompanied by missing transverse energy ($\cancel{E}_T = 33 \text{ GeV}$). The underlying process is consistent with a WZ production with the subsequent decays $W \rightarrow \mu\nu$ and $Z \rightarrow \tau\tau$. This hypothesis is supported by the fact that the two tau objects have opposite charge measured.

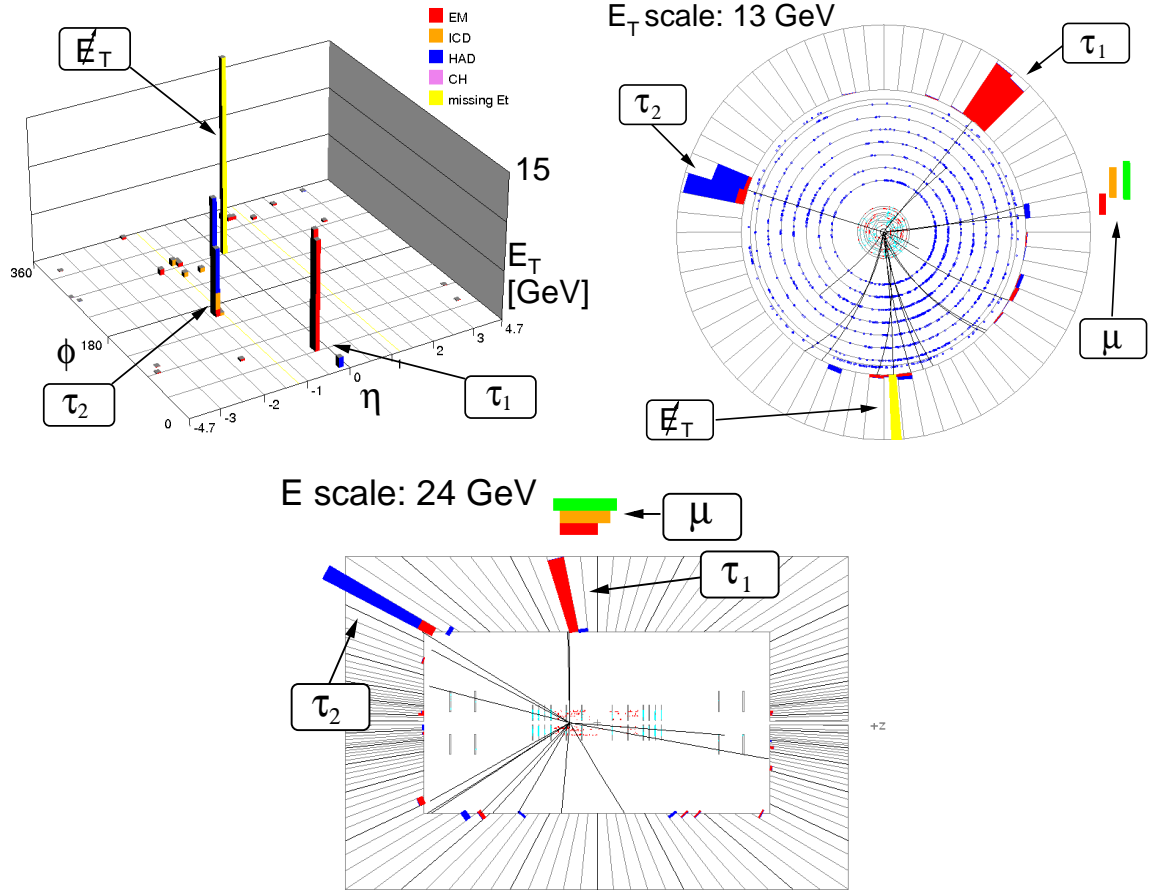


Figure 8.25: Event display of the event remaining in data after applying all selection criteria of the $\mu + \tau_1 + \tau_2$ selection. The energy deposition in the calorimeter in the η - ϕ -plane is shown (top left). In the r - ϕ view (top right) and the η - z view (bottom), the hits in the muon spectrometer and the tracks reconstructed in the tracking detector are indicated as well. Energy depositions in the electromagnetic (hadronic) calorimeter are indicated in red (blue).

The kinematic properties of the event remaining in data in the $\mu + \tau_1 + \tau_{LP}$ selection are listed in Tab. 8.8. Again, the muon is of high quality with hits reconstructed in all three layers of the muon spectrometer. A large energy fraction of the calorimeter cluster of the leading tau is deposited in the hadronic calorimeter ($\text{EMF} = 0.11$) and it has a high NN_τ output. The low- p_T tau consists of a track with small transverse momentum $p_T = 0.6$ GeV, and two EM clusters ($p_T^{\text{EM}_1} = 9.6$ GeV, $p_T^{\text{EM}_2} = 1.7$ GeV) resulting in a reconstructed tau mass of 2.6 GeV. The large value of the reconstructed tau mass and the large distance of the EM clusters to the tau track (at $\Delta\mathcal{R} \approx 1.0$) suggest the interpretation as a misidentified jet. This is supported by the fact that two further soft tracks are reconstructed in the direction of the low- p_T tau, which are located outside the cone considered in the calculation of the track isolation. Muon and leading tau have opposite charge assigned while the charge of both tau objects is identical.

Run number: 204 980		Event number: 71 622 290		
	p_T	η	ϕ	
μ	37 GeV	0.01	0.12	
τ_1	25 GeV	-0.02	0.89	$NN_\tau = 1.00$
τ_2	23 GeV	-1.25	2.86	$NN_\tau = 0.96$
\cancel{E}_T	$E_T = 33$ GeV		4.17	
$M(\mu, \tau_1)$	23 GeV			
$M(\mu, \tau_2)$	69 GeV			
$M(\tau_1, \tau_2)$	51 GeV			
$N(\text{Jets})$	0 ($p_T > 15$ GeV, excluding τ -jets)			

Table 8.7: Kinematic properties of the objects reconstructed in the event selected in data in the $\mu + \tau_1 + \tau_2$ selection.

Run number: 210 200		Event number: 63 188 024		
	p_T	η	ϕ	
μ	34 GeV	-0.84	0.19	
τ_1	12 GeV	0.71	4.64	$NN_\tau = 0.99$
τ_{LP}	12 GeV	0.23	0.34	$LH_\tau = 0.96$
τ_{LP} -track	0.6 GeV	1.14	0.25	$m_\tau = 2.6$
τ_{LP} -EM Cluster 1	9.6 GeV	0.17	0.35	
τ_{LP} -EM Cluster 2	1.7 GeV	0.18	0.33	
\cancel{E}_T	$E_T = 38$ GeV		3.16	
$M(\mu, \tau_1)$	48 GeV			
$M(\mu, \tau_{LP})$	23 GeV			
$M(\tau_1, \tau_{LP})$	22 GeV			
$N(\text{Jets})$	0 ($p_T > 15$ GeV, excluding τ -jets)			

Table 8.8: Kinematic properties of the objects reconstructed in the event selected in data in the $\mu + \tau_1 + \tau_{LP}$ selection.

Signal Efficiency of the Selection

The efficiencies of the three subselections of Fig. 8.26 decrease from $(1.23 \pm 0.06) \%$, $(0.60 \pm 0.04) \%$ and $(0.14 \pm 0.02) \%$ to $(0.07 \pm 0.01) \%$, $(0.06 \pm 0.01) \%$ and $(0.02 \pm 0.01) \%$ with increasing $\tan\beta$ for the $\mu + \tau_1 + \text{track}$, $\mu + \tau_1 + \tau_2$ and $\mu + \tau_1 + \tau_{LP}$ selection. The drastic decrease is caused by several effects which are all related to the increasing branching ratio into taus. Due to the increasing number of tau final states, the average visible p_T is reduced, which results in a reconstruction efficiency decrease. At the same time the number of muons in the final state decreases, which limits the trigger efficiency at large $\tan\beta$. This aspect is enhanced by the fact that the transverse momenta of muons originating from leptonic tau decays are significantly lower than those of muons resulting directly from the decay of a slepton or gaugino. However, as expected from the increasing branching ratio into tau leptons, the relative efficiencies of the selections relying on two hadronically decaying taus compared to the $\mu + \tau_1 + \text{track}$ selection increases together with $\tan\beta$, as illustrated in Fig. 8.26. For example at $\tan\beta = 3$, the ratio of the selection efficiencies of $\mu + \tau_1 + \tau_2$ and $\mu + \tau_1 + \text{track}$ selection amounts to 0.48, while at $\tan\beta = 30$ it amounts to 0.86. An even larger increase is found for the $\mu + \tau_1 + \tau_{LP}$ selection (0.11 at $\tan\beta = 3$, 0.29 at $\tan\beta = 30$).

In addition to the dependence on the branching ratio into the leptons of the three generations, the efficiency of the three subselections shown in Fig. 8.27 depends strongly on the kinematics of the final state. The kinematics are determined by the chargino mass $m_{\tilde{\chi}_1^\pm}$ and the difference of slepton and neutralino mass $m_\Delta = m_{\tilde{\ell}} - m_{\tilde{\chi}_2^0}$. The mass difference is calculated using the mass of the right handed selectron, which is about 1 GeV heavier than the lightest stau for the considered scenario. The increase of the selection efficiency together with $m_{\tilde{\chi}_1^\pm}$ results from the increasing transverse momenta of the leptons in the final state. In case of the dependence on m_Δ , two regions can be distinguished: the 3-body ($m_\Delta > 0$) and the 2-body decay region ($m_\Delta < 0$). In the 3-body region, the gauginos decay preferably via virtual sfermions and the efficiency reaches a plateau already for small positive m_Δ . Traversing the 2-body decay region from small to large negative m_Δ , first the neutralino decays into a real charged slepton and a charged lepton, $\tilde{\chi}_2^0 \rightarrow \tilde{\ell}\ell$. At small negative m_Δ the phase space for the lepton is reduced resulting in a soft transverse momentum that is below the kinematic threshold of the selection. Towards smaller m_Δ , the available phase space for the lepton increases resulting in a rising selection efficiency. At $m_\Delta \approx -35$ GeV, the decay of the lightest chargino into real sneutrinos, $\tilde{\chi}_1^\pm \rightarrow \tilde{\nu}\ell$, becomes kinematically allowed. First, the available phase for the lepton is small but it increases again with decreasing m_Δ , resulting in the illustrated shape of the selection efficiency. The decay of the second lightest neutralino to neutrinos, $\tilde{\chi}_2^0 \rightarrow \tilde{\nu}\nu \rightarrow \nu\nu\tilde{\chi}_1^0$, is not included in the consideration since it does not contribute to the trilepton signature.

Interpretation of the Results

The upper limits on the trilepton cross section at the 95 % CL are calculated using the likelihood-ratio method in the modified frequentist approach as discussed in Sec. A. Since for all SUSY points the same selection criteria are used, the shape of the limits follows the shape of the signal efficiency of the selection. The interpretation of the cross section limits is performed in several mSUGRA scenarios.

In the combination of the three subselections of the $\mu\tau_h\ell$ analysis, the overlap of the subselections is subtracted and all systematic uncertainties are taken into account including

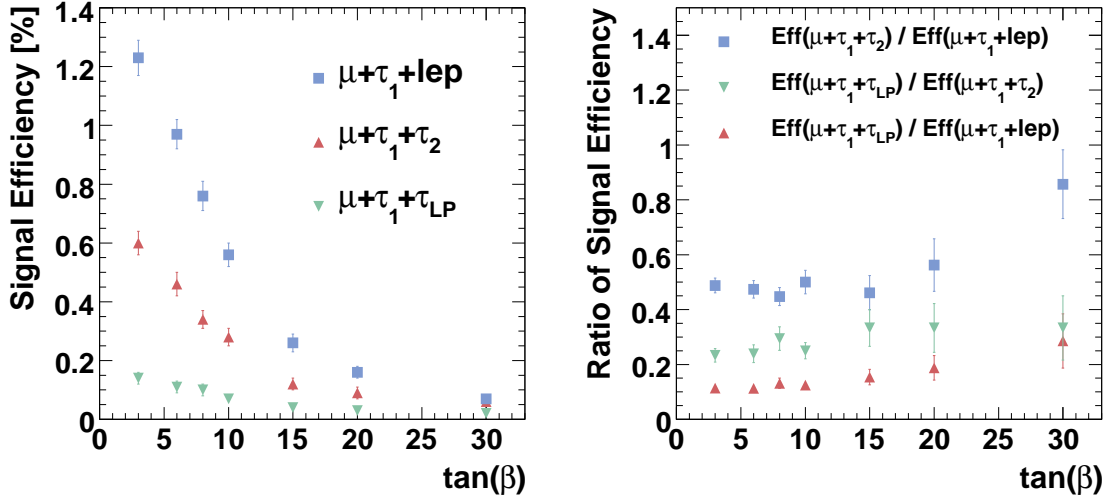


Figure 8.26: Efficiency of the three selections (left) and their ratios (right) as a function of $\tan\beta$. The parameters of the considered SUSY points are listed in Tab. 8.1. Only statistical uncertainties are given.

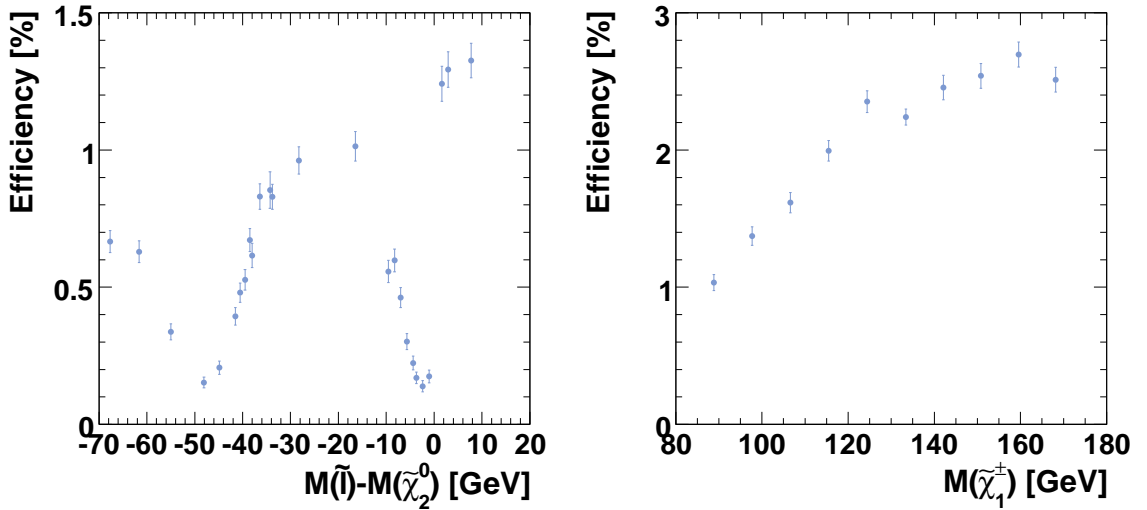


Figure 8.27: Efficiency of the $\mu\tau_h\ell$ analysis as a function of $m_\Delta = m_{\tilde{\ell}} - m_{\tilde{\chi}_2^0}$ (left) and $m_{\tilde{\chi}_1^\pm}$ (right). The sum of the efficiencies of the three subselections together with the statistical uncertainties is given.

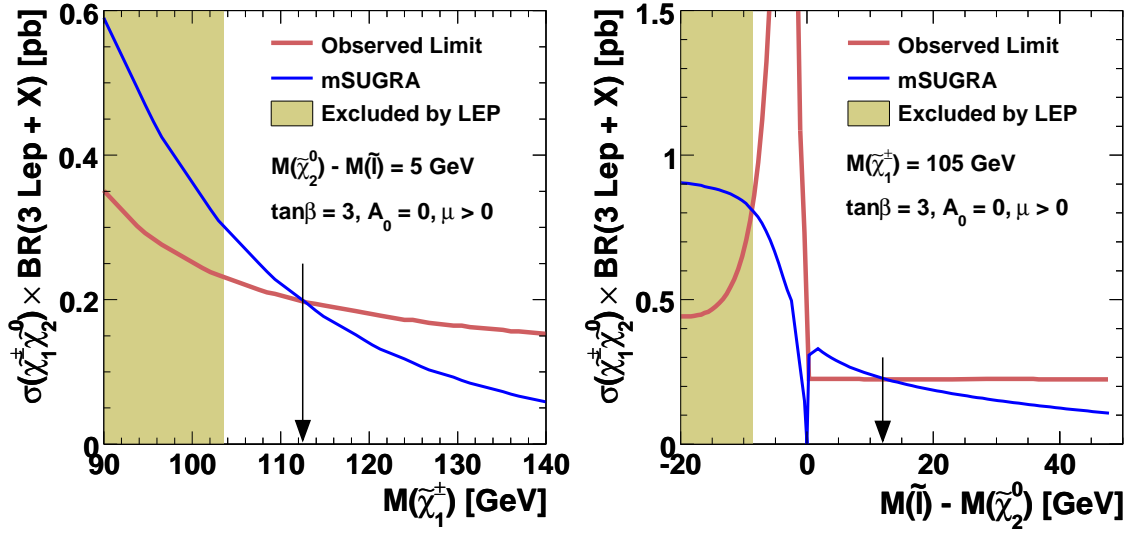


Figure 8.28: The observed upper limit on the trilepton cross section as a function of $m_{\tilde{\chi}_1^\pm}$ in the 3l-max scenario (left) and as a function of $m_\Delta = m_{\tilde{\ell}} - m_{\tilde{\chi}_2^0}$ (right). The limits from searches at LEP on the chargino mass $m_{\tilde{\chi}_1^\pm} > 103.5$ GeV [55] and on the selectron mass $m_{\tilde{e}} > 99.9$ GeV [54] are indicated. The expected cross section limit is not indicated since it is almost identical to the observed limit in terms of absolute value as well as shape.

their correlations between the three subselections, as discussed in Sec. 8.7.

The cross section limit is interpreted in the *3l-max scenario* as a function of $m_{\tilde{\chi}_1^\pm}$ for $\tan\beta = 3$, where the effects from slepton mixing are small. The 3l-max scenario is characterized by a maximally enhanced branching ratio of the lightest chargino and the second lightest neutralino into leptons in the 3-body decay region where the lightest chargino and the slepton are mass degenerate. Figure 8.28 (left) shows the combined limit. A comparison to the trilepton cross section predicted by the mSUGRA model shows that the $\mu\tau_h\ell$ analysis allows to exclude chargino masses up to $m_{\tilde{\chi}_1^\pm} = 112.5$ GeV in this scenario beyond the existing LEP upper limits of $m_{\tilde{\chi}_1^\pm} = 103.5$ GeV [55].

Figure 8.28 (right) shows the interpretation of the combined selections of the $\mu\tau_h\ell$ analysis as a function of $m_\Delta = m_{\tilde{\ell}} - m_{\tilde{\chi}_2^0}$ for $m_{\tilde{\chi}_1^\pm} = 105$ GeV and $\tan\beta = 3$. In this interpretation the $\mu\tau_h\ell$ analysis extends the existing LEP limits. For positive m_Δ where the 3l-max scenario is located, the region $1 \text{ GeV} < m_\Delta < 12 \text{ GeV}$ is excluded. For small negative m_Δ the limit diminishes since in the transition region from 2-body decays to 3-body decays, the second lightest neutralino decays into a real slepton and a soft lepton which is below the kinematic threshold of the selection. With increasing negative m_Δ , the sensitivity increases again. But for the considered scenario, the limit on the selectron mass $m_{\tilde{e}} > 99.9$ GeV from LEP searches can not be extended [54].

The cross section limit is interpreted in the 3l-max scenario as a function of $\tan\beta$, which allows a scan from minimal to maximal branching ratio into tau leptons. Figure 8.29 shows the expected and observed limit on the trilepton cross section as a function of $\tan\beta$ for

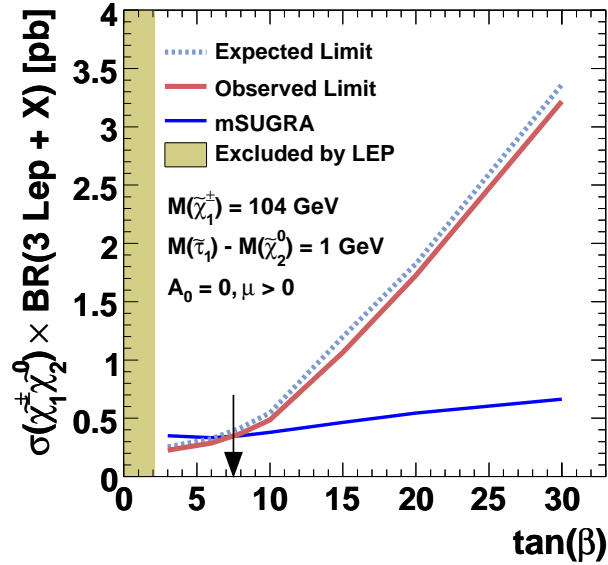


Figure 8.29: The observed and expected limit on the trilepton cross section as a function of $\tan\beta$ for the combination of the three subselections of the $\mu\tau_h\ell$ analysis. The limit from the LEP experiments $\tan\beta > 2.1$ is indicated [57].

$m_{\tilde{\chi}_1^\pm} = 104$ GeV. A comparison to the trilepton cross section predicted by the mSUGRA model shows that the $\mu\tau_h\ell$ analysis allows exclude the parameter space below $\tan\beta < 7.5$, which significantly extends the exclusion region from the LEP experiments [57].

In order to interpret the results more generally in the $(m_0, m_{1/2})$ -plane of mSUGRA model, SUSY points are selected within the reach of the presented analysis. They are chosen to allow a parameterization of the selection efficiency in the $(m_0, m_{1/2})$ -plane for $\tan\beta = 3$, $A_0 = 0$ and $\mu > 0$. For the selected SUSY points, summarized in Sec. C, signal Monte Carlo samples are generated. The resulting observed limit of the $\mu\tau_h\ell$ analysis is illustrated in Fig. 8.30. It allows to exclude a significant fraction of the mSUGRA parameter space beyond the existing excluded regions given by the lower limits from the LEP experiments of $m_{\tilde{\chi}_1^\pm} > 103.5$ GeV and $m_{\tilde{e}} > 99.9$ GeV. The $\mu\tau_h\ell$ analysis allows to exclude $m_{1/2}$ values below 203 GeV (corresponding to $m_{\tilde{\chi}_1^\pm} > 134$ GeV), strongly depending on m_0 . In terms of m_0 , the exclusion region reaches up to 100 GeV (corresponding to $m_{\tilde{e}} > 123$ GeV) at the LEP chargino limit. The excluded parameter space is separated into two parts at $m_\Delta \approx 0$ where the transition from the 2-body to 3-body decays of the lightest chargino and the second lightest neutralino takes place and the sensitivity of the trilepton searches is reduced.

8.8.2 Combination with Additional Trilepton Searches

The DØ Collaboration performed complementary searches for the associated production of the lightest chargino and the second lightest neutralino in the following final states: $e\ell$, $\mu\mu\ell$, $e\mu\ell$ and same-sign di-muon [150, 151, 152, 144]. The analyses are based on data corresponding to an integrated luminosity of up to 1.7 fb^{-1} . Currently, the update of these

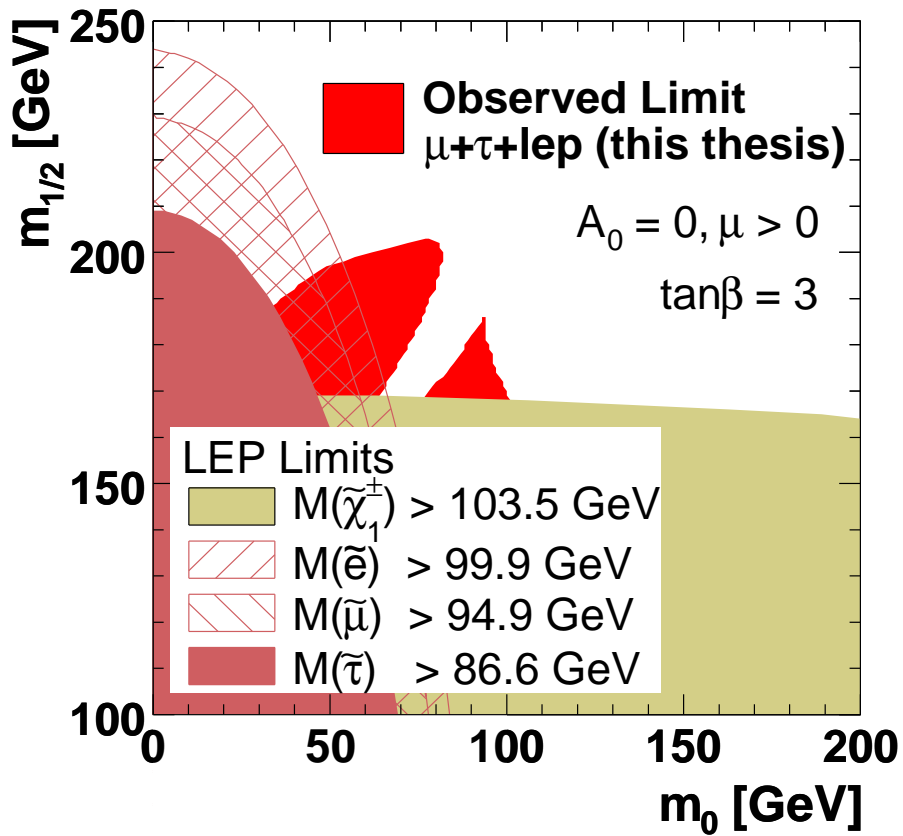


Figure 8.30: Exclusion region of the $\mu\tau_h\ell$ analysis in the $(m_0, m_{1/2})$ -plane for $\tan\beta = 3$, $A_0 = 0$ and $\mu > 0$. Additionally, the regions are indicated which are excluded by the LEP experiments [54, 55].

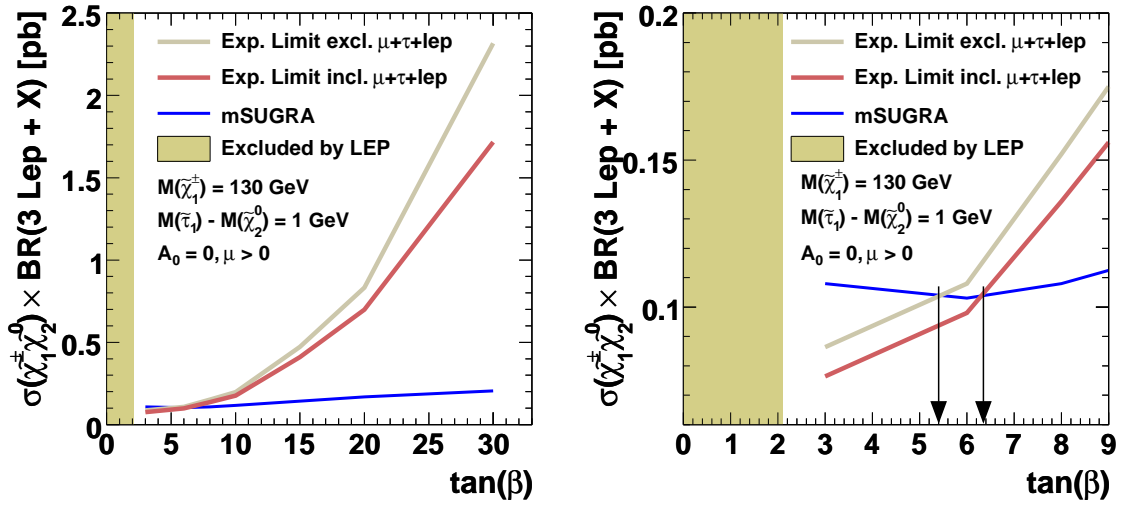


Figure 8.31: The expected upper limit on the trilepton cross section in a combination of $D\bar{O}$ trilepton searches excluding and including the presented $\mu\tau_h\ell$ analysis. The right figure presents a zoom of the left figure. The limit from the LEP experiments $\tan\beta > 2.1$ is indicated [57].

analyses is performed based on a data set of 2.2 fb^{-1} [141, 142]. The sensitivity of the combined results of these analyses and the $\mu\tau_h\ell$ analyses is studied. The overlap between the analyses is removed by disregarding data and Monte Carlo events in a given analysis if they are already selected by another analysis with a higher signal-to-background ratio. All systematic uncertainties are treated as fully correlated except the following which are regarded as uncorrelated: modelling of the $W + \text{jet}$ background, modelling of the multi-jet background, rejection factors and the likelihood for the $W + \text{jet}$ background suppression LH_W .

Figure 8.31 shows the expected upper limit on the trilepton cross section of the presented analysis in a combination with searches in the $e\ell\ell$, $\mu\mu\ell$ and $e\mu\ell$ final states based on a data set corresponding to an integrated luminosity of 1 fb^{-1} . For $m_{\tilde{\chi}_1^\pm} = 130 \text{ GeV}$, the $\mu\tau_h\ell$ analysis extends the sensitivity by approximately 15 % in terms of $\tan\beta$ and sensitivity can be expected up to $\tan\beta \approx 6.4$. The relative contribution of the $\mu\tau_h\ell$ analysis to the combination grows with $\tan\beta$, as expected from the increasing branching ratio into tau leptons.

The presented $\mu\tau_h\ell$ selection has the largest overlap with the $e\mu\ell$ selection since the misidentification rate of electrons as hadronically decaying tau leptons is large due to the similar signature in the detector. Between $\tan\beta = 3$ and $\tan\beta = 30$ the overlap varies in the range of 60 % to 23 % for the $\mu + \tau_1 + \text{track}$ selection, 64 % to 17 % for $\mu + \tau_1 + \tau_2$ selection and 50 % to 18 % for the $\mu + \tau_1 + \tau_{LP}$ selection. The overlap in the background amounts to $\approx 10 \%$ for all three subselections. The overlap with the $e\ell\ell$ and $\mu\mu\ell$ selection are significantly smaller for signal and background.

Figure 8.32 shows the expected exclusion region at the 95 % CL in the $(m_0, m_{1/2})$ -plane for a combination of the presented analysis and searches in the $e\ell\ell$, $\mu\mu\ell$ and $e\mu\ell$ final states based on a data set corresponding to an integrated luminosity of 2.2 fb^{-1} . At low values of m_0 and $m_{1/2}$, the combined result significantly extends the region in the mSUGRA parameter

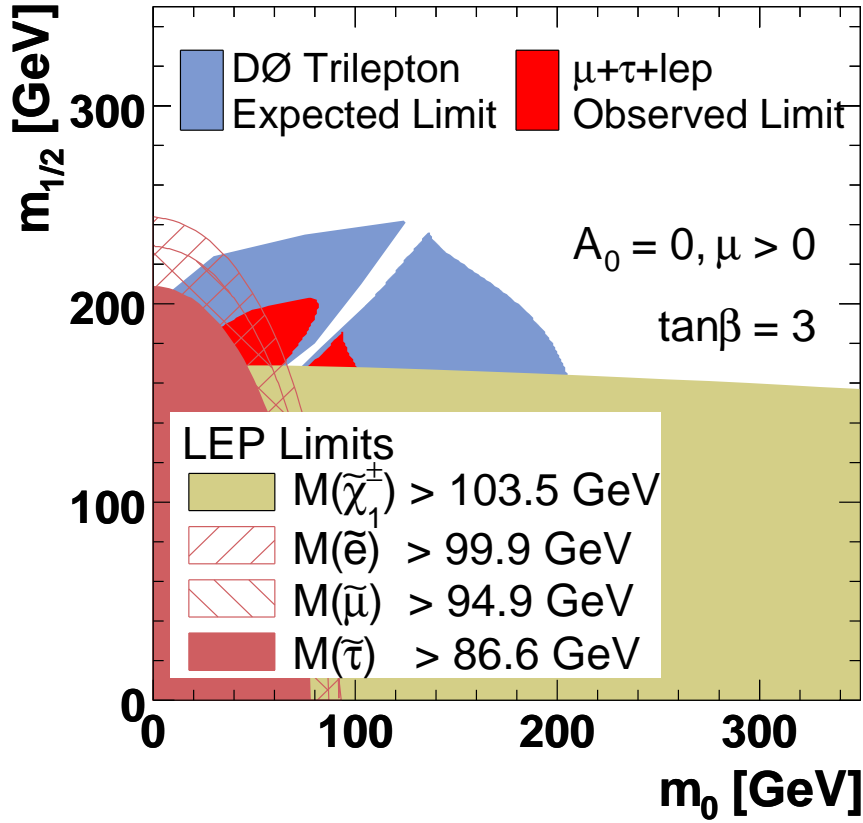


Figure 8.32: Expected exclusion regions at the 95 % CL in the $(m_0, m_{1/2})$ -plane for a combination of DØ trilepton searches. Additionally, the regions are indicated which are excluded by the LEP experiments [54, 55].

space which has already been probed by the LEP experiments. For values of $m_{1/2}$ close to the lower limit from the LEP experiments of $m_{\tilde{\chi}^\pm} > 103.5$ GeV, the sensitivity of the combined trilepton analyses reaches up to values of $m_0 = 180$ GeV, while for $m_0 \approx 100$ GeV the lower limit on $m_{1/2}$ is extended to $m_{1/2} \approx 240$ GeV (corresponding to $m_{\tilde{\chi}_1^\pm} > 167$ GeV). It is expected that the sensitivity gap at $m_\Delta = m_{\tilde{\ell}} - m_{\tilde{\chi}_2^0} \approx 0$ is partially closed by including the same-sign di-muon analysis in the combination [144]. The same-sign di-muon analysis is not affected by the reduced available phase space for the lepton from $\tilde{\chi}_2^0 \rightarrow \tilde{\ell}\ell$ decays at $m_\Delta = m_{\tilde{\ell}} - m_{\tilde{\chi}_2^0} \approx 0$. In the region where $m_{\tilde{\chi}_2^0} \approx m_{\tilde{\nu}}$, the shown projection uses an extrapolation of the reconstruction efficiencies of the additional analyses considered since the study of this transition region in case of the additional analyses has not been finalized at the time of writing.

8.9 Outlook

The sensitivity of the $D\bar{O}$ trilepton search is mainly limited by the amount of collected data statistics. It is expected that the accessible regions will increase with the amount of recorded data during Run II of the Tevatron. A further increase of sensitivity can be achieved by improved analysis techniques. The LHC, with the experiments ATLAS and CMS, will allow to study the SUSY parameter space beyond Tevatron limits.

8.9.1 Projection for the Tevatron

By the end of Run II of the Tevatron, the experiments $D\bar{O}$ and CDF are expected to record data corresponding to an integrated luminosity of about 7 fb^{-1} , which will allow to extend the reach towards larger m_0 , $m_{1/2}$ and also $\tan\beta$ significantly.

A study has been performed [146] in order to investigate the upper limits on the trilepton cross section as a function of integrated luminosity in the absence of a SUSY signal. Figure 8.33 shows the expected limit on the trilepton cross section as a function of $m_{\tilde{\chi}_1^\pm}$ for a combination of $D\bar{O}$ and CDF results under the assumption that CDF performs analyses with the same performance as the combined $D\bar{O}$ searches. Depending on $m_{\tilde{\chi}_1^\pm}$, the trilepton cross section can be excluded at the 95 % CL to the range of about 0.02 pb to 0.04 pb with the integrated luminosity expected by the end of Tevatron Run II. The shape is given by the increase of the selection efficiency with increasing $m_{\tilde{\chi}_1^\pm}$. In the region $m_{\tilde{\chi}_1^\pm} \approx 200 \text{ GeV}$, where $m_{\tilde{\chi}_2^0} > m_Z + m_{\tilde{\chi}_1^0}$ and the neutralino decays dominantly into real Z bosons, the selection will have to be modified, due to the selection criteria for the suppression of the background from $Z/\gamma^* \rightarrow \ell\ell$. Especially, relaxing the criteria on $M(\ell, \ell)$ will allow to increase the efficiency partially. Instead, tightened cuts on \cancel{E}_T and the p_T of the third lepton allow a suppression of the background. The limit on the trilepton cross section for $m_{\tilde{\chi}_1^\pm} \gtrsim 200 \text{ GeV}$ rises again to values similar to small $m_{\tilde{\chi}_1^\pm}$.

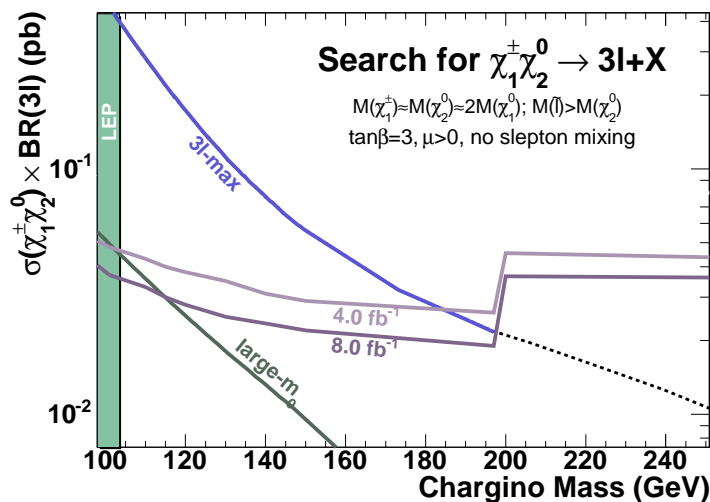


Figure 8.33: Projection of the expected limit at the 95 % CL on the trilepton cross section as a function of the mass of the lightest chargino for different integrated luminosities in a combination with results from CDF [146].

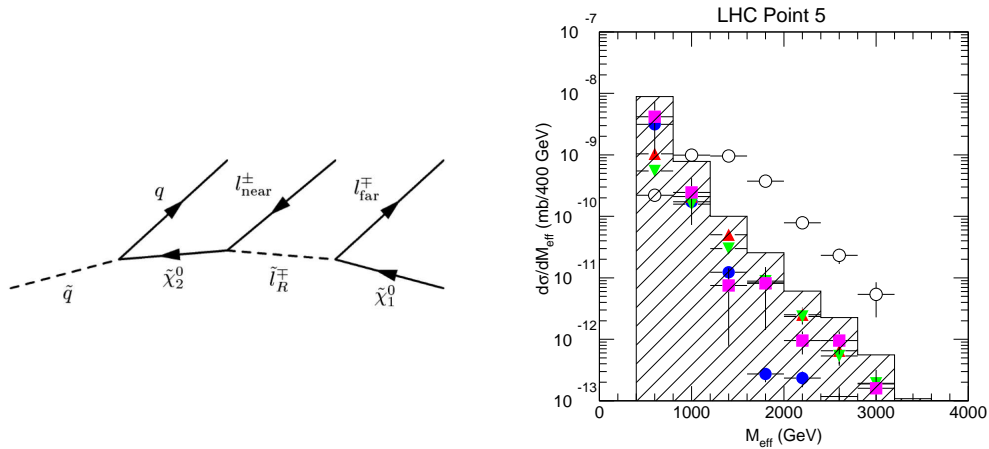


Figure 8.34: *Left*: Typical cascade decay of a gluino to quarks, leptons and \cancel{E}_T . *Right*: Distribution of the effective mass for Standard Model background processes and a SUSY signal (open circles) with the parameters $m_0 = 100$ GeV, $m_{1/2} = 300$ GeV, $A_0 = 300$ GeV, $\tan\beta = 2.1$ and $\mu > 0$. The sum of the background contributions (hatched histogram) consists of $t\bar{t}$ (solid circles), W +jets (triangles), Z +jets (downward triangles) and QCD jets (squares) [154].

8.9.2 Search for SUSY at the LHC

The squark/gluino production is the dominating production process for supersymmetric particles. It leads via cascade decays to final states which consist of various combinations of leptons, jets and \cancel{E}_T (Fig. 8.34 (left)). Final states containing leptons and \cancel{E}_T but no jets result from pair production of the lightest chargino or the associated production of the lightest chargino and the second lightest neutralino [153].

A quantity which allows to discriminate the SUSY signal from background and to determine the mass scale of SUSY particles is the *effective mass*, which is defined as the scalar sum of the visible transverse momenta of particles in the final state and \cancel{E}_T [154]. The SUSY signal is expected to be observed as an excess over the Standard Model background, as shown in Fig. 8.34 (right).

Within the mSUGRA model, studies have been performed to investigate the discovery potential of ATLAS and CMS. For moderate and large values of $\tan\beta$, this is illustrated for the ATLAS experiment in the m_0 - $m_{1/2}$ -plane for an integrated luminosity of 1 fb^{-1} in Fig. 8.35 (left) [155]. For large values of $\tan\beta$ and 100 fb^{-1} , the discovery reach is shown in Fig. 8.35 (right) for SUSY searches in various final states at the CMS experiment [156]. One year of data taking will provide sufficient data to probe squark/gluino masses up to 1.5-2 TeV, while for the design luminosity of 300 fb^{-1} SUSY masses in the range of up to 2.5 TeV are accessible.

The observation of deviations from the Standard Model is expected to be relatively simple, assuming they exist in nature. The challenge will be the determination of the origin of the deviation, i.e. to determine if the deviation can be explained by Supersymmetry or by any other of the various proposed extensions of the Standard Model. This requires the

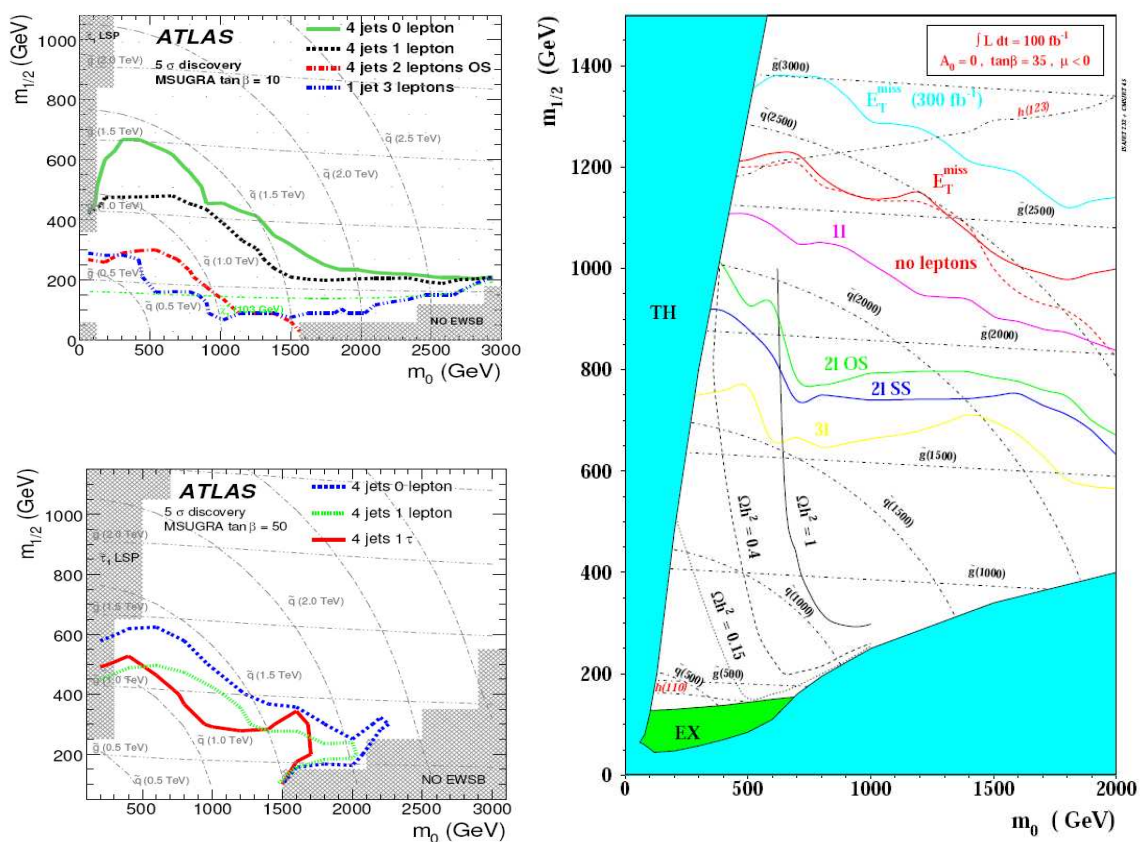


Figure 8.35: *Left*: Discovery reach (5σ) for the ATLAS experiment in jet analyses with various lepton requirements for an integrated luminosity of 1 fb^{-1} , for $A_0 = 0$, $\mu > 0$, $\tan\beta = 10$ (*top*) and $\tan\beta = 50$ (*bottom*). The dark shaded regions are excluded theoretically [155].

Right: The 5σ discovery reach for the CMS experiment in the m_0 - $m_{1/2}$ -plane for $A_0 = 0$ and $\tan\beta = 35$ for various lepton signatures (1l, 2l opposite sign, 2l same sign, 3l) and the signature $\cancel{E}_T + 2\text{jets}$ (\cancel{E}_T). The shaded areas are excluded by experiment (EX) or by theoretical constraints (TH). The black curves correspond to fixed values of squark and gluino masses and the relic dark matter density Ωh^2 [156].

measurement of the kinematics of decay cascades and to perform a global fit of the theoretical predictions to the observed data. The global fit is expected to allow to probe the compatibility of the data with the various SUSY models and e.g. to disentangle the different proposed mechanisms of SUSY breaking.

In particular if R -parity is conserved, the absolute measurement of the masses of supersymmetric particles is not possible since the final states contain LSPs, which escape detection. But the determination of endpoints of various mass distributions will allow to measure mass differences. Figure 8.36 (left) shows the invariant mass of opposite sign electrons and muons

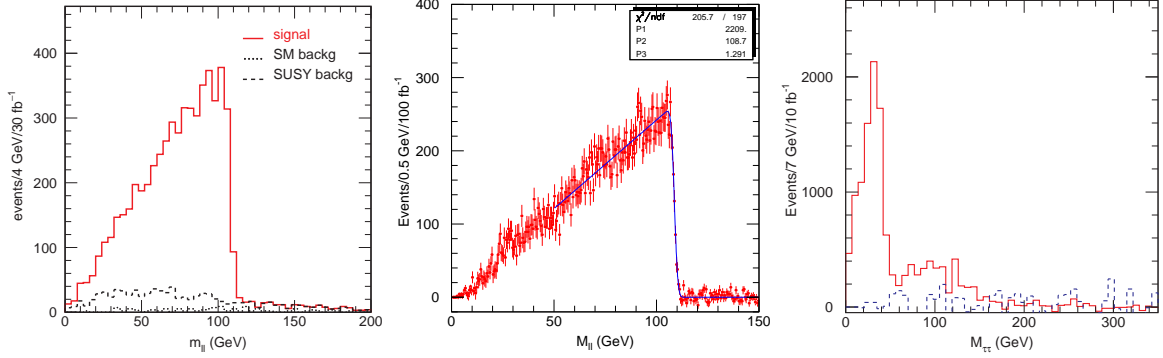


Figure 8.36: *Left:* Distribution of the di-lepton mass for a SUSY signal from the 2-body decay $\tilde{\chi}_2^0 \rightarrow \tilde{\ell}_R^\pm \ell^\mp \rightarrow \tilde{\chi}_1^0 \ell^+ \ell^-$ with background contributions from Standard Model and SUSY. The parameters of the chosen SUSY point are given in Fig. 8.34.

Center: Fitting the di-lepton mass distribution after flavor subtraction allows to determine the endpoint of the mass distribution to a high precision. The mass spectrum is shown for an integrated luminosity of 100 fb⁻¹ for the same SUSY point .

Right: Di-tau mass distribution for a SUSY point (solid histogram) with large branching ratio into taus ($m_0 = 200$ GeV, $m_{1/2} = 200$ GeV, $A_0 = 0$, $\tan\beta = 45$ and $\mu < 0$), the decays $\tilde{\chi}_2^0 \rightarrow \tilde{\tau}\tau$ and $\tilde{\chi}_1^\pm \rightarrow \tilde{\tau}\nu_\tau$ dominate. The background from misidentified taus is indicated by the dashed histogram [154].

for the decay $\tilde{\chi}_2^0 \rightarrow \tilde{\ell}_R^\pm \ell^\mp \rightarrow \tilde{\chi}_1^0 \ell^+ \ell^-$. After flavor-subtraction², a fit is used to determine the endpoint of the mass spectrum, which is a function of $m_{\tilde{\chi}_2^0}$, $m_{\tilde{\ell}_R}$ and $m_{\tilde{\chi}_1^0}$ (Fig. 8.36 (center)). A precision of below 1 GeV can be achieved by using data corresponding to an integrated luminosity of 30 fb⁻¹.

For SUSY scenarios with large $\tan\beta$, the splitting of $\tilde{\tau}_1$ and the sleptons of the first and second generation can be increased in such a way that the lightest chargino and the second lightest neutralino decay dominantly into tau leptons. In this scenario, the discovery using the distribution of the effective mass is still possible but the determination of the endpoints of the mass distributions is more difficult [154]. Figure 8.36 (right) shows the $M(\tau, \tau)$ distribution for a SUSY point where the 2-body decays $\tilde{\chi}_2^0 \rightarrow \tilde{\tau}\tau$ and $\tilde{\chi}_1^\pm \rightarrow \tilde{\tau}\nu_\tau$ dominate. For this distribution, the endpoint is expected at 60 GeV. Pairs of tau leptons which originate from the decays of $\tilde{\chi}_3^0$ and $\tilde{\chi}_4^0$ are reconstructed beyond the endpoint. In such a scenario, the determination of the endpoint should be possible to a precision of 5 %. For this type of analysis the accurate understanding of the tau identification is expected to be of crucial importance.

²The background to di-electron and di-muon pairs from two independent decays into leptons can be estimated by considering electron-muon-events.

Summary

Searches for new physics beyond the Standard Model were performed in final states comprising muons, hadronically decaying taus and missing transverse energy. In extensions of the Standard Model, these signatures may result from the production of still unobserved particles like Higgs bosons or supersymmetric particles. The used data sets of $p\bar{p}$ collisions were provided by the Tevatron accelerator at a center-of-mass energy of 1.96 TeV and were recorded by the DØ detector.

The first analysis searched for the production of neutral Higgs bosons Φ with subsequent decay to tau pairs using a data set corresponding to an integrated luminosity of $\mathcal{L} = 299 \text{ pb}^{-1}$. Selection criteria were developed to efficiently separate the signal from Standard Model background processes. Within the scope of the present thesis, the obtained results in the $\Phi \rightarrow \tau\tau \rightarrow \mu + \tau_h + X$ final state were combined with those obtained in the $\Phi \rightarrow \tau\tau \rightarrow e + \tau_h + X$ and $\Phi \rightarrow \tau\tau \rightarrow e + \mu + X$ final states with τ_h indicating a hadronically decaying tau. No evidence of a signal was found and an upper limit on the production cross section of neutral Higgs bosons decaying to tau pairs was set at the 95 % confidence level as a function of the Higgs boson mass M_Φ . The observed upper limit varies between 36.2 pb for $M_\Phi = 100 \text{ GeV}$ and 0.58 pb for $M_\Phi = 300 \text{ GeV}$.

In a combination with a search for the associated Higgs boson production in the $\Phi b(\bar{b}) \rightarrow b\bar{b}b(\bar{b})$ final state, the result was interpreted in the Minimal Supersymmetric extension of the Standard Model (MSSM). The MSSM Higgs sector comprises three neutral Higgs bosons (h, H, A), which have enhanced couplings to down-type fermions at large values of $\tan\beta$, the ratio of the vacuum expectation values of the Higgs fields. At leading order the Higgs sector is fully specified by two parameters generally chosen as the pseudo-scalar Higgs mass M_A and $\tan\beta$. Upper limits on $\tan\beta$ were determined in two benchmark scenarios (m_h^{max} and no-mixing scenario) for positive and negative values of the Higgs mass parameter μ . For $M_A < 160 \text{ GeV}$, typical upper limits on $\tan\beta$ were set in the range of $\tan\beta < 54$ to $\tan\beta < 80$. For larger Higgs masses the limits weaken and reach values of $\tan\beta \lesssim 100$ for $M_A \approx 200 \text{ GeV}$.

These results are complementary to the LEP II results, which are limited to $M_A \lesssim 92 \text{ GeV}$ for all values of $\tan\beta$ or to small values of $\tan\beta$ at large M_A . At the time of publication,

the results represented the world's most stringent limits on $\tan\beta$. Meanwhile, the limits were improved by updated results from the DØ and CDF collaborations based on data sets corresponding to an integrated luminosity of 1 fb^{-1} and 1.8 fb^{-1} , respectively.

The second analysis searched for the associated production of the lightest chargino and the second lightest neutralino with subsequent decays to three charged leptons (*trilepton signature*). This signature represents one of the most promising channels in the search for Supersymmetry at the Tevatron due to the small number of Standard Model background processes contributing to the final state. Selections were developed using multivariate analysis techniques to identify the signal in the final state consisting of a muon, a hadronically decaying tau, a third lepton of any generation and missing transverse energy.

In order to maximize the sensitivity for tau leptons, the third lepton was reconstructed using three different algorithms: isolated track, hadronically decaying tau and low energetic hadronically decaying tau. The former and the latter one were developed for this analysis. Low energetic taus were reconstructed based on the separately identified decay products of hadronical 1-prong tau decays. In order to verify the performance of the developed algorithm, it was used to select $Z/\gamma^* \rightarrow \tau\tau$ events in the $\mu + \tau_h$ final state. In these events the invariant mass of the visible decay products of the hadronically decaying taus was reconstructed.

After having applied all developed selection criteria, two events were observed in the data, which is consistent with the expectation from the Standard Model backgrounds. Since no evidence for a signal was found, upper limits on the trilepton cross section $\sigma(\tilde{\chi}_1^\pm \tilde{\chi}_2^0) \times \text{BR}(3\ell)$ at the 95 % confidence level were set as a function of the lightest chargino mass $m_{\tilde{\chi}_1^\pm}$, the lightest slepton mass $m_{\tilde{\ell}}$ and the branching ratio to tau leptons. In a scenario of degenerate slepton and chargino masses, values of $\sigma(\tilde{\chi}_1^\pm \tilde{\chi}_2^0) \times \text{BR}(3\ell) > 0.15 \text{ pb}$ were excluded for $m_{\tilde{\chi}_1^\pm} \approx 140 \text{ GeV}$.

The results were interpreted in the mSUGRA model where they restrict the parameter space beyond existing limits from the LEP experiments. The interpretation was performed in the plane stretched by m_0 and $m_{1/2}$ for $\tan\beta = 3$, $A_0 = 0$ and $\mu > 0$. The excluded parameter space reaches up to chargino masses of 134 GeV . The results were interpreted as a limit on $\tan\beta$ as well. In a scenario of light degenerate chargino and stau masses ($m_{\tilde{\chi}_1^\pm} = 104 \text{ GeV}$, $A_0 = 0$ and $\mu > 0$), values of up to $\tan\beta = 7.5$ were excluded, which significantly extends the LEP limit of $\tan\beta > 2.1$.

The impact of the presented analysis in a combination with additional trilepton searches in the $e\ell\ell$, $\mu\mu\ell$ and $e\mu\ell$ final states, which were not finalized at the time of writing, was studied. It was found that sensitivity is expected up to chargino masses of about 170 GeV depending on the specific scenario. The sensitivity in terms of $\tan\beta$ is extended significantly by the presented analysis due to its enhanced sensitivity to tau leptons in the final state.

The sensitivity of the search is mainly limited by the amount of available data. At the end of Run II of the Tevatron, the DØ and CDF collaborations expect to record data corresponding to an integrated luminosity of about 7 fb^{-1} per experiment. The sensitivity of combined DØ and CDF trilepton searches is expected to increase up to chargino masses of about 200 GeV in a scenario of degenerate slepton and chargino masses.

In the near future, the search for supersymmetric particles will be continued at the LHC with the experiments ATLAS and CMS. It is expected that the two experiments will be able to probe supersymmetric particle masses up to about 2.5 TeV and to observe or to rule out the existence of low-mass Supersymmetry.



Statistical Methods

In particle physics, two competing methods for calculating limits at a physical boundary are discussed, the Bayesian and the frequentist approach. Before introducing the frequentist approach, which is used in the present thesis, a brief overview of the basic terminology of statistical data analysis is given. Thorough introductions to the concepts of statistical data analysis can be found in various text books, e.g. [157, 158], while the method used for calculating combined limits is discussed in [36, 159, 160].

A.1 General Aspects

Interpretation of Probability

There are two main interpretation of probability used in the literature. In the most commonly used interpretation as a *relative frequency*, a probability $P(A)$ represents the fraction of times that the outcome A occurs in the limit that a measurement is repeated $n \rightarrow \infty$ times:

$$P(A) = \lim_{n \rightarrow \infty} \frac{\text{number of occurrences of outcomes } A}{\text{Number of measurements } n}. \quad (\text{A.1})$$

This interpretation is useful e.g. in particle physics where repeated particle collisions can be regarded as repeated experiments.

The interpretation as *subjective* or *Bayesian probability* is used e.g. to quantify systematic uncertainties. The elements of a sample space S are regarded as statements, called *hypotheses*, that are either true or false. The probability of a certain hypothesis is interpreted as the degree of belief that hypothesis H is true:

$$P(H) = \text{degree of belief that hypothesis } H \text{ is true.} \quad (\text{A.2})$$

One hypothesis of the sample space has to be true $P(S) = 1$. This interpretation of probability is more general and includes the interpretation as relative frequency if one considers the statement that an experiment will result in an outcome a certain fraction of times as a hypothesis.

Probability Density Function

For an experiment with the outcome x in a continuous range, the probability of observing a value in the interval $[x, x + dx]$ is given by $f(x)dx$ where $f(x)$ is called the probability density function (p.d.f.). The p.d.f. is always normalized to unit area.

Expectation values

The expectation value $E[u(x)]$ of any function $u(x)$ of a random variable x distributed according to the p.d.f. $f(x)$ is defined as

$$E[u(x)] = \int_{-\infty}^{+\infty} u(x)f(x)dx, \quad (\text{A.3})$$

with $E[u + v] = E[u] + E[v]$ and $E[cu + k] = cE[u] + k$ for any function $u(x)$ and $v(x)$, and constants c and k . The n^{th} moment of x is defined as

$$\alpha_n \equiv E[x^n] = \int_{-\infty}^{+\infty} x^n f(x)dx, \quad (\text{A.4})$$

and the n^{th} central moment of x is

$$m_n \equiv E[(x - \alpha_1)^n] = \int_{-\infty}^{+\infty} (x - \alpha_1)^n f(x)dx. \quad (\text{A.5})$$

Then the mean of the p.d.f. is given by $\mu_x \equiv \alpha_1$ and the variance by $V[x] \equiv m_2 = \alpha_2 - \mu_x^2$, with $V[cx + k] = c^2V[x]$. The *standard deviation* $\sigma_x = \sqrt{V[x]}$ is often used as a measure of the width of the distribution. The *covariance* of two random variables x and y is

$$\text{cov}[x, y] = E[(x - \mu_x)(y - \mu_y)] = E[xy] - \mu_x\mu_y, \quad (\text{A.6})$$

with the *correlation coefficient* $\rho_{xy} = \text{cov}[x, y]/\sigma_x\sigma_y$.

Probability Distributions

The number of success n in N trails of a random experiment with two possible outcomes and a success probability of p is given by the *binomial distribution*

$$f(n; N, p) = \frac{N!}{n!(N - n)!} p^n (1 - p)^{N - n}. \quad (\text{A.7})$$

The expectation value of n is $E[n] = Np$ and the variance is $V[n] = Np(1 - p)$.

For $p \rightarrow 0$, $N \rightarrow \infty$, while the product $Np \rightarrow \mu$ remains finite, the binomial distribution takes the form of a *Poisson distribution*

$$f(n; \mu) = \frac{\mu^n}{n!} e^{-\mu} \quad (\text{A.8})$$

for the integer random variable $n = 0, 1, 2, \dots, \infty$. The p.d.f. has one parameter μ , which represents the expectation value and the variance $E[n] = V[n] = \mu$. An example for a Poisson distributed random variable is the number of observed events of a certain type in a particle scattering experiment. Here, the expectation value of the number of observed events

is $\mu = \sigma\mathcal{L}\epsilon$, with the cross section σ , the integrated luminosity \mathcal{L} and the efficiency ϵ to observe and reconstruct the event in the detector.

For large values of μ the Poisson distribution approaches the *Gaussian distribution*:

$$f(x; \mu, \sigma^2) = \frac{1}{\sqrt{2\pi\sigma^2}} \exp\left(-\frac{(x - \mu)^2}{2\sigma^2}\right), \quad (\text{A.9})$$

with the expectation value $E[x] = \mu$ and the variance $V[x] = \sigma^2$. For a standard Gaussian, $\mu = 0$ and $\sigma^2 = 1$, the *cumulative distribution* $F(a) = \int_{-\infty}^a f(x)dx$ is related to the error function $\text{erf}(y)$ according to

$$F(a) = \int_{-\infty}^a f(x; 0, 1)dx = \frac{1}{2} \left[1 + \text{erf}(x/\sqrt{2}) \right]. \quad (\text{A.10})$$

Values of F are listed e.g. in [157]. The probabilities that x lies in the range of $\mu \pm 1\sigma$, $\mu \pm 2\sigma$, $\mu \pm 3\sigma$ are 68.3 %, 95.5 % and 99.7 %, respectively. The *central limit theorem* states that the sum of n independent continuous random variables x_i with mean μ_i and variances σ_i^2 becomes a Gaussian random variable with mean $\mu = \sum_{i=1}^n \mu_i$ and variance $\sigma^2 = \sum_{i=1}^n \sigma_i^2$ in the limit that n approaches infinity. The theorem is the foundation of treating measurement errors as Gaussian random variables.

Statistical tests

Statistical test are used to quantify the degree of consistency of an observed measurement with different given predictions, called *hypotheses*. In searches for new physics, a prediction of an established theory, the *null hypothesis* H_0 , is often compared to the prediction by a competing theory, the *alternative hypothesis* H_1 . An experiment is performed in order to decide whether to reject H_0 in favor of H_1 .

Let the experiment result in a finite amount of n measured values $\mathbf{x} = (x_1, \dots, x_n)$ with joint p.d.f.s $f(\mathbf{x}|H_0)$ and $f(\mathbf{x}|H_1)$. In order to investigate the agreement between observed data and a hypothesis, a variable $t(\mathbf{x})$ called *test statistic* is constructed, which differs maximally for the competing hypotheses. In general it could also be the original vector of data values \mathbf{x} . Figure A.1 illustrates the p.d.f.s $g(t|H_0)$ and $g(t|H_1)$ for the test statistic t under the assumption of H_0 and H_1 , respectively. In order to reject or accept H_0 , one defines a *critical region* $t > t_{\text{cut}}$. Its complement is called the *acceptance region*. If the observed value of t lies in the critical region, H_0 is rejected. The *significance level* of the test α is defined independently of H_1 as the probability to observe t in the critical region under the assumption of the hypothesis H_0 :

$$\alpha = \int_{t_{\text{cut}}}^{\infty} g(t|H_0)dt. \quad (\text{A.11})$$

As a consequence, there is the probability α of an *error of the first kind* to reject H_0 even if H_0 is true. The *error of the second kind* β is to the accept H_0 because the observed value of t is smaller than t_{cut} even if the hypothesis H_1 is true. The probability of an error of the second kind is:

$$\beta = \int_{t_{-\infty}}^{t_{\text{cut}}} g(t|H_1)dt \quad (\text{A.12})$$

and $1 - \beta$ is called the *power* of the test to discriminate against the alternative hypothesis H_1 . Typically for rejecting an established theory H_0 (claiming a discovery), it is required that

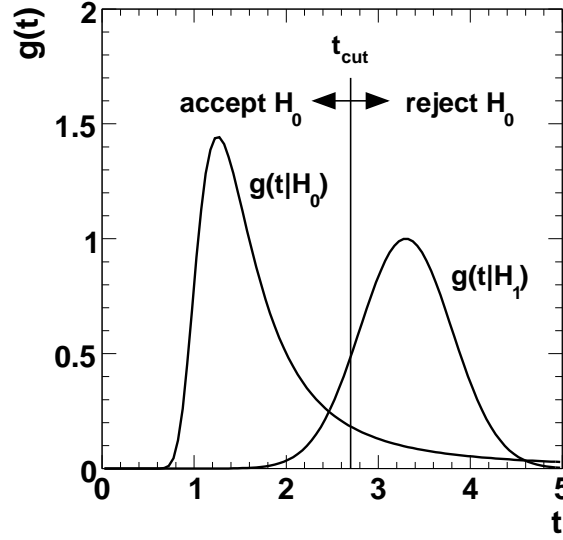


Figure A.1: Probability densities for test statistic t under the assumption of the hypotheses H_0 and H_1 .

$\alpha < 5.7 \times 10^{-7}$ (5σ), while for the exclusion of an alternative theory H_1 a value of $\beta < 0.05$ (1.96σ) is usually regarded as sufficient.

According to the *Neyman-Pearson lemma* the optimal test statistic with the maximal power and therefore the lowest probability of an error of the second kind for a certain α is given by the *likelihood ratio*

$$\lambda(\mathbf{x}) = \frac{f(\mathbf{x}|H_0)}{f(\mathbf{x}|H_1)}. \quad (\text{A.13})$$

Confidence Interval and Limits

A *confidence interval* is a parameter region which includes the true value of an unknown parameter θ with a certain probability. For a p.d.f. $f(x; \theta)$ with the outcome of an experiment x , the probability that the true values of θ lies inside the confidence interval at the *confidence level* $1 - \alpha$ is:

$$P(x_1 < x < x_2; \theta) = 1 - \alpha = \int_{x_1}^{x_2} f(x; \theta) dx \quad (\text{A.14})$$

Central intervals are constructed in such a way that the probabilities below x_1 and above x_2 are $\alpha/2$. Often *one-sided confidence intervals* are referred to as *upper* or *lower limits* where the probability on one side of the interval is zero.

A.2 Confidence Level Computation for Combined Searches with Small Statistics

The combination of results often increases significantly the sensitivity to small signals as they are expected in searches for new physics. Usually, the expected number of signal and

background events is small and only a few candidate events are observed in data. In particular, a combination of search results is desirable if the analyses are limited by the collected amount of data. Furthermore, binning the search results in their discriminant variables, e.g. reconstructed invariant mass, allows to increase the sensitivity by treating each bin as a statistically independent counting experiment.

For n independent counting experiments, a simple approach to constructing a test statistic is to use the number of events in a certain region of phase space, the *signal region*. Then the null hypothesis H_0 is given by the number of expected background events from the Standard Model, Poisson distributed with mean value b_i (*background hypothesis*). A signal of new physics is expected as an enhancement over the background, Poisson distributed with mean value $s_i + b_i$ (*signal+background hypothesis*). According to Eq. A.13, the likelihood ration, which is the optimal choice for a test statistic, is given by

$$Q = \frac{P_{\text{poiss}}(\text{data}|\text{signal} + \text{background})}{P_{\text{poiss}}(\text{data}|\text{background})} \quad (\text{A.15})$$

$$= \prod_{i=1}^n \left[\frac{e^{-(s_i+b_i)}(s_i + b_i)^{d_i}}{d_i!} \bigg/ \frac{e^{-b_i}b_i^{d_i}}{d_i!} \right] \quad (\text{A.16})$$

where the product runs over all combined counting experiments and d_i represents the number of observed events. This can be expressed as

$$-2 \ln Q = 2 \sum_{i=1}^n s_i - 2 \sum_{i=1}^n d_i \ln \left(1 + \frac{s_i}{b_i} \right), \quad (\text{A.17})$$

where it is found that the log-likelihood ratio is governed by a sum over the number of observed candidate events weighted by a factor depending on the signal-to-background ratio of the according counting experiment.

The confidence level (CL) for excluding the possibility of simultaneous presence of a signal from new physics and background (signal+background hypothesis) is

$$CL_{s+b} = P_{s+b}(Q \leq Q_{\text{obs}}) = \beta. \quad (\text{A.18})$$

This is the probability that the test statistic is smaller or equal to the observed value in data under the assumption of the presence of signal and background. The CL for the presence of only background is

$$CL_b = P_b(Q \leq Q_{\text{obs}}) = 1 - \alpha, \quad (\text{A.19})$$

which represents the probability that background processes give a smaller or an equal number of events than are observed.

Exclusion limits can be given in terms of the confidence level $(1 - CL_{s+b})$. But this has the unsatisfactory property that the signal (or even the background) may be excluded at a high confidence level if too few candidate events are observed to account for the estimated background. In order to be less sensitive to this effect, the confidence level in the *modified frequentist approach* is defined as the ratio of the pure frequentist confidence level CL_{s+b} and CL_b :

$$CL_s = \frac{CL_{s+b}}{CL_b} = \frac{\beta}{1 - \alpha}. \quad (\text{A.20})$$

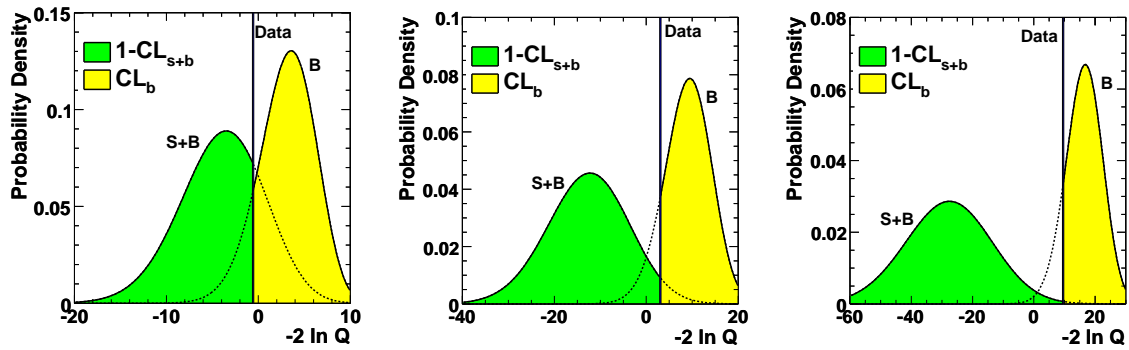


Figure A.2: Illustration of the evolution of the p.d.f.s of signal+background (S+B) and background hypothesis (B) from low sensitivity (left) to sensitivity for an exclusion at the 95 % CL (center) and to higher sensitivity (right).

This implies a small reduction of sensitivity but the resulting limit can not be more restrictive than the one obtained by using CL_{s+b} . A signal hypothesis is considered as excluded at the 95 % CL if $CL_s < 0.05$, as illustrated in Fig. A.2. An implementation of the CL_s method is available e.g. in the TLIMIT package [161], which is based on the usage of Poisson distributed pseudo experiments.

The *expected confidence intervals* are calculated assuming that the observed number of events is given by the number of expected background events in order to quantify how well an experiment performs in excluding a signal under the assumption of the absence of a signal.

Systematics

Systematic uncertainties and their correlations are taken into account using a generalization of the method of Cousins and Highland [162]. Their effect is computed by averaging over possible values of signal and background given by their systematic uncertainty probability distributions. These probabilities are assumed to be Gaussian distributed, while a lower cut off at zero removes negative values for signal and background.

B

Estimation of the Multi-Jet Background for the Chargino/Neutralino Search

Similar to the Higgs analysis, events from Standard Model processes that lead to final states with jets are an important background since jets can be misidentified as leptons and in particular as hadronically decaying tau leptons. In addition, muons resulting from bottom quark decays can pass the isolation criteria. Since the SUSY signal is expected at low lepton momenta, the relative contributions from this background are larger than in the Higgs analysis and a more detailed study is required.

The background contributions from multi-jet production are determined directly from data. Inverting the calorimeter isolation criteria and skipping the tracker isolation criteria for muons allows to define the multi-jet sample. It consists of events where the muons are not isolated and are part of a jet. The method is based on the assumption that the muon isolation and the shape of all kinematic distributions used in the selection are uncorrelated. Exceptions are addressed in the following.

Since the production rate for non-isolated muons, which are lying inside a jet, is much larger than for isolated muons where the signal is expected, the multi-jet sample needs to be normalized. In order to ensure that the normalization is not biased by other backgrounds, the following cuts select a data sample in which the background from multi-jet events dominates and in which the normalization procedure can be performed:

- A muon is reconstructed in the event with $p_T^\mu > 15$ GeV. In the multi-jet sample it is required to pass the inverted calorimeter isolation criteria, while for all other samples it is required to be isolated as defined in Sec. 4.3.
- One tau candidate is found in the event which fulfills all identification criteria of Sec. 8.3 except the cut on NN_τ . The cut on NN_τ is inverted in order to reject $Z/\gamma^* \rightarrow \tau\tau$ events. To ensure, that the selected topology is still similar to the one in the main analysis, loose cuts are applied on the NN_τ output: $NN_\tau > 0.10$ (τ -type 1) and $NN_\tau > 0.05$ (τ -type 2).

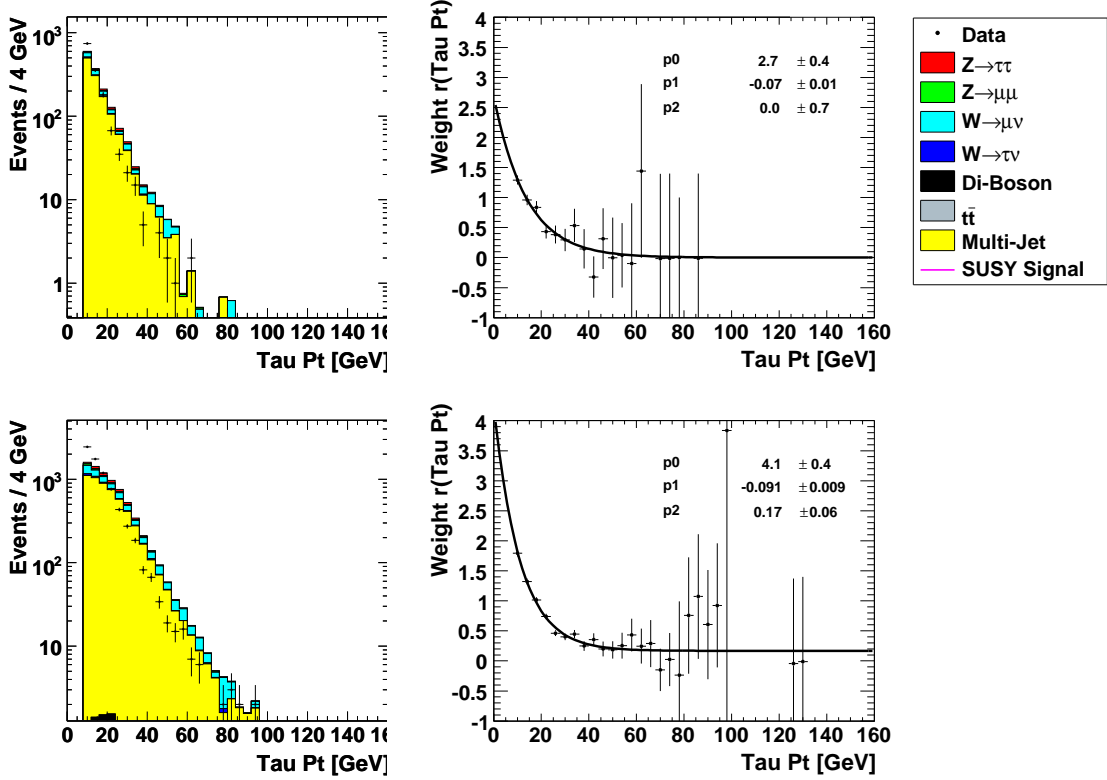


Figure B.1: The distributions of p_T^τ in the multi-jet dominated sample before applying the weight $r(p_T^\tau)$ for τ -type 1 (top) and τ -type 2 (bottom) including the obtained result of the fit of $r(p_T^\tau)$.

- An upper cut on the reconstructed missing transverse energy $\cancel{E}_T < 25$ GeV suppresses contributions from $W^\pm \rightarrow \ell^\pm \nu_\ell$ processes.
- Selecting events that contain only one muon allows to remove events from $Z/\gamma^* \rightarrow \mu\mu$.

Having applied these criteria to the data sample, to the multi-jet sample and to all Standard Model Monte Carlo samples, the remaining contributions are dominated by multi-jet events. One finds that the integral and the shape of several distributions do not agree in data and simulation. This is corrected in five steps in the normalization procedure, which is performed separately for each τ -type. The accurate estimation of the multi-jet contributions to the background is more complex than in the Higgs analysis due to the lower cuts on p_T^τ and NN_τ .

1. An overall normalization constant k scales the integral of the multi-jet sample to data.
2. As explained in Sec. 6.3, the inverted isolation criteria of the multi-jet sample lead to harder spectra of p_T^μ and p_T^τ . An exponential normalization function $r(p_T^\tau)$ compensates this difference:

$$r(p_T^\tau) = a_0 e^{p_T^\tau + a_1} + a_2. \quad (\text{B.1})$$

It is determined by fitting the quotient of the p_T^τ distributions in data and multi-jet sample after subtracting other background contributions (as simulated by Monte Carlo) from the data sample. Figure B.1 shows the distributions of p_T^τ before applying $r(p_T^\tau)$ as a weight to each event of the multi-jet sample including the results of the fit.

3. Having applied $r(p_T^\tau)$, one still finds differences in the distribution of \cancel{E}_T between the data and the multi-jet sample, as shown in Fig. B.2, which can be explained in the following way. In average, there is one additional jet present in each event of the multi-jet sample compared to the data sample since the non-isolated muon is part of a jet. The energy of this jet can be mismeasured, which leads to a decreased \cancel{E}_T -resolution and also to an increased amount of \cancel{E}_T in the multi-jet sample. This effect is compensated by applying a weight to each event in the multi-jet sample in the form of an \cancel{E}_T -dependent Gaussian (see Fig. B.2):

$$s(\cancel{E}_T) = \frac{b_0}{\sqrt{2\pi b_1}} \exp\left(-\frac{\cancel{E}_T^2}{2b_1^2}\right) + b_2. \quad (\text{B.2})$$

Applying this weight results in a significantly better agreement of the distribution of \cancel{E}_T related quantities (see Fig. B.3 (top)), confirming that the required correction is an consequence of the increased amount of \cancel{E}_T in the multi-jet sample.

4. After applying $r(p_T^\tau)$ and $s(\cancel{E}_T)$, a linear normalization function $t(\text{RMS}^\tau)$ fixes the differences in input distributions of the tau neural network (Fig. B.4):

$$t(\text{RMS}^\tau) = c_0 \text{RMS}^\tau + c_1. \quad (\text{B.3})$$

A definition of RMS^τ , which is a measure of the width of the tau cluster, is given in Sec. 4.4. This step becomes important as soon as the cut on tau neural net is applied. The multi-jet background would be underestimated without the cut already at the preselection level of the SUSY analysis.

5. After applying all previous factors, the events are weighted in bins of jet multiplicity $u(N_{\text{jets}})$ (Fig. B.5). This step especially affects the distribution of the scalar sum of all jets in the event H_T (as defined in Eq. (8.2)) since the multi-jet sample has in average one jet more than the data sample, which gives raise to larger H_T values as shown in Fig. B.3 (bottom).

Thus, the weight $f = k \times r(p_T^\tau) \times s(\cancel{E}_T) \times t(\text{RMS}^\tau) \times u(N_{\text{jets}})$ is applied to each event of the multi-jet sample. After this normalization process, which is done separately for each τ -type, data and simulated background show good agreement in the multi-jet dominated sample. Distributions of the used quantities at every stage of the normalization procedure are shown in [145].

It is important to mention that various modifications of the normalization procedure to the multi-jet sample have been considered. The explained method, in which the corrections are well motivated, gives the best agreement in terms of data and simulation and therefore the highest confidence that the multi-jet background is modelled in sufficient accuracy. Furthermore, it has to be kept in mind that the multi-jet background is no dominating background at the end of the selection of the SUSY signal.

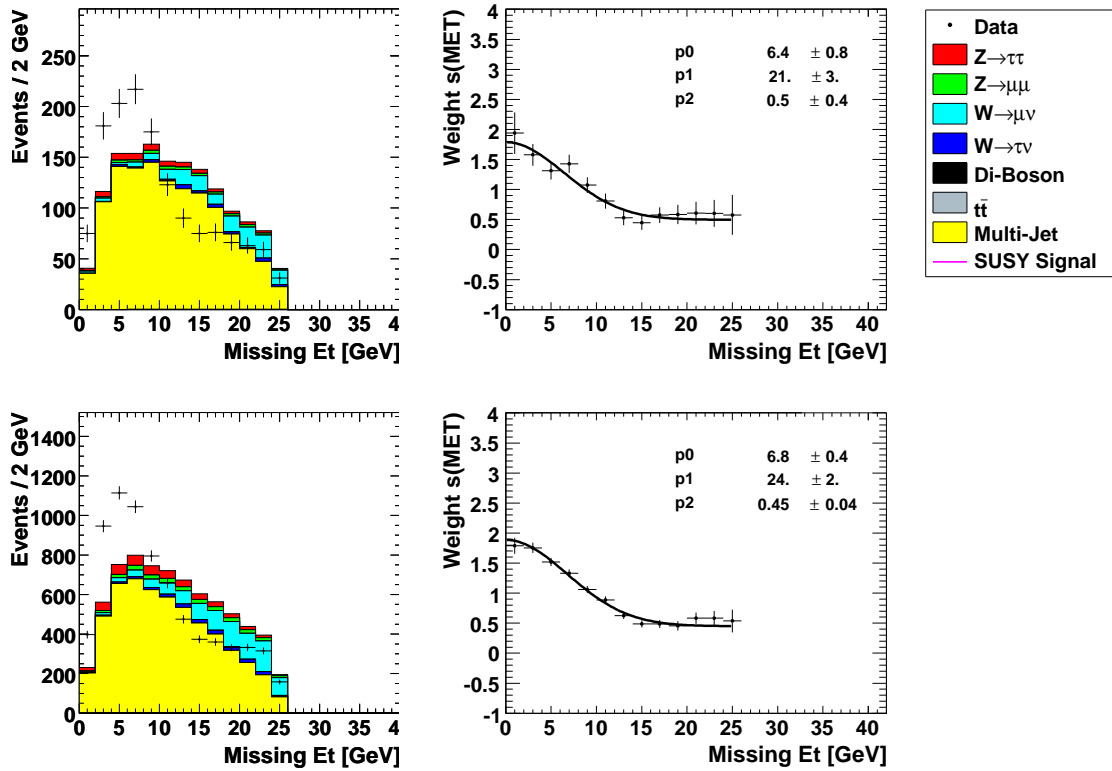


Figure B.2: The distributions of E_T in the multi-jet dominated sample before applying the weight $s(E_T)$ for τ -type 1 (top) and τ -type 2 (bottom) including the obtained result of the fit of $s(E_T)$.

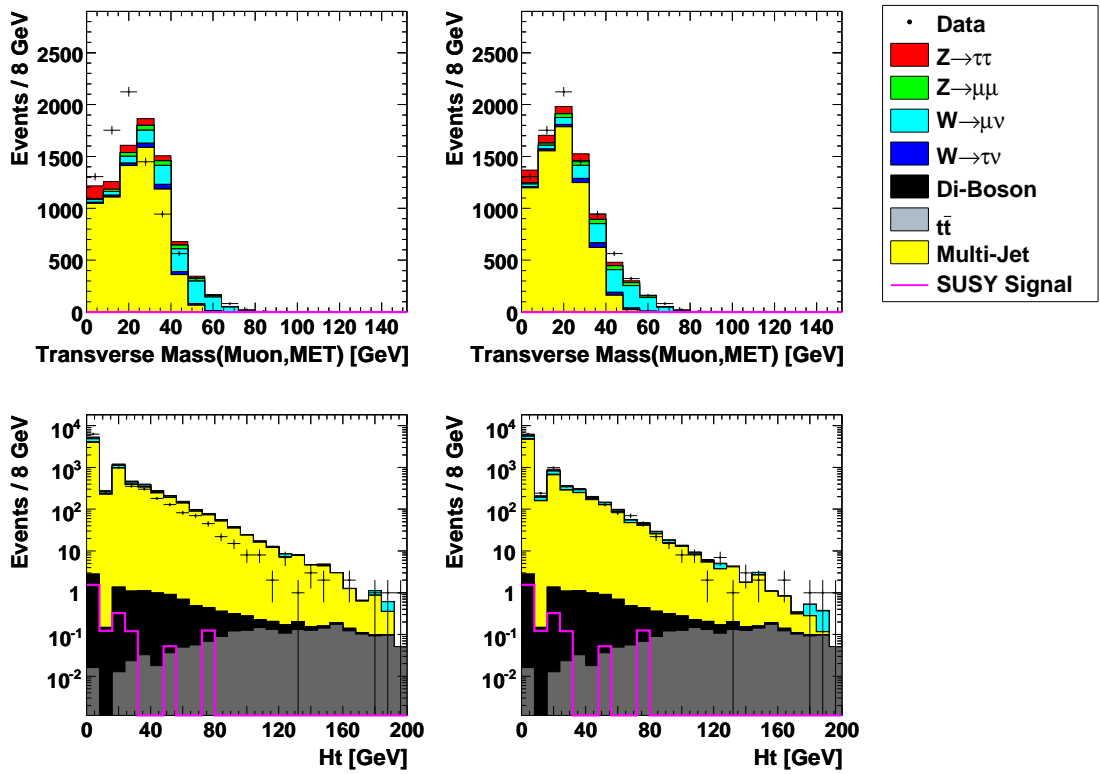


Figure B.3: The effect of the normalization of the multi-jet background is demonstrated in the sample dominated by multi-jet events for the distribution of H_T and m_T^μ (as defined in Eq. (8.2) and Eq. (6.2)). The accurate modeling of these two quantities is of particular importance for the later analysis since they are especially sensitive to the normalization procedure. The distributions are shown before (left) and after (right) applying the normalization factors.

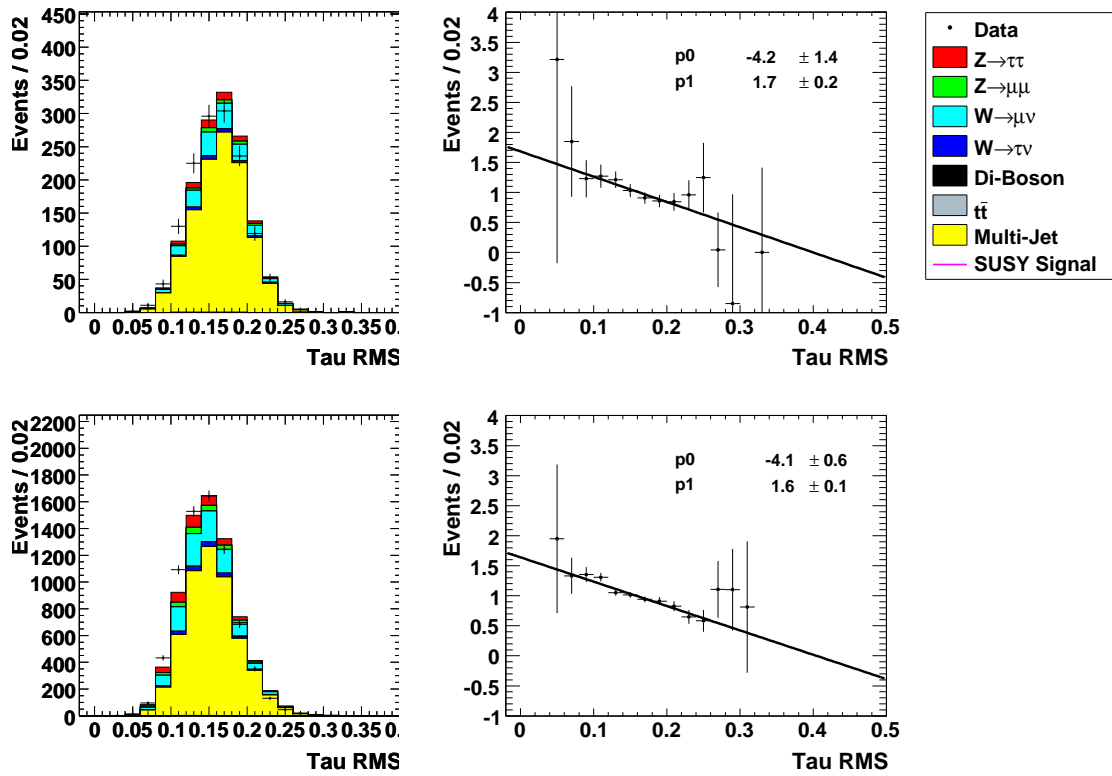


Figure B.4: The distributions of RMS^τ in the multi-jet dominated sample before applying the weight $t(\text{RMS}^\tau)$ for τ -type 1 (top) and τ -type 2 (bottom) including the obtained result of the fit of $t(\text{RMS}^\tau)$.

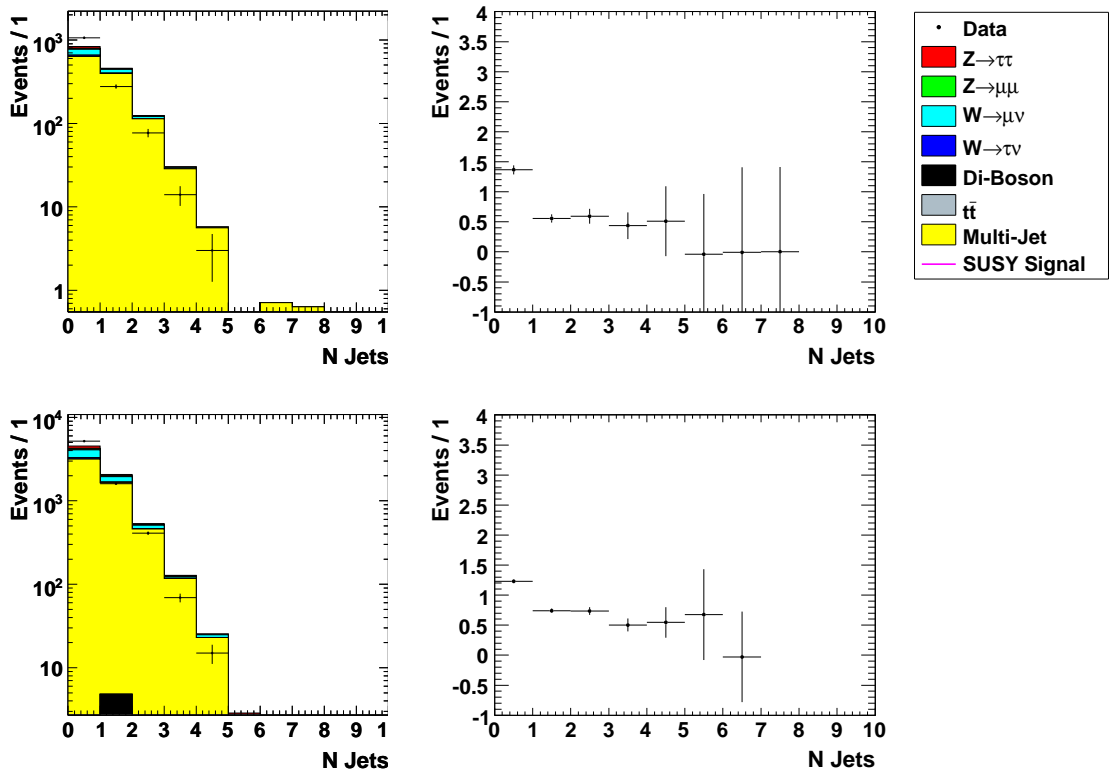
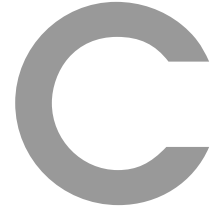


Figure B.5: The distributions of N_{jets} in the multi-jet dominated sample before applying the weight $u(N_{\text{jets}})$ for τ -type 1 (top) and τ -type 2 (bottom) including the obtained result of the fit of $u(N_{\text{jets}})$.



Generated mSURGA Monte Carlo Sample

Several SUSY signal samples are generated in order to interpret the results of the $\mu\tau_h\ell$ analysis and the combination with further trilepton analyses in the mSUGRA model. The SUSY points considered in this analysis are selected to allow for a parameterization of the selection efficiencies of all trilepton analyses in the $(m_0, m_{1/2})$ -plane.

The SUSY points for which a Monte Carlo sample is generated are indicated in Fig. C.1 in the $(m_0, m_{1/2})$ -plane. The remaining mSUGRA parameters are $\tan\beta = 3$, $A_0 = 0$ and $\mu > 0$. The SUSY points are grouped to five lines, so-called *scans*. The selection of the scans accounts for the two parameters $m_{\tilde{\chi}_1^\pm}$ and $m_\Delta = m_{\tilde{\ell}} - m_{\tilde{\chi}_2^0}$ that determine the kinematics in the parameter region where sensitivity is expected. Scans 1-4 are orthogonal to the transition line from 2-body decays to 3-body decays, where $m_\Delta = 0$, and allow a parameterization of the efficiencies as a function of m_Δ . In regions of rapidly changing branching ratio, the scan is performed in fine steps, i.e. for $m_{\tilde{\chi}_2^0} \approx m_{\tilde{\ell}}$ and $m_{\tilde{\chi}_2^0} \approx m_{\tilde{\nu}}$, while for regions with moderately changing branching ratios, the steps are wider. Scan 5 allows a parameterization as a function of $m_{\tilde{\chi}_1^\pm}$. Tables C.1-C.6 summarize the SUSY spectra of the generated SUSY Monte Carlo samples together with the trilepton cross section $\sigma(\tilde{\chi}_1^\pm \tilde{\chi}_2^0) \times \text{BR}(3 \text{ Leptons} + X)$.

The cross section is calculated using PROSPINO 2 [139] with the SUSY spectra determined by SOFTSUSY 2.0.14 [163]. The branching ratios are calculated by PYTHIA 6.323 [67], except in the 3-body decay region where the decay of lightest chargino and second lightest neutralino is mediated by sleptons and PYTHIA only approximates stau mixing effects. For this region, SDECAY 1.3 [164] is used. The Monte Carlo generator PYTHIA is used for the generation of the signal samples in combination with CTEQ6L1 parton distribution functions [66].

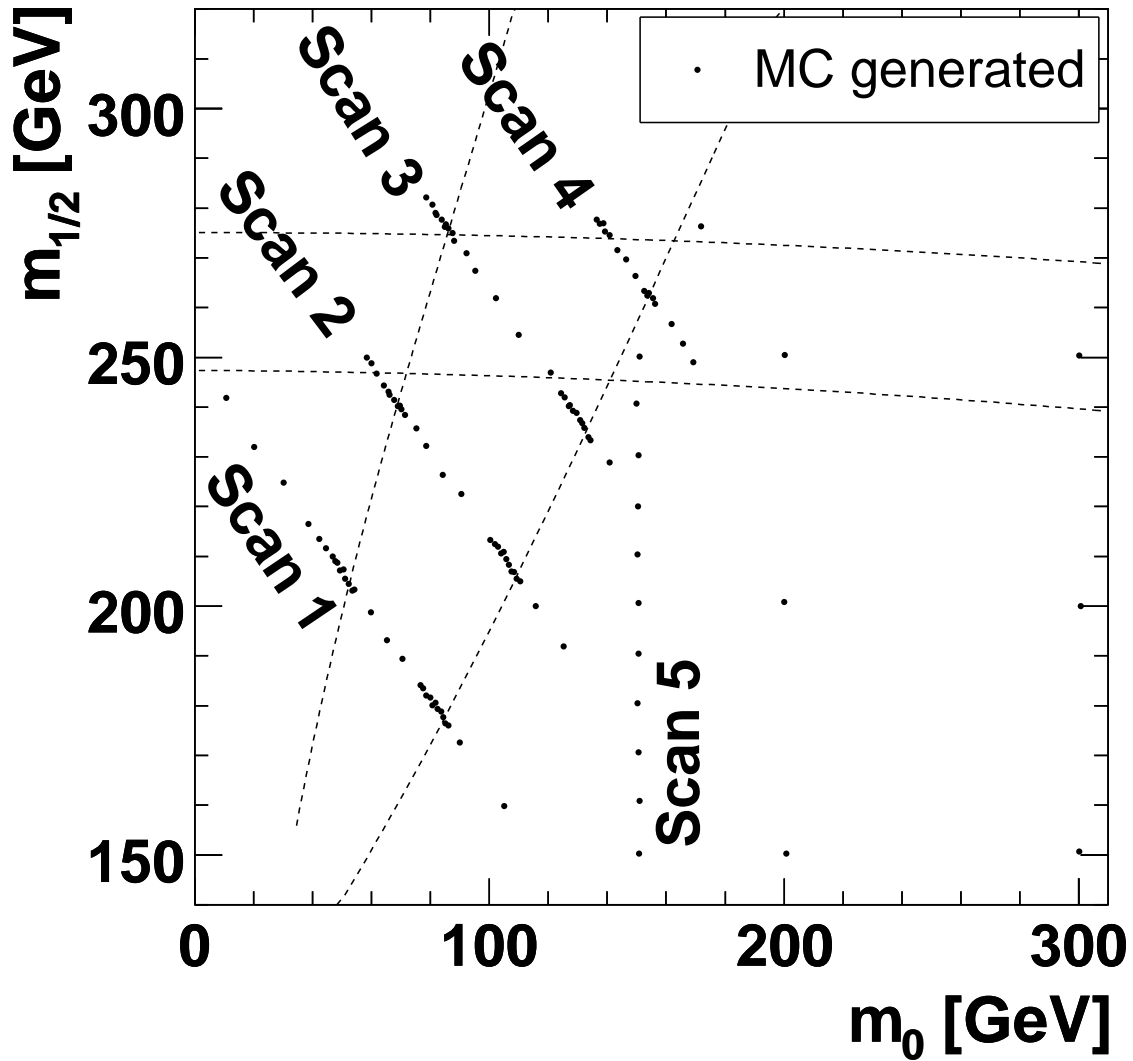


Figure C.1: Generated SUSY points in the mSUGRA model in the $(m_0, m_{1/2})$ -plane. The remaining mSUGRA parameters are $\tan\beta = 3$, $A_0 = 0$ and $\mu > 0$. The dashed lines indicate transition regions between different decay modes (see Sec. 8.1.3).

m_0 [GeV]	$m_{1/2}$ [GeV]	$m_{\tilde{\chi}_1^\pm}$ [GeV]	$m_{\tilde{\chi}_2^0}$ [GeV]	$m_{\tilde{\chi}_1^0}$ [GeV]	$m_{\tilde{e},\tilde{\mu}}$ [GeV]	$m_{\tilde{\tau}}$ [GeV]	$\sigma \times \text{BR}$ [pb]
10.0	241.0	167.6	167.2	90.2	99.6	98.2	0.0456
20.0	232.0	159.6	159.6	86.1	98.0	96.6	0.0688
30.0	224.0	152.6	152.9	82.5	97.9	96.5	0.1046
38.0	216.0	145.6	146.2	78.9	98.1	96.7	0.1615
42.0	213.0	143.0	143.7	77.6	98.8	97.4	0.1941
44.0	211.0	141.2	142.0	76.7	99.1	97.7	0.2152
46.0	210.0	140.4	141.2	76.2	99.7	98.3	0.2302
47.0	209.0	139.5	140.3	75.8	99.8	98.4	0.2415
48.0	208.0	138.6	139.5	75.3	100.0	98.6	0.2531
49.0	207.0	137.7	138.7	74.9	100.2	98.8	0.2667
50.0	207.0	137.7	138.7	74.9	100.7	99.3	0.2689
51.0	205.0	136.0	137.0	74.0	100.6	99.2	0.2880
52.0	204.0	135.0	136.2	73.5	100.8	99.4	0.2991
53.0	203.0	134.1	135.3	73.1	101.0	99.7	0.3074
54.0	203.0	134.1	135.3	73.1	101.6	100.2	0.3073
59.0	198.0	129.6	131.2	70.8	102.9	101.6	0.3558
65.0	193.0	125.1	127.0	68.5	105.1	103.8	0.4110
70.0	189.0	121.6	123.7	66.7	107.3	106.0	0.4580
76.0	184.0	117.2	119.6	64.4	110.1	108.8	0.4918
77.0	183.0	116.3	118.8	63.9	110.5	109.2	0.4891
78.0	182.0	115.4	118.0	63.5	111.0	109.7	0.4800
79.0	181.0	114.5	117.2	63.0	111.5	110.2	0.4590
80.0	180.0	113.7	116.3	62.6	111.9	110.7	0.4234
81.0	180.0	113.7	116.4	62.6	112.7	111.4	0.3917
82.0	179.0	112.8	115.5	62.1	113.1	111.9	0.1308
83.0	178.0	111.9	114.7	61.6	113.6	112.4	0.2931
84.0	177.0	111.0	113.9	61.2	114.2	112.9	0.1833
85.0	176.0	110.2	113.1	60.7	114.7	113.4	0.2723
86.0	175.0	109.3	112.3	60.3	115.2	113.9	0.2665
90.0	172.0	106.7	109.8	58.9	117.6	116.3	0.2557
105.0	159.0	95.4	99.3	52.7	127.0	125.8	0.2853

Table C.1: Parameters of the generated SUSY points for scan 1.

m_0 [GeV]	$m_{1/2}$ [GeV]	$m_{\tilde{\chi}_1^\pm}$ [GeV]	$m_{\tilde{\chi}_2^0}$ [GeV]	$m_{\tilde{\chi}_1^0}$ [GeV]	$m_{\tilde{e},\tilde{\mu}}$ [GeV]	$m_{\tilde{\tau}}$ [GeV]	$\sigma \times \text{BR}$ [pb]
58.0	249.0	174.6	174.3	93.8	117.1	115.9	0.0654
60.0	248.0	173.8	173.4	93.4	117.8	116.6	0.0694
61.0	246.0	172.1	171.8	92.5	117.7	116.5	0.0769
64.0	244.0	170.4	170.1	91.6	118.7	117.5	0.0875
65.0	243.0	169.6	169.3	91.1	119.0	117.7	0.0919
66.0	242.0	168.7	168.4	90.7	119.2	118.0	0.0957
67.0	241.0	167.9	167.6	90.3	119.5	118.3	0.0992
68.0	240.0	167.0	166.8	89.8	119.8	118.6	0.1024
69.0	240.0	167.0	166.8	89.8	120.3	119.1	0.1023
70.0	239.0	166.2	165.9	89.4	120.6	119.4	0.1050
71.0	238.0	165.2	165.1	88.9	120.9	119.7	0.1082
75.0	235.0	162.6	162.6	87.6	122.5	121.3	0.1175
78.0	232.0	160.0	160.1	86.3	123.5	122.4	0.1273
84.0	226.0	154.8	155.1	83.6	125.8	124.7	0.1484
90.0	222.0	151.4	151.9	81.9	128.9	127.8	0.1618
100.0	213.0	143.7	144.4	77.9	134.0	132.9	0.1784
101.0	212.0	142.8	143.6	77.5	134.5	133.4	0.1758
102.0	211.0	141.9	142.8	77.0	135.0	133.9	0.1714
103.0	210.0	141.1	141.9	76.6	135.6	134.5	0.1637
104.0	210.0	141.1	142.0	76.6	136.3	135.2	0.1556
105.0	209.0	140.2	141.1	76.2	136.9	135.8	0.1441
106.0	208.0	139.4	140.3	75.7	137.4	136.3	0.1283
107.0	207.0	138.5	139.5	75.3	138.0	136.9	0.0985
108.0	206.0	137.7	138.7	74.8	138.5	137.5	0.0082
109.0	205.0	136.8	137.8	74.4	139.1	138.0	0.0853
110.0	204.0	136.0	137.0	73.9	139.7	138.6	0.0827
115.0	200.0	132.6	133.7	72.2	142.8	141.8	0.0778
125.0	191.0	124.6	126.4	68.2	149.3	148.3	0.0810

Table C.2: Parameters of the generated SUSY points for scan 2.

m_0 [GeV]	$m_{1/2}$ [GeV]	$m_{\tilde{\chi}_1^\pm}$ [GeV]	$m_{\tilde{\chi}_2^0}$ [GeV]	$m_{\tilde{\chi}_1^0}$ [GeV]	$m_{\tilde{e},\tilde{\mu}}$ [GeV]	$m_{\tilde{\tau}}$ [GeV]	$\sigma \times \text{BR}$ [pb]
78.0	282.0	203.0	202.3	108.0	137.5	136.4	0.0218
80.0	280.0	201.3	200.6	107.1	138.1	137.0	0.0236
81.0	279.0	200.5	199.8	106.7	138.4	137.3	0.0243
82.0	278.0	199.6	198.9	106.3	138.7	137.6	0.0248
83.0	277.0	198.8	198.1	105.8	139.0	137.9	0.0251
84.0	276.0	198.0	197.3	105.4	139.3	138.2	0.0253
85.0	276.0	198.0	197.3	105.4	139.9	138.8	0.0249
86.0	275.0	197.1	196.5	105.0	140.2	139.1	0.0253
87.0	274.0	196.3	195.6	104.6	140.6	139.5	0.0257
88.0	273.0	195.4	194.8	104.1	140.9	139.8	0.0266
92.0	270.0	192.9	192.4	103.2	142.6	141.5	0.0292
95.0	267.0	190.4	189.9	101.9	143.7	142.7	0.0321
102.0	261.0	185.3	184.9	99.3	146.9	145.9	0.0394
110.0	254.0	179.5	179.1	96.2	150.9	149.8	0.0527
120.0	246.0	172.7	172.6	92.8	156.5	155.5	0.0593
124.0	242.0	169.4	169.3	91.1	158.7	157.7	0.0594
125.0	241.0	168.6	168.4	90.6	159.2	158.3	0.0583
126.0	240.0	167.7	167.6	90.2	159.8	158.8	0.0567
127.0	240.0	167.7	167.6	90.2	160.6	159.6	0.0542
128.0	239.0	166.9	166.8	89.8	161.2	160.2	0.0517
129.0	238.0	166.1	166.0	89.3	161.8	160.8	0.0482
130.0	237.0	165.3	165.1	88.9	162.3	161.4	0.0422
131.0	236.0	164.4	164.3	88.5	162.9	162.0	0.0277
132.0	235.0	163.6	163.5	88.0	163.5	162.6	0.0203
133.0	234.0	162.8	162.7	87.6	164.1	163.2	0.0276
134.0	233.0	161.9	161.8	87.2	164.7	163.8	0.0269
140.0	228.0	157.5	157.7	85.0	168.7	167.7	0.0255

Table C.3: Parameters of the generated SUSY points for scan 3.

m_0 [GeV]	$m_{1/2}$ [GeV]	$m_{\tilde{\chi}_1^\pm}$ [GeV]	$m_{\tilde{\chi}_2^0}$ [GeV]	$m_{\tilde{\chi}_1^0}$ [GeV]	$m_{\tilde{e},\tilde{\mu}}$ [GeV]	$m_{\tilde{\tau}}$ [GeV]	$\sigma \times \text{BR}$ [pb]
136.0	277.0	199.4	198.9	106.5	175.6	174.7	0.0161
137.0	276.0	198.6	198.1	106.1	176.2	175.3	0.0164
138.0	276.0	198.6	198.1	106.1	177.0	176.1	0.0162
139.0	275.0	197.8	197.3	105.7	177.5	176.6	0.0166
140.0	274.0	196.9	196.4	105.2	178.1	177.2	0.0174
143.0	271.0	194.4	194.0	104.0	179.8	178.9	0.0174
146.0	269.0	192.8	192.3	103.1	181.8	180.9	0.0173
149.0	266.0	190.3	189.9	101.8	183.6	182.7	0.0169
152.0	263.0	187.8	187.4	100.5	185.4	184.5	0.0102
153.0	262.0	187.0	186.6	100.1	186.0	185.1	0.0045
154.0	262.0	187.0	186.6	100.1	186.8	185.9	0.0062
155.0	261.0	186.1	185.8	99.7	187.5	186.6	0.0080
156.0	260.0	185.3	184.9	99.2	188.1	187.2	0.0079
161.0	256.0	182.0	181.7	97.5	191.5	190.6	0.0076
165.0	252.0	178.7	178.4	95.8	194.1	193.2	0.0079
169.0	249.0	176.2	175.9	94.5	197.0	196.1	0.0080

Table C.4: Parameters of the generated SUSY points for scan 4.

m_0 [GeV]	$m_{1/2}$ [GeV]	$m_{\tilde{\chi}_1^\pm}$ [GeV]	$m_{\tilde{\chi}_2^0}$ [GeV]	$m_{\tilde{\chi}_1^0}$ [GeV]	$m_{\tilde{e},\tilde{\mu}}$ [GeV]	$m_{\tilde{\tau}}$ [GeV]	$\sigma \times \text{BR}$ [pb]
150.0	150.0	88.8	93.0	48.9	164.8	163.8	0.1898
150.0	160.0	97.7	101.1	53.8	166.1	165.1	0.1357
150.0	170.0	106.6	109.4	58.7	167.5	166.5	0.0994
150.0	180.0	115.5	117.7	63.4	169.0	168.0	0.0746
150.0	190.0	124.4	126.0	68.0	170.6	169.6	0.0565
150.0	200.0	133.4	134.4	72.5	172.2	171.2	0.0432
150.0	210.0	142.1	142.8	77.1	173.8	172.9	0.0333
150.0	220.0	150.8	151.2	81.5	175.6	174.7	0.0260
150.0	230.0	159.6	159.6	86.0	177.4	176.5	0.0202
150.0	240.0	168.1	168.0	90.4	179.3	178.3	0.0157
150.0	250.0	176.7	176.4	94.8	181.2	180.3	0.0114

Table C.5: Parameters of the generated SUSY points for scan 5.

m_0 [GeV]	$m_{1/2}$ [GeV]	$m_{\tilde{\chi}_1^\pm}$ [GeV]	$m_{\tilde{\chi}_2^0}$ [GeV]	$m_{\tilde{\chi}_1^0}$ [GeV]	$m_{\tilde{e}, \tilde{\mu}}$ [GeV]	$m_{\tilde{\tau}}$ [GeV]	$\sigma \times \text{BR}$ [pb]
200.0	150.0	90.8	94.3	49.7	211.2	210.3	0.0580
200.0	200.0	134.8	135.5	73.0	217.0	216.1	0.0185
200.0	250.0	177.8	177.4	95.2	224.2	223.4	0.0046
300.0	150.0	95.1	97.4	51.5	307.3	306.4	0.0017
300.0	200.0	138.0	138.1	73.8	311.3	310.5	0.0023
300.0	250.0	180.1	179.5	95.7	316.4	315.6	0.0001
171.0	276.0	199.1	198.6	106.0	203.7	202.8	0.0014

Table C.6: Parameters of additionally generated SUSY points.

List of Tables

1.1	Fermions of the Standard Model	2
1.2	Bosons of the Standard Model	3
1.3	Couplings of the Standard Model Higgs boson to fermions and massive gauge bosons.	6
1.4	Superfield content of the Minimal Supersymmetric Standard Model	14
1.5	Factors to Higgs boson couplings predicted by the MSSM with respect to the Standard Model	16
1.6	SUSY parameters for the no-mixing and m_h^{\max} benchmark scenarios	17
3.1	Major parameters of the Tevatron	36
3.2	Thickness of the different calorimeter layers	40
4.1	Tau decay channels and branching ratios	49
4.2	Input variables for the three neural networks used for tau identification	53
5.1	List of the used single muon triggers	63
5.2	Description of the trigger names	64
5.3	Cross section times branching ratio and number of generated events for the different Standard Model background Monte Carlo samples	65
5.4	Parameters used for the correction of the track p_T resolution	71
6.1	Branching ratios of the possible $\Phi \rightarrow \tau\tau$ final states	77
6.2	Number of generated Monte Carlo events for the process $\Phi \rightarrow \tau\tau$	79
6.3	Summary of the selection criteria	82
6.4	Systematic uncertainties	89
6.5	Number of events observed in data and expected for background at different stages of the selection	91
6.6	Efficiency of the selection for a neutral MSSM Higgs boson	92
6.7	Numbers of events observed in data and expected for background for the three combined analysis channels	93
7.1	Summary of the selection criteria of the tau mass signal	110
7.2	Number of events observed in data and expected for background at different stages of the tau mass selection in $Z/\gamma^* \rightarrow \tau\tau$ events	114
8.1	SUSY parameters for the signal points considered in the SUSY analysis	124
8.2	Summary of the selection criteria	131
8.3	Number of selected events in data and of expected background events after each step of the selection	132

8.4	Signal efficiency and number of signal events expected after each step of the selection	133
8.5	Summary of the relative systematic uncertainties	148
8.6	Number of events observed, background events expected and signal events expected after applying all selection criteria	151
8.7	Kinematic properties of the objects reconstructed in the event selected in data in the $\mu + \tau_1 + \tau_2$ selection	153
8.8	Kinematic properties of the objects reconstructed in the event selected in data in the $\mu + \tau_1 + \tau_{LP}$ selection	153
C.1	Generated SUSY points in the mSUGRA model (scan 1)	183
C.2	Generated SUSY points in the mSUGRA model (scan 2)	184
C.3	Generated SUSY points in the mSUGRA model (scan 3)	185
C.4	Generated SUSY points in the mSUGRA model (scan 4)	186
C.5	Generated SUSY points in the mSUGRA model (scan 5)	186
C.6	Parameters of additionally generated SUSY points	187

List of Figures

1.1	Standard Model Higgs potential	5
1.2	Tevatron limit on the Standard Model Higgs production cross section	6
1.3	The resulting $\Delta\chi^2$ of a fit to electroweak precision data	7
1.4	Radiative corrections to the squared Higgs boson mass from fermions and bosons	8
1.5	Energy scale dependence of the couplings in the SM and in a MSSM scenario.	9
1.6	Example of the running of the soft supersymmetry breaking parameters	19
1.7	Prediction for M_W in the Standard Model and the MSSM as a function of the top quark mass	20
1.8	Combined LEP limits on the slepton and chargino mass	21
1.9	Combined LEP exclusion region in the $(m_0, m_{1/2})$ -plane	22
1.10	Combined LEP exclusion region in the $(\tan\beta, m_{\text{LSP}})$ -plane	23
1.11	DØ and CDF Run I upper limit on the associated production cross section of lightest chargino and second lightest neutralino times branching ratio into three leptons	23
1.12	Combined LEP exclusion regions in the $(M_A, \tan\beta)$ -plane	24
2.1	Cross sections and number of expected events for selected processes at the Tevatron	26
2.2	Parameterization of PDFs	28
2.3	Schematic view of the Drell–Yan production of a lepton pair in a $p\bar{p}$ collision	29
2.4	NLO QCD contributions for Drell–Yan processes	30
3.1	Tevatron luminosity	34
3.2	Schematic view of the Fermilab accelerator chain	35
3.3	The upgraded DØ detector	37
3.4	The central tracking system	38
3.5	Transverse momentum resolution of the tracking detector	38
3.6	Isometric view of the central and two end calorimeters	39
3.7	Schematic view of a portion of the DØ calorimeter	40
3.8	Schematic side view of the muon system	41
3.9	Overview of the DØ trigger and data acquisition system	42
3.10	Block diagram of the DØ trigger system	43
3.11	GEANT simulation of an electron in the DØ detector.	45
4.1	Reconstruction efficiency of tau leptons	50
4.2	Schematic illustration of the signatures of the three τ -types in the detector	51
4.3	Distribution of the neural network input variables for τ -type 1	54
4.4	Distribution of the neural network input variables for τ -type 2	55
4.5	Distribution of the neural network input variables for τ -type 3	56

4.6	Distribution of the neural network output for each τ -type	57
4.7	Jet energy correction for data	58
4.8	Jet energy correction for Monte Carlo	59
5.1	Leading order Feynman graphs for $Z + \text{jet}/\gamma$ production	66
5.2	Leading order Feynman graphs for $W + \text{jet}/\gamma$ production	66
5.3	Leading order Feynman graphs for di-boson production	66
5.4	Leading order Feynman graphs for $t\bar{t}$ production	66
5.5	Level 1 trigger efficiency for scintillator and wire requirements	67
5.6	Level 2 trigger efficiency for a muon with $p_T > 3$ GeV and $p_T > 5$ GeV	68
5.7	Level 3 trigger efficiency for a track with $p_T > 10$ GeV	68
5.8	Trigger efficiencies as function of p_T , η_{det} and ϕ for the SUSY analysis	69
5.9	Muon reconstruction efficiency measured for Higgs analysis	69
5.10	Muon reconstruction efficiency for SUSY analysis in data and Monte Carlo	70
5.11	Track reconstruction efficiency	71
5.12	Correction factor of the generated boson transverse momentum	72
6.1	Cross section for neutral MSSM Higgs production as a function of their masses for $\tan\beta = 5$ and $\tan\beta = 40$	74
6.2	Feynman diagrams for the neutral MSSM Higgs boson production processes and subsequent decay into tau leptons	75
6.3	Feynman diagrams for the neutral MSSM Higgs boson production processes	75
6.4	Branching ratios of the MSSM Higgs bosons	76
6.5	Relative Higgs width as a function of $\tan\beta$	77
6.6	Cross section for $p\bar{p} \rightarrow \Phi \rightarrow \tau\tau$ as a function of M_Φ for different $\tan\beta$	79
6.7	Parameterization of the weighting functions for the multi-jet background	81
6.8	Distributions of p_T^τ before and after applying the p_T^τ dependent weights	81
6.9	Properties of τ -type 1 at the stage of preselection	83
6.10	Properties of τ -type 2 at the stage of preselection	84
6.11	Properties of τ -type 3 at the stage of preselection	85
6.12	Distribution of $M(\mu, \tau\text{-track})$ and CHF	86
6.13	Distributions of p_T^μ , p_T^τ , E_T , M_{vis} and τ -type after applying the cut on the neural network output	87
6.14	Distributions of M_W at different stages of the selection	88
6.15	Distribution of M_{vis} after applying all selection criteria for the each τ -type	90
6.16	Signal efficiency as a function of M_ϕ	94
6.17	Distribution of M_W after all cuts for the sum of all τ -types	94
6.18	Distributions of M_{vis} of all channels of the limit calculation	95
6.19	Distribution of M_{vis} for the $e\mu$ and the sum of $e\tau_h$ and $\mu\tau_h$ final states	96
6.20	The observed and expected 95 % CL limits on the cross section times branching ratio for $\Phi \rightarrow \tau\tau$ production	97
6.21	Regions which are excluded at the 95 % CL in the $(M_A, \tan\beta)$ -plane for the m_h^{max} and the no-mixing scenario	99
6.22	Regions with sizeable contributions of $\sigma(p\bar{p} \rightarrow h, H) \times \text{BR}(\tau\tau)$ to the total cross section and sizeable differences of $M_{h,H}$ and M_A	100
6.23	Invariant mass of the two leading jets from bottom quarks and expected and observed cross section limit for $\Phi b(\bar{b}) \rightarrow b\bar{b}b(\bar{b})$	100

6.24	Excluded regions in the $(M_A, \tan \beta)$ -plane for the m_h^{\max} and the no-mixing scenario after the combination of $\Phi \rightarrow \tau\tau$ and $\Phi b(\bar{b}) \rightarrow b\bar{b}b(\bar{b})$ analysis	101
6.25	Current DØ results from the search for $\Phi \rightarrow \tau\tau$ using 1 fb^{-1} of data	102
6.26	Current CDF results from the search for $\Phi \rightarrow \tau\tau$ using 1.8 fb^{-1} of data	103
6.27	Projected exclusion potential for combined DØ and CDF searches for $\Phi \rightarrow \tau\tau$ and combined sensitivity of the ATLAS and CMS experiments for the discovery of MSSM Higgs bosons	103
7.1	Distance of tau decay products as function of $p_T^{\tau, \text{vis}}$ and the distribution of the visible tau mass at Monte Carlo generator level in $Z/\gamma^* \rightarrow \tau\tau$ events	106
7.2	Schematic illustration of the signature of a low energetic tau decay in the detector and reconstruction efficiency for low energetic tau leptons	107
7.3	Variables used for LH_τ	109
7.4	Distribution of LH_τ	110
7.5	Distribution of quantities used in the selection of the tau mass signal at the stage of preselection	112
7.6	Distributions of the likelihood LH_τ	113
7.7	Distribution of p_T^τ after all selection criteria have been applied and correction factor for Monte Carlo events	113
7.8	Signal of the visible tau mass in the $\mu\tau_h$ final state and the reconstructed invariant mu-tau mass	115
8.1	Leading order diagrams for the production of chargino/neutralino pairs in quark-antiquark collisions	118
8.2	Next-to-leading order cross section (left) and resulting k -factor (right) for chargino/neutralino pair production as a function of the gaugino masses	118
8.3	Decay modes of the chargino via a W boson and via a sfermion	119
8.4	Decay modes of the neutralino via a Z boson and via a sfermion	120
8.5	Regions of changing kinematics and trilepton cross section in the $(m_0, m_{1/2})$ -plane	121
8.6	Generator level distribution of the transverse momentum of the three leptons for typical SUSY points considered in the analysis	122
8.7	Masses of SUSY particles and branching ratios for chargino and neutralino decays as function of $\tan \beta$	124
8.8	Cut values on the NN_τ output as a function of p_T^τ	125
8.9	Distributions of the di-muon selection	126
8.10	Distributions of the $\mu\tau_h$ selection	127
8.11	Distributions of the $W^\pm \rightarrow \mu^\pm \nu_\mu$ selection	128
8.12	Distributions of p_T^μ , $p_T^{\tau_1}$ and \cancel{E}_T at the level of preselection	134
8.13	Distributions of $\text{Sig}(\cancel{E}_T)$ at the level of preselection and before the cut is applied	135
8.14	Distributions of m_T^μ and $m_T^{\tau_1}$ at the level of preselection and before the cut is applied	136
8.15	Distributions of $\Delta\phi(\mu, \tau_1)$ and H_T at the level of preselection and before the cut is applied	137
8.16	Distributions of p_T^{track} and $M(\mu, \text{track})$ in the $\mu + \tau_1 + \text{track}$ selection	138
8.17	Distributions of $M(\tau_1, \text{track})$ and $\Delta\phi(\text{track}, \cancel{E}_T)$ in the $\mu + \tau_1 + \text{track}$ selection	139

8.18	Distributions of the variables used for the construction of the likelihood discriminator to separate the SUSY signal from $W^\pm \rightarrow \mu^\pm \nu_\mu$ background events	141
8.19	Distributions of the resulting likelihood discriminator $\text{LH}_W^{\text{track}}$ used for the separation of SUSY signal and $W^\pm + \text{jets} \rightarrow \mu^\pm \nu_\mu + \text{jets}$ background and the rejection as a function of the signal efficiency for a given cut	141
8.20	Distributions of $p_T^{\text{track}} \times \cancel{E}_T$ and $\text{LH}_W^{\text{track}}$ in the $\mu + \tau_1 + \text{track}$ selection	142
8.21	Optimization for the best expected limit	143
8.22	Distributions of variables used in the $\mu + \tau_1 + \tau_2$ selection	145
8.23	Distributions of p_T^{LP} and LH_τ in the $\mu + \tau_1 + \tau_{LP}$ selection	146
8.24	Distributions of variables used in the $\mu + \tau_1 + \tau_{LP}$ selection	147
8.25	Event display of the event selected in data in the $\mu + \tau_1 + \tau_2$ selection	152
8.26	Efficiency of the three selections as function of $\tan \beta$	155
8.27	Efficiency of the $\mu\tau_h\ell$ analysis as a function of m_Δ and $m_{\tilde{\chi}_1^\pm}$	155
8.28	The limit on the trilepton cross section as a function of $m_{\tilde{\chi}_1^\pm}$ and m_Δ	156
8.29	The limit on the trilepton cross section as a function of $\tan \beta$	157
8.30	Exclusion region of the $\mu\tau_h\ell$ analysis in the $(m_0, m_{1/2})$ -plane	158
8.31	The limit on the trilepton cross section as a function of $\tan \beta$ in a combination with complementary trilepton searches	159
8.32	Expected exclusion regions in the $(m_0, m_{1/2})$ -plane for a combination of all $D\emptyset$ trilepton searches	160
8.33	Projection of the $D\emptyset$ upper boundary on the trilepton cross section	161
8.34	Diagram of a cascade decay of a gluino and distribution of the effective mass	162
8.35	Discovery reach of the LHC experiments ATLAS and CMS in the $(m_0, m_{1/2})$ -plane for various SUSY signatures	163
8.36	Di-lepton mass distributions for a SUSY signal and background, and an example fit for the determination of the endpoint	164
A.1	Probability densities for a test statistic under the assumption of the hypotheses H_0 and H_1	170
A.2	Illustration of the evolution of the p.d.f.s with increasing search sensitivity	172
B.1	Distributions of p_T^τ in the multi-jet dominated sample	174
B.2	Distributions of \cancel{E}_T in the multi-jet dominated sample	176
B.3	Effect of the normalization of the multi-jet background on the distribution of m_T^μ and H_T	177
B.4	Distributions of RMS^τ in the multi-jet dominated sample	178
B.5	Distributions of N_{jets} in the multi-jet dominated sample	179
C.1	Generated SUSY points in the mSUGRA model	182

Bibliography

- [1] F. Halzen and A.D. Martin, *Quarks and Leptons*, John Wiley & Sons, 1984.
- [2] B.R. Martin and G. Shaw, *Particle Physics*, John Wiley & Sons, 1997.
- [3] P.D.B. Collins, A.D. Martin and E.J. Squires, *Particle Physics and Cosmology*, John Wiley & Sons, 1989.
- [4] R.N. Mohapatra, *Unification and Supersymmetry*, Springer Verlag, New York, Berlin, Heidelberg, 2003.
- [5] H. Baer and X. Tata, *Weak Scale Supersymmetry*, Cambridge University Press, 2006.
- [6] J. Terning, *Modern Supersymmetry*, Oxford Science Publications, 2007.
- [7] G. Altarelli, R. Barbieri and F. Caravaglios, *Electroweak Precision Tests: A Concise Review*, Int. J. Mod. Phys. **A13** (1998) 1031.
- [8] Y. Fukuda et al., *Evidence for Oscillation of Atmospheric Neutrinos*, Phys. Rev. Lett. **81** (1998) 1562.
- [9] W. Greiner, S. Schramm and E. Stein, *Quantum Chromodynamics*, Springer Verlag, New York, Berlin, Heidelberg, 2002.
- [10] J.F. Gunion, H.E. Haber, G. Kane and S. Dawson, *The Higgs Hunter's Guide*, Perseus Books, 1990.
- [11] G. Abbiendi, *Search for the Standard Model Higgs Boson at LEP*, Phys. Lett. **B565** (2003) 61.
- [12] Tevatron New Phenomena and Higgs Working Group, *Combined CDF and DØ Upper Limits on Standard Model Higgs Boson Production with up to 2.4 fb⁻¹ of data*, hep-ex/0804.3423, 2008.
- [13] LEPWWG, ALEPH, DELPHI, L3 and OPAL experiments, <http://lepewwg.web.cern.ch/LEPEWWG/>.
- [14] C. Kraus et al., *Final Results from Phase II of the Mainz Neutrino Mass Search in Tritium β Decay*, Eur. Phys. J. **C40** (2005) 447.
- [15] Tevatron Electroweak Working Group for the CDF and DØ Collaborations, *A Combination of CDF and DØ Results on the Mass of the Top Quark*, hep-ex/0803.1683, 2008.
- [16] M. Drees, *An Introduction to Supersymmetry*, hep-ph/9611409, 1996.

- [17] E. Komatsu et al., *Five-Year Wilkinson Microwave Anisotropy Probe (WMAP) Observations: Cosmological Interpretation*, Submitted to the Astrophysical Journal Supplement Series, astro-ph/0803.0547, 2008.
- [18] Y.A. Golfand and E.P. Likhtman, *Extension of the Algebra of Poincare Group Generators and Violation of p Invariance*, JETP Lett. **13** (1971) 323.
- [19] D.V. Volkov and V.P. Akulov, *Possible Universal Neutrino Interaction*, JETP Lett. **16** (1972) 438.
- [20] J. Wess and B. Zumino, *A Lagrangian Model Invariant Under Supergauge Transformations*, Phys. Lett. **B49** (1974) 52.
- [21] W. de Boer and C. Sander, *Global Electroweak Fits and Gauge Coupling Unification*, Phys. Lett. **B585** (2004) 276.
- [22] A. Salam and J. Strathdee, *On Superfields and Fermi-Bose Symmetry*, Phys. Rev. **D11** (1975) 1521.
- [23] A. Salam and J. Strathdee, *Supergauge Transformations*, Nucl. Phys. **B76** (1974) 477.
- [24] L. O’Raifeartaigh, *Spontaneous Symmetry Breaking for Chiral Scalar Superfields*, Nucl. Phys. **B96** (1975) 331.
- [25] P. Fayet and J. Iliopoulos, *Spontaneously Broken Supergauge Symmetries and Goldstone Spinors*, Phys. Lett. **B51** (1974) 461.
- [26] G. R. Dvali and Alex Pomarol, *Anomalous $U(1)$ as a Mediator of Supersymmetry Breaking*, Phys. Rev. Lett. **77** (1996) 3728.
- [27] R. N. Mohapatra and A. Riotto, *Supersymmetric Models with Anomalous $U(1)$ Mediated Supersymmetry Breaking*, Phys. Rev. **D55** (1997) 4262.
- [28] L. Randall and R. Sundrum, *Out Of This World Supersymmetry Breaking*, Nucl. Phys. **B557** (1999) 79.
- [29] G.R. Farrar and P. Fayet, *Phenomenology of the Production, Decay, and Detection of New Hadronic States Associated with Supersymmetry*, Phys. Lett. **B76** (1978) 575.
- [30] G. Bertone, D. Hooper and J. Silk, *Particle Dark Matter: Evidence, Candidates and Constraints*, Phys. Rep. **405** (2005) 279.
- [31] M. Shiozawa et al., *Search for Proton Decay via $p \rightarrow e^+ \pi^0$ in a Large Water Cherenkov Detector*, Phys. Rev. Lett. **81** (1998) 3319.
- [32] Y. Hayato et al., *Search for Proton Decay Through $p \rightarrow \bar{\nu} K^+$ in a Large Water Cherenkov Detector*, Phys. Rev. Lett. **83** (1999) 1529.
- [33] H.E. Haber and G.L. Kane, *The Search for Supersymmetry: Probing Physics Beyond the Standard Model*, Phys. Rep. **117** (1985) 75.
- [34] H. Nilles, *Supersymmetry, Supergravity and Particle Physics*, Phys. Rep. **110** (1984) 1.

-
- [35] S.P. Martin, *A Supersymmetry Primer*, hep-ph/9709356v4, 2006.
- [36] S. Eidelman et al., *Review of Particle Physics*, Phys. Lett. **B592** (2004) 1.
- [37] A. Djouadi, J.L. Kneur and G. Moultaka, *SuSpect: A Fortran Code for the Supersymmetric and Higgs Particle Spectrum in the MSSM*, Comp. Phys. Comm. **176** (2007) 426.
- [38] C. Csaki, *The Minimal Supersymmetric Standard Model (MSSM)*, Mod. Phys. Lett. **A11** (1996) 599.
- [39] G. Degrossi et al., *Towards High-Precision Predictions for the MSSM Higgs Sector*, Eur. Phys. J. **C28** (2003) 133.
- [40] M. Carena, S. Heinemeyer, C.E.M. Wagner and G. Weiglein, *Suggestions for Benchmark Scenarios for MSSM Higgs Boson Searches at Hadron Colliders*, Eur. Phys. J. **C26** (2003) 601.
- [41] V.D. Barger, M.S. Berger and P. Ohmann, *The Supersymmetric Particle Spectrum*, Phys. Rev. **D49** (1994) 4908.
- [42] S. Heinemeyer et al., *Precise Prediction for M_W in the MSSM*, JHEP **0608** (2006) 052.
- [43] S. Heinemeyer, W. Hollik and G. Weiglein, *Electroweak Precision Observables in the Minimal Supersymmetric Standard Model*, Phys. Rep. **425** (2006) 265.
- [44] A. Djouadi et al., *Leading QCD Corrections to Scalar Quark Contributions to Electroweak Precision Observables*, Phys. Rev. **D57** (1998) 4179.
- [45] A. Djouadi et al., *Supersymmetric Contributions to Electroweak Precision Observables: QCD corrections*, Phys. Rev. Lett. **78** (1997) 3626.
- [46] S. Heinemeyer and G. Weiglein, *Leading Electroweak Two-Loop Corrections to Precision Observables in the MSSM*, JHEP **0210** (2002) 072.
- [47] J. Haestier, S. Heinemeyer, D. Stockinger and G. Weiglein, *Electroweak Precision Observables: Two-Loop Yukawa Corrections of Supersymmetric Particles*, JHEP **0512** (2005) 027.
- [48] G.W. Bennett et al., *Measurement of the Negative Muon Anomalous Magnetic Moment to 0.7 ppm*, Phys. Rev. Lett. **92** (2004) 161802.
- [49] V.M. Abazov et al., *Search for $B_s \rightarrow \mu^+ \mu^-$ at $D\bar{O}$* , Phys. Rev. **D76** (2007) 092001.
- [50] T. Aaltonen et al., *Search for $B_s \rightarrow \mu^+ \mu^-$ and $B_d \rightarrow \mu^+ \mu^-$ Decays with 2 fb^{-1} of $p\bar{p}$ Collisions*, Phys. Rev. Lett. **100** (2008) 101802.
- [51] K.W. Edwards et al., *Search for Baryons in the Radiative Penguin Decay $b \rightarrow s\gamma$* , Phys. Rev. **D68** (2003) 011102.
- [52] P. Koppenburg et al., *An Inclusive Measurement of the Photon Energy Spectrum in $b \rightarrow s\gamma$ Decays*, Phys. Rev. Lett. **93** (2004) 061803.

- [53] L. Roszkowski, R. Ruiz de Austri and T. Nihei, *New Cosmological and Experimental Constraints on the CMSSM*, JHEP **0108** (2001) 024.
- [54] LEPSUSYWG, ALEPH, DELPHI, L3 and OPAL experiments, LEPSUSYWG/04-01.1, <http://lepsusy.web.cern.ch/lepsusy/Welcome.html>.
- [55] LEPSUSYWG, ALEPH, DELPHI, L3 and OPAL experiments, LEPSUSYWG/01-03.1, <http://lepsusy.web.cern.ch/lepsusy/Welcome.html>.
- [56] LEPSUSYWG, ALEPH, DELPHI, L3 and OPAL experiments, LEPSUSYWG/02-06.2, <http://lepsusy.web.cern.ch/lepsusy/Welcome.html>.
- [57] LEPSUSYWG, ALEPH, DELPHI, L3 and OPAL experiments, LEPSUSYWG/04-07.1, <http://lepsusy.web.cern.ch/lepsusy/Welcome.html>.
- [58] A. Heister et al., *Absolute Mass Lower Limit for the Lightest Neutralino of the MSSM from e^+e^- Data at \sqrt{s} up to 209 GeV*, Phys. Lett. **B583** (2004) 247.
- [59] B. Abbott et al., *Search for the Trilepton Signature from Associated Gaugino Pair Production*, Phys. Rev. Lett. **80** (1998) 1591.
- [60] K. Ackerstaff et al., *Search for Chargino and Neutralino Production in e^+e^- Collisions at $\sqrt{s} = 161$ GeV*, Phys. Lett. **B389** (1996) 616.
- [61] F. Abe et al., *Search for Chargino Neutralino associated Production at the Fermilab Tevatron Collider*, Phys. Rev. Lett. **80** (1998) 5275.
- [62] The ALEPH, DELPHI, L3, OPAL Collaborations and The LEP Working Group for Higgs Boson Searches, *Search for Neutral MSSM Higgs Bosons at LEP*, hep-ex/0602042, 2006.
- [63] T. Sjöstrand, *2006 European School of High-Energy Physics, Aronsborg, Sweden, 18 Jun-1 Jul 2006: Proceedings*, CERN-2007-005, 2007.
- [64] V. M. Braun, *2000 European School of High-Energy Physics, Caramulo, Portugal, 20 Aug-2 Sep 2000: Proceedings*, CERN-2001-003, 2001.
- [65] Guido Altarelli and G. Parisi, *Asymptotic Freedom in Parton Language*, Nucl. Phys. **B126** (1977) 298.
- [66] J. Pumplin et al., *New Generation of Parton Distributions with Uncertainties from Global QCD Analysis*, JHEP **0207** (2002) 012.
- [67] T. Sjöstrand, L. Lonnblad, S. Mrenna and P. Skands, *PYTHIA 6.3 Physics and Manual*, hep-ph/0308153, 2003.
- [68] S. Jadach, Z. Was, R. Decker and Johann H. Kuhn, *The Tau Decay Library TAUOLA: Version 2.4*, Comp. Phys. Comm. **76** (1993) 361.
- [69] P. Golonka et al., *The Tauola-Photos-F Environment for the TAUOLA and PHOTOS Packages, Release II*, Comp. Phys. Comm. **174** (2006) 818.
- [70] T. Gleisberg et al., *SHERPA 1.α, a Proof-of-Concept Version*, JHEP **0402** (2004) 056.

-
- [71] M. L. Mangano et al., *ALPGEN, a Generator for Hard Multiparton Processes in Hadronic Collisions*, JHEP **0307** (2003) 001.
- [72] S. Eidelman et al., *Review of particle physics*, Phys. Lett. **B592** (2004) 1.
- [73] T. Sjöstrand et al., *High-Energy-Physics Event Generation with PYTHIA 6.1*, Comp. Phys. Comm. **135** (2001) 238.
- [74] Bo Andersson, *The Lund Model*, Camb. Monogr. Part. Phys. Nucl. Phys. Cosmol. **7** (1997) 1.
- [75] Fermi National Accelerator Laboratory, <http://www.fnal.gov>.
- [76] Fermilab Beams Division, *Run II Handbook*, <http://www-bd.fnal.gov/runII/index.html>, 2003.
- [77] DØ Collaboration, <http://www-d0.fnal.gov>.
- [78] CDF Collaboration, <http://www-cdf.fnal.gov>.
- [79] Large Hadron Collider, <http://lhc.web.cern.ch/lhc/>.
- [80] Fermilab Accelerator Division, <http://www-bd.fnal.gov/>.
- [81] TeVI Group, *Design Report Tevatron 1 Project*. FERMILAB-DESIGN-1984-01.
- [82] D. Mohl, G. Petrucci, L. Thorndahl and Simon van der Meer, *Physics and Technique of Stochastic Cooling*, Phys. Rep. **58** (1980) 73.
- [83] S. Abachi et al., *The DØ Detector*, Nucl. Instrum. Meth. **A338** (1994) 185.
- [84] DØ Collaboration, *The Upgraded DØ Detector*, Nucl. Instrum. Meth. **A565** (2006) 463.
- [85] DØ Muon Group: V.M. Abazov, *The Muon System of the Run II DØ Detector*, Nucl. Instrum. Meth. **A552** (2005) 372.
- [86] J. Anderson et al., *The DØ Central Track Trigger*, IEEE Trans. Nucl. Sci. **51** (2004) 345.
- [87] M. Fortner et al., *The Level-2 Muon Trigger at DØ*, IEEE Trans. Nucl. Sci. **49** (2002) 1589.
- [88] DØ Collaboration, <http://www-d0.fnal.gov/D0Code/source/d0reco>.
- [89] DØ Data Format Working Group, *Recommendations Regarding Common Analysis Format Content*, DØ Note 4647.
- [90] DØ Common Samples Group, <http://www-d0.fnal.gov/Run2Physics/cs/index.html>.
- [91] R. Brun and F. Rademakers, *ROOT: An Object Oriented Data Analysis Framework*, Nucl. Instrum. Meth. **A389** (1997) 81.
- [92] Y. Fisyak and J. Womersley, *DØGSTAR, DØ GEANT Simulation of the Total Apparatus Response*, DØ Note 3191.

- [93] DØ Collaboration, <http://www-d0.fnal.gov/computing/MonteCarlo/simulation/d0sim.html>.
- [94] CERN Computing Application Software Group and Networks Division, *GEANT, Detector Description and Simulation Tool*, CERN Program Library Long Writeup W5013, 2003.
- [95] G. Borisov, http://www-d0.fnal.gov/global_tracking/talks/20030228/talk-adm-030228.ps.
- [96] A. Khanov, *HTF: Histogramming Method for Finding Tracks*, DØ Note 3778.
- [97] A. Garcia-Bellido, S. Lager, F. Rizatdinova, A. Schwarzman and G. Watts, *Primary Vertex Certification in p14*, DØ Note 4320.
- [98] Y. Peters, A. Schwarzman and M. Strauss, *Certification of the Adaptive Primary Vertex in p17*, DØ Note 5192.
- [99] DØ Muon ID group, *Muon Identification Certification for p14 Data*, DØ Note 4350.
- [100] DØ Muon ID Group, *Muon Identification Certification for p17 Data*, DØ Note 5157.
- [101] DØ Tau ID Group, *Reconstruction of Tau Leptons in Hadronic Final States at DØ Run II*, DØ Note 4210.
- [102] DØ Tau ID Group, *Tau Identification with Neural Networks for p17 Data*, DØ Note 5094.
- [103] DØ Tau ID Group, *Tau Identification Certification for p14*, DØ Note 4453.
- [104] DØ Jet Energy Scale Group, *Jet Energy Scale Determination at DØ Run II (Final p17 Version)*, DØ Note 5382.
- [105] B. Andrieu and E. Busato, *Jet Algorithms in the DØ Run II Software: Description and User's Guide*, DØ Note 4457.
- [106] A. Harel, *Jet ID Optimization*, DØ Note 4919.
- [107] DØ Data Quality Group, http://www-d0.fnal.gov/computing/data_quality.
- [108] DØ Trigger Studies Group, *ORing Single Muon Triggers in p17 Data*, DØ Note 5329.
- [109] DØ Collaboration, *Triggermeister Web Page*, http://www-d0online.fnal.gov/www/groups/tm/tm_main.html.
- [110] T. Edwards et al., *The Updated DØ Luminosity Determination – Short Summary*, DØ Note 4328.
- [111] T. Edwards et al., *Determination of the Effective Inelastic $p\bar{p}$ Cross Section for the DØ Run II Luminosity Measurement*, FERMILAB-TM-2278-E.
- [112] R. Hamberg, W. L. van Neerven and T. Matsuura, *A Complete calculation of the order α_s^2 correction to the Drell–Yan K factor*, Nucl. Phys. **B359** (1991) 343. [Erratum-ibid. B644:402, 2002].

-
- [113] T. Nunnemann, *NNLO Cross Sections for Drell-Yan, Z and W Production using Modern Parton Distribution Functions*, DØ Note 4476.
- [114] DØ New Phenomena MC web page, http://www-clued0.fnal.gov/~nunne/cross-sections/mcfm_cross-sections.html.
- [115] N. Kidonakis and R. Vogt, *Theoretical Status of the Top Quark Cross Section*, Int. J. Mod. Phys. **A20** (2005) 3171.
- [116] H.L. Lai et al., *Global QCD Analysis of Parton Structure of the Nucleon: CTEQ5 Parton Distributions*, Eur. Phys. J. **C12** (2000) 375.
- [117] B. Tiller and T. Nunnemann, *Measurement of the Differential Z^0 Boson Production Cross Section as Function of Transverse Momentum*, DØ Note 4660.
- [118] TeV4LHC Higgs working group, *Higgs cross sections at hadron colliders*, <http://maltoni.home.cern.ch/maltoni/TeV4LHC/>.
- [119] M. Carena, J.S. Conway, H.E. Haber and J.D. Hobbs, *Report of the Higgs Working Group of the Tevatron Run 2 SUSY/Higgs Workshop*, hep-ph/0010338, 2000.
- [120] DØ Collaboration, *Search for $h_f \rightarrow \gamma\gamma$ with the DØ detector at $\sqrt{s} = 1.96$ TeV*, Submitted to Phys. Rev. Lett., hep-ex/0803.1514, 2008.
- [121] M. Frank et al., *The Higgs Boson Masses and Mixings of the Complex MSSM in the Feynman-Diagrammatic Approach*, JHEP **0702** (2007) 047.
- [122] S. Heinemeyer, W. Hollik and G. Weiglein, *The Masses of the Neutral CP-even Higgs Bosons in the MSSM: Accurate Analysis at the Two-Loop Level*, Eur. Phys. J. **C9** (1999) 343.
- [123] S. Heinemeyer, W. Hollik and G. Weiglein, *FeynHiggs: A Program for the Calculation of the Masses of the Neutral CP-even Higgs Bosons in the MSSM*, Comp. Phys. Comm. **124** (2000) 76.
- [124] M. Carena, S. Heinemeyer, C.E.M. Wagner and G. Weiglein, *MSSM Higgs Boson Searches at the Tevatron and the LHC: Impact of Different Benchmark Scenarios*, Eur. Phys. J. **C45** (2006) 797.
- [125] CDF collaboration, DØ Collaboration and the Tevatron Electroweak Working Group, *Combination of CDF and DØ Results on the Top-Quark Mass*, hep-ex/0507091, 2005.
- [126] DØ Collaboration, *Measurement of $\sigma(p\bar{p} \rightarrow Z) \cdot \text{BR}(Z \rightarrow \tau\tau)$ at $\sqrt{s} = 1.96$ TeV*, Phys. Rev. **D71** (2005) 072004.
- [127] V. Büscher, C. Nöding, M. Titov and I. Torchiani, *Search for Neutral Higgs Bosons Decaying to Tau Pairs*, DØ Note 4952.
- [128] DØ Collaboration, *Search for Neutral Higgs Bosons Decaying to Tau Pairs in $p\bar{p}$ Collisions at $\sqrt{s} = 1.96$ TeV*, Phys. Rev. Lett. **97** (2006) 121802.

- [129] CDF Collaboration, *Search for Neutral Higgs Bosons of the Minimal Supersymmetric Standard Model Decaying to Tau Pairs in $p\bar{p}$ Collisions at $\sqrt{s} = 1.96$ TeV*, Phys. Rev. Lett. **96** (2006) 011802.
- [130] DØ Collaboration, *Search for Neutral Supersymmetric Higgs Bosons in Multi-Jet Events at $\sqrt{s} = 1.96$ TeV*, Phys. Rev. Lett. **95** (2005) 151801.
- [131] DØ Collaboration, *Search for Higgs Bosons Decaying to Tau Pairs in $p\bar{p}$ Collisions with the DØ Detector*, Submitted to Phys. Rev. Lett., hep-ex/0805.2491, 2008.
- [132] CDF Collaboration, *Search for Neutral MSSM Higgs Bosons Decaying to Tau Pairs with 1.8 pb^{-1} of Data*, CDF Note 9071.
- [133] DØ Collaboration, *Search for Higgs Neutral Bosons in Multi-b-Jet Events in $p\bar{p}$ Collisions at $\sqrt{s} = 1.96$ TeV*, Submitted to Phys. Rev. Lett., hep-ex/0805.3556, 2008.
- [134] CDF Collaboration, <http://www-cdf.fnal.gov/physics/projections/>.
- [135] V. Büscher and K. Jakobs, *Higgs Boson Searches at Hadron Colliders*, Int. J. Mod. Phys. **A20** (2005) 2523.
- [136] L. Duflot and M. Ridet, *The CellNN Algorithm: Cell Level Clustering in the DØ Calorimeter*, DØ Note 3923.
- [137] DØ Collaboration, *Search for Squarks and Gluinos in Events with Jets and Missing Transverse Energy using 2.1 fb^{-1} of $p\bar{p}$ Collision Data at $\sqrt{s} = 1.96$ TeV*, Phys. Lett. **B660** (2008) 449.
- [138] CDF Collaboration, *Search for Gluinos and Squarks in Multij-Jets plus Missing Transverse Energy Final States*, CDF Note 9229.
- [139] W. Beenakker et al., *The Production of Charginos/Neutralinos and Sleptons at Hadron Colliders*, Phys. Rev. Lett. **83** (1999) 3780.
- [140] V. Barger and C.E.M. Wagner, *Report of the SUGRA Working Group for Run II of the Tevatron*, hep-ph/0003154, 2000.
- [141] O. Mundal, *Search for the Associated Production of Charginos and Neutralinos in $p\bar{p}$ Collisions at 1.96 TeV*, PhD thesis in preparation.
- [142] V. Büscher, M. Hohlfeld and O. Mundal, *Search for the Associated Production of Chargino and Neutralino in the $e + \mu + \ell$ Final State in 2 fb^{-1}* , DØ Note in preparation.
- [143] C. Nöding, *Search for New Physics in $e + \tau$ Final States in $p\bar{p}$ Collisions at 1.96 TeV*, PhD thesis, 2006.
- [144] DØ Collaboration, *Search for the Associated Production of Chargino and Neutralino in the Like-Sign Di-Muon Channel*, DØ Note 5126-CONF, 2006.
- [145] I. Torchiani, *Search for the Associated Production of Charginos and Neutralinos in the $\mu + \tau + \ell$ Final State in $\mathcal{L} = 1$ fb^{-1}* , DØ Note 5630.

-
- [146] U. Blumenschein, *Search for the Associated Production of Charginos and Neutralinos in $p\bar{p}$ Collisions at 1.96 TeV*, PhD thesis, 2004.
- [147] A. Höcker et al., *TMVA - Toolkit for Multivariate Data Analysis*, physics/0703039, 2007.
- [148] M. Arthaud et al., *Muon Momentum Oversmearing for $p17$ Data*, DØ Note 5444.
- [149] N. Makovec and J.F. Grivaz, *Shifting, Smearing and Removing Simulated Jets*, DØ Note 4914.
- [150] V. Büscher, H. Fox, O. Mundal and M. Titov, *Search for the Associated Production of Chargino and Neutralino in the $e + e + \ell$ Final State*, DØ Note 5131.
- [151] V. Büscher, H. Fox and Olav Mundal, *Search for the Associated Production of Chargino and Neutralino in the $\mu + \mu + \ell$ Final State*, DØ Note 5326.
- [152] V. Büscher, H. Fox, O. Mundal and M. Titov, *Search for the Associated Production of Chargino and Neutralino in the $e + \mu + \ell$ Final State*, DØ Note 5298.
- [153] W. Beenakker, R. Höpker, M. Spira and P.M. Zerwas, *Squark and Gluino Production at Hadron Colliders*, Nucl. Phys. **B492** (1997) 51.
- [154] ATLAS Collaboration, *ATLAS: Detector and Physics Performance Technical Design Report, Vol. II*, CERN-LHCC-99-15, 1999.
- [155] Atlas Collaboration, *CSC Note, Supersymmetry*, In preparation.
- [156] S. Villa, *Discovery Potential for SUGRA/SUSY at CMS*, CMS CR 2003/033, 2003.
- [157] R.J. Barlow, *Statistics*, John Wiley & Sons, 1989.
- [158] G. Cowan, *Statistical Data Analysis*, Oxford Science Publications, 1998.
- [159] T. Junk, *Confidence Level Computation for Combining Searches with Small Statistics*, Nucl. Instrum. Meth. **A434** (1999) 435.
- [160] V. Büscher et al., *Recommendations of the Ad-Hoc Committee on Limit-Setting Procedures to be Used by DØ in Run II*, DØ Note 4629.
- [161] *TLimit, C++ Class for Limit Computation in ROOT*, Code adapted from MCLimit code from T. Junk.
- [162] Robert D. Cousins and Virgil L. Highland, *Incorporating Systematic Uncertainties into an Upper Limit*, Nucl. Instrum. Meth. **A320** (1992) 331.
- [163] B.C. Allanach, *SOFTSUSY: A Program for Calculating Supersymmetric Spectra*, Comp. Phys. Comm. **143** (2002) 305.
- [164] M. Muhlleitner, A. Djouadi and Y. Mambrini, *SDECAY: A Fortran code for the decays of the supersymmetric particles in the MSSM*, Comp. Phys. Comm. **168** (2005) 46.

Acknowledgements

First of all I would like to thank Karl Jakobs for giving me the opportunity to graduate in his group and for his support during the lots of highs and lows of my time as PhD student. Even if our meetings were rare during your stay at CERN, they were always very motivating. And thanks for being so convincing that I often agreed happily to points that I did not intend to agree to in the first place.

Let me go on with a big “thank you” to all my DØ colleagues which helped me with the analyses. I would like in particular thank the following:

I thank Volker for all I could learn from him, the effort he put into the analyses and for always knowing a solution no matter how challenging the situation was. Without your support, in particular after you went to Bonn, this thesis would not have been possible.

Ralf, I thank you for lots of fruitful discussions, reading all the pages up to the end and especially for the trips to the mountains. Gallenstock is still calling! I would like to thank also Harald for helpful discussions and to say sorry for the broken bike on Roskopf.

Olav, even if you escaped to Bonn, thanks for sitting in the same boat as me and for lots of discussions on the tripletons. It has been fun to work with you. Henrik, thank you for the trips to the Alps, for lots of good wine, the ice cream breaks and for being my DØ PhD companion in the group. Carsten, thanks for convincing me to stay with DØ in the very beginning, for being my office mate for a long time and for keeping my spirits high: “Breathe in – breathe out!”. Jens, sorry for escaping to the 3rd floor and thanks for helping fight against the small but steady challenges of the software. Björn, thanks for being there and for taking care of the computer at Fermilab. Ulla, thanks for your unbreakable motivation for physics and in particular for the tripletons. Ralf, Cano and Daniela, I would like to thank you for a great stay in Florida. *Gamsa hamnida* to Su-Jung for being our tour guide in Seoul.

Of course, there are lots of ATLAS people in the 2nd and 3rd floor that I owe a big thanks to. You are too many to list all of you. Giacinto, Inga, Susanne and Uli, thanks for the biking; Evelyn and Jörg, thanks for being there during long evenings in the office; Stefan, thanks for the challenges on the race track; thanks to Andrea and Michael and “Vielen Dank, Herr Doktor, und Grüße an die Gemahlin.” Simon, thanks for explaining the hardware, and to the other Simon: thanks for the beer, it only has to wait a few more lines.

Thank you Alberto and Jürgen for being there when I was in need of a theoretician.

Thank you Chris, for helping with the paper work, and Ines, for always filling the cookies depot. Sorry that you are named almost at the end of this page but this means you come right before my parents.

I thank my parents for their never-ending support in every way, for always having an open door and just thank you that you are there. Carolin, “meine Lieblings Schwester”, thanks for lots of motivation, the mathematics, for helping with the grammar and for fighting with the typos. I am almost on my way to Firenze. Doug, I had a good time staying in your place and thanks for lots of nice trips with the camera! I would like to thank Christina for proof-reading, Helga and Arno for the wine, Alex for appearing every now and then in the office, Ernst for two nice days of biking in the Black Forest and Walter for a challenging trip to France.

Last but not least, merci vielmal Silke, for always lifting my spirits and for your patience and understanding.